DEVELOPMENT OF SHORT STEEL FIBER REINFORCED ALUMINIUM BASED COMPOSITES BY P/M ROUTE

Ph.D. THESIS

by

SIDHARTH JAIN

DEPARTMENT OF METALLURGICAL AND MATERIALS ENGINEERING
INDIAN INSTITUTE OF TECHNOLOGY ROORKEE
ROORKEE – 247667, INDIA
JUNE, 2014

DEVELOPMENT OF SHORT STEEL FIBER REINFORCED ALUMINIUM BASED COMPOSITES BY P/M ROUTE

A THESIS

Submitted in partial fulfilment of the requirements for the award of the degree of

DOCTOR OF PHILOSOPHY

in

METALLURGICAL AND MATERIALS ENGINEERING

by

SIDHARTH JAIN

DEPARTMENT OF METALLURGICAL AND MATERIALS ENGINEERING
INDIAN INSTITUTE OF TECHNOLOGY ROORKEE
ROORKEE – 247667, INDIA
JUNE, 2014

INDIAN INSTITUTE OF TECHNOLOGY ROORKEE
ROORKEE

CANDIDATE'S DECLARATION

I hereby certify that the work which is being presented in the thesis, entitled **"DEVELOPMENT OF SHORT STEEL FIBER REINFORCED ALUMINIUM BASED COMPOSITES BY P/M ROUTE"** in partial fulfilment of the requirements for the award of the degree of **Doctor of Philosophy** and submitted in the Department of Metallurgical and Materials Engineering, Indian Institute of Technology Roorkee, Roorkee is an authentic record of my own work carried out during the period from January, 2009 to June, 2014 under the supervision of Dr. V. Agarwala, Professor, Department of Metallurgical and Materials Engineering, Indian Institute of Technology Roorkee, Roorkee and Dr. K. Chandra, Professor (Visiting), Center of Excellence: Nanotechnology, Ex-Professor, Department of Metallurgical and Materials Engineering, Indian Institute of Technology Roorkee, Roorkee.

The matter presented in this thesis has not been submitted by me for the award of any other degree of this or any other institute.

(**SIDHARTH JAIN**)

This is to certify that the above statement made by the candidate is correct to the best of our knowledge.

(V.Agarwala)
Supervisor

(K. Chandra)
Supervisor

Date:

The Ph.D. Viva-Voce Examination of **Mr. Sidharth Jain,** Research Scholar, has been held on _____

Signature of Supervisors | Chairman, SRC | Signature of External Examiner

Head of the Deptt. / Chairman ODC

ABSTRACT

Light alloy MMC systems based on Al and Mg matrices with ceramic reinforcements of particulate, whisker and short fiber morphologies have been well developed and extensively investigated. Metal-metal MMC systems have been considerably less researched on account of intermetallic phase at the interface, which is generally unstable, brittle, suitable for limited structural applications and susceptible to environmental degradation. However, potential structural and non-structural application areas like high temperature application, corrosion resistance, magnetic materials and wear resistant elements have been explored for such class of materials. The aim of the present work is to develop aluminium P/M based composites reinforced with short steel fibers for wear resistant and elevated temperature service.

Al-0.5 wt. % Mg matrix powder blend was sintered in N_2 atmosphere. The role of Mg as a sintering aid was determined by SEM in backscatter mode to highlight pore morphology and necking phenomenon. Particle to particle bridging and pore filling aided by Mg particles was revealed.

A steady growth of the reaction interface with pressing time was observed in Al-0.5Mg-10 wt.% short steel fiber green preforms vacuum hot pressed at 823 K under 50 MPa linearly increasing stress. Line scans along the steel fibers, confirmed the presence of a reaction interface, and formed as a result of inter-diffusion of Fe and Al. The interface growth kinetics followed a parabolic law which was indicative of a diffusion controlled mechanism. The value of parabolic rate constant, determined from slope of the straight line portion of the curve was 1.41×10^{-12} m^2 s^{-1} at 823 K.

The untreated fibers had a cold worked structure composed of ferrite and pearlite. Surface modification and heat treatment of fibers was carried out in a fluidized bed reactor, to alter their surface chemistry and thereby inhibit growth of brittle Fe-Al intermetallics. Nitriding treatments for the fibers resulted the development of case, composed of γ'-Fe4N and ε-$Fe_{2-3}N$ phases with respect to different nitriding durations. Chromizing of the short steel fibers resulted in loss of hardness and absence of any hard carbides due to the low carbon content of steel fibers, 0.38wt.% C and absence of Cr

Chromizing treatment on steel fibers was successful in partially inhibiting growth of Fe_xAl_y type of reaction interface. Aluminizing treatment resulted in formation of a strongly adherent

layer composed of $FeAl_3$ of about 7μm thickness (890 VHN). $FeAl_3$ is significantly more ductile than Fe_2Al_5, and hence. Upon sintering under similar conditions, a tongue like growth of this reaction interface towards the Al-0.5Mg matrix is observed with Kirkendall voids at regular intervals.

It was observed that density, hardness and porosity increased with increasing content of short steel fibers. Matrix hardness increased to a maximum of 78 VHN for 30.wt.% reinforcement from 34 VHN for monolithic composition Regions lying within agglomerates of fibers were left unfilled during cold compaction; these unfilled spaces are retained as voids post sintering. An appreciable increase in matrix microhardness is observed from 10 to 20 wt.% reinforcement content, whereas the same was not obtained from 20 to 30 wt.%. For 10 wt.%, the volume fraction of fibers (3.7 vol.%) was insufficient to cause matrix hardening; for 30 wt.%, the unfilled voids within agglomerates of the steel fibers, negate the effect of matrix strengthening, as determined, there was a marked increase in porosity volume fraction from 20 to 30 wt.% reinforced composites.

In the present investigation, the reaction interface of a maximum 15 μm width was found to be composed of steel fiber/ $FeAl_3$ (θ)/ FeAl (β) and Fe_3AlC (κ)/ Fe_2Al_5 (η)/ Al-0.5 wt.% Mg matrix determined by XRD, EDS and microhardness measurements.
Increase in flow stress composites was observed at 250ºC against the monolithic composition.
Ball-on-disc dry sliding wear of the composites revealed an order of magnitude increase in room temperature as well as elevated temperature wear resistance with increasing reinforcement content.

Sintered compacts in the form of briquettes were close die forged and rolled to remove retained porosity and achieve an overall enhancement in mechanical properties. Increments in hardness and flexural strength were observed. Forging of composites resulted in de-agglomeration and redistribution of short fibers in the Al-0.5Mg matrix. Reinforcement banding as a result of deformation processing- generally observed in hard particulate/whisker reinforced MMC's was avoided by constrained forging employed in this work. Fiber pull-out and fracture were found to be the primary failure mechanisms. The strength of the composites was found to be lower than that of monolithic composition (141 MPa- 10wt.%; 127 MPa- 20 wt.% and 87 MPa-30 wt.%) with reduction in ductility; which increased to 213 MPa- 10wt.%; 212 MPa- 20 wt.% and 176 MPa for 30 wt.% reinforced composition, which were higher than ROM estimates.

Reduction of 25:1 by extrusion of sintered billets, conforming to a true strain of 3.21 for Al-0.5Mg, produced elongated ligament like grains, almost nil retained porosity, with gain boundaries oriented along the extrusion direction. Tensile strength was equivalent to that achieved by forging with similar ductility. Preferential alignment of steel fibers, along extrusion direction, was visible for extruded Al-0.5 Mg-25 wt.% steel fiber composites. Fiber breakage resulted due to use of a flat face extrusion die. Fractographs for composite also indicated bunching of fibers, responsible for failure by debonding of fibers from the matrix.
Room temperature pin-on-disc wear test of sinter-forged specimens revealed a transition from delamination mode of adhesive wear to less severe abrasive wear mechanism with increasing reinforcement content. Decrease in CTE was observed with increasing reinforcement content.

Pre-alloyed AA6061 (Al-0.19Fe-0.68Si-0.30Cu-1.1Mg-0.3Cr) powder was cold consolidated and sintered at 625 ºC**;** conforming to 10 vol.% liquid fraction, ensuring presence of transient liquid phases of Mg_2Si. Sintered densities of 92 for unreinforced AA6061 increased to near 99% upon closed die forging with an ultimate tensile strength of 356 MPa in T6 aged condition. Incorporation of short steel fibers resulted in formation of complex AlFeSi ternary intermetallics for AA6061 based composites, thereby deterioration in ageing response and mechanical properties was observed. An increase in flow stress for hot compression of forged alloy based composites, revealed a lag in flow stress, accompanied by reduction in cavitation induced damage.

Comprehensive tribological testing and analysis of wear tracks and debris showed increase in room temperature wear resistance of alloy based composites at higher loads and increased speeds. A decrease in coefficient of thermal expansion as reported for all composites compared to pure compositions.

ACKNOWLEDGEMENTS

"Every search begins with beginners luck and ends with the victors being severely tested"- The Alchemist, Paulo Coelho. Fortunately the path is shown by a guiding beacon and support is derived from many fellow pilgrims, helping one to reach his destination. With great gratitude I would like to express my deepest regard for my supervisors Prof. Vijaya Agarwala, Professor Metallurgical and Materials Engineering Department (MMED) and presently Head of Department, Center of Excellence: Nanotechnology, IIT Roorkee, Prof. Kamlesh Chandra, Ex-Professor MMED and presently Professor (Visiting) Center of Excellence: Nanotechnology, IIT Roorkee; for providing me with the opportunity to excel under their guidance. Without their inspiration, support, constant review, constructive inputs and critical evaluation of my research work; it would not have been possible to conclude this thesis.

I am thankful to Prof. S.K. Nath, Head, MMED and Prof. P.K. Ghosh, Ex. Head, MMED for their co-operation in extending the necessary facilities during my course of work. I would like to wholeheartedly thank Prof. S. Ray, Ex-Professor MMED, for supporting the fabrication of extrusion set-up; Dr. B.V. Manoj Kumar (MMED) for allowing the use of tribometer and Dr. V. V Dabhade (MMED) for permitting the use of powder pressing dies and dilatometer and many helpful discussions.

I also wish to thank the staff of the Department of Metallurgical and Materials Engineering, Indian Institute of Technology, Roorkee, in particular Mr. Raj Kumar Sharma, Mr. Rajinder S. Sharma, Mr. Shakti Gupta, Mr. Kuldeep Sharma, Mr. Dinesh Kumar, Mr. Ashish Kush, Mr S.M. Giri, Mr.Pradeep Kumar, Mr. H.K. Ahuja and Mr. Dhan Prakash. Many thanks are due to Mr. S.K. Saini, Mr. A.K. Saini and Mr. S. D. Sharma of Institute Instrumentation Centre, IIT Roorkee for extending all the help for characterization by XRD, SEM-EDX and DSC.

I wish to duly acknowledge the support in the form of Visiting Occupational Traineeship provided by Prof. P.D. Hodgson for visit to Institute of Frontier Materials (IFM), Deakin University, Geelong, Australia, Dr. D.M. Fabijanic for supervising my research work at IFM, Dr. Andrew Sullivan for electron microscopy, Robert Pow, Mohan Shetty and Katrina Morgans for all the help extended with metallography, XRD and materials processing. Thanks to Angie and Mark for making my stay a pleasant experience.

Support provided by Mr. Jessu Joyce, U.S. Bronze Powders Inc., USA, and Mr. Doris Mehta, Subhmets, Mumbai in the form of aluminium powders is duly acknowledged. Timely fabrication of forging dies and extrusion set-up by Mr. Saji Mr. Philip of Precision Engineering Works, Delhi is gratefully acknowledged. Thanks are due to Dr. Andy Zhao and Mr. Suyash Nadkarni of DSI Inc. USA for training on Gleeble-3800 thermomechanical simulator.

I wish to thank my seniors, colleagues and dear friends- Dr. Anil Kumar Chaturvedi, Dr. A.A.S Ghazi, Dr. Sachin Tyagi, Dr. Somnath Bhattacharya, Dr. Rajath Hegde, Dr. Rajneesh Garg, Dr. V.N. Shukla, Mr. Tilak Joshi, Mr. Debesh Devdutta Mishra, Ms. Preeti Makkar, Mr. Yashwant Mehta, Mr.Nageswara Rao, Mr. Sunkulp Goel, Mr. Brijkishore, Mr. Ravi Ranjan, Mr. Sheriar Reza Adnan, Mr. Ashok Kumar Jain, Mr. Himanshu Kumar Jain, Mr. Atul Jain, Mr. Sandeep Rohilla, Mr. Sandeep Dixit and many others for their constant moral support and camaraderie.

I would like to express respect and great admiration for my father Dr. Jinendra Kumar Jain, my mother Dr. Sarveshwari Jain, my wife Archana and loving daughter Shreya for being the guiding light and encouraging force behind this endeavor.

I would like to humbly dedicate this thesis to my parents, Archana and Shreya.

(SIDHARTH JAIN)

TABLE OF CONTENTS

LIST OF FIGURES

Chapter 3

Chapter 4

Chapter 5

LIST OF TABLES

LIST OF RESEARCH PUBLICATIONS

Papers published in International Journals

1. **S. Jain,** K. Chandra, and V. Agarwala, "Microstructure and Mechanical Properties of Vacuum Hot Pressed P/M Short Steel Fiber Reinforced Aluminium Matrix Composites" *ISRN Materials Science,* Volume 2014, pp. 1- 9. DOI http://dx.doi.org/10.1155/2014/312908

2. **S. Jain**, D. Fabijanic, K.Chandra, V. Agarwala, "Microstructure and Mechanical Properties of Nitrided and Chromized Short Steel Fiber Reinforced Aluminium based P/M processed Composites" pp. 335-338 (vol. 690), *Materials Science Forum*. DOI 10.4028/www.scientific.net/MSF.690.335

3. **Sidharth Jain,** Vijaya Agarwala, and Kamlesh Chandra, "Microstructure and Mechanical Properties of Vacuum Hot Pressed P/M Short Steel Fiber Reinforced Aluminium Matrix Composites", *Journal of Composites,* (Accepted for publication and under review, manuscript Ref. No. 539819.v1).

4. **Sidharth Jain**, Vijaya Agarwala, and Kamlesh Chandra "Mechanical Properties and Wear Behavior of Steel Fiber Reinforced PM6061 Composites", *Powder Metallurgy,* Manney Publishing, United Kingdom. (Manuscript submitted and under review)**.**

Papers presented in International Conferences

1. **S. Jain**, D. Fabijanic, K.Chandra, V. Agarwala, Development of short steel fiber reinforced Al-0.5wt.% Mg P/M composites: Microstructure and mechanical properties", *Processing and Fabrication of Advanced Materials-XXII*, pp. 409-414 18-20 Dec, 2013, Singapore.

2. **S. Jain**, K.Chandra, V. Agarwala, "Thermomechanical Processing of PM7075 and PM6061" presented at PM-13, *International Conference of the Powder Metallurgy Association of India*, 07-09 Feb, 2013, Pune, India.

3. **S. Jain**, D. Fabijanic, K.Chandra, V. Agarwala, "Powder Metallurgy Processing of Aluminium-Short Steel Fiber Composites" presented at PM-12, *International Conference of the Powder Metallurgy Association of India,* 02-04 Feb, 2012, Mumbai, India.

4. **S. Jain**, K. Chandra, V.Agarwala, "Microstructure and Mechanical Properties of P/M Processed Short Steel Fiber Reinforced Aluminium Matrix Composites" December 13-15, *ICRACM-2010,* Limoges, France- presented and published in proceedings.

Papers presented in National Conferences & Seminars

1. **S. Jain**, D. Fabijanic, and K.Chandra, V. Agarwala "Wear & Friction Behavior of Aluminium-Short Steel Fiber P/M Composites", presented at *Microstructure-2011*, National Seminar, IIT Roorkee, November 04-05, IIT Roorkee.

2. **S. Jain**, K.Chandra, V. Agarwala "Hot Pressing of P/M Processed Hybrid AlMMC", *National Conference on Physical Simulation & 2nd Gleeble User Workshop*, March 16-17, 2010, RDCIS, SAIL-Ranchi- presented and published in proceedings.

3. **S. Jain**, K.Chandra, V. Agarwala "Processing of Aluminium Matrix Composites by Squeeze Casting", *63rd Annual Technical Meeting, The Indian Institute of Metals*, Nov.16-17, 2009, pp. 142-143, Kolkata- published in proceedings.

ABBREVIATIONS

P/M : Powder Metallurgy

MMC : Metal Matrix Composites

AMC : Aluminium Matrix Composites

SSF : Short Steel Fibers

ROM : Rule of Mixtures

SEM : Scanning Electron Microscopy

XRD : X-Ray Diffraction

DSC : Differential Scanning Calorimetary

UTS : Ultimate Tensile Strength

RI : Reaction Interface

HV : Vickers Microhardness

CTE : Coefficient of Thermal Expansion

COF : Coefficient of Friction

wt.% : Weight Fraction in %

vol.% : Volume Fraction in %

Chapter 1
INTRODUCTION

The term "composite" broadly refers to a material system which is composed of a discrete constituent (the reinforcement) distributed in a continuous phase (the matrix), and which derives its distinguishing characteristics from the properties of its constituents, from the geometry and architecture of the constituents and from the properties of the boundaries (interfaces) between different constituents. Composite materials are usually classified on the basis of the physical or chemical nature of the matrix phase e.g., polymer matrix, metal-matrix, ceramic-matrix, intermetallic-matrix and carbon-matrix composites. A metal matrix composite (MMC) combines a single material, a metallic base, with a reinforcing constituent, which may be metallic or non-metallic. There are several reasons why MMCs have generated considerable interest within the materials community for nearly 30 years:

i. The "composite" approach to metallurgical processing is the only pathway for production of entire classes of metallic materials. The approach offers significant alterations in the physical properties of metallic materials like enhanced elastic moduli. Composites also offer the only pathway for producing materials with tailored physical property combinations: e.g., low thermal expansion combined with high thermal conductivity, a combination of importance for electronic packaging (Shercliff and Ashby, 1994).
ii. MMCs offer significant improvements with regards to several properties like tolerance of high temperature, transverse strength, hardness, resistance to aggressive environments including chemicals, cryogenic or organic fluids, atomic oxygen and ultraviolet radiation, high dimensional stability, good impact, corrosion and wear resistance, reduced moisture absorption, non-flammability, while significantly outclassing ceramics in toughness and ductility (Campbell, 2006; Lindroos and Talvitie, 1995; Miracle, 2005; Surappa, 2003).

A vast range of MMC materials have been conceived and studied, this range comes from the large number of permutations of metal matrices and reinforcements and the more specific combinations of reinforcement size, morphology and distribution. MMCs based on Ag, Al, Be, Co, Cu, Fe, Mg, Ni and Ti matrices have been investigated and are commercially produced.

Discontinuously reinforced aluminium composites account for the largest MMC production by mass, with SiC and Al_2O_3, particles, short fibers and whiskers, followed by TiC being the reinforcements of choice (Rittner, 2000). In monolithic alloys, the phases that precipitate or

exist have distinct crystallographic relation with the matrix and the phase boundary can be coherent or incoherent. In composites, the dispersoids do not have any type of crystallographic relation with the matrix and interface is always incoherent (Pai and Pillai, 1999).

Liquid metallurgical techniques dominate the fabrication methods employed for MMC fabrication, on account of low cost and scalability. Many variants are reported, namely: stir casting (Hashim, et al., 1999), vortex casting (Clyne, 2000), infiltration (Kevorkijan, 2004) etc. Squeeze casting has been reported to overcome the many drawbacks of other competing processes (Yue & Chadwick, 1996). Powder metallurgical processing of MMCs is based on blending of the constituents, followed by either their cold consolidation or direct sintering, accomplished with or without application of pressure, followed by secondary consolidation (forging, extrusion or rolling) (Kaczmar, et al., 2000; Rosso, 2006;Torralba, et al., 2003). Aluminium P/M has been described as a versatile processing technique on account of its ability to modify alloy chemistry to suit specific functions whilst producing a near-net-shape product, wherein, important operating parameters include particle size distribution, blending techniques, pressing, and sintering (Kipouros, Caley, & Bishop, 2006).

Metal-metal MMC systems develop reactive interfaces at high processing temperatures that tend to be brittle and hence have been less explored. For the steel reinforced aluminium system, optimum properties of steel-aluminium composites have been realized upon close control of the RI thickness (Pai, et.al, 1983; Mannan, et.al, 1983). Several techniques have been explored to limit the constituent interactions, pre-coating the steel wire with aluminium (Tiwari, et.al, 1987) coating of Cu or Ni (Mandal, et. al, 2008) vibration and tensioning of continuous steel wires (Agarwala et.al, 1998) addition of Si or Cu to the melt (Byong-Eun Yoon, 1996). Kobayashi & Yakou, 2002, have reported preferential growth of iron-rich intermetallic phases, Fe_3Al and FeAl, by diffusion treatments for enhanced toughness, good wear resistance, oxidation and corrosion resistance and specific strength properties.

The present investigation is based on incorporation of short steel fibers in P/M aluminium matrices and their characterization. Important considerations for this work include the selection of materials, blending of the constituents, sintering of aluminium and post-sinter secondary consolidation to achieve porosity free artifacts. The developed composites will be characterized for mechanical behavior, tribological characteristics, and thermo-physical properties like coefficient of thermal expansion with analysis of steel-aluminium interface.

The results of the present research work have been analyzed and discussed in light of available literature to propose an insight into mechanical, thermomechanical, tribological and thermophysical characteristics of the developed of short steel fiber reinforced aluminium based P/M composites.

The thesis is presented in 6 chapters.

Chapter 1 contains an "**Introduction",** on the salient features of aluminium powder metallurgy with emphasis on monolithic and reinforced compositions, sintering, limitations and advantages of aluminium powder metallurgy with critical appraisal of industrial applicability of such elements with regards to evolution of final properties. Feasibility and important characteristics of steel-aluminium based composites, developed earlier has been outlined.

Chapter 2 describes the "**Literature Review",** which critically catalogues contributions from available literature pertinent to fabrication of aluminium based composites with traditional ceramic based reinforcements employing liquid as well as powder metallurgical processing techniques. Several aspects on the role of powder shape and size, cold consolidation, sintering atmosphere, alloying additions, sintering aids, liquid phase fraction, sintering time and temperature have been studied and summarized to offer an understanding on the sintering behavior of pure aluminium and alloyed powder compositions. Effects of post-sinter secondary working processes like forging, rolling and extrusion have been documented with role of strain, strain rate and deformation temperature on microstructure and mechanical property evolution of monolithic alloys and composites. Steel-aluminium based composites developed by workers have been studied with respect to processing parameters, role of reaction interface, techniques for modification and control of the reactive interlayers and their effect on mechanical, thermophysical and tribological behavior of the composites.

Chapter 3 presents **"Formulation of Problem"** in light of theoretical and practical aspects in chemistry formulation, fabrication and characterization of short steel fiber incorporated aluminium composites based on continuity of Fe_xAl_y interface between the dispersion and matrix in ensuring a good bond resulting in efficient load transfer to the steel reinforcement; control of reaction interface chemistry and morphology and thereby properties of the MMC by coatings of Cu, Ni, and traditional surface modifications of nitriding, chromizing and aluminizing on the short steel fibers; suitability of powder metallurgical (P/M) processing due to lower hot consolidation temperatures to near-full density; characterization of elevated temperature mechanical and tribological behavior of steel-aluminium MMC system; incorporation of short steel fibers in age hardenable and high strength aluminium alloys like 6061 and 7075. Quantitative and qualitative comparison with expensive ceramic reinforcement based composites, generally well investigated in aluminium based MMC systems.

Chapter 4 deals with **"Experimental Procedure"** presenting the experimental techniques and procedures followed for initial raw material characterization, matrix and reinforcement

blending, cold consolidation, sintering and secondary working. The processed compacts were characterized for microstructure evolution, composition and thickness of the reaction interface and fractography by standard metallographic practice, X-ray diffraction (XRD), scanning electron microscopy (SEM) and energy dispersive spectroscopy (EDS); density and densification parameter, microhardness across the matrix, reaction interface and reinforcement; room temperature and elevated temperature tribological testing using ball-on-disc configuration and compressive strength alongwith transverse rupture strength. Tensile, compression, flow stress specimens and hemispherical wear pins were machined from forged briquettes and extruded rods for mechanical and tribological characterization. Flat tensile samples were punched out from rolled strips. Recrystallization and effect of thermomechanical working on monolithic compositions was investigated by electron back scattered diffraction (EBSD). Wear tracks and wear debris were analyzed under SEM and EDS. Coefficient of thermal expansion for all forged compositions was evaluated by a linear dilatometer under Ar gas atmosphere.

Chapter 5 reports "Results and Discussions", from the formulated experimentation. Powder morphology, size distribution and oxygen content have been reported. Effect of surface treatments by nitriding, chromizing and aluminizing on short steel fibers has been determined by microstructural examination, XRD and microhardness. Efficacy of surface treatments on restricting the fiber-matrix interfacial reaction has been evaluated by phase analysis, microhardness and micrography. Green and sintered densities have been determined and reported in terms of percentage theoretical nominal densities of matrices and composites. Densification parameter, used to evaluate the effect of sintering on final density has been compared with porosity volume fraction. Effect of reinforcement content on damage evolution has been determined by room temperature and elevated temperature compression test. As-sintered hardness and flexural strength has been determined. Ambient and elevated temperature wear behavior has been determined in terms of wear volume loss, COF; wear mechanism and effect of reinforcement content has been reported by analysis of wear tracks and debris. Tensile strength of as-forged, forged-rolled and extruded compositions has been compared with ROM. Failure mechanism has been determined from analysis of fracture surfaces. Structure-property correlations have been discussed for mechanical and tribological properties. CTE has been compared with ROM and Schapery models.

Chapter 6 summarizes the major **"Conclusions"** from the present research work and indicates scope for future work in the chosen subject.

Chapter 2

LITERATURE REVIEW

2.1 Introduction

The literature review is carried out as a part of the thesis work to provide an overview on the development of Aluminium matrix composites (AMC's); characterization of AMC's with regards to constituent morphology, microstructure, mechanical and thermophysical properties, tribological behavior, strengthening and damage mechanisms and major areas of application. Aspects related to powder metallurgical (P/M) processing of AMC's have been presented, covering advantages offered by P/M fabrication routes against liquid metallurgical (LM) systems. P/M processing of aluminium powder based alloys and composites has been discussed, covering, composition and chemistry, sintering characteristics, post-sinter secondary consolidation, characterization and application areas. Development of steel reinforced aluminium matrix composite materials has been reviewed chronologically to offer a comprehensive understanding of processing methods and properties evaluation of the metal-metal composite system with reactive interface.

2.2 MMC Processing Techniques

Among the various techniques available for processing of MMCs (Fig. 2.1), liquid metallurgical processes have been dominant on account of their simplicity, economy and scalability for large volume production. Liquid phase processes, with many variants, most notably squeeze casting (Bader, et al., 1985; Feng, et al., 2008; Ghomashchi and Vikhrov, 2000; Seyed Reihani, 2006; Vijayaram, et al., 2006; Yue and Chadwick, 1996; Jain, et al., 2009; Maleki, et al., 2008) has been most efficient in overcoming segregation, porosity and wettability issues between the reinforcement and the matrix.

Ghomashchi and Vikhrov, 2000, have suggested that the fine structure and superior mechanical properties of squeeze cast components are on account of changes in undercooling of molten alloy, changes in composition and relative volumes of forming phases of the solidifying melt, changes in heat transfer coefficient and density due to reduction in porosity under pressure.

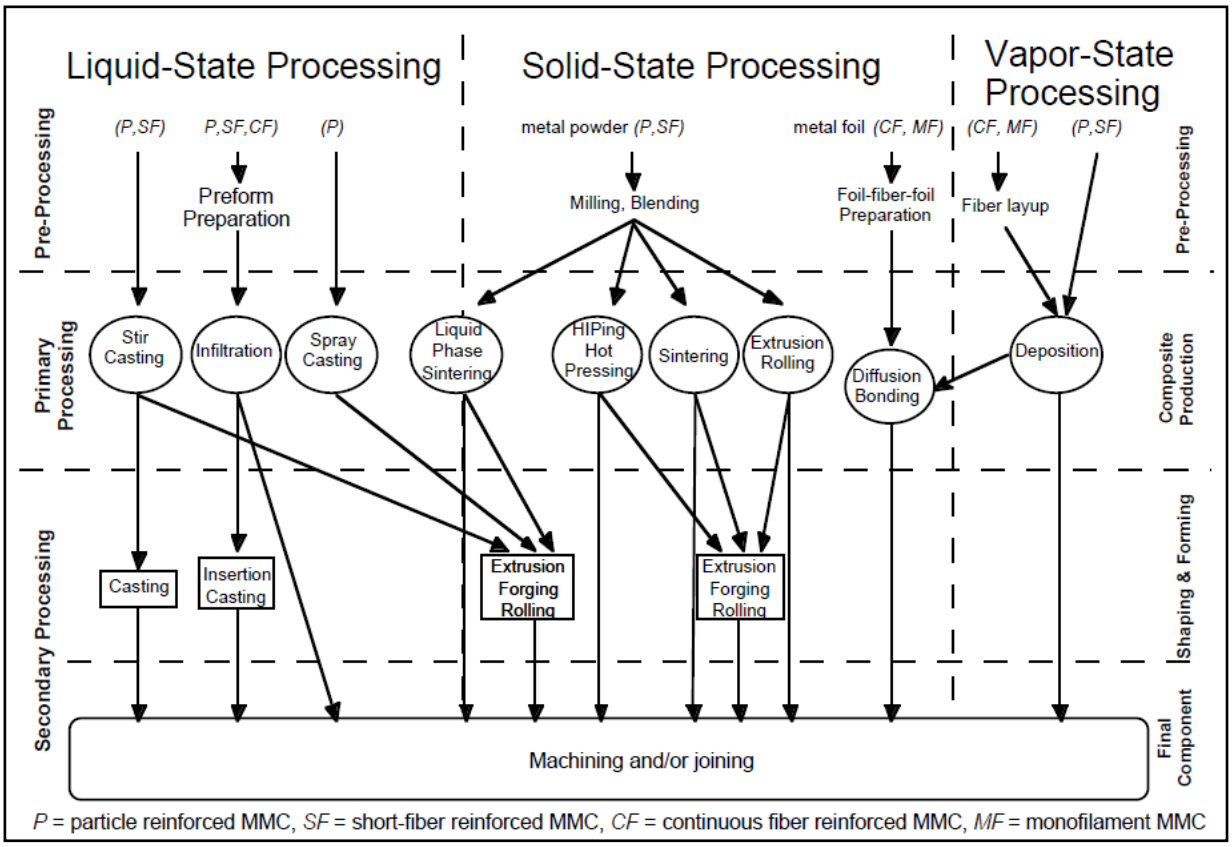

Fig. 2.1 Processing routes for fabrication of MMCs (Clyne, 2001)

Yue and Chadwick, 1996, have reported better mechanical properties of squeeze cast components in comparison to wrought products, with near-net shape processing. Some prominent applications for light metal MMC systems processed by squeeze casting have been reported as automotive wheels, gear blanks, Al- alloy automotive pistons, brass and bronze bushings (Vijayaram et al., 2006).

Seyed Reihani, 2006, fabricated AAl6061/30vol.% SiC particle reinforced composites with mean particle size of 16 and 22 µm by squeeze casting route. The elastic modulus increased from 70 to 83 GPa. Similarly, the yield strength and ultimate tensile strength increased from 110 and 144 to 172 and 194 MPa, respectively. However, a marked decrease in ductility of the composites arising from addition of SiC was reported, primarily due to increase in the dislocation density of the matrix. Wear resistance was comparable to pearlitic gray cast iron, with significantly lower apparent hardness of the composites.

Feng et al., 2008, developed hybrid aluminium matrix composite reinforced with 22 vol.% $Al_{18}B_4O_{33}$ whisker and 3 vol.% WO_3 particles, by squeeze casting, they reported an increase in elastic modulus from 69 GPa to 96 GPa , yield and ultimate tensile strength from 24.27 to 250.7 MPa and 47.9 to 287.3 MPa respectively. They attributed this strengthening to the large

difference in coefficient of thermal expansion of Al matrix, 23 x 10^{-6} $^{\circ}C^{-1}$ with $Al_{18}B_4O_{33,}$ 1.9 x 10^{-6} $^{\circ}C^{-1}$, leading to thermal mismatch and higher dislocation density.

Currently the most common production method of composite materials is inert gas pressure-assisted or pressure-less infiltration of porous reinforcement preforms by alloys of aluminium or magnesium to yield near-net or net shape components with reinforcement volume fractions as high as 70%. This method has been successfully used to fabricate AMCs reinforced by short ceramic fibers, continuous ceramic fibers, SiC particles, Al_2O_3 particles, graphite flakes and SiC whiskers (Kevorkijan, 2004; Yang and Chung, 1989; Aghajanian and Rocazella, 1991; Lai and Chung, 1994; Lasagni, et al., 2008).

Kevorkijan, 2004, investigated pressureless, low-pressure and moderate- pressure N_2 gas infiltration of SiC particulate preforms to develop upto 52 vol.% SiC reinforced Mg- MMCs. He reported excessively long times, upto 24h, for complete infiltration of the preforms under pressureless condition, 0.5h under moderate 0.8MPa pressure and upto 7h under low 0.3MPa, pressure. Significant increase was reported in elastic modulus: 45GPa to 103GPa, yield strength: 27.5MPa to 525 ± 25MPa for all the infiltration pressures, with a drastic loss in elongation from 7% to 0.5% for the monolithic and reinforced compositions respectively.

Yang and Chung, 1989, have reported a combinatorial approach, using vacuum infiltration, inert gas pressure assisted infiltration and squeeze casting to infiltrate and subsequently squeeze-solidify the aluminium alloy matrix into various preforms of short ceramic fibers, continuous ceramic fibers, SiC whiskers and particles. The advantages reported were reduced damage and distortion of the fibrous preforms vis-à-vis squeeze casting, lower melt temperature and better penetration of pores.

Powder metallurgical (P/M) processing is based on blending of matrix powders and reinforcing elements (particles, platelets or whiskers), their cold consolidation to a green compact, sintering at a temperature below the melting point but sufficiently high to develop significant solid-state diffusion followed by secondary working (forging, extrusion or hot pressing) (Huda, et al., 1993; Kaczmar, et al., 2000; Rosso, 2006) to full density. P/M methods offer the ability to modify the alloy chemistry and retain control over the matrix-reinforcement interface, whilst producing a near net shape product (Kipouros, et al., 2006). Certain advantages offered by P/M processing of MMCs have been summarized below:

i. Lower temperature can be used during preparation of a P/M based composite compared to liquid metallurgy, resulting in reduced interaction between the matrix and the reinforcement thereby minimizing interfacial reactions.
ii. Degree of wetting of the reinforcement by the matrix is an important consideration in liquid processing, not the case in P/M processes.

iii. P/M techniques permit preparation of certain class of composites that cannot be prepared by liquid metallurgy. It has been reported (Kaczmar et al., 2000) that SiC whiskers will dissolve in molten Ti alloy matrix, while dissolution can be minimized by using P/M route. It has also been shown that SiC fibers are highly compatible with solid aluminium but only fairly wettable with liquid aluminium.

iv. Uniform dispersion of particulate or short fiber reinforcements is readily achievable using conventional blending techniques (Rosso, 2006).

2.3 Whisker/Short Fiber Reinforced AMCs

2.3.1 Interfacial mechanics and damage in short fiber reinforced composites

Aluminium matrices have been reinforced by ceramic short fibers or whiskers (diameter less than 2μm) of Al_2O_3, SiC and carbon, for effective load transfer from the matrix to the reinforcement, fiber length is required to be greater than the critical length l_c (Girot, et al., 1987). The effect of continuous aligned fibrous reinforcement in predominantly ductile aluminium matrices has been best described by the rule of mixtures (ROM) equation, but to accurately account for strength contribution by discontinuous fibers oriented randomly in an aluminium alloy matrix (Friend, 1987) has proposed the following model for estimation of critical fiber length (l_c) based on volume fraction (V_f) of reinforcing short fibers.

$$\sigma_c = \sigma_{uf} + \sigma_m^*(1 - V_f) \quad \text{.....(2.1)}$$

$$\sigma_c = \sigma_{uf} V_f (l - \frac{l_c}{2l}) + \sigma_m^*(1 - V_f) \quad \text{.....(2.2)}$$

$$\sigma_c = C\sigma_{uf} V_f (l - \frac{l_c}{2l}) + \sigma_m^*(1 - V_f) \quad \text{.....(2.3)}$$

$$l_c = \frac{\sigma_{uf} d}{2\tau} \quad \text{.....(2.4)}$$

Eq. 2.1 is the standard ROM equation for determining composite strength (σ_c) in the case of perfectly aligned continuous fibers of infinite length, where σ_{uf} is the ultimate tensile strength of the fibers and σ_m^* is the stress shared by the matrix at failure strain of the fiber. To account for randomly oriented short fibers, a term l_c is introduced in Eq. 2.2, from Eq. 2.4, where d is the fiber diameter and τ gives the interfacial shear stress at the fiber-matrix interface. The critical fiber length, l_c, signifies the effective length of finite fibers, which are loaded under tension. An empirical constant C (Eq. 2.3) provides the correction for spatial orientation of randomly oriented fibers against an axial force vector. From experimentation the values of 3/8 or 1/5 have been ascribed to constant C, for random planar orientation and a completely

random 3-D array, respectively. In the absence of published literature for matrix-fiber interfacial shear strength, (Friend, 1987), has suggested replacing τ with τ_{ym}, shear yield stress of the matrix; which can be approximated as 0.5 σ_{ym}, i.e. half of the matrix alloy yield strength in tension. Eq. 2.3, for randomly oriented short fibers ($l > l_c$), further reduces to:

$$\sigma_c = \frac{1}{5}\sigma_{uf} V_f \left(1 - \frac{\sigma_{uf} d}{2 l \sigma_{vm}}\right) + \sigma^*_m (1 - V_f) \quad \text{.....(2.5)}$$

A lower bound (for unreinforced matrix, $V_f = 0$; $\sigma_c = \sigma_{um}$) and the upper bound (reinforcement only, $V_f = 1$; $\sigma_c = 0$) of Eq. 2.1 can be plotted against experimentally obtained values for σ_c with varying V_f. As shown in Fig. 2.2, graphically an estimate for minimum reinforcement volume fraction V_{MIN} and critical fiber volume fraction V_{CRIT} can thus be made.

In addition to the purely mechanistic treatment of composite strength presented above (Zhu, et al., 1994) have included the effect of coefficient of thermal expansion mismatch and the thermal stresses generated by this difference at the fiber-matrix interface to derive a modified ROM expression. Effect of grain refinement in the matrix alloy due to higher dislocation density at the interface is also included. The model was able to better predict the composite strength in comparison to the suggestions by (Friend, 1987); for 20 vol.% δ-Al_2O_3 reinforced Al-7Si matrix composite.

It is well established that thermal mismatch stresses are generated at the interface upon cooling of the composite generating a compressive radial constriction on the fiber. Externally applied loads cause failure of the composite by: (1) coalescence of interfacial vacancies (2) debonding at the interface (3) frictional sliding (4) decohesion by cavitation; (1 and 4) occur at the fiber ends, (2 and 3) towards the central portion (body) of the fiber (Clyne and Watson, 1991). Onset of plastic flow is almost readily shown in the stress-strain curve of a short fiber composite, with a negligible elastic region.

Plastic yielding is observed throughout the matrix. Fracture of the composite by fiber failure result from cavitation openings at the fiber ends, created in a yielding matrix. Interface thickness, in case of reactive fiber-matrix systems, promotes stress relaxation by sliding, decohesion, cavitation and debonding before sudden failure, but only upto a certain thickness of the interface so formed as shown in Fig. 2.3.

Damage evolution in short fiber reinforced composites has been defined as a progressive loss in composite strength and stiffness by initiation of microcracks and cavities under applied load (Vedani and Gariboldi, 1996).

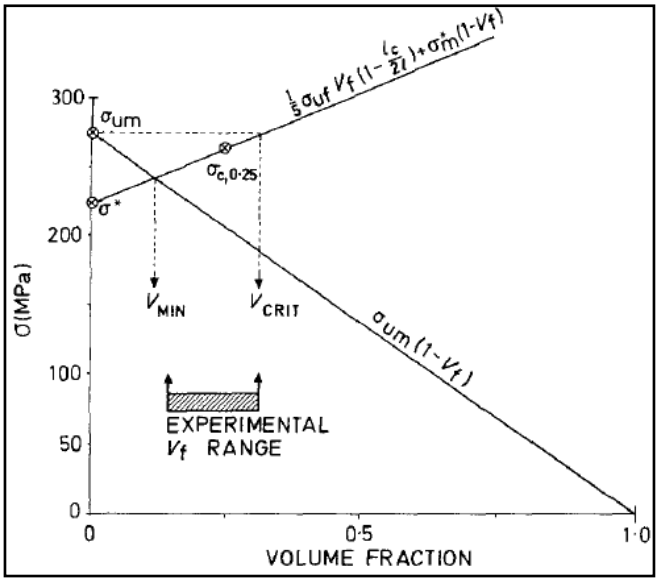

Fig. 2.2 Estimation of critical fiber volume fraction by modified ROM (Friend, 1987;Yu, et al., 2007; Kainer, 2006b)

Damage evolution in short fiber reinforced composites has been defined as a progressive loss in composite strength and stiffness by initiation of microcracks and cavities under applied load (Vedani and Gariboldi, 1996).

Surface and sub-surface cracking in a glass fiber reinforced polypropylene composite under tensile loads, has been investigated by (Choi and Takahashi, 1992), surface cracks formed at the fiber ends transgress at right angles into the ductile matrix without actually causing fiber debonding, whereas the sub-surface cracks, formed due to shear stresses at the fiber-matrix interface grow along the fiber length, as shown in Fig. 2.4, leading to fiber-matrix debonding.

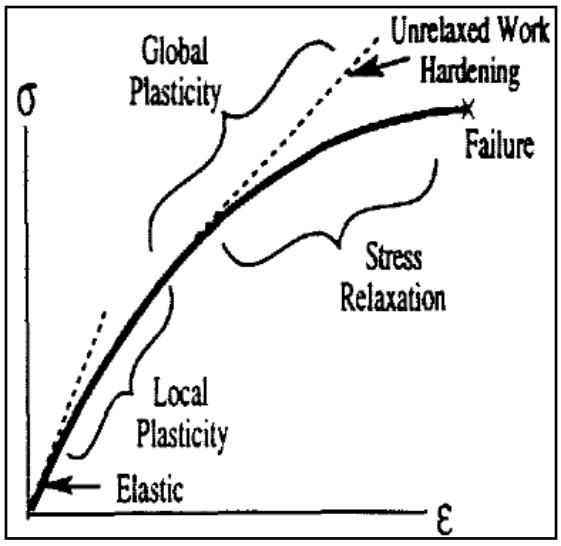

Fig. 2.3 Stress-strain behavior of a short fiber composite (Clyne and Watson, 1991)

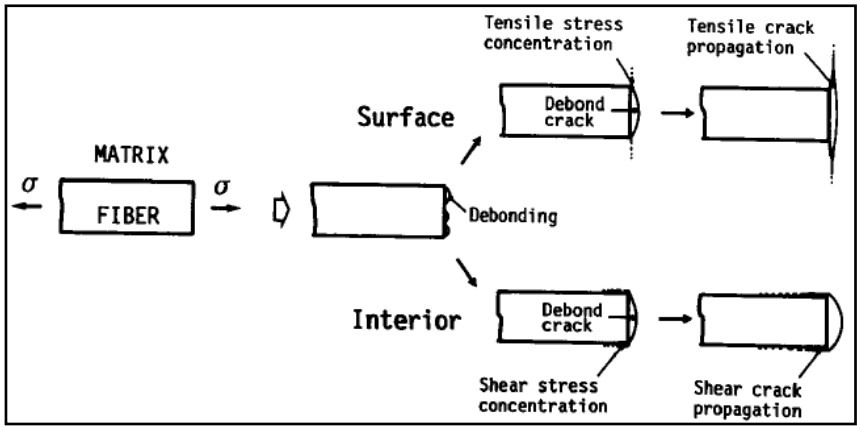

Fig. 2.4 Mechanism of crack formation at fiber ends (Choi and Takahashi, 1992)

As in the case of particulate reinforced composites, wherein, particulate agglomeration is found to be responsible for as-cast porosity in the composite (Ghosh and Ray, 1987); fiber agglomeration has been reported to provide conditions for cavitation. Whitehouse and Clyne, 1994, have experimented with different morphologies of SiC, particulate- spherical/angular and short fibers upto 20 vol. % fabricated by squeeze infiltration and P/M (followed by extrusion) for commercial purity aluminium matrix. Room temperature failure was reportedly due to cavitation induced debonding of the short fibers, starting at the fiber ends. Damage by cavitation was accelerated for P/M composites in comparison to cast counterpart. The nascent oxide film over powder particles forms aligned stringers along the extrusion direction, since there is limited inter-particle bonding in the P/M composite, these stringers are reported to favor cavitation along the aligned direction, but offer resistance to void growth and coalescence normal to the extrusion direction. Hence, larger void content is reportedly tolerated by the P/M composite before failure.

Extensive studies are available in literature for characterization of damage evolution (Tavangar, et al., 2005) and ductility (Weber, et al., 2005) in short fiber reinforced aluminium composites, where the workers have investigated the effects of fiber orientation and volume fraction on composite integrity, ductility and damage evolution.

Cavitation induced failure in close vicinity of the fracture surface (neck) is characteristic of MMCs tested at elevated temperatures. This effect is termed as strain localization. (Whitehouse and Clyne, 1993; Whitehouse and Clyne, 1994) have reported an increased effect of stress relaxation, due to a plastic matrix at high temperature; observations have shown that during initial period of straining, the void content is lower than room temperature, but once it reaches a critical value, sudden coalescence is followed by failure. The stabilizing effect of aligned oxide stringers at room temperature is lost at elevated temperature; they are no longer

able to arrest void growth normal to extrusion direction, reaching failure at much lower total strain than cast counterparts.

2.3.2 Tribological and wear characteristics of AMCs

Wear has been defined as a systems response to the imposed conditions, called a tribo-system (Kato, 2000), rather than a material property. Based on the multiple parameters being operative during a particular occurrence of material loss by wear, distinct wear mechanisms have been outlined, with sub-classifications, namely: mechanical wear- (adhesive, abrasive and fatigue wear), chemical wear- (corrosive wear) and thermal wear- (melt and diffusive wear) (Kato, 2002).

The incorporation of ceramic particles/whiskers/short fibers in an aluminium alloy increases its load-bearing capacity and hence the load and sliding speed range within which dry sliding wear is mild. This has been investigated in detail by many researchers and opens new opportunities for the employment of aluminium based metal-matrix-composites (AMCs) in applications where sliding resistance is of concern. Some investigations have also analyzed the wear behavior of AMCs in the case of external heating, in the temperature range up to 200°C or 500°C. It has been found that wear increases as temperature is increased, because of the thermal softening of the composite, and becomes severe at a critical temperature. Friction coefficient was also observed to increase and this was attributed to an increase in the adhesion forces. Most experimental investigations were carried out using hard steel as a counter face.

Theory of dry sliding wear proposed by the Archard's model, given by the following equation:

$$W = k\,(L\,d\,/\,3H) \ldots\ldots\ldots\ldots\ldots\ldots\ldots\ldots\ldots\ldots\ldots \text{(2.6)}$$

were wear volume loss (W) is directly influenced by the normal load (L) and sliding distance (d) but inversely related to (H) the hardness of the material and k denotes the wear coefficient (Friction, Lubrication and Wear Technology, 1992). Originally developed for adhesive wear, the equation was found suitable to predict wear behavior of materials under abrasive contact. However, a direct usage of the equation was not possible for MMCs, due to the complex interplay of constituents (Hutchings, 1994).

Several factors, singular and combinatorial, have been found to be responsible for tribological behavior of discontinuously reinforced AMCs, namely: Extrinsic factors- sliding distance, normal load, sliding velocity, reinforcement orientation, external temperature and surface finish. Intrinsic factors- reinforcement type, reinforcement size, reinforcement shape, heat treatment, reinforcement volume fraction and spatial distribution (Sannino and Rack, 1995).

2.3.3 Wear characteristics of short fiber reinforced AMCs

P/M 7091 (Al-1.59-Cu-2.28Mg-6.11Zn-0.40Co-0.07Fe) alloy reinforced with 20 vol.% SiC whiskers (0.5 μm diameter, aspect ratio = 6) were tested for abrasive wear resistance against SiC papers of varying grit size (Wang and Rack, 1991a). Composite hardness was related to whisker alignment, reported to be maximum for whiskers aligned normally to the test surface. Wear resistance decreased with increasing grit size upto 60 μm, steadily increasing wear was observed thereafter with increasing grit size of the counterface paper. Whisker reinforced composite displayed consistently better wear loss than particulate composite having similar volume fraction of reinforcement. Minor improvement in wear loss is reported for normally aligned whiskers. Material loss by grooving and whisker pull-out was observed. The anisotropy created by preferential alignment of reinforcement in extruded P/M composite has a direct bearing on the wear performance for both particulate and short fiber composites (Sahin and Murphy, 1998; Sahin, 1998), a direct difference created by an effective area fraction of the hard ceramic reinforcement at the contact plane (Hutchings, 1994).

Wang and Rack, 1991b, have investigated the dry sliding wear behavior of P/M 2124 alloy with upto 20 vol.% SiC whisker reinforced composite against a 17-4 PH steel disk. Wear rate decreased with increasing reinforcement content for the composite pins, consequently an increase in wear loss was reported for the steel disk. Coefficient of friction was largely insensitive to reinforcement content. Wear regime consisted of two parts: an initial run-in period followed by a steady state sliding. The wear mechanism for the composite pins changed from abrasive in the initial part of test to adhesive in the steady state part, as evident by debris morphology, which changed to plate like from initially fine particulate type. Surface finish is reported to play an important role during the initial run-in duration (Alahelisten et al., 1993), where hard SiC whiskers are able to abrade the steel disk, absent in case of mirror polished composite pins against a smoother disk. Sub-surface examination of worn composite pins revealed a severely deformed zone for upto 100 μm from the contact plane, with plastic flow of the matrix along the sliding direction.

Formation of a third-body tribolayer composed of hard ceramic wear debris generated as a result of asperity fracture is an important aspect of MMC wear behavior, following which, after an initial high wear volume loss, there is a steady improvement in pin wear resistance, aided by the abrasive action of these embedded particles in the softer aluminium alloy matrix.

Transition from mild to severe wear rates for different AMCs has been investigated by (Alpas and Zhang, 1994) for AA6061, AA2024 and AA2124 matrices reinforced with fine/coarse particulate Al_2O_3 and SiC. Based on the effect of applied normal load three broad wear rate regimes were marked as low load (1-10 N) upto 10^{-5} mm^3 m^{-1}; intermediate (30-150 N) upto

10^{-3} mm^3 m^{-1} and severe (230-300 N) with a wear rate of upto 10^{-1} mm^3m^{-1}; similar transition of wear regimes was reported for all combinations of matrices and reinforcement size/volume fraction. For AA6061 based composites the wear rate was found to increase by a factor of 10 for sliding against a ceramic counterface in comparison to hardened steel. Composites with coarse particles exhibit lower wear rate at low loads; but this advantage does not appear in intermediate and higher load regimes. Increasing the volume fraction of reinforcement, shifts the transition loads to higher values for respective matrices, maximum benefits are attained in the intermediate regime, which extends into the severe wear rate zone load range. Tribo-layer formation was observed in the low load regime from the XRD analysis of wear debris, it was found to be composed of Fe-oxides, abraded by the action of ceramic reinforcements. The in-situ oxidized debris are known to lower the coefficient of friction by providing a lubricating effect. Increasing the reinforcement particle size, resulted in higher abrasion of the steel counterface, whilst, limiting damage to the composite pin. Nearly equivalent wear rates were reported for monolithic and reinforced pins in the intermediate regime, the authors have attributed this feature to negligible increment in the load carrying capacity of the matrices under severe plastic deformation induced surface failure of the test pins. Ceramic particles further provide paths for cracks and decohesion, thereby releasing excess material at the tribo-contact plane. The severely deformed zone is reported to grow about 10 times in the highest load test regime, sub contact plane temperatures rise to about 0.4 T_m (melting point of the matrix alloy on the absolute scale)- defined as the critical temperature for onset of severe wear by plastic delamination.

Formation of a complex tribo-layer has also been reported by (Iwai, et al., 1995) for P/M 2024/upto 16 vol.% SiC whisker reinforced composites under dry sliding tests. Transition from initial severe wear to mild wear is quicker for increasing reinforcement content due to reduced adhesion by presence of small ceramic debris between the composite and counterface (Akbulut et al., 1998). Wear rates are found to be dependent on the size of wear debris (Miyajima and Iwai, 2003) for both particulate and short fiber reinforced composites undergoing dry sliding wear against a hardened steel counterface. Increasing the volume fraction of reinforcement content resulted in smaller sized particles at the tribo-interface, thereby reducing wear rate (Yu, et al., 1996). The dependence of reinforcement volume fraction with a normalized wear rate (wear rate of MMC divided by wear rate of monolithic alloy) was examined by the workers and the highest increase in wear resistance was achieved in case of short fibers followed by whiskers and particulates, in that order, for increase in respective volume fractions.

Elevated temperature wear of AA6061/20 vol.% Al_2O_3 particulate reinforced composites has been investigated by (Singh and Alpas, 1995). The composite exhibited mild wear till 200ºC, beyond which severe wear was reported. Increase in load further enhances the wear rate at higher temperature. The transition temperature for onset of severe wear from the present work is reported as 200ºC for the composite and 150ºC for the unreinforced alloy, beyond which seizure was observed. Wear by excessive plastic deformation generating large flaky debris, as a result of delamination failure (Suh, 1977) of the composite and monolithic alloy were recorded above the respective transition temperatures. The composite had a slightly higher flow stress till 200ºC in comparison to the alloy, but the delayed onset of severe wear at higher temperature was ascribed to localized work hardening of sub-surface layers of the composite against bulk flow softening (Singh and Alpas, 1996). This work hardening was due to severe shear strains at the contact plane, of the order of 10^3, and comminution of alumina particles.

2.4 Matrix-reinforcement Interfaces in MMCs

Most MMC systems are non-equilibrium systems from a thermodynamic standpoint, i.e., there will always exist a chemical potential gradient across the particle/matrix or fiber/matrix interface, which, under favorable kinetic conditions gives rise to diffusion and/or chemical interactions between the constituent components. The interface reaction layer(s) thus formed will generally have characteristics different from the either one or both of the constituents. A proper continuity between the reinforcement and the matrix is a must, as well interfaced composite can give much superior properties (fracture toughness, stiffness, fatigue, coefficient of thermal expansion, thermal conductivity and creep) by synergistic effects (Pai and Pillai, 1999).

Rajan et al., 1998, have reviewed interfacial chemical reactions between SiC reinforced aluminium composites reported in various studies, formation of brittle Al_4C_3 at the interface has been found to be deleterious to the overall composite strength and integrity, remedial measures, that include preheating of the SiC particulates in air so as to provide an oxide covering, has been reported to avoid the direct interaction and formation of Al_4C_3 by forming Al_2O_3, which is compatible with aluminium alloys. Depletion of Mg present in the matrix alloy is also reported by formation of spinel $MgAl_2O_4$ in Al_2O_3 reinforced composites; which leads to under-realization of matrix strength during subsequent ageing cycles.

Several workers have devised coating processes on the reinforcements to limit/contain/inhibit or modify the chemistry of the reaction interface, most notably by PVD (physical vapor deposition), CVD (chemical vapor deposition), electrolytic and electroless coatings, sol-gel processes and cementation etc. (Rajan et al.,1998; Clyne, 2000). Reinforcement wettability, an

important parameter in liquid metallurgical MMC processing, has also been reported to be altered by metallic coatings (Ni, Cu) on ceramic particulates and whiskers (Leon and Drew, 2002).

2.4.1 Chemical Vapor Deposition (CVD) in Fluidized Bed Reactor (FBR)

In a fluidized bed, fine particles of a ceramic (usually Al_2O_3) are made to behave like a liquid by the action of a gas stream that moves up through a vertical column. The gas is fed through a porous diffuser at the bottom of the vertical column, which is radiantly heated from outside as shown in Fig. 2.5. An aggressive bubbly bed is preferred for heat treatment and/or surface coating operations, with a hydrogen wash prior to start of coating for descaling/deoxidizing of substrates (Fabijanic, and Hodgson, 2010). Important process parameters include gas flow rate, type of diffuser, reactor dimension and temperature of operation (ASM International, 1991). In a comprehensive review of possible FBR-CVD treatments and coatings, (Reynoldson, 1995) has categorized treatments above 723ºC: carburizing and carbonitriding, case depth carburizing, Toyota diffusion (TD) coatings- (CrC, NbC, VC etc.) and boronizing. Nitrocarburizing and nitriding, duplex coatings of Cr, W, Ti, V, Zr on pre-nitrided or pre-carburized surfaces are conducted below 723ºC. Major advantages of FBR-CVD surface treatments include reduced cycle times, better control of microstructure and interface chemistry, non-equilibrium phases, low capital cost with economies of scale. A review of some low temperature CVD coatings by FBR is presented hereafter, to understand the characteristics of surfaces produced by these methods for possible surface modification of short steel fibers.

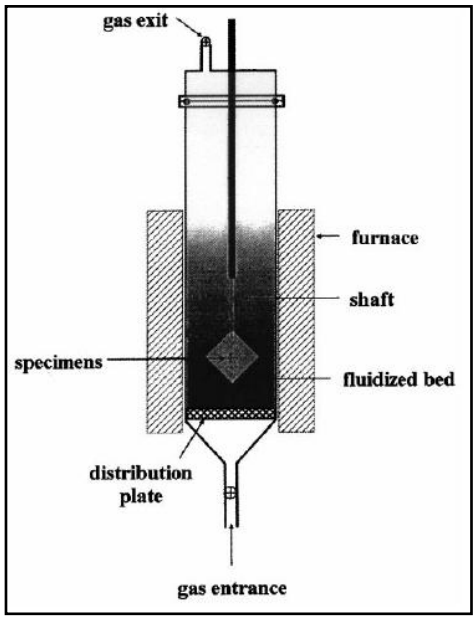

Fig. 2.5 Schematic representation of a FBR (Pérez, et al., 1999)

2.4.1.1 Chromizing

Chromizing refers to the process of depositing a Cr-rich surface on a steel substrate. Carbon content below 0.1wt.% results in soft chromizing, when substrate carbon content exceeds 0.3wt.% it is termed as hard chromizing. (Ralston, et al., 2011) have investigated chromizing of AISI 1020 steel by chemical vapor deposited active Cr using fluidized bed reactor (FBR). Fluidizing bed was composed of pure Cr powder (10 wt.%) in Al_2O_3 particles. Pure argon was the fluidizing gas and HCl gas was used as the activator medium. Test coupons were cooled under nitrogen to room temperature. The authors have reported the following mechanisms for deposition of active Cr on steel substrate (Pérez, et al., 1999):

$Fe_{(steel\ substrate)} + CrCl_2\ (g) \rightarrow FeCl_2 + Cr\ (s)$ (interchange)

$CrCl_2 + H_2\ (g) \rightarrow Cr\ (s) + 2HCl\ (g)$ (reduction)

$CrCl_2 \rightarrow Cr\ (s) + Cl_2\ (g)$ (decomposition)

The authors have suggested the deposition to be governed by interchange and reduction reactions. A Cr-rich layer of about 5 µm in thickness is reported after 3 h at 1000 ºC. Porosity free layer was found to be composed of Cr_7C_3- a hard combined carbide, without any Fe or Cr oxides near the substrate. An increase in the passivity range has been found by corrosion tests, making the plain carbon steel almost "stainless".

2.4.1.2 Aluminizing

CVD of aluminium over austenitic stainless steel (AISI 304) has been investigated by (Pérez et al., 1999) in a FBR by using pure aluminium powder as a precursor generator of reactive sub-halide Al species. Fluidizing gas used was a mix of 10 vol.% H_2- 1vol.% HCl- balance Ar. Aluminizing was carried out at 525ºC for different durations. Mechanism of sub-halide (Al_xCl_y) compounds formed have been reported by (Sánchez, et al., 2007), based on the Gibbs free energy of sub-halide precursors, AlCl, $AlCl_2H$ and $AlCl_2$ were the most probable candidates identified. These precursors react with other unstable products to deposit Al on the substrate as per the following two reactions:

$AlCl + AlCl2 \rightarrow Al + \Delta G_{f550^oC}\ AlCl_3 = -152$ kJ

$3AlCl \rightarrow 2Al + \Delta G_{f550^oC}\ AlCl_3 = -181$ kJ

Maximum working temperature of the process is limited by melting of aluminium (660ºC). Coating thickness/deposition rate can be controlled by increasing activator gas content in the fluidizing gas mix. Major phases analyzed in the deposited layer were $FeAl_3$, $Al_{13}Fe_4$ and NiAl.

2.4.1.3 Nitriding

Nitriding of steel in a FBR involves (1) loading of the retort with a fluidizing medium, generally spherical (~ 300 µm) alumina particles (2) introduction of a nitrogen containing gas into the FBR (3) heating the FBR retort (<650ºC) (4) safely disposing off the spent flue gases (Usta, et al., 2004). Dissolution of nitrogen is limited to 0.1% in iron, excess nitrogen combines with iron to form Fe_4N (γ), if nitrogen is more than 6% γ transforms to ε ($Fe_{2\text{-}3}N$). A composite containing both γ and ε is observed as a white layer over the substrate, with increased hardness resulting in enhanced corrosion and wear resistance, longer ratcheting fatigue life and better thermal endurance properties (Baczewska, et al., 2011; Türk, et al., 2005; Usta, et al., 2004; Baczewska et al., 2010).

2.5 Powder Metallurgy of Aluminium and Aluminium Alloys

Aluminium powder metallurgy has matured as a fabrication technique after the availability of almost all major alloy types. Generally prepared by inert gas atomization, a large variety of grades either completely pre-alloyed or partially pre-alloyed with elemental pre-mixes are now available to achieve component cost/weight reduction in automobiles, aerospace, electronic packaging, leisure and sport, to name a few areas of intervention (Pickens, 1981) . Aluminium Powder Metallurgy (P/M) offers components with equivalent mechanical and fatigue properties in comparison to wrought products of similar compositions. Lower density for overall weight reduction, corrosion resistance, with the ability of surface modification by coatings, high thermal and electrical conductivity, particularly useful in electronic packaging and thermal management of high frequency electronic equipment, excellent machinability with a good response to finishing processes are some of the benefits achieved (Marketing and the Technical and Standards Committees of the Pigments and Powder Division of The Aluminium Association, 1986). Classical benefits of powder metallurgy, primarily, higher material utilization alongwith lower energy consumption are not only retained in aluminium P/M but rather amplified on account of higher strength to modulus ratio (specific strength) of finished components. Aluminium P/M has been described as a versatile processing technique on account of its ability to modify alloy chemistry to suit specific functions whilst producing a near-net-shape product, wherein, important operating parameters include particle size distribution, blending techniques, pressing, and sintering (Kipouros et al., 2006).

2.6 Sintering of Aluminium

The sintering of aluminium is difficult due to the presence of thermodynamically stable oxide shell on the particle surface which hinders wetting and solid-state diffusion (Kondoh, et al., 2001). A dew point of less than -140°C or an oxygen partial pressure of $\leq 10^{-50}$ atm. is required to reduce Al_2O_3 at standard sintering temperatures (Liu, et al., 2007; Lumley, et al., 1999; Schaffer, et al., 2005), such conditions are impossible to achieve by conventional means in either laboratory or industrial fabrication systems, hence, a controlled atmosphere is required for sintering of aluminium. Several aspects on the role of atmosphere, powder shape and size, alloying additions, sintering aids, liquid phase fraction, sintering time and temperature have been studied. They are summarized as below, to offer an understanding on the sintering behavior of pure aluminium and alloyed powder compositions.

2.6.1 Effect of sintering atmosphere

In the sintering of aluminium powder based systems, the effect of atmosphere can only be studied in relation to the presence of elements that aid in disruption of oxygen from the tenacious layer of Al_2O_3. (Pieczonka, et al., 2008) extensively studied the dilatometric shrinkage of 99.5% purity aluminium powder over a 600°C sintering temperature for upto 150 min duration under flowing dry N_2-H_2 (maximum 5 vol.% H_2), N_2-Ar ; N_2, Ar, and vacuum. Initial findings pointed out to any noticeable shrinkage by N_2 only, addition of H_2, even in small amounts reduces the shrinkage, similar effect is observed with Ar, although at higher Ar content than H_2. Transverse rupture strength (TRS) of N_2 sintered samples was highest, however, it was not conclusively established that nitriding of the aluminium powder, in turn, caused reduction of the Al_2O_3 and was responsible for metallurgical bonding between aluminium particles. The nitriding of the powder particles will only occur if it is preceded by reduction or rather disruption of the Al_2O_3 layer, in this case, attributed to a self-gettering mechanism due to the presence of trace additions (as impurity) of Mg in the aluminium powder. This Mg content diffuses to the boundary of the particle and disrupts the Al_2O_3 film, exposing aluminium to N_2, as evident by the following reactions:

$$3Mg + 4Al_2O_3 \rightarrow 3Al_2MgO_4 + 2Al$$

$$2Al + N_2 \rightarrow 2AlN$$

This is a self-replicating reaction and is generally referred to as a self-gettering mechanism, wherein oxygen is removed from the Al_2O_3 layer by forming the spinel Al_2MgO_4 and AlN.

Formation of AlN, is a pre-cursor to shrinkage, and even small amounts of H_2, inhibit AlN, thereby delaying shrinkage. Graphically, this has been illustrated in Fig. 2.6.

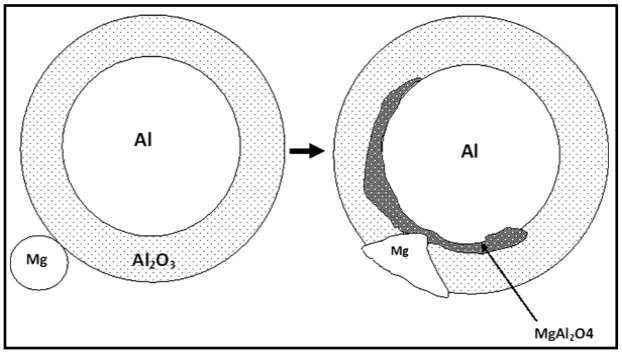

Fig. 2.6 Graphical representation of spinel ($MgAl_2O_4$) formation over an aluminium particle (Padmavathi and Upadhyaya, 2011)

Kondoh et al., 2001, have investigated the effect of Mg on the sintering behavior and mechanical properties of Al-12Si pre-alloyed powder with elemental Sn additions under N_2 atmosphere. Presence of Sn, resulted in negligible nitridation of both the pressed compacts and raw powders, owing to a persistent liquid phase that covered the particles; however, the presence of Mg aided nitriding, even with presence of liquid Sn at the sintering temperature. Consequently, an increased intensity of metallic α-aluminium has been detected aided by Mg, through 0.0-1.0 wt.% addition. Even under the influence of Sn (upto 1.0 wt.%); Mg results in disruption of large surfaces of Al_2O_3, incompletely wetted by liquid Sn; leading to formation of AlN. The presence of Mg, results in higher sintered densification by a factor of 2, smaller pores and a better metallurgical bond between the particles; higher elongation to failure and a dimpled fracture surface as opposed to premature brittle fracture along prior particle boundaries (PPB's) in chemistries with only Sn additions.

Densification of a green body is attained by pore closure or pore filling. (Schaffer et al., 2005) have extensively studied the role of N_2, Ar, N_2-5vol.% H_2, Ar–5 vol.% H_2 (all gases with dew points below -60°C,< 2 ppm oxygen) and vacuum on the sintering characteristics of Al-Mg-Si-Cu, Al-Cu-Mg and Al-Mg-Si species of elemental powder blends. Initial densification kinetics are similar for N_2, Ar and vacuum, it is in the later stages of sintering that N_2 exhibits higher kinetics. This is attributed to the formation of AlN, which by itself, is not responsible for wetting of aluminium, rather Al_2O_3 has a larger contact angle, almost double in magnitude with molten aluminium, which suggests that Ar and vacuum should exhibit similar or better wettability for liquid aluminium. The release of liquid aluminium is only facilitated by spinel formation as discussed above and not by AlN. It is the formation of AlN that aids pore filling by creating a negative pressure at the pore site due to consumption of the N_2 gas at the pore site

in comparison to Ar, which is non-reactive with aluminium, hence creating a back pressure and hindering pore closure. Densification in vacuum is somewhat midway N_2 and Ar. H_2 in combination with both N_2 and Ar is detrimental to densification due to formation of unstable hydrides like AlH_3 and Al_2H_6 that decompose at low temperatures, in spite of high solubility in molten aluminium, H_2 is diffused-out and further creates a back pressure at the pore sites and inhibits pore filling. This phenomenon has not been conclusively explained but was in agreement with pore morphology. Pools of liquid fraction were found with large grain sizes at filled up pore sites. Effectiveness of sintering atmosphere for these classes of powder blends was ranked as N_2 > vacuum > Ar > N_2 –H_2 = Ar- H_2. The effect of N_2 on sintering characteristics of aluminium has been discussed by (Schaffer and Hall, 2002); the self-gettering mechanism of oxygen depletion and spinel formation is limited to the inner core of a green compact, through networks of interconnected pores. This is explained by the low partial pressure of oxygen deep within the green body. The outer regions, like the surface in contact with furnace wall, remain largely unsintered; consequently N_2 is more effective at low green densities, wherein, large networks of continuous interconnected pores exist.

Martín and Castro, 2003, have reported better sintered densification in vacuum over N_2 for 2xxx species of pre-alloyed aluminium powders at all temperatures and durations against flowing high purity N_2; but the higher sintered densities obtained in vacuum did not translate into better age hardening response, primarily due to the slow cooling rate achieved under vacuum against flowing N_2, this was attributed to the amount of liquid phase present under liquid phase sintering and also the resulting morphology (shape and size) of precipitates after slow cooling; discussed further in the next section.

2.6.2 Effect of liquid phases on sintering densification

In the preceding section it has been established that for sintering of aluminium powder, the oxide layer has to be disrupted or reduced. A mechanism of self-gettering seems to be the dominant player under a dry nitrogen atmosphere, as discussed above. Following this pre-requisite, there also exists a need for development of a transient or persistent liquid phase to wet over the aluminium particles and aid sintering densification. Considering these pre-conditions, it is imperative that compositions for aluminium P/M are developed wherein these factors are built-in.

Schaffer et al., 2001, have shown an optimum Mg content of ~ 0.15 wt.% causes sufficient shear stress to break up the oxide film (generally 5-15 nm thick in gas atomized powders). The role of Mg was confirmed in Al-Sn, where liquid Sn only wets Al in the presence of Mg, it seeps out otherwise (m.p. of Sn 232°C). The maximum solid solubility of Sn is <0.15%,

whereas, Aluminium is completely soluble in liquid Sn and the diffusivity of Al in liquid Sn is about five times greater than the self diffusivity of liquid Sn (Schaffer, 2004). Sercombe and Schaffer, 1999a, have reported a 20% increase in properties upon introduction of 0.1wt% Sn in a traditional 2xxx series alloy (Al–4.4Cu–0.8Si–0.5Mg).

Citing the work of German and co-workers, (Schaffer et al., 2001) summarized the key factors for designing an ideal liquid phase sintering system: The additive should have a lower melting point than the base, a low melting point eutectic is less beneficial as liquid fraction does not form spontaneously. The solubility of the additive in the base should be low, ensuring segregation on particle boundaries, which maximizes the liquid volume fraction. Solid solubility of the base with the additive is not an essential, but liquid solubility of the base with the liquid additive is a necessary condition. High diffusivity of the base in the additive liquid ensures high rates of mass transport and therefore rapid sintering.

Sercombe and Schaffer, 1999b, have investigated the effect of trace additions of Sn, Pb, In, Bi and Sb (all <0.1 wt.%) on sintering densification of Al-4.0Cu-0.15Mg alloy. The maximum solid solubility of copper in aluminium is 5.65% at 548.2°C and the liquid phase is composed of a eutectic between Al and Al_2Cu (θ); any additive that delays the solidification of the liquid eutectic will increase the sintering densification. It was observed that even about >0.05 wt.% Sn, was sufficient to bind all the vacancies in aluminium, which reduced the diffusion of Cu into Al, whereby the liquid eutectic persisted for longer duration. Sn was ahead of Cu in the solid solution owing to its higher diffusion coefficient in aluminium. The volume of liquid phase present is the same, with Sn in trace amounts, but the duration to achieve equilibrium is longer with respect to the sintering cycle, resulting in enhanced densification. The effect is similar for other elements like Pb, Sb and Bi, which also enhance sintering densification. Addition of Ni and Zn has no effect as they possess very weak vacancy binding energies.

MacAskill et al., 2010, studied a ternary Al–1.5Mg–1.5Sn alloy, with Mg having both a master-alloyed and an elemental presence. It was observed that Sn alone, in spite of being the liquid phase, was not able to wet the aluminium, it was only with the presence of Mg that the wetting was activated. Higher densification was achieved in alloys with elemental Mg (upto 99.5% theoretical density). Sn was instrumental in lowering the mass gain observed in sintered samples, thereby, resulting in increased sintered density, but this effect was pronounced in the presence of elemental Mg. This phenomenon can be attributed to higher wettability induced by Mg, wherein Sn was better able to coat the exposed aluminium particles and hinder AlN formation. Considering only the elemental source of Mg, the ductility, under tension, increased upto 1.5 wt.% Sn and decreased thereafter. In the sintering response of a traditional 7xxx series Al–8Zn–2·5Mg–1Cu alloy mixed with trace additions (upto 0.16 wt.%) of Pb, Sn, Bi, Sb and

Se; it was observed that, the base composition alongwith Sb and Bi resulted in a net expansion, Se had no effect while Sn and specifically Pb were beneficial (Schaffer and Huo, 2000). Maximum improvement in tensile strength was observed with the addition of a pre-alloyed Zn-Pb master alloy; however elemental Pb alongwith the master alloy negated the improvements. The mechanism behind this observation was not explained and left to further investigation. Zn is the most important element in the 7xxx series high strength alloys, primarily on account of being able to form a low temperature eutectic (380°C) with aluminium and its ability to form a persistent liquid phase for enhancing sintering densification and further improving the ageing response; but the solid solubility of Zn in aluminium makes it a non-ideal candidate as a sintering aid, even with traces of Pb. The addition of Cu, however, created a net shrinkage at the sintering temperature; the benefits are attributed to improved wetting and formation of $CuAl_2$ intermetallic at the particle boundaries; adding up to a critical liquid volume fraction of 12%, in the present case of a supersolidus liquid phase sintering system (SLPS).

German, 1997, has stated that a SLPS occurs when a pre-alloyed powder is heated to a temperature between the solidus and liquids and the liquid phase nucleates within each particle. Densification occurs by viscous flow, which starts when the fractional liquid coverage of the grain boundaries reaches 73%. This liquid phase evolving out of the pre-alloyed particles is very sensitive to heating rates (40 $Kmin^{-1}$ in this case with a 20 min sintering hold), wherein, slower rates cause homogenization activated by solid-solid solutionizing at the sintering hold. Hence, the processing parameters are equally important to ensure SLPS. In this section, only the effect of liquid phase over sintered densification and age hardening response has been covered; other process parameters will be discussed in succeeding sections.

Martín and Castro, 2003, have investigated the effect of processing parameters on liquid phase sintering (LPS) of some common pre-alloyed aluminium powder mixes corresponding to age hardenable 2xxx, 6xxx and 7xxx wrought counterparts. Of the 2xxx pre-alloyed powder, two compositions were investigated, both showed initial swelling due to presence of a liquid phase, which helped in further densification during later stages of sintering. Higher sintering temperatures for the 6xxx alloy resulted in better final density, due to larger liquid fraction which aided progressive densification; however, the age hardening response under T4 (natural ageing) did not significantly differ for the two sintering temperatures, indicating grain coarsening, whereby benefits out of higher density did not translate into higher hardness; hardening phases namely Al_2Cu, Mg_2Si and $MgZn_2$ were detected for the three alloys respectively, in the as sintered state.

Delgado et al., 2005, have investigated the addition of Al-12Si (eutectic) pre-alloyed powder to pre-alloyed as well as elemental AA2014 as a sintering aid. The mechanism described here was

reduction in the contact angle of the liquid phase with the aluminium particle, thereby, increasing the time for Al_2Cu (θ) to stay in the liquid phase, which forms at 548°C. This aluminium-copper eutectic is transient in nature and in low Cu levels may be completely absorbed into α-aluminium. The Al-Si eutectic forms at a higher temperature, 578°C. Increased densification alongwith improved mechanical properties was observed at sintering temperatures in the 580-620°C range, with the addition of Al-12Si. Hence, increased wetting of the low temperature Al-Cu eutectic can be aided by introduction of another liquid phase, with reduced contact angle; will ensure delayed absorption into α-aluminium, increasing the duration of transient aspect and hence improved densification.

Bishop et al., 2000, have reported significant improvements in mechanical properties by trace additions of Ag-3.0 wt.% and Sn-2.0wt.% in an inert gas atomized Al–4.4Cu–0.8Si–0.8Mn–0.5Mg (AA2014) pre-alloyed powder. SnO_2 and $AgNO_3$ were the sources for Sn and Ag respectively. Sn supports the formation of Al_2Cu (θ) type of precipitates in Al-Cu systems; Ag helps in rearrangement of the θ' precipitates along a different habit plane ({111} instead of {100}) (Ω) with a hexagonal morphology instead of tetragonal. Aluminium, being a FCC material, deforms by slip along close packed {111} planes. Since Ω forms on the same family of planes it offers a more direct obstacle to dislocation motion than θ', thereby resulting in improvements in mechanical properties. However, the supersolidus temperature of sintering allowed higher liquid fraction of Sn, exacerbated by longer sintering cycle time (16 h), resulted in a Sn localization on grain boundaries and formation of a Sn-Al composite (authors claim to be useful in wear resistant applications). Ag did alter the morphology of θ' and resulted in increased strength, but no significant gains were reported in corrosion resistance.

The general sequence of precipitate ageing after a solutionizing and quench treatment in 7xxx can be expressed as: Supersaturated solid solution → Guinier-Preston zones (GPZ) → η' ($MgZn_2$) → η ($MgZn_2$) (Chinh et al., 2004) . It is generally accepted in PM aluminium based systems for age hardenable alloys that compacts in the sintered state are considered as T1 temper; in solutionized and naturally aged condition as T4 aged and if subject to artificial ageing treatment, in T6 aged condition. The 7xxx class of alloys is known for high strength due to maximum ageing response amongst all age hardenable alloys. Similar performance is expected in PM on account of high solubility of Zn in the aluminium matrix; Cu improves the wetting behavior and Mg, even in low concentrations, facilitates oxide film break-up and enhances sintering densification by self diffusion of aluminium across particle boundaries (Eksi et al., 2004). Chinh et al., 2004, have investigated the effect of Cu on the mechanical properties of Al-Zn-Mg alloys in the IM (ingot metallurgy) system and have reported that addition of Cu facilitates smoother transition from GP zones to η', thereby retarding the rate of

hardening in the early stages of natural ageing. Cu also alters the precipitate morphology from largely spherical to a mix of spherical and ellipsoidal; the spherical precipitates are free from Cu, largely composed of $MgZn_2$, the ellipsoidal shape is a result of strained interface, responsible for strength enhancement .

LaDelpha et al., 2009, have confirmed the presence of fine intermetallic phases on particle boundaries by point scan EPMA (electron probe micro analysis) in sintered compacts (T1 temper); further confirmed as η ($MgZn_2$) by XRD (x-ray diffraction) alongwith α- aluminium; detection of GP zones and η' was not possible due to their solid solubility in α- aluminium. After T6 (solutionized-quenched and artificially aged), the intermetallics visible after T1 were dissolved and XRD did not detect any phases; however microstructure revealed the presence of some Sn- rich phases and possibly Fe rich Al-Mg-Cu quaternary intermetallics (Fe being a common impurity in atomized aluminium powders). The α- aluminium was found be enriched in Cu, Zn and Mg, signifying sufficient homogenization. Thermodynamic studies by analysis of heat flow in a DSC (differential scanning calorimeter) revealed distinct exothermic (formation of hardening precipitates) and endothermic signatures (dissolution of precipitates) (Lloyd and Chaturvedi, 1982). The following thermodynamic behavior was observed till 525°C at 10°Cmin^{-1} for both T1 and (T6) conditions (LaDelpha et al., 2009):

$$\underset{81^0C(N/A)}{GPZ\ formation} \rightarrow \underset{150^0C(200^0C)}{GPZ\ dissolution} \rightarrow \underset{200^0C(237^0C)}{formation\ of\ \eta/\eta'} \rightarrow \underset{250^0C(255^0C)}{growth\ of\ \eta} \rightarrow \underset{297^0C(330^0C)}{dissolution\ of\ \eta/\eta'} \rightarrow \underset{441^0C(N/A)}{melting\ of\ S-phase}$$

The hardness achieved by the PM alloy was equivalent to that of wrought 7075 in T6 treated condition. Calorimetric studies on the precipitation behavior showed that that it followed the η ($MgZn_2$) based sequence typical of 7XXX series wrought alloys. In the T-6 condition, GP zones were the dominant strengthening precipitates. Elevated temperature exposure to tensile specimens of the alloy showed visible reduction in tensile strengths at temperatures corresponding to dissolution of η/η'. The effect was more pronounced in T-6 treated specimens. Fatigue life was compared with a similar wrought alloy and statistically shown to be within a 50% probability of failure; this was largely attributed to residual porosity (~1 vol.%), which acts as a stress raiser, thereby increasing fatigue crack sensitivity of the PM alloy.

Mohammadi et al., 2010; Shahmohammadi et al., 2007, have investigated the phase evolution in elementally prepared Al–5.6Zn, Al–5.6Zn–2.5Mg and Al–5.6Zn–2.5Mg–1.6Cu (wt-%) powder mixes. In the Al-Zn powder mix, an expansion was recorded at 420°C, corresponding to bilk melting of Zn; this liquid phase was transient in nature owing to excessive dissolution of Zn in aluminium at this temperature; however, this liquid phase aided in a net densification at the sintering temperature (600°C). Influence of Mg to the Al-Zn powder mix aided net densification after an initial dilatation due to melting of Zn by formation of an intermetallic eutectic between $Mg_{17}Al_{12}$ and Mg; further heating to the sintering temperature resulted in ternary intermetallics of Al-Zn-Mg. Densification was aided by presence of these intermetallics and pore filling effects due to capillarity and particle rearrangement. For the A-Zn-Mg-Cu compacts, initial swelling was even more pronounced, but densification was aided at the sintering temperature by formation of Al-Cu eutectic in liquid phase (Schaffer et al., 2001). The effect of reduced porosity, aided by LPS, has a direct bearing on the mechanical properties of the alloy system investigated. The addition of Mg and Cu to the Al-Zn alloy has a strengthening effect by precipitation hardening; this effect is even more amplified by reduced porosity levels. Increasing the Zn and incorporation of Al-Mg master alloy powder particles is reported to give better strength and overall ageing response.

Showaiter and Youseffi, 2008, investigated the sintering behavior of Al–1.0Mg–0.6Si–0.25Cu (corresponding to wrought 6061) using elemental powders with additions of 0.12 Pb, 0.1 Sn or 0.4 Ag (wt.%) as sintering aids. Sintered densities were higher for the same compaction pressure and sintering temperature under N_2, in comparison to vacuum, the mechanisms for such an observation have been outlined in *Section 2.2.2*. Amongst the sintering aids employed, addition of 0.12 wt.% Pb was most effective (almost 100% theoretical density was achieved); Sn and Ag additions did result in enhanced densification but to a lesser degree. EDX (energy dispersive x-ray) analysis of intermetallic precipitates revealed the presence of Al–Mg_2Al_3–Mg_2Si (450°C) and Al–Si–Mg_2Si (555°C) phases; further signifying the dominance of Mg_2Si as the strengthening precipitate. Localized large sized pores were visible in specimens without any sintering aids due to formation of a transient liquid phase, which on slow furnace cooling and homogenizing generated a net expansion and growth of pre-existing pores owing to Kirkendall effect. The addition of Pb, Sn and Ag has been shown to reduce the surface tension and facilitate the wetting of supersolidus liquid phase over the aluminium particles (German, 1997); however it is widely reported that the solidified liquid phase, rich in low melting point constituents as either intermetallics or eutectics, will be detrimental to mechanical properties by inducing brittleness and premature failure.

Youseffi et al., 2006, have shown from thermodynamic analysis of pre-alloyed 6061 compacts the formation of a persistent liquid phase (sintering temperature 620°C, 1h sintering hold, N_2 atmosphere) owing to incipient melting of the powder. Intermetallic phases detected were Mg_2Si+Mg_5Al_8 (449°C); Mg_5Al_8 (450°C) and Mg_2Si (595°C). As reported earlier by the same workers, for elemental powders of same alloy composition, the dominant sintering mechanism was transient liquid phase sintering, whereas with pre-alloyed powder, sintering progressed under a persistent supersolidus liquid phase. A simplified mechanism for sintered densification under SLPS mechanism and Mg_2Si precipitation has been graphically illustrated in Fig. 2.7.

Sercombe, 2003, has shown that elemental additions of Mg (instrumental in disruption of tenacious oxide layer over aluminium particles) and Sn/Pb (generation of a persistent liquid phase) is most effective in sintered densification of uncompacted (loose) pre-alloyed 2124 and 6061 powders, the research was conducted as a simulated experimentation of SLS (selective laser sintering); wherein layer-wise deposited polymer blended loose powder feedstock is sintered by a laser beam as the energy source. The presence of a liquid phase, at sintering temperatures (610°C for 2124 and 635°C for 6061) ensuring about 20 vol.% of liquid fraction, aided densification, further activated by the presence of elemental Mg (*mechanism discussed in section 2.6.1*). 0.1 wt.% of Sn was sufficient for 6061 whereas 0.5 wt.% was required for 2124.

Schaffer, 2004, have summarized that aluminium PM is seeing an increased interest beyond current applications areas limited by fatigue and stress applications, in marine, hand tools, office machinery and like. However, with judicious understanding of sintering mechanisms, near-net-shape, fully dense components can be realized without resorting to expensive pre-alloyed powders and capital intensive secondary thermomechanical processing. Such alloy design for aluminium PM and composites will open new application areas driven by automotive and aerospace, harnessing, light weight, high compressibility, low sintering temperatures, easy machinability and good corrosion resistance to the advantages offered by existing PM technologies.

2.6.3 Effect of particle morphology on sintering densification

The particle size and shape of the aluminium and alloying element particles have a direct relationship with sintering kinetics. Effect of particle size and shape on sintering densification for a Al-4Sn elemental, uncompacted, powder mix has been studied by (Liu et al., 2007); employing various size distributions and shapes (3, 5 and 15 µm-spherical) and (6, 7 and 15 µm-irregular). It was noted upon sintering under Ar atmosphere at 620°C, that the particle shape had an important bearing on the sintering behavior of the powders. An outer un-sintered layer is usually retained; this region is devoid of the liquid phase and the autogeneous gettering

is more effective in the inner core. This un-sintered outer layer was of lesser thickness in irregular shaped powders in comparison to spherical powders. In the inner regions, the spherical powders displayed large voids and connected pores, unlike irregular powders that showed very evenly distributed smaller pores, with visible neck growth. The oxide layer could not have disrupted by mechanical deformation as the powders were uncompacted, no sintering aid like Mg or N_2 were employed, hence the justification given for oxide disruption was based on Hooke's law for stress arising on account of differential thermal expansion of aluminium

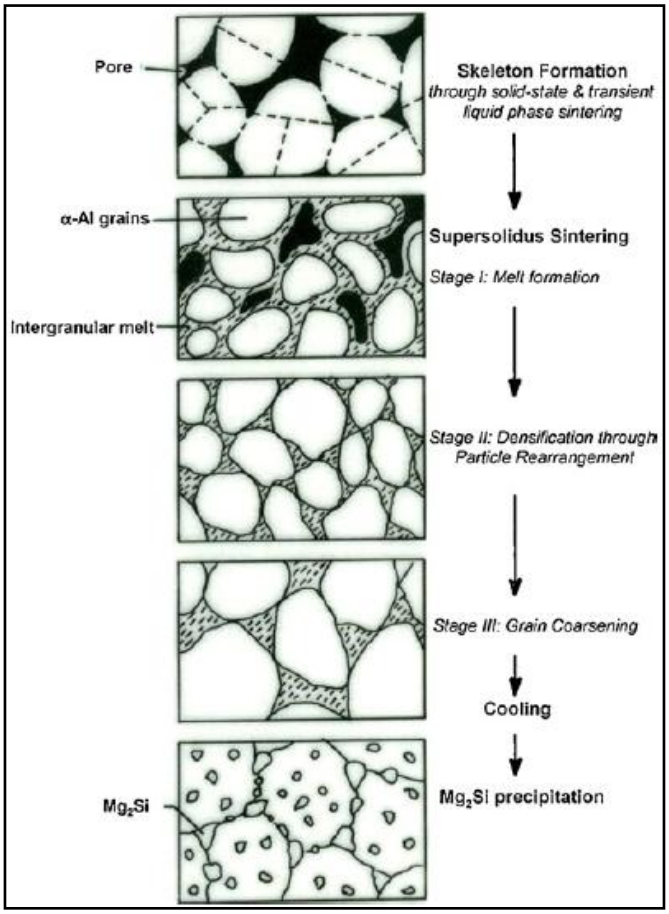

Fig. 2.7 Graphical representation of supersolidus liquid phase sintering of pre-alloyed 6061 (Padmavathi, Upadhyaya, and Agrawal, 2011)

and alumina layer, given by equation: $\sigma = E(\alpha_{Al} - \alpha_{Al_2O_3})\Delta T$; where E is the modulus of alumina, α is the thermal expansion coefficient, and ΔT is the temperature change. A temperature increase of 600°C will generate about 4,000 MPa in alumina, more than enough to rupture the oxide film. This stress will further create stress concentrations over irregular shaped particles, leading to cracking of the oxide film at more sites than spherical shaped powder particles. However, this breakage will immediately heal with the oxygen present in atmosphere; this continuous dynamic breakage and repair phenomenon will be more

pronounced in irregular particles compared to spherical ones, thereby, offering a more effective autogeneous gettering of oxygen from both the inner core and outer layers of the green compact.

Lumley and Schaffer, 1996, have investigated the sintering densification with coarse (120-150 µm) and fine (<45 µm) Zn, Sn and Cu for Al-5Sn, Al-l0Zn, and Al-5.5Cu powder blends, (aluminium powder with d_{50} of 60 µm). The amount of liquid phase was similar for coarse and fine Sn. For fine Zn powder, a completely homogenized solid solution of α-aluminium with Zn was obtained after the sintering hold at 620°C, without any liquid phase detected at particle boundaries, an un-sintered microstructure resulted with limited inter-particle connectivity. For coarse Zn powder, the reaction with α-aluminium occurred over a temperature range forming large liquid pools and initiating liquid phase sintering; homogenization was achieved by further hold at the sintering temperature. Quantitative metallographic examination revealed presence of a liquid phase present for three times longer with coarse zinc particles, with double the amount of liquid formed. For Cu powders the sintering liquid is a eutectic which forms above 548°C. At 575°C melt pools formed around large Cu particles whereas limited liquid forms with small Cu powders. At 600°C, the fine powders had completely reacted and the volume of liquid phase had reached a maximum attaining equilibrium over the next 5 min. For coarse Cu powders, at 600°C, grain and particle boundaries were penetrated by liquid and particle rearrangement took place in melt pools. Which continued for the remainder of the sintering time with formation of liquid networks; resulting in extensive sintering densification for the entire duration of the sintering hold of 40 min (3% increase in density upto 92% of theoretical for fine and 7% increase, upto 94% of theoretical density for coarse). Pore morphology with large additive powder sizes is composed of large porosities farther apart, with well bonded intra-pore sintered regions; whereas, with small additive powder particles, the pores are inter-connected, more uniformly distributed with largely unsintered/unbonded intra-pore regions.

Lumley and Schaffer, 1998, investigated the effect of additive Cu particle size (fine <45 µm, intermediate 75-106 µm and coarse 125-150 µm) on sintering densification and resulting mechanical strength of Al-4Cu elemental powder mix. It was found that higher heating rates with all sizes of Cu resulted in increased densities; the tensile strength was highest with intermediate size or fine particles with a high heating rate, the yield (0.2% proof) strength was independent of particle size.

Similar microstructures were obtained as reported by (Lumley and Schaffer, 1996) for large particle size, good sintering densification with large sintered/bonded regions, separated by large sized pores. Intense densification and bonding was revealed with intermediate sized Cu, with fewer and smaller retained pores. Fine Cu resulted in smaller more evenly distributed

porosity. Higher strengths were attributed to increased ductility of the aluminium matrix and suppression of premature failure on account of large poorly sintered zones. The failure initiating sites were poorly bonded/unsintered regions rather than large pores. It was inferred, like in castings, that the load bearing capacity depends on a stable metallurgical bonding, in this case, sintering densification and resulting well bonded matrix, rather than overall bulk density. Higher heating rates ensured rapid evolution of liquid phase, which acts as a pore filler, especially in systems like Al-Cu, wherein, diffusivity rates of Cu in matrix α-aluminium are high.

2.7 Deformation Processing of Aluminium P/M Alloys

Thermo-mechanical deformation processing by forging, hot pressing, extrusion or rolling of powder (compacts) in encapsulated-vacuum de-gassed; cold pressed or sintered states have been widely reported in literature as industrially acceptable techniques to enhance the mechanical properties of components for demanding applications (Kuhn, 1978). Increments in strength, impact energy and fatigue resistance have been attributed to reduction in porosity, combined with better metallurgical bonding between particles on account of shear induced rupture of oxide film (Abdel-Rahman and El-Sheikh, 1995; Upadhyaya, 1997). Evolution of a typical material microstructure after press and sinter of aluminium based powders has been shown in Fig. 2.8. It is largely composed of retained prior particle boundaries (PPB's) and sub-particle grains, rearranged particles, free standing or interconnected pores and an intermittent oxide layer.

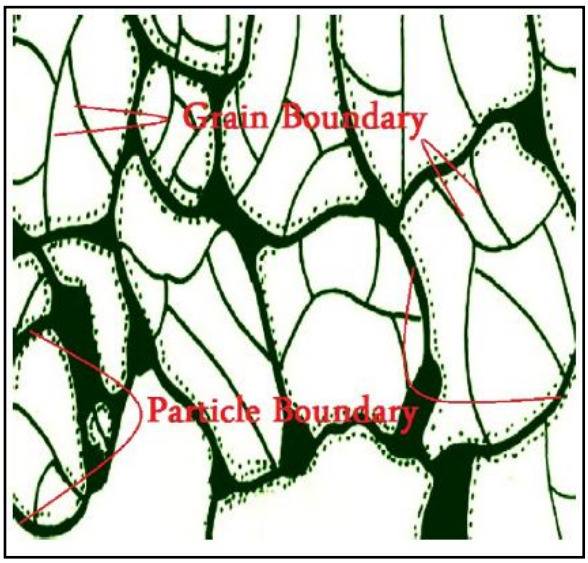

Fig. 2.8 Typical microstructure of a pressed and sintered material (Mazahery and Shabani, 2012)

To achieve optimum properties in aluminium based powder alloys, (Greasley and Shi, 1993) have outlined important stages prevalent during deformation based consolidation, as: (1) homogenization of as-rapidly solidified sub-structure of particles, leading to uniform dissolution of alloying elements, dispersoids, precipitates and phases (2) disruption of nascent oxide layer (3) creation of precipitate free zones due to high diffusion rates over free surfaces and excessive plastic work (4) effect of local strain fields that influence recovery, recrystallization and grain growth (5) upper bounds of hot working temperature and strain rate to avoid incipient melting and hot shortness. By hot plain strain compression testing of sinter-extruded AA2014 pre-alloyed powder compacts over a range of temperatures, strain rates and imposed strain, (Greasley and Shi, 1993), have reported that strains of 0.8, (extrusion ratios of 2·5:1), are insufficient to dissolve PPB's. Strains of 1·6 (extrusion ratio 5:1) are sufficient to remove PPB's at deformation temperature $\geq 0.7\ T_m$. Strains of 2.4 (extrusion ratio 11:1) are sufficient to remove PPB's at all deformation temperatures. At strains ≥ 2.4 and strain rates $\geq 6{\cdot}9\ s^{-1}$, stable microstructures are attained at all working temperatures. The upper limit for extrusion temperatures to avoid incipient melting and onset of hot shortness is about 70 K lower than that determined by thermodynamic analysis for that alloy, due to frictional heat at the billet-die contact surface.

2.8 Deformation Processing of Aluminium P/M based Composites

Discontinuously reinforced aluminium (DRA) based composites formulated by incorporation of hard ceramic particulates/platelets/whiskers/short fibers as reinforcements have been subject to various secondary hot consolidation operations like extrusion, forging, rolling, and swaging etc., to achieve near theoretical density for optimum mechanical properties.(Srivatsan, et al., 1991) have listed various commercial manufacturers of powder metallurgical AMC's as either intermediate extruded stock for forging and/or direct use. The authors have summarized the various steps in fabrication of P/M AMC's as (1) sieving of constituent matrix powders for size control (2) blending of reinforcing particles (dominantly α-hcp or β-bcc SiC particles) with the matrix powder (3) cold consolidation of the composite to leave sufficient interconnected porosity for degassing (4) final consolidation by hot working techniques like forging, hot pressing, extrusion or rolling. Popular alloys identified for AMC's correspond to traditional AA2124, AA6061, AA7090 and AA7091; other non-conventional matrices correspond to rapidly solidified Al-Fe-Ce and Al-Cu-Mg-Li. A recent and detailed compilation of AMC's is available at (MMC Assess, n.d.).

2.9 Forging

Generically, the terms forging, powder-forging and sinter-forging in powder metallurgy, equivalently denote the cold/warm or hot consolidation of either loose powders, sintered or semi-sintered compacts, under different levels of constraints over the job being worked. In general, loose powder (powder compacts), irrespective of material chemistry, are reported to experience three principal modes of compact consolidation by forging, as hypothesized by (Griffiths, et al., 1976), namely (1) free axis-symmetric compression, in absence of lateral constraints (2) upsetting, regarded as plane-strain compression with restrained flow along one principal direction (3) re-pressing under total constraint in a closed die configuration. Pore closure characteristics were presented as: (1) pore closure in pressing direction with pore alignment along lateral direction-minimum densification under a tri-axial stress state (2) pore closure in pressing direction followed by enhanced densification due to lateral restriction imposed under a bi-axial stress state (3) pore closure in pressing direction to near full density by fully constrained deformation of the powder (compact), respectively, for the three deformation modes discussed above. The lateral spread of pores results in a particle to particle shearing effect, which is responsible for elongation and final closure of pre-existing, predominantly spherical pores with increasing deformation strain and/or restrictions posed by a rigid die for upsetting or re-pressing modes. Closed die upsetting will eventually approach re-pressing mode in the latter stages of deformation, when the flowing material contacts the die walls. The imposed lateral strain during upsetting is limited by the workability of the material, wherein there is a development of high tensile strains due to pore flattening, leading to cracks (Upadhyaya, 1997).

Determining factors in powder forging include alloy composition, preform porosity, particle size, oxygen content, shape of preform and projected area in addition to processing variables like compact and die temperature, lubricant, imposed strain and strain rate. (Venugopal, et al., 1990) have reported on the average strain rates (actual strain rates depend upon specimen temperature) attained by different forging presses during forging of commercially pure titanium. Hydraulic presses in manual or automated operating mode generate 10^{-1} s^{-1} in comparison to a Weingarten friction screw-type press which is capable of upto 10 s^{-1}; followed by a mechanical percussion press offering an average strain rate of upto 32 s^{-1}. For realization of porosity free sinter-forged steel components, (Hendrickson, et al., 2000) have outlined the following prerequisites (1) the applied forging stress should be at least 5 times greater than the bulk flow stress of the material being forged (2) excessive lateral plastic flow by upset forging is not a sufficient pre-condition for attaining pore closure and enhanced ductility of the component, in fact, large deformation strains may impact tooling life and cause surface

cracking on the preform (3) the tool-workpiece contact time should be limited to a few milliseconds- only achievable by presses capable of high ram speeds (4) for components undergoing high tensile and/or fatigue service, the residual porosity should be below 0.5% alongwith very low oxygen content (5) tooling and forging equipment integrity coupled with real-time monitoring of ram speed, blow force control and overall cycle time which includes preform loading, forging and ejection under an automated environment is vital to process robustness.

2.9.1 Forging of monolithic aluminium P/M alloys

Odani, 1994, reports on the development of high strength sinter forged aluminium alloys under SUMI-ALTOUGH^{TM} series of non-equilibrium (alloying beyond solubility limits posed by conventional processing) dispersion strengthened alloys, formed by rapid solidification processing (RSP). Mechanical and thermal properties of sinter forged components from alloy species corresponding to Al-Si, Al-Si-X, Al-X and Al-C (X- Fe, Ni, Mn, Cr) have been found to be higher than conventional IM (ingot metallurgy) aluminium alloys (Das, et al., 1990). Specific gains are reported in high-temperature strength, wear resistance and elastic modulus. Typical applications include compressor vane, piston and cylinder liner, connecting rod and heat sinks for electronic packaging. The author describes the processing steps as cold consolidation by CIP (cold isostatic pressing) followed by hot extrusion and finally forging under closed dies to yield complex 3D near-net-shape components. Key process variables include rapid heating of compacts for forging, utilizing induction heating, enabling lower hydrogen pick-up for crack free outer surfaces.

Iwata, et al., 1989, describe a method for fabricating pistons by powder forging of rapidly solidified Al-20Si-4.8Fe-2.2Cu-1.2Mg-1.1Mn, pre-alloyed powder. The major steps included cold compaction, canning and degassing at 400-500ºC under high vacuum, followed by extrusion at 350-500ºC, de-canning the extrudate and forging of the extruded stock under shaped dies at 400-500ºC to yield a rough piston, which was further solutionized and artificially aged. The maximum strain was limited to 43% with a strain rate of 0.24. The inventors were able to overcome surface cracking by limiting the oxygen content to below 600 ppm by vacuum degassing against starting powder with an oxygen content of upto 2000 ppm. The role of major alloying additions has been justified as: Fe- high modulus, Si- abrasion resistance, Cu- interparticle bonding under high Fe/Si content and age hardenability, Mn- dispersoid strengthening at elevated temperature.

Siegert and Ringhand, 1994, have outlined the benefits of pre-consolidated (by extrusion) forging stock that can be worked on conventional forging equipment to fabricate powder forged connecting rods by closed die flashless forging for improved surface finish, better feedstock utilization and higher fatigue resistance, possible fabrication routes have been shown in Fig. 2.9 DISPAL^{TM} series of RSP powders reported in the study comprise of spray deposited DISPAL-S^{TM} (Al-17Si-5Fe-3.5Cu-1.1Mg-0.6Zr), age hardening included in billet pre-heating cycle for forging, and reaction milled DISPAL-M^{TM} (Al-12Si-1C-1O) carbon and oxide dispersion strengthened, for elevated temperature and high stress applications. Optimal workability window, which relies on strain, strain rate and temperature, has been determined by hot torsion tests.

Dashwood and Schaffer, 2002, have investigated the effect of deformation strain profile on pore closure during hot upset forging of high density (~96%) sintered Al–3.8Cu–1Mg–0.8Si–0.1Sn P/M alloy preforms over 350-500ºC, employing strain rates of 1, 10^{-1}, 10^{-2} and 10^{-3}. The stress-strain data confirmed with Norton-Hoff equation, which recommends compatibility conditions for viscoplastic flow of materials under hot deformation as: $\sigma = k\,\dot{\varepsilon}^{m}$, where σ is the average flow stress, k is the strength constant, $\dot{\varepsilon}$ is the strain rate and m represents the strain rate sensitivity index. The values of m were equivalent for wrought AA2024 on account of low sintered porosity and increased with increasing forging temperature. An increase in porosity was observed while moving away from the center of the preform, due to a circumferential hoop stress that develops over the freely expanding outer layers during upsetting. Higher densification, by pore closure under a net compressive stress, was achieved for higher temperatures, in spite of lower strain distribution in comparison to lower temperatures.

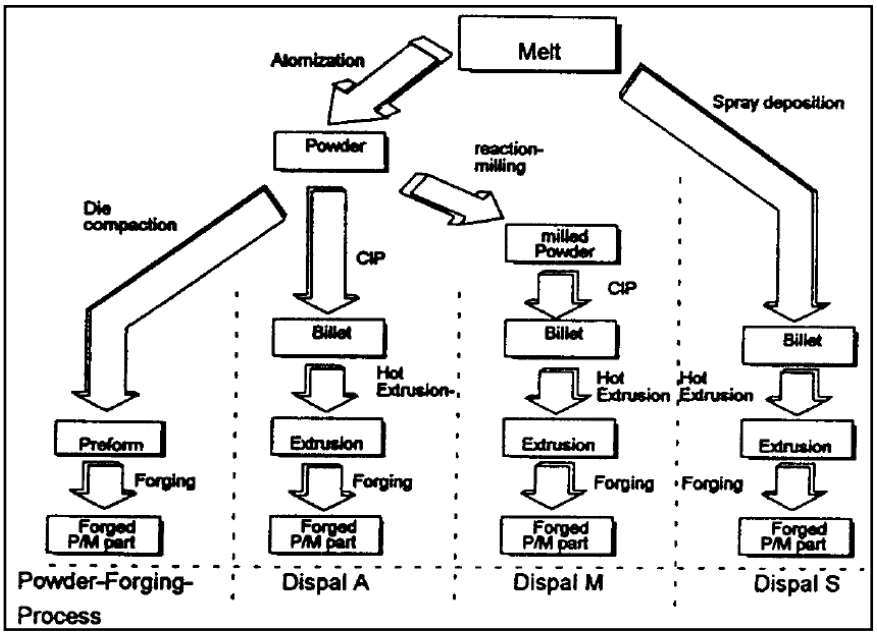

Fig. 2.9 Processing routes for powder forged connecting rods (Siegert and Ringhand, 1994)

This effect was attributed to softening and dissolution of $CuAl_2$ (θ) phase with increasing temperature, resulting in homogeneous deformation and increased strain rate sensitivity at higher temperatures.

Park, et al., 2001, optimized the alloy chemistry by additions of Cu, Si, Mn, Mg and Ni to pre-alloyed Al-4.5Cu-0.5Mg-0.7Si (Si was varied from 0.5-1.5 wt.%) and sintering conditions by varying the sintering temperatures from 560-600ºC and sintering time from 20-30 min for fabrication of powder forged aluminium alloy pistons. Optimal parameters were established as: Si-1.5 wt.%, 25 min and 580ºC. The aspect (*d/h*) ratio of sintered preforms was maintained at 1.0, 1.2 and 1.5 for determination of hot workability. Preforms were incrementally formed to the final shape of the piston, by visual inspection and FEM analysis, the authors' were able to optimize the starting shape of the sintered preform for final forging, such that the forged piston was free of any density gradients and surface cracks, with complete die-filling. Forging temperature was optimized at 420ºC; with die maintained at 250ºC. Tensile strength (T6-condition) of the optimized powder forged piston was upto 500 MPa, almost twice than that recorded for conventionally gravity cast piston and about 60% more than wrought forged counterpart of equivalent hardness. Disruption and dissolution of oxide layer over powder particles is known to strengthen secondary worked aluminium P/M alloys by pinning gain boundaries during recovery, thereby retarding recrystallization (Hansen, and Bay, 1972), alongwith imparting enhanced wear resistance. Even higher strength differential, in comparison to conventional pistons, is reported by the authors (Park, et al., 2001) when sintering atmosphere was changed from argon to nitrogen.

Ichikawa and Morita, 2010, have extensively experimented with the composition, sintering and preform hot forging process parameters for achievement of optimal mechanical properties (T6-UTS > 500 MPa; elongation > 2%) for monolithic AA7075 powder metallurgical alloy. The experimentation was designed to enable formation of strengthening phases of type $MgZn_2$ (η); $Al_2Mg_3Zn_3$ (T) and $CuAl_2$ (θ), during ageing, by selective addition of pre-alloyed master alloy batches alongwith pure aluminium to ensure compactability; without excessive amounts of Zn- may leach out of the compact during sintering; Mg- generate excessive liquid phase during formation of spinel and compact distortion may result and Cu- may form Cu-Zn binary intermetallics, detrimental to strength and elongation. Addition of low melting point sintering aids like Sn, Sb and In, (Pb and Cd discarded on grounds of toxicity) in elemental or binary (Sn-Zn; Sn-Bi) or ternary (Sn-Zn-Bi; Sn-Ag-Bi) eutectics; commercially available as lead-free solders; to aid densification by evolving a persistent liquid phase was limited to below 0.5wt.%. Particle size limitations are imposed on elemental additions of Zn, Cu and Mg or pre-alloyed master batches of Al-Zn and Al-Mg-Cu to below 200 mesh (74 μm) and 100 mesh

(140 μm) on elemental aluminium, for uniform wetting of aluminium particles by eutectics and easy cold consolidation. Threshold values for green density are 90% of theoretical density at 200 MPa and 95% at 400 MPa; higher compaction pressures result in adhesion of aluminium skin to the die walls. During sintering the temperature ramp-up rate after 400ºC to the sintering hold should be rapid, to avoid Zn flow-out of the compact skeleton. During cooling cycle, the rate of cooling should be accelerated till 400ºC, to avoid precipitate coarsening and grain growth. Dry nitrogen gas (dew point < -40ºC) atmosphere is best suited for disruption of tenacious oxide layer over the aluminium particles. The inventors' have proposed constrained die upset forging for deformation based densification of the sintered compacts. Such forging is characteristic of pore closure achieved by combination of compressive and lateral strains. The degree of deformation, defined as the ratio of projected area of the sintered preform to the forged specimen is limited to 40% for cold forging and 70% for hot forging. A 3% upsetting (re-pressing) ratio is sufficient to achieve pore closure in near fully dense sintered compacts. External cracks are generated at upsetting ratios greater than 70%. Lateral deformation enhances mechanical properties by dynamic recrystallization and fracture of precipitates.

MacAskill, et al., 2009, have compared the effect of cold (RT) and hot (320-500ºC) rotary swaging on sintered Al-1.5Cu-2.5Mg-5.5Zn (AA7075). Rotary swaging can be best described as a metal forming technique which involves longitudinal drawing out of the stock by high strain rate repetitive forging, ensuring homogeneous strain distribution and absolutely no loss of material. Cold swaging of sintered compacts in the as-sintered state (T1), resulted in cracks, which were reportedly overcome by annealing and solutionizing of sintered compacts prior to swaging, with appreciable increase in density and tensile strength, but deterioration in elongation was observed. The time interval between solutionizing and cold swaging may have led to evolution of precipitates, which caused micro-cracks and hence elongation to failure was limited for both the annealed and solutionized specimens. An upper-bound of 500ºC was attained for hot swaging to avoid hot-tearing caused by incipient melting and solute segregation. Gains in density were largely independent of swaging temperature with equal increments reported for 300-500ºC (~99.6 %). For samples swaged at 300 and 350 ºC tensile strengths were equal to cold swaged counterparts, with higher ductility ~5% compared to < 2%. Maximum strength (T6) was obtained for samples hot swaged at 450 and 480ºC, which were higher than wrought AA7075-T6. Maximum elongation was reported for a swaging temperature of 500ºC (6.5%). As-swaged samples exhibited better ageing response in comparison to sintered samples on account of a homogenized microstructure. The DSC signatures in the form of endothermic peaks, which signal dissolution of precipitates (η and η'), were very similar to wrought AA7075, used for comparison. Fatigue behavior of hot swaged

samples in T6 condition showed much improvement over sintered samples, primarily due to reduced porosity. A fatigue limit of 250 MPa was attained for sinter-hot swaged material, surpassing wrought AA7075 (210 MPa) for 10^7 cycles.

Bishop, et al., 2011, investigated isothermal hot deformation behavior of sintered AA2024 and AA7075 pre-alloyed compacts within 360-520ºC, employing true strain rates of 10^{-3}, 10^{-2}, 10^{-1} and 10^0 s^{-1}. The authors' have proposed hot working of the sintered compacts to disrupt and disperse the oxide layer over powder particles and eliminate post-sinter residual porosity, which in the current study, resulted in very low elongation to failure for the sintered specimens, albeit with reasonably higher tensile strengths in both as-sintered (T1) and artificially aged (T6) states. An almost linearly increasing dependence was reported for flow stress with increasing strain rates, at a given temperature. Similarly, a decrease in flow stress with increasing temperature, was observed at a given strain rate. Hot-deformed densities were in the range of 99.5% of theoretical density for both the alloys. Linear variation of flow stress with temperature and strain rate is indicative of excellent forgeability of sintered compacts in the aluminium P/M system. Strength increments (T6) were of the order of 28% and 22% for AA7075 and AA2024 respectively in comparison to as-sintered state, with almost 5 fold improvement in tensile ductility. The hot worked P/M alloys surpassed similar wrought alloys in tensile strength and elongation, both species tested in T6- artificially peak aged condition.

Mosher, et al., 2011, have modeled isothermal hot forging characteristics of sintered hypoeutectic Al-6Si-4.5Cu-0.5Mg (Al-6Si) and hypereutectic Al-15Si-2.6Cu-0.5Mg (ALUMIX-231^{TM}, Ecka Granules, Germany) aluminium based pre-alloyed compositions over 360-480ºC, employing true strain rates of 10^{-3}, 10^{-2}, 10^{-1} and 10^0 s^{-1} for a total upsetting strain of 0.75. Flow stress increased with starting higher green densities and strain rates, with ALUMIX-231^{TM} exhibiting higher values than Al-6Si. Reduction in peak flow stress was observed with increasing temperature. The flow curves were characteristic of peak stress followed by softening, most likely promoted by dynamic recrystallization (DRX). Higher densification (increase in compact density over sintered density) was generally achieved by hot upsetting temperatures below 480ºC at slower strain rates for both the alloys. Strain rate and upsetting temperature had little effect on final forged density, which in both the cases, was more sensitive to starting sintered density and consequently compaction pressure. Highest forged density of 98.3% was reported for ALUMIX-231^{TM} and 99.6% for Al-6Si, both compacted at 600 MPa. Al-6Si was more amiable to hot deformation, as pore closure and sound distribution of hard Si particles was achieved; in contrast ALUMIX-231^{TM} had little post-sinter porosity, and higher volume fraction of hard Si particles, which upon forging, generated voids by agglomeration and inter-particle cracking. The activation energy for

deformation Q (kJ mol^{-1}) for the two alloys, was in the range of 275-295 kJ mol^{-1}, which the authors' found to be about 50 kJ mol^{-1} higher than studies conducted on other aluminium P/M alloys with lower alloying contents, on account of higher resistance imposed on dislocation motion.

Simulated hot deformation of sintered P/M alloy 2324 (Al-4.4Cu-1.5Mg-0.2Sn) was carried out by (Mann, et al., 2011) over 350-500ºC, under true strain rates of 10^{-3}, 10^{-2}, 10^{-1} and 10^{0} s^{-1} for a total upsetting strain of 0.75. Near dense sintered compacts having theoretical density ~99.5%, displayed a peak stress followed by flow softening; the peak flow stress increased with increasing strain rate and decreased with increasing upsetting temperature. Flow stress behavior and peak flow stress was equivalent to wrought AA2024 alloy, deformed using similar parameters. Full densification of the P/M alloy was reportedly achieved at all combinations of strain rates and deformation temperature, indicative of excellent forgeability of the alloy. Flow stress data was used to determine temperature compensated strain rate, as the Zener-Hollomon (ZH) parameter denoted by Z in equation: $Z = A \sinh(\sigma\alpha)^n = \dot{\varepsilon}\, e\, (Q/RT)$; where A, n represent material constants, σ is the peak flow stress (MPa), α stress multiplier (MPa^{-1}), $\dot{\varepsilon}$ strain rate (s^{-1}), Q activation energy of deformation (kJ mol^{-1}), R ideal gas constant (kJ mol^{-1} K^{-1}), T deformation temperature (K). The ZH parameter can be used to predict the peak flow stress of materials under hot deformation, beyond the range of temperatures and strain rates employed in experimentation. Comparison of material constants α, n and ln (A) for P/M2324 and AA2024, showed smaller values of these material constants, with higher activation energy for the P/M alloy, indicative of higher peak flow stresses. Hot swaging of sintered bars at the solutionizing temperature (495ºC) of the P/M alloy is reported to limit the formation of any liquid phase whilst maintaining precipitates in solution, thereby reducing peak flow stress. Tensile strength increment of 25% and 3 fold increase in elongation to failure is observed for sinter-swaged bars in comparison to sintered bars in T6 condition. Void coalescence and dimple formation is indicative of ductile fracture; an increase in dimples and decrease in angular cleavage features is reported from fractographic analysis of as-sintered, sinter-swaged and wrought alloy. Formation of co-continuous network of spinel ($MgAl_2O_4$) during sintering and its disruption by swaging led to increase in strength at the cost of ductility for P/M alloy in comparison to wrought alloy. Microstructurally, the strengthening phases Al2Cu (θ) and Al_2MgCu (S) were detected in both the wrought and P/M alloys in addition a complex $Al_7Cu_2(Fe,Mn)$ was detected in the wrought composition.

Malas, et al., 2004, have determined from simulated hot deformation studies on vacuum hot pressed P/M 2024 alloy, that, complexities related to microstructural inhomogeneities along PPB's are more prevalent in deformation processing of P/M systems. Phenomena of wedge-

induced cracking and adiabatic shear banding are active at low and high strain rates respectively; thereby severely restricting the workability window for P/M alloys in comparison to wrought and cast counterparts of similar composition. For the P/M 2024 alloy investigated, they have reported a dynamic recovery (DRV) regime to be operative below 400ºC; while DRX is the dominant mechanism in the 400-450ºC range under 10^{-4} to 10^{-2} s^{-1} strain rates. They have underscored the significance of dynamic recrystallization (DRX) as an important pre-condition for attaining microstructural homogeneity by dissolution of as-sintered PPB's, leading to improvements in strength and ductility.

Asgharzadeh and Simchi, 2008, studied the hot deformation of sintered (~12% porosity) and sinter-extruded (~1% porosity) Al-1.4Mg-0.6Si-0.24Cu pre-alloyed P/M alloy, conforming to wrought AA6061. Sintered compacts exhibited poor ductility at temperatures below 450ºC. Formation of shear bands, segregating the dead zone, shear intensive zone and bulged zone were identified in extruded samples after deformation. In the bulged region the as-extruded columnar grains are reported to have been retained after hot upsetting at lower temperatures; at higher deformation temperatures, the as-extruded microstructure transformed to fine equiaxed grains. The shear zone was found to be composed of very fine equiaxed grains. Porosity was retained in the bulged section. The work shows extensive strain softening at higher temperatures and lower strain rates. Low temperature deformation of sintered specimens promotes noteworthy strain hardening, this is attributed to increase in apparent hardness of the compact affected by pore closure and increase in effective load bearing surface. The workers have proposed a DRX simulated deformation mechanism of the P/M alloy due to grain partitioning by resistance offered by disrupted Al_2O_3 film to free transport of dislocations; hardening precipitate Mg_2Si also promotes formation of sub-grains resulting in a fine equiaxed structure. (Taleghani, et al., 2012) have investigated the hot deformation of cold compacted Al-Zn-Mg-Cu (complying with AA7075) pre-alloyed P/M alloy over different strain rates and temperatures. They have reported an initial peak stress followed by a near constant flow stress for most temperature-strain rate combinations. During deformation of porous compacts, having different green densities based on cold consolidation stress, dynamic flow softening-represented by gradual decrease in flow stress was observed with increasing deformation temperature. This phenomenon is attributed to attainment of peak flow stress due to pore annihilation, followed by concurrent DRX and DRV, which promote softening. At higher strain rates, possibility of adiabatic heating is reported to promote flow softening for compacts with higher green density. Compacts with higher porosity, suffered from cracking, yielding lower flow stress. The deformation activation energy was higher for compacts with higher starting green densities and vice-a-versa.

Topping, et al., 2013, have reported on high strain rate forging (HSRF) of hot isostatically pressed (HIP) cryomilled P/M 5083 alloy for development of bulk nano-structured material. Canned and degassed batches of cryomilled P/M 5083 were consolidated by HIP'ing at different temperatures ranging from 125-500ºC, followed by HSRF at 400ºC, employing an initial ram speed of 6000 mms^{-1}. HIP'd compacts with different levels of porosity were consolidated to full density by HSRF. The strength increments reported in the work were due to Hall-Petch effect attained by control over grain size; dislocation pile-ups by HSRF; solid solution strengthening by dispersoids and Orowan loops formed around finely dispersed nitrides (AlN) and oxides (Al_2O_3/$MgAl_2O_4$); these secondary phases in the form of dispersoids and disrupted oxides are thermally stable (Tang, et al., 2007) and their preferential presence at PPB's retards further grain growth by promoting Zener pinning at particle boundaries. The authors have reported an increase in average grain size (detrimental to mechanical properties attained by ultra fine grain substructure) by increasing the HIP'ing temperature, rather than HSRF, which promoted strength increments by increasing dislocation density and Orowan mechanisms as stated above. Dislocation-particle interactions as a function of deformation strain rate are described by (Humphreys and Kalu, 1987); wherein the respective rates of dislocation arrivals climb/pile-up around a particle depend upon the particle size, temperature and deformation strain rate. At low strain rates the dislocations climb and traverse over the particle, at higher strain rates, dislocations accumulate around the particle generating higher work hardening rates. Tang et al., 2007, have shown that the fragmented oxide stringers over deformed nano-crystalline aluminium P/M particles are around 30 nm in size, these particles effectively pin the grains and successfully avoid grain growth, even during low strain rate hot working regimes like rolling.

2.9.2 Forging of aluminium P/M based composites

This section will limit the discussion to forging as an inexpensive yet effective means for post sinter consolidation of P/M aluminium matrix based composite materials. Patented literature (Sawtell, et al., 1996) describes the omission of degassing prior to hot consolidation of cold compacted aluminium alloy based SiC particulate composite. Composites with upto 50 vol.% reinforcement loading were developed by heating the cold compact (minimum 375ºC) in air or an inert environment, followed by hot upsetting, forging, extrusion or rolling. The inventors have claimed equivalent mechanical properties (UTS, elongation to failure, fracture toughness and fatigue limit) by simplification of the overall fabrication process, which bypasses expensive canning and degassing steps, previously associated with hot consolidation of such class of DRA's. The mechanism of prior oxide film disruption and development of matrix

interparticle bonding is aided by the abrasive action of hard ceramic reinforcement. The inventors claim to extend this simplified processing to nearly all commercial aluminium P/M alloy and magnesium matrix based composites. (Hunt, 2000a) has discussed the suitability of incorporation of a large variety of reinforcements in P/M aluminium matrices, without the limitations posed in other liquid phase fabrication processes. The primary advantage accruing from low cost direct powder forging of P/M DRA composites for near-net shape fabrication of automobile components processed using conventional equipment. (Hunt, 2000b) has compared the specific properties (density normalized) values of different candidate materials for automobile connecting rod and reported on powder forged P/M 2080/15 vol.% SiC_p as a suitable DRA composite with equivalent specific modulus and specific fatigue strength in comparison to Ti-6Al-4V and ductile C.I.

Badini, et al., 2001, have summarized the general observations encountered by previous studies during deformation processing of DRA composites as: 1) propensity for microstructural degradation by opening up of voids and cracks 2) fracture of reinforcing phase increases with increasing strain rate or decreasing deformation temperature 3) forgeability follows the same behavior as monolithic alloys showing decrease in flow stress with increasing temperature or decreasing strain rate 4) conditions for obtaining defect free forgings are either at higher temperatures or lower strain rates, which the authors remark as being commercially unviable 5) metal matrix composites with matrices of wrought alloy compositions exhibit better forgeability than matrices with Al-Si based cast compositions. (Badini, et al., 2001) have reported defect free forging of HIP'd P/M 2124/26 vol.% SiC_p composite using an upsetting ratio of 3.5:1 at 340ºC - 440ºC, employing a strain rate of $0.14s^{-1}$. Particle cracking or development of cavitation voids at the reinforcement-matrix interface was not observed after forging; however, reinforcement banding- preferential alignment of SiC particles along a plane perpendicular to the forging direction was visible. The authors attribute the defect free processing to the fine size of the SiC particles (< 3 μm). An increase in tensile ductility was reported for as-forged composites in comparison to as-received material in both as-forged and T4 (solutionized and quenched) state.

Sanctis and Evangelista, 1996, have reported higher sensitivity to processing parameters (temperature and strain rate) for DRA composites in comparison to monolithic alloys. The deformation sensitivity at low temperatures and higher strain rates is governed by the reinforcement, while the matrix dominates at deformation regimes employing higher temperatures and lower strain rates. During the formability assessment of aluminium alloy 359 reinforced with 20 vol.% SiC_p, reinforcement cracking with particle-matrix decohesion at 350ºC and $10s^{-1}$ is attributed to limited recovery and excessive dislocation grouping around

SiC particles; at 500ºC and $0.003s^{-1}$ wedge cracking is induced by stress accumulation at matrix grain boundary junctions. Malas et al., 2004, have shown the significance of attaining stable apparent activation energy, which exhibits a wide variation from 377-1047 kJ mol^{-1} while deforming P/M 2024 reinforced with 20 vol.% SiC_w. Avery limited range of temperature (475-525ºC) and strain rate (10^{-4} to 10^{-2} s^{-1}) was found to promote DRX of the matrix; already enhanced by presence of reinforcing whiskers. Specimens deformed within the slim window of safe workability were reported to be free from whisker fragmentation/decohesion, cavitation voids, matrix cracking and grain growth.

Chawla, et al., 2002, have evaluated the mechanical properties of sinter forged P/M 2080 alloy reinforced with 20 vol.% SiC_p (average size 29 μm). The process has been schematically shown in Fig. 2.10. Important advantage with direct powder-forged consolidation of DRA composites vis-à-vis extrusion has been highlighted as the realization of net/near-net shape objects, with elimination of bulk machining, which, in case of ceramic reinforced materials is not only difficult but economically unfeasible for price-sensitive auto components. Machining of extruded DRA stock is reported to be more suitable for realization of high-performance aerospace components. The authors have reported preferential alignment of platelet-like SiC particles perpendicular to forging axis, termed as "pancaking". However, this phenomenon, called "reinforcement banding" was less than that observed in extruded DRA composites due to limited deformation strain employed in forging. The sinter-forged composite had higher strength with low elongation to failure in comparison to extruded counterpart, the reason cited for such behavior is the low strain deformation under forging causes lesser particle fracture. Extrusion induces higher particle damage, thereby lowering their effective load bearing capacity, but higher deformation strain in extrusion ensures better metallurgical bonding between Al-Al particles, resulting in increased elongation to failure.

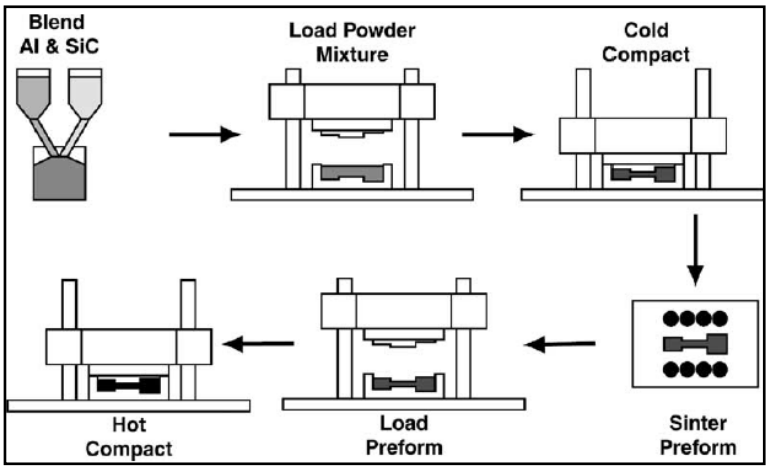

Fig. 2.10 Schematic representation of sinter forging process (Chawla, et al., 2002, Hunt, 2000b)

Effect of reinforcement particle size has also been studied by (Chawla et al., 2002) for sinter-forged composites, wherein, reducing the SiC particle size from 29 μm to 5 -10 μm creates non-uniform distribution of SiC by particle agglomeration, leading to higher matrix-reinforcement interfacial area, which is of lower strength, leading to failure by "pull-out" or matrix-particle interface decohesion. In comparison with sinter-extruded counterparts, where strength increased with reducing reinforcement particle size, on account of reduced interparticle spacing, responsible for reduced void coalescence during tensile deformation. The authors attribute fatigue performance of deformation processed composites to the presence of Fe-rich inclusions at the specimen surface which act as crack nucleation sites, otherwise; generally particulate composites offer better fatigue life under high-cycle/low-stress tests than unreinforced alloys due to load sharing by the high modulus reinforcement. Fatigue behavior of sinter-forged composites was equivalent to sinter-extruded composites except in the high-cycle test regime, wherein poor interparticle bonding resulted in diminished fatigue life.

Baker et al., 1996, have reported the breakdown of particulate-whisker agglomerates by using a combination of closed and open die forging for fabrication of P/M 6061 SiC particulate and SiC whisker reinforced hybrid composites. The heated and degassed cans were hot forged at 530 ^{o}C, employing strains of 35% under a closed die followed by open die upsetting to a strain of 40%. Single step closed die forging resulted in composites with reinforcement agglomeration, which was overcome by a secondary step of open die upsetting. This resulted in better mechanical properties (elongation and ultimate strength). The authors also defend the high forging temperature (530^{o}C), being equal to the degassing temperature to avoid blister formation on the composite surface. The composites displayed an accelerated ageing response in comparison to monolithic alloy due to availability of nucleation sites near dislocations generated by difference in coefficient of thermal expansion of matrix and reinforcement.

Chaturvedi, et al., 2009, have evaluated the dry sliding wear behavior of multi-component (upto 25 wt.% loading of SiC particles/ Graphite-MoS_2-Sb_2S_3) AMC's for brake pad applications. The authors have reported a novel powder forging technique which involves cold forging of powder mix in a shaped die followed by closed die forging of open atmosphere heated (550ºC) brake pad preform, to fabricate a net-shape, near-full density component for direct use. The advantages ascribed to low temperature processing by avoiding high temperature sintering, include: (1) absence of any reaction products, formed during sintering, like Al_4C_3- a brittle phase formed by the reaction of Al matrix and SiC particles/Graphite flakes, which is detrimental to composite ductility (Abouelmagd, 2004); (2) simplification of the process by avoidance of protective atmosphere, usually very dry nitrogen, for sintering of the AMC preform.

2.10 Extrusion

Hot consolidation by extrusion of aluminium powder based alloy or composite formulations has been reported to be a versatile single step (loose powder) or double step (cold compacted powder) or as a post-sinter secondary processing technique to achieve stable metallurgical characteristics by development of strong interparticle bonds through strain induced disruption of oxide skin covering the powder particles. As common to hot deformation processes, the important parameters in extrusion of aluminium P/M systems, include (individually or in combination) the strain (reduction), strain rate, die geometry, alloy composition, extrusion temperature (die container/billet) and lubrication. Extrusion of AMC's is further complicated by matrix-reinforcement interactions, reinforcement morphology, microstructural integrity (particle/fiber cracking, banding) and level of anisotropy. Aspects related to extrusion of monolithic and reinforced aluminium P/M have been presented in the following sections, to offer an understanding of the process, its range in accommodating reinforcements of different morphologies alongwith the shortcomings of extrusion based consolidation.

2.10.1 Extrusion of monolithic Aluminium P/M alloys

Woods, et al., 1998, have examined the structure of extruded powder aluminium; they have reported a ligament like morphology of the deformed powder particles, which are surrounded by stringers of aluminium oxide (Sheppard, etal., 1983), preferentially aligned along the extrusion direction. These stringers are homogeneously distributed and offer structural integrity to the extruded part by pinning grain growth within their boundary (Topping et al., 2013); evident by higher stress to failure of the P/M extrudate in comparison to cast pure aluminium, processed in similar fashion. Failure under tensile stress is accompanied by slippage of deformed powder particles, as they present a barrier to interparticle bonding, opening up into voids at particle ends at larger tensile strains.

From the microstructural investigations and FEM based stress-strain modeling of low reduction ratio (upto 3.2:1) hot extruded pure aluminium powder (Kumar, et al., 1987), have reported varying pressure and strain fields. These localized areas are seen to differ in quantum of interparticle bonding and retention of prior particle boundaries. Evolution of microstructural features has been attributed as: (1) coarse grain or mechanically interlocked particles, without any visible deformation- high extrusion pressure/low strain rate- near die corner at the exit (2) elongated particles and sub-particle grain structure along extrusion direction- high extrusion pressure/moderate strain rate- at the center of the extrudate after die exit (3) highly elongated particles with fibrous structure along extrusion direction - moderate pressure/high strain rate- at the center of the extrudate- prior to die exit (4) partially elongated particles and sub-particle

grain structure- moderate extrusion pressure/low strain rate- near center of unextruded portion of billet.

The findings reported above are consistent with the work of (Galanty et al., 2002) for cold extrusion of pure aluminium powder under low reduction ratios. The authors' further claim that the extrudate properties and microstructure are independent of preform rheology, i.e. loose powder or a cold consolidated preform and starting preform green density.

Investigation of extrusion pressure requirements was analyzed by (Kumar, et al., 1982) for aluminium powder extrusion over a range of reduction ratios (1.6:1, 7:1 and 80:1). They have reported the suitability of using wedge shaped dies with different entry angles instead of square edged dies, for reduced energy consumption and increased tensile strength of the extruded products.

Analysis of pressure requirement for aluminium powder extrusion has been performed by (Sheppard and McShane, 1976), starting with the standard equation for estimating extrusion pressure, given as: $p/\sigma = a + b \ln R$, where, a and b are constants signifying work of deformation and redundant work respectively, σ is the flow stress of the material and reduction ratio is given by R. Powder extrusion should follow the general equation, albeit with different values of constants owing to the complex nature of powder extrusion against a cast billet of similar composition. (Sheppard and McShane, 1976) had further stated on the singular dependence of extrusion pressure on reduction ratio only, which was challenged by (Kumar, et al., 1982), based on their investigations on square as well as wedge shaped dies, arguing, that a lower b/a ratio (higher useful work) obtained for wedge dies in comparison to square dies, does not allow for a direct application of formulae valid for extrusion of cast billets to powder extrusion.

From the examination of surface integrity of aluminium powder extrusions, (Kumar, et al., 1985) concluded that the treatment of individual particles as a coherent continuum, a necessary pre-condition for analysis of pressure/strain fields during deformation, was valid only under situations where inter-particle deformation induced bonding was sufficient and continuous. The authors have reported to observe such transition, individual particles coalescing to form a bulk, under wedge shaped dies, wherein, the zone of homogeneous deformation covers a larger portion of the deforming mass. In comparison to a high strain gradient (varying velocity), from center of the deformation zone to the die wall; experienced by the powder in square shaped dies.

Inter-particle friction generated during sliding and/or interlocking of aluminium particles has been shown to increase the redundant portion of total work by (Sheppard, et al., 1983), the authors have stated that this redundant work is used in disruption of the oxide film and hence

powder extrusion could be a direct substitute for sintering. Extrusion pressure is found to increase with decreasing powder particle size, on account of more number of interlocks per particle that must be sheared during extrusion. The fine grain structure obtained after extrusion of an Al-Mg prealloyed powder exhibited grain growth upon solutionizing; the authors reported a loss in yield strength following solutionizing and ageing. Gain in strength was achieved after directly ageing the extrudate, eliminating solutionizing step, as extrusion ensured that a large fraction of the solute always remained in solution.

Carvalho, et al., 1990, have reported more uniform distribution of *S*-phase (Al_2CuMg) particles during extrusion of canned and degassed prealloyed powder conforming to AA7075 in comparison to a similar cast ingot alloy. An increase in recrystallized grain size was observed with increasing extrusion temperature for the powder metal alloy. At lower extrusion temperatures the powder alloy is reported to have consistently finer grain structure in comparison to the ingot. Development of large localized pores was observed after solutionizing the powder metal extrudate; the authors attributed this to the presence of adsorbed hydrogen, which was not fully evacuated at the degassing stage. Soaking time at the extrusion temperature is reported to have a major influence on extrusion pressure for both the alloy systems. A nominal soaking time period of 60 min prior to extrusion was found to be insufficient for attaining the desired process temperature, extrusion pressure decreased with increasing soaking durations for both the alloys. The flow stress of powder alloy was about 13% less than the ingot alloy; the reduced pressure requirement for powder extrusion was due to incomplete bonding of particles which allows for relatively less intensive shearing at a delayed coalescence stage. Mechanical properties of the extruded powder alloy in the T6 condition are affected by porosity, whereas, presence of large complex intermetallic particles deteriorates the ingot alloy.

For the hot consolidation by extrusion of rapidly solidified Al-6Fe prealloyed powder, (Hodiamont, et al., 1991) have outlined the importance of low processing temperature for retention of the fine as-rapidly solidified grain structure. Authors have reported a threshold temperature of 380ºC for extrusion to retain the fine starting structure of the powder as beneficial in retarding grain growth, likely to be experienced by the extrudate at elevated service temperatures.

Powder metal alloy pre-mixes are a blend of pure aluminium powder and prealloyed particles, which offer better compressibility (admixed solid lubricant) and sintering characteristics (evolution of a transient liquid phase, *Section 2.6.2*) in comparison to single phase prealloyed compositions.

Jabbari, et al., 2014, have investigated the extruded microstructures and mechanical properties of pre-mixed blend conforming to AA7075 (ALUMIX- 431D^{TM}, Ecka Granules, Germany) in green, de-lubricated and sintered state as extrusion stock. Prior to extrusion, a bimodal microstructure composed of separate α-aluminium and intermetallic rich particles were observed in the first two compacts in comparison to an indistinguishable homogeneous phase for the sintered compact. Such a segregated microstructure is also manifest in the extrudates, wherein, separate bands of α-aluminium and intermetallic are reported for the green and de-lubricated billets, in contrast to a highly recrystallized, homogeneous structure for the sintered billet. The authors attribute this recrystallization to inhibited dynamic recovery (DRV) by the second phase intermetallics, finely distributed in α-aluminium matrix. Finer grains at the outer periphery of the pre-sintered extrudate were due to higher deformation strain. Mechanical properties were evaluated for all the three extrudates; hardness, yield and ultimate strength were highest for the pre-sintered billet followed by de-lubricated and cold pressed states. Elongation to failure was equivalent for all the three conditions. (Zubizarreta, et al., 2009) have reasoned that particle-particle contacts are most in number for pre-sintered billets, hence inter-diffusion of alloying elements is favored in comparison to partially disrupted oxide skin covering both alloy and aluminium particles in the green or stress relieved billets. Similarly, higher dynamic recrystallization (DRX) initiated recrystallization is evident at the extrudate periphery due to higher imposed deformation strain, evolving a near equiaxed structure, compared to a largely elongated grain structure at the center due to limited recrystallization by dynamic recovery (DRV). The combination of extrusion induced bulk alloying, recrystallization, strain hardening and precipitation of hardening phases is most prevalent in pre-sintered specimens; hence the mechanical properties are enhanced in comparison to green and stress relieved counterparts.

Novel compositions of aluminium based rapidly solidified powders for their distinctive properties, namely (1) strength at room and elevated temperature (2) creep resistance and superplasticity (3) improved tribological and damping capabilities; in extruded bulk artifacts has been critically reviewed by (Jones, 2004). As an example, he cites the case of conventional 7xxx series (Al-Zn-Mg-Cu) alloy system that tends to lose structural integrity around $0.4T_m$ (melting point on absolute scale); rapidly solidified composition of Al–9.5Zn–3Mg–1.5Cu–4Mn–0.5Zr–0.04Ag, consolidated by cold isostatic pressing followed by extrusion is reported to achieve an ultimate tensile strength of 800MPa with 5% elongation to failure at room temperature and above 300MPa after a 100 h exposure at 300ºC (minimum performance requirement for aircraft materials, specified by United States Air Force). Strength

enhancements at elevated temperature have been attributed to a fine grain size (below 40 nm) aided by the presence of nano-scale dispersoids (rod like complex Al-intermetallics).

Powder metal extrusion of aluminium alloys has evolved into a versatile consolidation technique which several workers have employed for energy efficient single step conversion of machining waste, generated in form of chips, swarf, turnings etc., to reusable aluminium extruded stock (Suzuki, et al., 2007). Economic viability of the process against re-melting the scrap has been presented by (Samuel, 2003); upto 60% in material value is reportedly saved by solid-state recycling, furthermore, granulated aluminium is adaptable to cold compaction, sintering and defect free extrusion of complex profiles (Güley, et al., 2010; Tekkaya et al., 2009).

The technique has been further simplified by (Fogagnolo, et al., 2003) by avoiding conversion of chips to granules. They have reported direct cold pressing or hot pressing of machining waste into billets for hot extrusion. Microstructural homogeneity was not attained and chips from two different alloys resulted in a two phase extrudate (Sherafat, et al., 2009), but reasonably good tensile strengths were obtained. Excessive cost associated with hot pressing did not produce appreciable gains in final mechanical properties. Aluminium alloy 6061- Al_2O_3 composite machined into chips and processed likewise, resulted in an extrudate with increased tensile strength than the parent composite, presumably due to grain refinement by higher dislocation density in the machined composite chips.

2.10.2 Extrusion of aluminium P/M based composites

Extrusion has emerged as an important consolidation method for discontinuously reinforced aluminium P/M composites (Lloyd, 1994). Fig. 2.11 shows the major steps of fabricating aluminium P/M composites (1) blending of constituent matrix and reinforcement powders (2) green consolidation by cold isostatic pressing (3) canning and degassing (4) hot pressing the degassed can (4) direct extrusion of the can (5) removal of skin by machining to obtain the finished composite bar. Different routes of the above mentioned methodology have been developed as shown in Fig. 2.12 (Torralba, et al., 2003)**,** as discussed for extrusion of monolithic aluminium alloys, deformation induced coalescence of the participating matrix and reinforcement particles is obtained by direct extrusion of the powder blend, ensuring lowest temperature processing for minimum interaction. Extrusion can also be preceded by sintering to attain microstructural homogeneity and densification of the compact. A degassed can filled with the powder mix is also shown to be extruded directly, without intermediate hot pressing.

In-situ formation of fibers from spherical glass beads by extrusion of P/M aluminium alloy-glass beads powder blend has been reported by (Thompson et al., 1976). Boric oxide (B_2O_3)

and B_2O_3- silica (SiO_2) beads having a softening point lower than extrusion temperature were selected to autogenously form a fibrous shape, thereby producing a two phase composite with Al, Al-Mg-Si and Al-Mg-Si-Mn prealloyed powder matrices. The authors have reported upto 160% increase in ultimate tensile strength for 10 wt.% B_2O_3 reinforced aluminium matrix composite, with similar yield strength, deteriorated impact energy and elastic modulus. A maximum of 14 wt.% B_2O_3 could be satisfactorily formed without causing bursting at the die exit, caused by expansion of the glass fiber.

Cracking at the glass-matrix interface was attributed to difference in coefficients of thermal expansion. The authors increased the bead particle size to achieve reasonable impact strengths in comparison to unreinforced matrix alloys extruded under similar conditions, but a 10-fold increase in reinforcement particle size resulted in severely diminished tensile strength for the composites so produced.

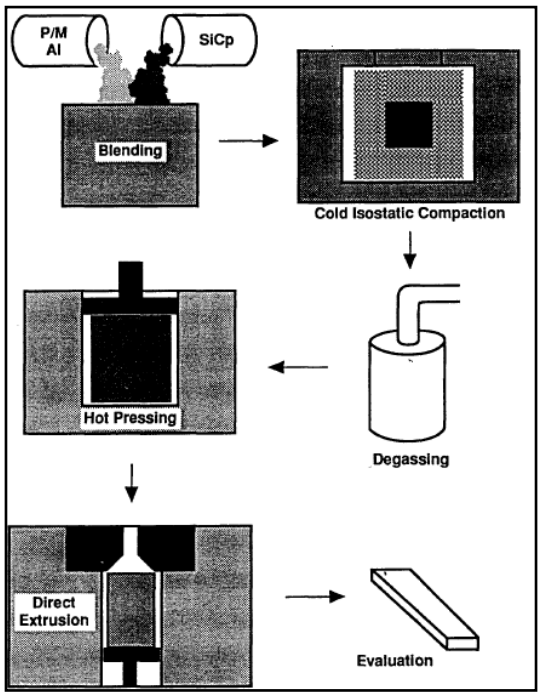

Fig. 2.11 Schematic representation of aluminium P/M composite fabrication by extrusion (Lloyd, 1994)

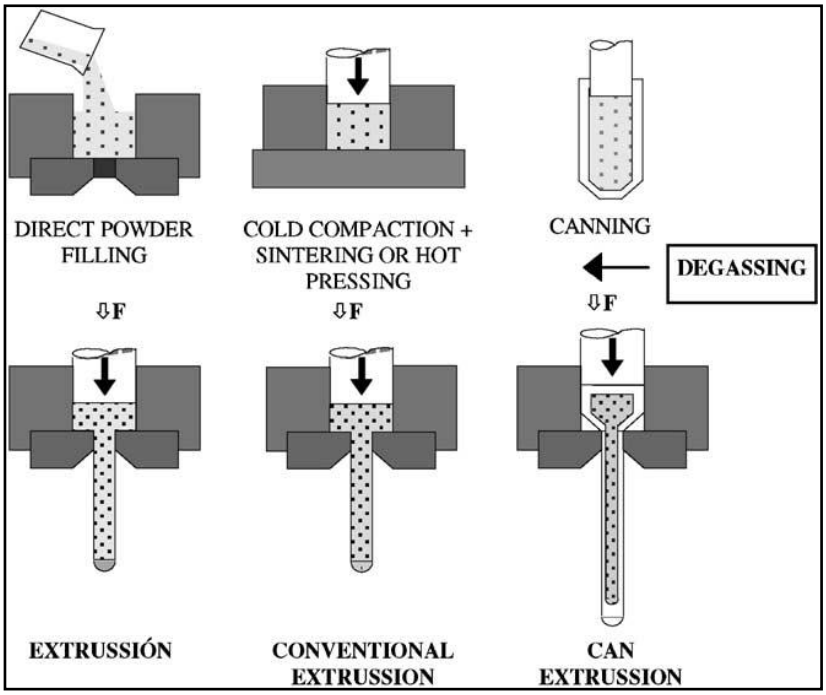

Fig. 2.12 Schematic representation of different routes for aluminium P/M composite fabrication by extrusion (Torralba et al., 2003)

B_2O_3- SiO_2 reinforced Al-Mg-Si and Al-Mg-Si-Mn alloy extrusions were reported to be insensitive to ageing, the authors (Thompson, et al., 1976b) attributed this effect to the depletion of magnesium from the matrix alloy towards B_2O_3- SiO_2 glass; during solutionizing of the composite, a model for two simultaneous interdiffusion processes has been presented, viz. Mg dissolution in Al matrix and Mg reacting with glass. To overcome the loss of Mg from the matrix alloy, a separate addition of about 2 wt.% was made resulting in recovery of ageing response, manifest in ultimate tensile strength (285 and 345 MPa respectively in peak aged condition for both the composites respectively). During fabrication of a similar composite system (Sheppard, et al., 1983; Sheppard, et al., 1983b) have observed the presence of spinel ($MgAl_2O_4$) as a reaction product at the glass-matrix interface, further suggesting that such class of composites should be developed with tailor made aluminium alloys free of magnesium.

In a critical review of particulate reinforced aluminium composites consolidated by extrusion (Davies, 1995) draws the distinction between extruded composites for intended use as long structural members viz. tubes, pipes, drive shafts etc. and choice of extrusion for obtaining a porosity free element for further physio-mechanical characterization. For both P/M and cast composites, matrix alloy composition conforming to AA6061 remains the first choice on account of excellent extrudability and realization of post-extrusion heat treated properties. Ceramic reinforcements of choice include SiC, Al_2O_3, Si_3N_4 and TiB_2. Advantages offered by P/M surely out span cast processing except in cost, ease and scale. Size difference between the

matrix alloy powder particles and reinforcement is an important factor in composite P/M extrusion; it is the primary reason for particulate agglomeration. For fibrous reinforcements, fiber cracking and loss of aspect ratio is observed, following extrusion. In general, the extrusion pressure requirements are higher with slower ram speeds for composites in comparison to plain alloys. Akin to extrudability limit diagrams for commercial aluminium alloys, the author has proposed limits to extrudability for discontinuously reinforced composites. The safe window is smaller for composites; incipient melting of low melting point phases in the matrix alloy is found to commence 10-15ºC earlier with same billet surface temperature. "Stick-slip" defect at the extrudate surface, results from low ram speed at low temperature, and this defect is further compounded by die wear, caused by hard ceramic particles. P/M composites have been reported to show higher ultimate tensile strength, yield strength and elongation than cast composites following extrusion. The author attributes (1) a more homogeneous structure (2) network of very fine alumina (3) finer starting sub-structure (4) retention of alloying components in the matrix, as some of the reasons.

For the extrusion of SiC and Al_2O_3 whisker reinforced P/M 6061 composites (Stanford-Beale and Clyne, 1989) have remarked the use of highest extrusion temperature without causing hot shortness; use of a plain alloy pad ahead of the composite billet to fill the streamlined die and provide cladding over the extrudate for better surface finish; lowest strain rate- limited by rate of billet cooling; smaller reinforcing fiber diameter for easy alignment by bending during deformation and choice of matrix alloy based on high rates of component volume diffusion to achieve a homogeneous distribution of precipitates throughout the product volume.

An extensive experimentation has been carried out to optimize extrusion process parameters like average strain rate (ram speed), die shape, billet temperature and reduction ratio for achieving sound extrudate surface finish in stir cast and P/M aluminium alloy 2124/20 vol.% SiC particulate reinforced composites (Goswami et al., 1999). The P/M composite was extruded at considerable lower load than stir cast composite, with consistently better surface finish. Design of a dish shaped extrusion die has been reported to allow a uniform strain field at different locations of the billet during deformation, whilst avoiding dead metal zone at the billet periphery, resulting in a gradual almost equivalent distribution of reinforcing phase throughout the extrudate cross section. Higher billet temperature (500ºC)- bound by hot tearing and lowest ram speed (5 mms^{-1})- bound by lubricant failure, leading to "stick-slip" at higher speeds is reported to aid in maintaining surface integrity of the extrudate in a semi-industrial level study (3 kg billet, minimum 2 m extrudate).

The dish-shaped constant strain rate die has been examined by (Kang, et al., 2000) for the extrusion of AA6061/Al_2O_3 whisker reinforced stir-cast composite. Enhanced mechanical

properties were obtained for the constant strain rate die in comparison to traditional conical entry die for both ultimate strength and elongation, cleavage bands were visible in fractographs of extrusions through conical dies, against remarkably more dimple formation for extrudates processed through constant strain rate die.

Effect of extrusion ratio on formation of banded microstructure has been investigated by (Prasad, et al., 2001) for the extrusion based consolidation of P/M 2124/30 vol.% SiC particulate composites. Formation of aligned stringers along the extrusion direction alongwith banding of SiC particles was reported to be a function of reduction ratio. Stringer width decreased with increasing extrusion ratio, resulting in increased matrix microhardness. Thinner stringers, formed at higher reduction (20:1), were found to be more homogeneous and displayed higher strength and hardness. Ageing response also increased with increasing reduction ratio due to higher dislocation density in the extrudate, which provided more sites for precipitate nucleation; also reported by (Ortiz and Salvador, 2000) for ageing of extruded P/M 6061/(5-15 vol.%) Si_3N_4 particulate reinforced composites, wherein increase in composite hardness (T6) was less dependent on reinforcement volume fraction, but largely on reinforcement distribution and tendency for agglomerate formation. Accelerated ageing for the extruded composites (time to achieve peak hardness) is attributed to presence of hard reinforcement particles and fracture initiated disruption and distribution of oxide layer into the matrix, offering preferential sites for particle simulated nucleation (PSN) of β-Mg_2Si precipitates.

Fly ash (Al_2O_3-SiO_2)/(2-10 wt.%) reinforced elemental P/M 6061 composites were directly consolidated by extrusion following cold pressing by (Kumar, et al., 2009). The workers have reported near full density, in spite of avoiding sintering. Alloy formation was confirmed by detection of Mg_2Si phase through XRD and TEM observation. A 16:1 reduction at 500ºC was sufficient to obtain a well dispersed composite upto 6 wt.% reinforcement fraction. Mechanical properties were better in comparison to sinter extruded counterparts (Kumar, et al., 2010), with increments in proof and ultimate strength. Sintering step may have led to depletion of Mg, present as an elemental addition in the alloy, by reaction with fly ash particles and formation of spinel ($MgAl_2O_4$); which was avoided by direct extrusion of the cold consolidated billet.

Extrusion induced reinforcement particle damage has been investigated by (Lawrence, et al., 1993) for SiC particulate (3, 20 and 30 µm) reinforced P/M aluminium vacuum hot pressed billet extruded at 50:1 reduction ratio. The workers have employed scanning acoustic microscopy to evaluate surface damage on the SiC particles. Observations relate to higher damage of the particles with increasing particle size, volume fraction and aspect ratio of the

reinforcement. Mechanically, the shear stresses endured by the particles during extrusion cause surface rupture, leading to inter-particle transgression of failure path during tensile tests.

2.11 Interfacial Chemistry of Aluminium-Iron System

Interaction of dissimilar metals at elevated temperatures leads to formation and growth of complex intermetallic reaction products. In case of metal matrix composites, the final properties of the composites are defined by the characteristics of the matrix, reinforcement and the in-situ reaction products formed at their interfaces. It is therefore pertinent to this work that an understanding of the mechanism, morphology and characteristics of reaction products, formed in the aluminium-iron system, is developed. This section will focus on all relevant aspects of formation of different phases (Fe_xAl_y type) of intermetallics, covering the effect of temperature, time and alloy composition.

The formation and growth of intermetallic layers in Fe-Al couples is governed by diffusion coefficients of iron into aluminium: 53 x 10^{-4} m^2 s^{-1} (793-922 K) and aluminium into iron: 1.8 x 10^{-4} m^2 s^{-1} (1003-1673 K), from the binary phase diagram given in Fig. 2.13; depending on individual contents and temperature following reaction products are formed Fe_3Al, FeAl, $FeAl_2$, Fe_2Al_5 and $FeAl_3$; carbon content in steel and silicon in aluminium are known to inhibit inter-diffusion and growth of RI (Kobayashi and Yakou, 2002). Intermetallic compounds thus formed with higher aluminium content ($FeAl_2$, Fe_2Al_5 and $FeAl_3$) are besieged by brittleness. The growth of intermetallic layer is diffusion controlled, where RI thickness (X) w.r.t time (t) can be expressed by a parabolic rate constant (K) as: $X = K\, t^{1/2}$; and $K = K_o \exp(-Q/RT)$; where K_o is a constant, R is the gas constant, Q is the activation energy and T is temperature on the absolute scale.

Near-equilibrium or equilibrium phases are well described in binary phase diagrams, however, conditions encountered in general processing are far from such standard conditions. (Bouche, et al., 1998) have studied the intermetallic phases formed at 700-900ºC between pure iron and pure aluminium. They have observed a tongue-like “serrated” morphology of reaction interface growing into the iron coupon dipped in aluminium melt. The interface was composed of a thick layer of Fe_2Al_5(η) on the iron side, terminating into a thinner $FeAl_3$(θ) at the aluminium end. Other phases like $FeAl_2$, FeAl and Fe_3Al (aluminium rich) could not be detected. The growth of both the detectable phases is governed by the parabolic law (diffusion controlled) for longer durations; the authors report a breakdown in the standard diffusion kinetics at the start of interaction. Growth of Fe_2Al_5 into iron has shown a sharp needle like morphology at the beginning of interaction, broadening out into a tongue with immersion time. Fe_2Al_5 forms a

fine polycrystalline grain structure at the interface with $FeAl_3$ and large elongated grains were observed at the boundary with iron, with no structural similarity.

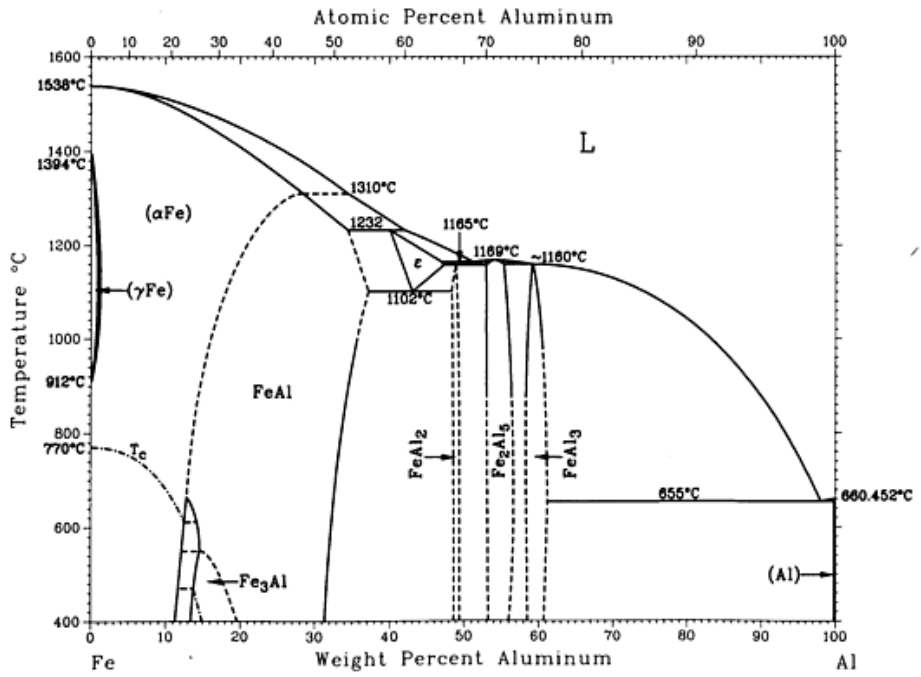

Fig. 2.13 Iron- aluminium equilibrium phase diagram (Massalski and Kattner, 1990)

Shahverdi, et al., 2002, have investigated the interfacial reaction products evolved by the reaction of molten aluminium (800ºC) with solid iron coupons. A signature "serrated" (dendritic) reaction interface (RI) is reported to grow into the iron coupon; growth of the RI is time dependent and the intermetallic dendrites increase in both width and length with dipping time. Phases detected were placed as: $Fe/Fe_2Al_5(\eta)/FeAl_3(\theta)/Al$. $Fe_2Al_5(\eta)$ and $FeAl_3(\theta)$ were separated by contrast in backscattered electron imaging (BSE) with $Fe_2Al_5(\eta)$ as the lighter, more dominant gray phase compared to a weaker, darker grey $FeAl_3(\theta)$. The difference between the two phases is also manifest in microhardness measurements, 700-800 VHN for $Fe_2Al_5(\eta)$ and 900-1000 VHN for $FeAl_3(\theta)$. Free energy of formation of $FeAl_3(\theta)$ is -22.89 $kJmol^{-1}$ compared to -19.62 $kJmol^{-1}$ for $Fe_2Al_5(\eta)$; the authors have argued that vacancies along the *c*- axis of orthorhombic $Fe_2Al_5(\eta)$ allow for faster diffusion kinetics to control the reaction, in spite of a higher thermodynamic probability for $FeAl_3(\theta)$ formation. Higher hardness of the $FeAl_3(\theta)$ interlayer ensured its rupture and eventual spalling from the aluminium side due to thermal mismatch stresses generated during cooling of the coupon.

Kobayashi and Yakou, 2002, have determined hardness values of FeAl and Fe_3Al interlayers to be 600 VHN and 320 VHN respectively in comparison to 1000 VHN for Fe_2Al_5, which is also reported to be excessively brittle.

Preferential growth of aluminium rich Fe_2Al_5 (η) against other reaction products has also been reported by (Naoi and Kajihara, 2007) for solid-solid diffusion in a sandwich Al/Fe/Al test sample in the 550-640 ºC temperature range for upto 120 h holding time. The growth is controlled by a parabolic law as described by (Kobayashi and Yakou, 2002) and grain growth observed in Fe_2Al_5 (η) inter-layer was indicative of volume diffusion.

Shahverdi, et al., 2002b, have observed that the growth kinetics of intermetallic RI, which they found to be simultaneously controlled by growth and dissolution of the intermetallic layer. Inflexion points in the slope of parabolic rate constant at the beginning and ending stages of the RI growth, point towards the process being reaction rate dependent at these stages and singularly diffusion controlled in the middle. Schematically, it can be seen from Fig. 2.14, that iron diffuses into liquid aluminium forming Fe_2Al_5, further growth of the RI depends upon dissolution of the reaction product (Fe_2Al_5); aluminium diffuses first towards the iron rich side and a reversal of growth direction ensues.

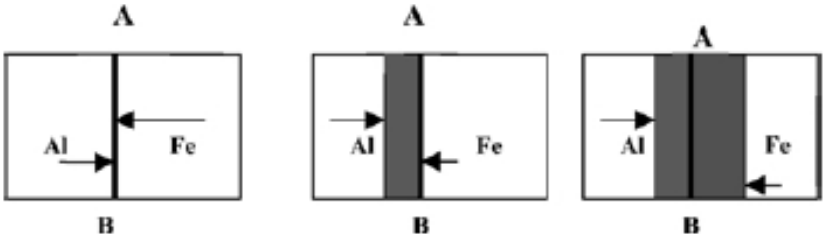

Fig. 2.14 Schematic representation of intermetallic growth across an iron-aluminium interface A-B, diffusion intensity is denoted by arrow length (Shahverdi, et al., 2002b)

More recently, an exhaustive study has been conducted by (Springer, et al., 2011) for evaluating the inter-diffusion products formed during solid/mushy/liquid state bonding of Al-0.08 wt.% steel and Al5Si-0.08 wt.% steel pairs. *Our interest is limited to solid state diffusion*. A typical "serrated" interface is reported, composed of two distinct inter-layers, separated by varying degree of "grayness" under SEM, a spotted precipitate was also observed, which increased in density with time. Phases identified by EDS and EBSD across the Al-steel diffusion couple at 600ºC were: Al/Fe_2Al_5 (η)/AlFe (β)/$AlFe_3C$ (κ)/steel. Fe_2Al_5 (η) was the dominant phase; $AlFe_3C$ (κ) was reported to decrease in thickness with increasing annealing (isothermal holding) time. θ-phase, present for solid/liquid interdiffusion was absent in the solid-solid diffusion study. AlFe (β) and $AlFe_3C$ (κ) observed at 600ºC (solid/solid) are reported to be absent at 675ºC (solid/liquid). For Al5Si-steel couple tested at 600ºC (solid/mushy state) the interface was composed of: Al5Si/$Al_{4.5}FeSi$ (τ_6)/indeterminate layer/ Fe_2Al_5 (η)/steel. Again Fe_2Al_5 (η) was the dominant phase, thicker than that observed for solid/solid Al-steel pair; contrary to earlier studies conducted at higher temperatures (780-

900ºC) (Eggeler, et al., 1986), wherein, Si was reported to occupy the excess vacancies that exist along the *c*- axis of orthorhombic $Fe_2Al_5(\eta)$ and retard the growth by modifying diffusion conditions. By estimation of parabolic rate constants for the solid/mushy state for Al5Si-steel pair (Springer, et al., 2011) have shown an increase in thickness $Fe_2Al_5(\eta)$ component.

Stoloff, et al., 2000, have earmarked iron rich aluminides for low cost high temperature oxidation and corrosion resistant applications. Structural applications are limited due to environmental embrittlement at ambient to moderate temperatures, which is a constant drawback of iron aluminides. Alloying with Cr and B has been explored to develop this class of iron rich aluminides for attaining structural integrity.

2.12 Aluminium- Steel MMC Systems

Several workers have pursued the continuous reinforcement of aluminium alloys by stainless steel or steel wires using liquid metallurgical processes, to offer a cost-competitive improvement in overall properties of monolithic aluminium alloys. Investigations have shown the formation and growth of a complex intermetallic reaction interface (RI) of type Fe_xAl_y composed of Fe_3Al, FeAl, $FeAl_2$ (ζ), Fe_2Al_5 (η) and $FeAl_3$ (θ) phases. A well interfaced composite can give much superior properties by synergistic effects arising from effective load transfer from the weak matrix to the strong reinforcement; however, the intermetallic nature of the RI leads to excessive hardness, low ductility, susceptibility to crack propagation and environmental embrittlement. Optimum properties of the developed composites have been realized upon close control of the RI thickness.

Karpinos, et al., 1974, investigated the reaction interface (RI) formed between plasma spray deposited pure aluminium powder (50-100 µm average particle size) over continuous (18%Cr-10%Ni- Ti-stabilized) stainless steel wire of 200 µm diameter to fabricate unidirectionally reinforced monolayers; which were further diffusion bonded together to form the bulk composite under pressure at 500°C for 30min. The matrix hardness was found to have increased after diffusion bonding, owing to reduction in porosity, however, a slight loss in the hardness of reinforcement is reported. Elemental analysis by electron probe microanalysis (EPMA) for aluminium and iron, revealed a sharp interface without any reaction products. Mechanical tests indicated that failure of the composite was at about 70-80% of the ultimate strength of the wire. Absence of the RI was attributed to low temperature (< 200°C) processing during plasma spray of aluminium powder, preventing formation of any brittle reaction products.

Friedrich, et al., 1974, investigated the effect of RI thickness on tensile strength of pure aluminium melt continuous-draw-coated Mo-maraging steel wire (100 µm diameter) to

fabricate coated wires corresponding to 20 vol.% reinforcement; further hot pressed into bulk rectangular composite plates. The RI was found to be composed of Fe_2Al_5 phase, which grows uniformly at the diametric wire-matrix interface upto ~ 20 µm. They reported an increase in tensile strength of the composite upto a critical RI thickness of about 6µm, beyond which rapid deterioration was observed. Since the system is composed of the matrix, RI and the reinforcement; the composite strength depends on the volume fraction of the RI, which in the present case is brittle (but stronger than the ductile matrix), hence lesser the RI volume fraction, higher the composite strength. An optimum RI thickness is modeled, based on the site of failure initiation (RI or reinforcement) according to their relative volume fractions. In the first case, wherein, the RI volume fraction is below the optimum level, failure will start from the reinforcement and from the rule of mixtures, the RI will contribute in increasing the composite strength. In the second case, wherein, the RI volume fraction is higher than the optimal level, the crack initiation will commence from the RI at multiple points- causing reinforcement failure due to stress concentration at crack initiation sites- finally resulting in debonding between fiber and RI as the multiple cracks in RI act as stress raisers. The optimal RI thickness is also proposed to be dependent on the fracture strain of the reinforcing wires, such that, lesser the fracture strain larger the RI volume fraction that can be tolerated without degrading the strength of the composite.

Karpinos, et al., 1978, have analyzed the development of RI formed at the diffusion bonded interface of pure aluminium and continuous wires of (16%Ni-4%Co-5%Mo-Ti stabilized) and (18%Cr-10%Ni-Ti stabilized) steel after annealing treatment at 540-580°C upto 100 h. As bonded composites displayed a sharp interface, free from any reaction products; annealed specimens consisted of 2 distinct regions separated by different colors. They have observed a lighter region closer to the reinforcement with a microhardness of 1280 HV (Vickers microhardness obtained using standard diamond indentor) and was reported to be Fe_2Al_5 intermetallic; the darker region, away from the reinforcement - adjacent to the matrix, had a microhardness of 830 HV- reported to be $FeAl_3$ intermetallic phase. Other elements (Ni, Co and Ti) could be detected locally in the RI, owing to their diffusion along grain boundaries. To quantify the effect of transformations associated with annealing on bare wires of both the compositions, it was established, that upto 10 h holding did not appreciably decrease the strength of the wires, 20-30% loss of strength was recorded for annealing durations of 50 and 100 h respectively. This effect was subtracted from the strength of the fabricated composites and it is shown that upto a critical RI thickness of 7-8 µm, there is an overall increase in the tensile strength of the composites- RI contributes with effecting load transfer from soft ductile matrix to high strength reinforcement, in agreement with model suggested by (Friedrich et al.,

1974). Examination of fracture surfaces, further corroborates this model, with the optimal RI composites failing in a similar fashion as composites without any RI; failure initiating from the reinforcement wire and progressing outward to the RI, indicative of a tough rupture. For composites with RI of greater than the optimum range, brittle fracture was observed, with failure initiating from the RI leading to crack openings that act as stress raisers and cause premature failure of the reinforcing wires; the matrix fails in a ductile manner with dimple formation. The deleterious effects of an over-the-optimum RI are reported to slightly diminish at elevated temperatures (20-400°C), as there is an increase in RI and reinforcement wire ductility coupled with excessive flow-softening of the ductile matrix, thereby making the RI a direct load bearing member in the composite system.

Pai and Kulkarni, 1983, fabricated vacuum infiltrated composites with stainless steel (AISI 304) and nichrome (80wt.% Ni-20wt.% Cr) reinforcement wires of diameter 152 µm, in commercially pure aluminium and Al-10wt.% Mg alloy matrices. The composites were exposed to different temperatures (200 to 650°C) for upto 100 h durations. For stainless steel reinforced composites, they reported an intermittent origin of RI beyond 400°C; uniform radially outward growth of RI was observed for longer periods of holding (100 h) at 550°C. In the nichrome wire reinforced composites, the RI progressed inwards into the wires, starting from 350°C onwards; leading to complete dissolution of the wires in 100 h. Effect of RI on strength degradation was equally more pronounced in nichrome reinforced composites in comparison to stainless steel. It is concluded, as discussed above, that apart from the optimal RI thickness, the growth morphology of the RI also significantly impacts the load bearing capacity of the composite.

Mannan, et al., 1983, estimated the kinetics of growth of RI in AISI 316 stainless steel – aluminium couples, prepared by dip aluminizing followed by diffusion annealing over a 763-913 K temperature range. They reported a parabolic law for growth of the RI of type: $X^2 = k\,t$, where k is a temperature dependent rate constant and follows an Arrhenius- type behavior, given as $k = k_0 \exp\left(-\frac{Q}{RT}\right)$; where the activation energy Q can be calculated from the plot of log k v/s $1/T$; k can be estimated from the intercept of log X v/s log t plots on the ordinate (Q = 166 kJ mol^{-1}, k = 7 x 10^{-4} m^{2}s^{-1} were calculated). The RI was found to be composed of two separate regions of appreciably higher hardness than the matrix or the reinforcement and was composed of well-defined ternary intermetallic products like $Al_3(Fe,Cr)$, $Al_6(Fe,Cr)$ and $Al_9(Fe,Cr)_2$. The inclusion of Cr alongwith Fe in the RI can be attributed to diffusion along grain boundaries, as discussed by (Karpinos, et al., 1978).

Bhagat, 1985, presented a systematic study on hot pressed pure aluminium powder- stainless steel wire reinforced composites under a pressure of 155 MPa for 1 to 60 min at

760 K to 880 K, with different volume fractions of continuous fibers placed introduced in planar, alternating layers with the matrix powder. For reinforcement volume fractions in the range 10-35%, optimum tensile strengths were achieved at 760-820 K. For the same volume fraction, strength peaked at 800 K. For a fixed volume fraction, lower pressing times (1 to 20 min) resulted in higher strengths; notable deterioration was observed beyond 10 min to 30 min and little effect thereafter upto 60 min. The effect of pressure at different temperatures to attain peak strength, showed a build up to maximum strength and then a fall over a pressure range of 40-200 MPa; with the peak strength pressure increasing with lowering temperatures; in essence, that for a required peak strength for a given volume fraction/time/temperature, 2 values of pressure are available. A threshold curve was established to determine the optimum pressure with respect to temperature for attaining a strength equal to that predicted by rule-of-mixtures (ROM) for a given volume fraction/time; the decay-type curve shows lower pressures with increasing temperatures for ROM strength of the composite. The author reinforces the versatility of powder-metallurgical processing of the composite system, on the ability to control the processing parameters and confirms the effects of higher processing temperature as more detrimental to the strength of the composite in comparison to longer pressing times; primarily on account of uncontrolled growth of a complex brittle intermetallic RI, composed of Fe_xAl_y species alongwith non-stoichiometric complex intermetallics of (A1, Ni, Fe, and Cr); also reported by (Mannan et al., 1983). Ideal parameters (800K/1 min/140 MPa) resulted in about a 4 μm uniform RI, with very trace amounts of Ni and Cr, largely composed of FeAl, Fe_2Al_5, and Fe_2Al_7; exhibited higher strengths than those predicted by ROM, also reported by (Friedrich et al., 1974; Karpinos et al., 1978). For estimation of the rate constant for RI growth in composites fabricated by hot pressing, (Bhagat, 1989) investigated the interface thickness against hot pressing time- this growth in thickness was reported to be governed by a parabolic rate constant as discussed by (Mannan et al., 1983). The growth curve was found to be composed of 3 distinct regions, with the slowest rate constant in the initial part of hot pressing- presumably due to the oxide layer on the fibers, which acts as a diffusion barrier. Once this oxide layer has been ruptured, the mechanism of RI growth moves to a diffusion controlled system and the rate constant reaches a maximum value. As this layer builds upto about 20 μm, earlier described as the limiting size for uniform radial growth by (Mannan et al., 1983), the growth slows down. An ideal RI thickness of 2-4 μm has been described for efficient load transfer from the matrix to the reinforcement, in agreement with earlier findings discussed in this section. This is achieved within the first 750 s of hot pressing. Hence to achieve the optimal RI thickness, the first region, which displays the slowest parabolic rate constant (calculated value 0.7 x 10-16 m^2s^{-1}), is of vital importance.

Morooka, et al., 1985, have described a powder rolling technique that involves continuous co-feeding of aluminium powder and pre-tensioned stainless steel wires over hot rolls to develop large sized composite plates. A peak tensile strength of 300 MPa is reported for about 7 vol.% reinforcement. The elastic modulus of the composite followed ROM, indicative of negligible porosity. An increase in high temperature stability of the composite was reported over pure aluminium.

Tiwari, et al., 1987, carried out fiber pull-out tests on a AISI 304 mono-wire embedded in Al-Mg-Si matrix alloy after annealing of the composite at 823 K for 0.5-24 h durations. The interfacial shear strength was estimated from the failure load, failure being cited as tensile failure of the reinforcing wire or pull-out from the matrix. In both the instances of exposure to annealing hold and pull-out test at room temperature and pull-out test at annealing temperature, a 5% degradation in interfacial shear strength was observed till temperatures upto 500 K (24 h exposure) and 540 K (0.5 h exposure); beyond which a rapid decrease was reported. Similar to earlier findings (Karpinos et al., 1978, Mannan et al., 1983), the RI was found to be composed of 2 distinct zones; the 2 step failure mode- crack initiation from the brittle intermetallic layer- followed by interfacial crack propagation towards the ductile matrix resulting in debonding of the reinforcement is similar to as suggested by (Friedrich et al., 1974). Crack initiation from the outer layer of the RI (aluminium rich) was attributed to mismatch in coefficient of thermal expansion (CTE) with respect to the stainless steel and iron rich inner core of the RI. The interfacial shear strength, a measure of pull-out resistance, is correlated to be inversely proportional to square root of the RI thickness, with a good level of confidence. Higher microhardness values were reported for the RI, annealed at higher temperatures and longer periods of time; with precipitation of intermetallics aiding the growth of the RI simultaneously with diffusional growth; the system is built-up of 2 distinct components, an initial stage with a uniform rate and a final stage which is faster and follows a nearly parabolic growth rate (Mannan et al., 1983); such acceleration at the later stage of RI growth can be attributed to diffusion of other alloying elements along grain boundaries (Karpinos et al., 1978, Mannan et al., 1983). Pull-out strength was reported to be independent of stainless steel wire diameter.

Bhagat, 1988, presented a generalized model for evaluation of growth kinetics of intermetallic RI by squeeze cast fabrication of AISI 304 stainless steel continuous wire reinforced age hardenable A1-0.7 Mg-0.6 Si-0.8 Mn-0.4 Fe matrix alloy composites; utilizing a die pre-heating temperature of 550°C and melt temperature of 850°C under 110 MPa pressure. The model suggests that in squeeze casting and infiltration of reinforcement preforms, the growth of RI and dissolution of the solid progress against each other- the initial stage of growth is governed by chemical kinetics of reaction between the components-which later changes to a

diffusion controlled growth of the RI. To ensure optimal fiber-matrix bonding, the process has to be completed in a short time such that the contact time period between the fibers and matrix melt is minimized. The higher melt temperature vis-à-vis hot pressing resulted in a thicker RI layer; composed of complex intermetallics and hence tensile strengths in this case, for all reinforcement volume fractions, were inferior to those predicted by ROM.

Delannay et al., 1993, have presented an overview of Al, Zn and Cu based composites reinforced with ceramic and metallic wires, processed powder metallurgically or by squeeze casting. In the case of Zn-27% Al alloy reinforced with AISI 3I6L and mild steel fibers, it was found that the RI was dependent on the cooling rate after melt infiltration of the fiber preform, as discussed by (Bhagat, 1988); consequently a heterogeneous RI was developed through the casting section- with large growth observed near the die center to negligible growth near the die wall due to progressive solidification proceeding inward from the die wall. This was also attributed to the low affinity of Zn towards Fe in comparison to Al, which segregates and reacts preferentially with the steel fibers; providing a natural barrier to Zn-steel interaction. To quantify interface adhesion of the fibers with the matrix, the authors have suggested a statistical method, wherein all fiber pull-outs will result in an uneven fracture surface; whilst moving from Zn-27Al through Zn-50Al, Zn-75Al to 100 Al, increase in the fracture surface roughness-on account of fiber-matrix debonding was reported- further suggesting the higher affinity of Al responsible for higher RI thickness-leading to premature fiber pull-out, as modeled by (Friedrich et al., 1974). The coefficients of thermal expansion (CTE's) determined for 4 composites of Zn-8%Al-1%Cu-0.02%Mg (ZA8) alloy matrix reinforced with continuous carbon, alumina, AISI 316L and mild steel fibers, showed lowest values for ZA8-mild steel pair, even lower than that calculated by ROM. The authors have described the composite strain as the sum of thermal strain ($\alpha_f.\Delta T$) on the fiber and an elastic component exerted on the fiber by the matrix; these stresses balance out at high temperatures. Fracture toughness of ZA8-mild steel/stainless steel pairs was found to be higher than other composites, primarily on account of inherent ductility of the reinforcing fiber in contrast to brittle alumina fibers. The steady state creep rate of the metallic fiber reinforced composites was similar to that of the unreinforced alloy- although, higher creep resistance was expected from the fibers at the test temperature of 150°C, indicative of higher adhesion between the fibers and matrix- resulting in plastic flow, at much lower stresses, of the fibers beyond their elastic range. However, fiber diameter dependence was observed on creep resistance with smaller diameter fibers (both ceramic and metallic) offering the lowest steady state creep rate. Keeping in view the higher fracture toughness with steel/stainless reinforcement; the authors suggest a low-cost composite in comparison to expensive ceramic/carbon fibers. For fabrication of Zn-alloy based composites,

the authors suggest the suitability of pressure die casting as a more industrially acceptable technique. For processing of higher melting point matrices, like Cu, powder metallurgy techniques are best favored, as they ensure overall lower processing temperatures, thereby limiting the matrix-reinforcement interactions.

Vaillant and Petitet, 1995, evaluated the RI morphology and composition under inert gas hydrostatically co-pressed Al/Al-0.4Mg-10Si-0.2Cu/Al-0.3Mg-0.2Si-4.5Cu alloy matrices with pure Fe and mild steel couples. In the case of pure Al- pure Fe pairs under pressure, the RI is composed of Fe_2Al_5 (adjacent to Fe) and $FeAl_3$ (adjacent to Al) phases- similar in structure and morphology as in open atmosphere, which upon annealing for prolonged durations result in growth of Fe_2Al_5 (η) phase. Al is not detected in the reinforcement and is consumed in RI layer build-up as Fe_2Al_5 (η); similar RI is detected with mild steel with a thinner RI. With Al-0.3Mg-0.2Si-4.5Cu -mild steel pair, a thinner RI is formed with about 1 wt.% Cu- which is responsible for inhibiting growth of RI. A porous interface is formed while processing at atmospheric pressure; fully dense interface resulted at imposed hydrostatic pressure. Higher diffusion of Cu was observed upon annealing for short durations, presence of βCu_2FeA1_7- formed as a result of diffusion of Cu into $FeAl_3$ (θ), was suggested in the layer adjacent to the matrix. Formation and growth of Fe_2Al_5 (η) phase is completely inhibited by preferential diffusion of Si in case of Al-0.4Mg-10Si-0.2Cu-mild steel pair; the intermetallic RI is found to contain θA1FeSi adjacent to steel and αA1FeSi adjacent to the matrix, under hydrostatic stress. At atmospheric pressure, the RI found to be composed of 3 layers- made up of θA1FeSi (adjacent to steel), a transition layer of αA1FeSi and βA1FeSi (adjacent to matrix). Such preferential interaction of alloying additions has also been reported by (Delannay et al., 1993) for Zn-Al alloy matrix-mild/stainless composite systems, as discussed earlier in this section. Pull-out strengths of samples fabricated at atmospheric conditions are remarkably lower than pressed composites, on account of shrinkage of the matrix and development of cleavages at the matrix-RI interface; whereas contiguous interfaces free from shrinkage cleavages are formed under pressure.

Durrant, et al., 1996, have investigated the interfacial bond strength of untreated/oxidized/Al-alloy coated/Ti-coated short cylindrical mild steel inserts squeeze cast in Al-7Si matrix. Processing parameters like insert surface roughness and temperature have been optimized to develop a basis for substitution of steel/cast iron in automobile components, most notably pistons and cylinder liners. The uncoated inserts were preheated to 300°C and 900°C; a cracked interface was obtained without any evidence of intermetallics for both the initial insert temperatures, with an oxide layer (Fe_3O_4) of about 5 μm in contact with the matrix for 900°C insert temperature. The mean shear strength observed during punch out tests was higher for elevated insert temperature. Absence of a RI at 300°C is reported on account of accelerated

solidification of the melt under pressure, from Fe-Al phase diagram it was established that $FeAl_3$ (θ) forms at 655°C (Shahverdi et al., 2002) , sufficient time was not available at this temperature for a RI to form; for 900°C, the presence of an impervious oxide layer hindered RI growth, even though the liquid was available for a slightly longer duration. For inserts hot dip-coated in Al-10Fe, a RI composed of Fe_2Al_5 (η) and $FeAl_3$ (θ), 140 µm thick was formed; upon squeeze casting with Al-7Si, an almost uniform RI (Fe_2Al_5 (η)) was formed with a co-continuous oxide layer in between the RI and the matrix covering about 30% of the interface circumference. Push-out loads were considerably higher in this case as compared to uncoated inserts; with shear failure of the Al-7Si matrix, resulting in a near linear load displacement curve with a maxima before failure; the maximum recorded shear strength is of the same order as reported for squeeze cast Al-7Si. Since the failure site lies within the matrix, interaction of pre-coated insert was largely independent of insert surface finish. For plasma sprayed Ti coated inserts, as sprayed rough surface was used alongwith a smoothened surface, prepared by grinding, to ascertain effect of insert surface finish on push-out strength. The insert was introduced for squeeze casting at 300°C and 900°C; no RI was detected at 300°C, at 900°C presence of a complex Al-Ti-O intermetallic was reported adjacent to the matrix. Push-out loads were of the same order as for dip-coated inserts (higher for 300°C insert temperature), with linear maxima; failure was cited in the Al-7Si matrix around the insert. An order of magnitude difference was reported in the interfacial shear strengths with as-sprayed inserts having higher values than ground inserts. Grinding of the inserts reduced the surface amplitude of the coating, consequently, the coefficient of friction was also reduced, even in cases where interface bonding is weak (as in Ti-Al7Si), the interface morphology-"jagged edge" appearance can provide asperity locking, thereby, delaying premature interface failure by causing plastic flow and eventual failure of the matrix under shear-yield conditions.

Hwang, et al., 1997, investigated the activation energy and rate constant for uniform growth of RI between alternating layers of pure aluminium foil and stainless steel, continuous, fibers hot pressed at 500°C/575°C/600°C under 70 MPa for 15 min-32 h durations. The growth of the interface obeyed a parabolic law $X^2 = k\,t$; as reported by (Mannan et al., 1983) and work of (Bhagat, 1989). The value of the temperature dependent parabolic rate constant was evaluated by the slope of straight line in the plot of RI thickness X v/s $t^{1/2}$. The value reported in this study was about twice the value obtained by (Mannan et al., 1983)- on account of pressure (70 MPa) assisted diffusion in the present case- almost half as reported by (Bhagat, 1989) in the steady state growth region, due to higher pressure (140 MPa) used in that study. The RI growth followed a diffusion controlled parabolic growth in the second stage, flattening out after a certain RI thickness is reached, in agreement with (Bhagat, 1989). The authors have also

proposed a geometric correction by incorporating an annular diffusion path, with fiber-RI/RI-matrix interface radii as the extremities, instead of classical diffusion across a flat rectangular interface, generating a more accurate estimate of the parabolic rate constant. The activation energy estimated from experiments at 500°C/575°C/600°C under 70 MPa for 15 min-32 h durations- for the geometrically appropriated annular diffusion layers was 152 kJ mol^{-1}; about 8% lower than 166 kJ mol^{-1} reported by (Mannan et al., 1983)- presumably on account of applied pressure in the present case. The RI was found to be composed of $Fe(Cr,Ni)Al_2$, $Fe(Cr,Ni)Al_3$ and $(Fe,Cr,Ni)_2Al_7$ and other intermetallics with compositional variations, based on radial positions within the annular RI. The morphology of the RI changed from a uniform ring like shape around the reinforcement for hot pressed samples to more non-uniform irregular growth morphology for samples annealed at longer durations without any imposed pressure.

Baron, et al., 1997, squeeze infiltrated sintered steel (1080) and stainless steel (AISI 409) porous preforms with age hardenable Al-8.3Si-3.5Cu-1.1Fe alloy under varying conditions of pre-aluminizing time, pressure, melt temperature and infiltration velocity. The RI was predominantly more in the central regions of the steel-Al alloy composite in comparison to the outer periphery and bottom layer of the preform in contact with die wall, with 2 distinct zones having different Al/Fe contents and a Si maxima within the RI; on account of slower solidification, also reported by (Delannay et al., 1993) for steel preforms infiltrated by Zn-Al alloy melt. In case of stainless steel-Al alloy pair, the RI thickness was much smaller and more uniform throughout the infiltrated composite with 2 distinct regions having different Al/Fe contents, as in steel-Al pair, Si content reached a maxima within the RI, however, Cr was not detected across the RI. Optimal processing parameters for highest tensile strength in case of steel-Al alloy pair were shorter pre-aluminizing hold-lower melt temperature-higher pressure-resulting in a RI of about 18% volume fraction. Significant increase in elastic modulus did not translate to improvements in strength for steel-Al alloy pair vis-à-vis monolithic alloy. In case of stainless steel-Al alloy pair, the enhancement of elastic modulus was lower than steel-Al; but substantial improvements were reported in tensile and yield strength albeit with lower elongation for processing conditions having lower melt temperature-other parameters were less sensitive to mechanical outcomes in both the cases. In contrast to studies discussed earlier (Friedrich et al., 1974; Karpinos et al., 1978) , with fibrous morphology of steel/stainless steel reinforcements, wherein for low/optimum RI thickness, failure initiates at steel/stainless steel wires-ductile failure with necking- the reinforcement morphology (particulate) in the present case ensured failure initiation from within the RI for all composites, irrespective of processing conditions. The lesser porosity (rel. density 0.7) in the sintered AISI 409 preform resulted in faster heat dissipation from the melt, thereby the solidification progressed faster leading to

lower volume fraction of RI than steel-Al alloy system (rel. density 0.6); the presence of a strong chromium oxide layer also inhibited the dissolution of Cr and formation of complex ternary intermetallics, as reported in earlier works of (Mannan et al., 1983; Bhagat, 1985; Hwang et al., 1997). Agarwala, et al, 1998, fabricated Al-1.5Si-4.6Cu-1.1Fe castings, reinforced with 100 µm diameter continuous stainless steel (Fe-16Cr-8Ni-0.12C) wires. Improved reinforcement-matrix interaction was reported under a vibrating field (70 min^{-1}), imposed on pre-tensioned wires, resulting in a uniform RI of about 10 µm thickness, mainly composed of Fe_3Al (305 HV) intermetallic. Under absence of vibration or pre-tension, the wires were found to be non-uniformly displaced due to turbulence and flotation offered by the melt.

Agarwala, et al, 1999, infiltrated steel wires of diameter 0.4 mm with Al-4.5Cu-0.25Si-0.25Ti-Mg/Mn-0.1 (wt.%) alloy by gravity casting technique, the RI interface formed after casting was found to grow with annealing time at 500-525°C upto 15h. A marked increase in wear resistance was reported for reinforced compositions against monolithic cast alloy and with increasing number of wires in the composite. The RI was found to be composed of Fe_3Al, FeAl, Fe_2Al_5, $FeAl_2$, intermetallics; the growth of RI thickness followed a near linear dependence on annealing time and temperature. Wear resistance and tensile strength of the composite was improved with significant reduction in ductility after annealing treatment due to growth in RI volume fraction, generally the hardness values of the intermetallic phases (450 HV) is an order of magnitude higher than the aluminium matrix (50 HV) and mild steel wires (150 HV), leading to higher adhesive wear resistance. The RI and retained porosity volume fractions, as determined from quantitative metallography were incorporated in the rule-of-mixture equation to account for composite elastic modulus and hardness; thereby theoretically designing the composite properties based on number of reinforcement wires.

Ganesh and Gupta, 2001, melt infiltrated AA 1050 over interconnected spiral preforms (shown in Fig. 2.15) of galvanized AISI 1008 wire (diameter 0.9 mm), followed by extrusion of as-cast composite cylinders. The spiral preforms attained upto 5 vol.% of the composites.

A marked reduction in porosity was obtained following extrusion of the cast composites; necessary for ensuring matrix continuity and overall composite integrity. The CTE values for the composite were than those predicted by ROM; as discussed by (Delannay et al., 1993). An efficient load transfer from the matrix to the reinforcement was observed, resulting in improved tensile strength, however, this enhancement in strength was less sensitive to increase in level of reinforcement interconnectivity from 61%-83%, compared to 98%. Deterioration in composite ductility was reported on account of brittle RI, offering lower cavitation resistance to the soft matrix.

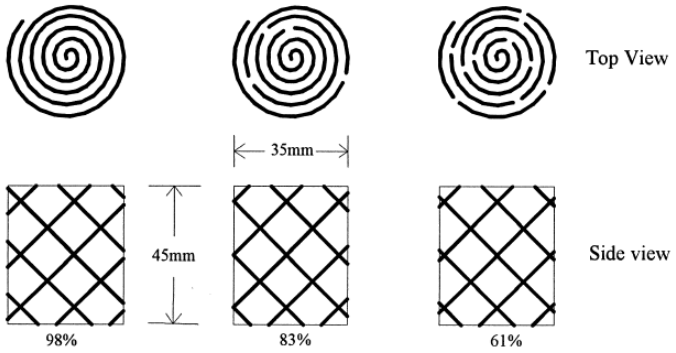

Fig. 2.15 Schematic representation of interconnected wire preforms conforming to different levels of interconnectivity (Ganesh and Gupta, 2001)

Ganesh, et al., 2001, have also reported the fabrication of Zn- coated mild steel wire-mesh (1.2 mm diameter) interconnected preforms by disintegrated melt deposition (spray deposition) of aluminium matrix over the preforms; followed by extrusion of spray cast composite billets to yield nearly fully dense composites. A continuous, non-porous, interface was observed with an increased microhardness of the matrix in close vicinity of the reinforcement, on account of residual stresses generated by a 2:1 mismatch in CTE of the reinforcement and the matrix, however, no RI was found to have been formed.

A decrease in the CTE of the composite was reported due to reinforcement interconnectivity offering resistance to matrix expansion, this decrease in composite CTE was higher than that evaluated by ROM:

$$\alpha_c = \alpha_f V_f + \alpha_m V_m \qquad \text{(Eq. 2.7)}$$

or the Schapery equation: used for predicting longitudinal CTE for fiber reinforced composites given as:

$$\alpha_c = \frac{\alpha_f V_f E_f + \alpha_m V_m E_m}{V_f E_f + V_m E_m} \qquad \text{(Eq. 2.8)}$$

where, α, V and E are the CTE, volume fraction and elastic modulus with notations c, f and m for composite, reinforcing fiber and matrix respectively. The elastic modulus was found to increase for the composite with similar yield and ultimate strength as the monolithic alloy. Fractographs revealed mixed-mode failure with fiber pull-out indicative of crack initiation from hard areas near the wires and ductile failure of the wires-indicating sufficient load transfer from the matrix, in agreement with mechanisms discussed previously.

Ganesh, et al., 2002, have proposed, from a galvanic corrosion standpoint, the suitability of such composite systems (steel wire mesh interconnects in aluminium matrix) in wet service conditions; based on galvanic potential E_{Al} = -1.662 V and E_{Fe} = -0.44 V, placed closer in the galvanic index, will be less reactive as a pair. Al matrix will form the anode with a much larger area with respect to Fe cathode, thereby reducing active galvanic corrosion in wet environments. Gupta, et al., 2006 have investigated the mechanical properties of Al-melt-Ti particulate, spray deposited over steel wire-mesh interconnected reinforcement preforms, followed by extrusion. Al-Fe reaction products were not detected, resulting in a sharp interface; however, TiO_2 was detected and Al_3Ti intermetallic was formed as a layer around the Ti particles with a continuous integral interface with the Al matrix. The matrix hardness was reported to be about 67% higher than the monolithic alloy on account to higher dislocation density around Al_3Ti and TiO_2 phases, with improvements in yield and ultimate tensile strength at the cost of ductility. A reduction of about 44% was achieved in the grain size of the composite against monolithic alloy, with reduction in CTE. The authors have compared the degradation of ductility, in this case, with conventional ceramic (SiC-particulate) reinforced composites with higher reinforcement volume fractions and have concluded better deformation tolerance due to the interconnected nature of the reinforcement. The strengthening effects of dominant ceramic reinforcements are largely underutilized owing to higher CTE mismatch and poor wettability with aluminium matrices; whereas, metal-metal composite systems present good bonding over the interfaces and higher composite integrity with relatively lesser loss of ductility.

Wong, et al., 2006, have reported highest yield and ultimate tensile strength for Al-SiC spray deposited steel wire mesh interconnected reinforced hybrid composites in comparison to pure Al, Al-SiC and Al-steel formulations, fabricated by process discussed earlier (Ganesh and Gupta, 2001; Ganesh, et al., 2001). Similar reduction in CTE and ductility was also obtained, with maximum matrix hardness for the Al-SiC-steel hybrid composite. The improvement (increase) in the dynamic elastic modulus was least affected by incorporation of SiC-particles in comparison to hybrid and Al-steel composites. Ductile failure of the reinforcing wires, indicated effective load transfer from the particulate reinforced matrix to the steel sub-structure, contained in the hybrid composite. The enhancement in mechanical properties of hybrid composite vis-à-vis singularly reinforced Al-SiC, specifically dynamic elastic modulus and strength were attributed to better interface bonding between the interconnects and aluminium matrix and formation of dislocation arresting substructure.

Viala, et al., 2002, produced Al7Si bi-metallic castings over spheroidal graphite cast iron (SGCI) inserts, pre-aluminized (upto 100 μm) by dip coating in Al7Si (Fe content kept at

under-saturated level- below 3wt.%); followed by casting of Al7Si over the aluminized inserts. RI of 12 µm was formed at the insert-aluminium interface in the as-cast state, composed a thin layer of Fe_2Al_5 (η) adjacent to SGCI, an intermediate layer of $Al_{7.5}Fe_2Si$ and an outer layer of $Al_{4.5}FeSi$ as irregular outgrowths extending to the aluminium alloy. The pre-aluminizing and final casting steps contribute to formation and growth of the complex RI, as a result of simultaneous reactive exchange and dissolution of phases from the insert and matrix. Pre-aluminizing the insert is a rapid process with about 4 min required for uniform surface wetting of the insert, with evolution of ternary αFe(Al,Si) solid solution and η, τ_1 (Al_3Fe_3Si), θ ($Al_{13}Fe_4$) intermetallics. The low amount of Fe in the melt ensures a thin layer of Fe_2Al_5 (η); otherwise found to grow rapidly upto 40 µm in Fe super-saturated Al7Si. Upon transfer for casting of the pre-coated insert, the brittle oxide layer is ruptured by the melt; the RI does not grow due to dissolution of Fe-rich phases to the melt. With fall in temperature both the growth and dissolution retard, with insert surface becoming over saturated in Fe. For samples subject to post casting heat treatment, the RI thickness was found to be double than as-cast composites, due to growth of η (Al_3Fe_3Si) and a complex layer of Al-Fe-Si ternary intermetallics with Kirkendall voids, formed as a result of uncontrolled solid-solid diffusion of Al from the alloy to Fe/ Fe_2Al_5 (η). The authors have reported significant weight reductions in a simple automobile component with a structurally sound oil-tight bond; however deterioration of the bond due to porosity at the RI upon heat treatment, severely limits the hardenability of this composite system.

Mandal, et al., 2004, have studied the and tribological behavior of Al-2wt.%Mg matrix reinforced with short steel fibers (obtained from chopping steel wool, 100 µm average diameter, 550-850 µm length, 2.5-10 wt.%) discontinuously reinforced composites prepared by stir casting route. Choice of Mg as the alloying element was based on enhancements offered in wettability and reinforcement distribution by lowering melt surface tension. To modify the RI between steel-aluminium, the fibers were coated with Cu (2 µm) and Ni (1.6 µm) by electroless deposition technique. Elongation to failure was highest in case of composites with Cu coated fibers, uncoated and Ni coated compositions displayed lower ductility; similar behavior was observed in wear resistance, under dry sliding conditions employing pin-on-disc test configuration. The formation of a continuous interface without any brittle reaction products was cited as the reason for superior properties of Cu coated compositions. The wear rates for the composites, calculated by volumetric loss, were significantly lower than unreinforced matrix. At lower load (10N) the predominant wear mechanism for unreinforced matrix alloy is delamination, which, changes to formation of grooves by microcutting and ploughing for composites. Increase in groove width followed by local delamination is attributed to increase in

normal load for reinforced composites for all fiber chemistries, indicative of enhanced plastic flow of the soft matrix. For Cu-coated fibers the wear rate is reported to be less sensitive to load in the range of 10-30N; transcending to severe wear at 40N applied normal load. From the analysis of wear debris, the authors have detected the presence of a complex third-body tribolayer composed of Al, Fe, Al_2O_3 and Fe_2O_3; with origin of Fe from the reinforcement fibers as well as the hardened steel counterface. A steady decrease in the coefficient of friction with increasing sliding distance was attributed to the presence of a fine oxide tribolayer, formed by repeated fracturing of debris between the mating pin and counterface, reported to act as a solid lubricant (Deuis, et al., 1997). An increase in the particle size of wear debris is reported with increasing normal load, with a shift from oxidative wear at lower load (10N) to adhesive delamination and plastic flow at higher loads; the presence of oxide volume fraction has not been detected analytically, but the debris morphology was indicative of shear induced cracking, characteristic of oxidized particles. The presence of hard reinforcement fibers increases the hardness of the composite formulations, thereby increasing their wear resistance by delaying the onset of severe wear. The authors have proposed a robust statistical relation to predict the actual wear loss using classical Archard's wear rate equation.

Mandal, et al., 2006, have investigated the mechanical properties of the composite system discussed earlier (Mandal et al., 2004); better distribution of as-coated fibers is reported with a uniform matrix-reinforcement interface in case of Cu coated fibers, with a decrease in fiber length on account of fiber breakage during melt stirring and solidification. Elemental line scans by energy dispersive X-ray spectroscopy (EDS) showed uniform presence of Mg in the composites, with highest concentrations of Fe and Cu at the RI. Cu also promotes solid solution strengthening of the Al matrix by formation of $CuAl_2$ eutectic, with better reinforcement-matrix bonding, thereby affecting load transfer to the reinforcement. Fe-Ni intermetallics formed during Ni coating of the fibers results in brittle phases over the fibers, decreasing the strength of the composite system. Retained porosity is lowest in unreinforced alloy, followed by Cu-coated, followed by uncoated and Ni-coated fibers. Hardness enhancement of the matrix has been attributed to dislocation pile-up at the fiber-matrix interface and dissolution of Cu in the aluminium. Cu-coated fibers offer the highest enhancement in tensile strength, by restriction of Fe-Al contact and a well-bonded interface, however, an overall reduction in elongation to failure is reported by incorporation of fibers for all chemistries. Fractographic examination of fracture surfaces has revealed dimple formation and coalescence of voids in case of Cu-coated fibers, whereas, fiber fracture and pull-out was the dominant failure mechanism in case of uncoated and Ni- coated fibers, evidently due to formation of brittle intermetallics at the RI.

Mandal, et.al, 2007a, have analyzed the elemental constituents from debris generated in pin-on-disc test for composites described above, they have reported a decrease in elemental Fe content with increase in normal load, attributing to the formation of Al_2O_3 and Fe_2O_3 at lower loads (10-30N), indicative of a oxidative wear mechanism; which changes to severe wear by delamination and plastic flow at higher load (40N). In essence, the wear behavior is akin to an Al-alloy at low loads (oxidative-abrasive-adhesive); which transitions to severe material loss by delamination and plastic flow of pin material as the load is increased. A power law equation of the type as suggested by Archard was robust enough to predict specific wear loss as discussed earlier by (Mandal et al., 2004).

Mandal, et al., 2007, have reported significant reduction in as-cast porosity levels after hot rolling of the composites. An appreciable increase in yield and tensile strengths alongwith apparent hardness was observed due to grain refinement and solid solution strengthening in Cu-coated composition. The density and hardness increments were linearly related to level of reduction achieved by hot rolling. Fiber fragmentation and redistribution, allowing higher dislocation pile-up at reinforcement-matrix interface was reported as the dominant factor for enhancements in mechanical properties. Higher hardness increase in Ni-coated fiber composites was attributed to excessive fiber fragmentation due to brittle nature of RI.

Mandal, et al., 2008, have shown an optimum level of copper coated short steel fiber at 5 wt.% for enhanced tensile strength of the composites; they have reported a decrease in strength with 10 wt.% reinforcement content due to increasing porosity. Failure initiation has been shown to start from the RI. Failure of the Al-2Mg matrix was ductile with presence of dimples with fiber pullout from the soft matrix (Mandal, et al., 2007b).

2.13 Summary of the Literature Review

The purpose of the above concluded literature review was developing a state-of-art theoretical and applied framework for fabrication and characterization of different properties of short fiber reinforced aluminium matrix composites by powder metallurgical processing. Listed below are important findings from respective sections/sub-sections of the review alongwith pertinent gaps, which are identified.

1. *Section 2.2*: Processing of AMCs by liquid metallurgical techniques is widely reported, in spite of their drawbacks. Complex techniques like squeeze casting and infiltration are able to overcome some of these impediments, however, in case of reactive matrix-

reinforcement conditions, P/M route should be preferred on account of lower processing temperature, for limiting growth of diffusion controlled reaction products.

2. *Section 2.3*: Discontinuously reinforced AMCs utilizing randomly distributed short fibers have consistently been reported to show superior performance than particulate reinforced AMCs, for the same level of incorporation.
3. *Section 2.3.1- 2.3.2*: Strengthening, damage evolution and wear mechanisms in short fiber reinforced AMCs are well documented in literature for ceramic reinforced systems, limited investigations are available for metallic fiber reinforced AMCs. The role of Fe-oxide(s) from abraded steel counterface in tribo-layer formation, under dry sliding of ceramic reinforced AMCs, is found to act as a solid lubricant, reducing wear loss and coefficient of friction.
4. *Section 2.4*: To ensure effective load transfer from the matrix to the reinforcement, certain degree of interfacial interaction is desirable. In case of ferrous reinforcement, the interface can be modified by CVD cum heat treating of the reinforcing fibers. Reactive diffusion based surface coatings, namely nitriding; chromizing and aluminizing will not only provide a barrier between the constituents but can also be utilized to increase the hardness of short steel fibers.
5. *Section 2.5*: Benefits of Al-P/M have been reviewed in light of higher strength-to-modulus ratio, near-net-shape forming capability etc.
6. *Section 2.6*: Barriers to sintering of aluminium particles are well known. Effective use of sintering aids, protective atmosphere, transient and super-solidus liquid phases, selection of powder particle size and morphology, all influence the final outcome. Alloy design for Al-P/M is reported to involve the use of elemental, prealloyed and premixed constituents that aid in cold consolidation and sintering densification by making available transient and/or supersolidus liquid phases, however, limited literature is available on completely prealloyed powders. Though not an ideal scenario, but secondary consolidation like forging and extrusion is known to offer equivalent metallurgical characteristics.
7. *Section 2.7- 2.8*: Thermomechanical processing by forging or extrusion, following sintering, is reported to be necessary for realizing zero-porosity, fully dense Al-P/M artifacts. Effect of various process parameters like strain, strain rate, temperature and flow behavior has been reviewed. Most of the studies are of theoretical interest, employing either very slow strain rates or very high deformation temperatures. It is necessary to evaluate these deformation based consolidation methods at high strain rates, controlled strain and moderate temperatures to fully understand the effect of these

parameters on pre-sintered prealloyed powder based compacts and composites. Correlation of imposed deformation strain with microstructure and deformed microstructure to final properties is proposed.

8. *Section 2.9*: Mechanisms of formation and growth of Fe-Al intermetallics has been reviewed, mostly conducted at temperatures above the melting point of aluminium and none for interaction of Al-P/M with steel. Understanding the interfacial reaction and growth kinetics of the reaction interface is vital to development of these composites. Evaluation of the reaction products and growth kinetics is proposed.
9. *Section 2.10*: Metal-metal MMC systems have been considerably less researched against dominant ceramic reinforced composites due to the unstable and brittle intermetallic interfaces, poor electrical conductivity, environmental embrittlement etc. Up-to-date literature on Al-Steel MMC systems, reports on only a single instance of development of short steel fiber reinforced, vortex cast AMC. Enhancements in mechanical and tribological behavior have been reported by altering the interface with metallic coatings that promote wettability and interface continuity. Characterization of elevated temperature strength, wear behavior and coefficient of thermal expansion is required to fully understand this class of metal-metal MMC system. Incorporation of steel based reinforcements is generally limited to Al, Al-Mg or Al-Si alloys; it is proposed to develop the same with regular high strength alloys, to offer a comparison with dominant ceramic reinforced AMCs. Deformation processing studies on this AMC system are few, most notably extrusion of continuous interconnected wire reinforced cast composite. It is further proposed to characterize the various properties of forged, rolled and extruded short steel fiber reinforced Al-P/M composites.

Chapter 3

FORMULATION OF PROBLEM

3.1 Introduction

Aluminium powder metallurgy has emerged as an established materials processing technique for development of monolithic alloy based components as well as particulate and short fiber reinforced composites for demanding performance applications that surpass the ability of standard alloy formulations. Al-P/M based components are now well accepted in transportation, aerospace, industrial equipment, precision equipment, leisure and sport, electronic packaging and other domains. Higher material utilization combined with a better strength to weight ratio and lower total energy consumption has made Al-P/M the preferred route for many emerging application areas.

Aluminium alloy based discontinuously reinforced composites have largely relied on ceramic particulates, whiskers and short fibers as dominant reinforcing phases, based on limited mutual interaction, further helped by lower processing temperatures in P/M processing. Metallic reinforcements have largely been unexplored due to higher probability of forming complex, uncontrolled intermetallics that are known to degrade matrix properties.

The present investigation is based on development of short steel fiber reinforced AMCs by powder metallurgical route, employing the steps of reinforcement-matrix blending, solid state sintering, and secondary consolidation by forging, rolling and extrusion. The developed composites will be characterized for physio-mechanical properties like hardness, tensile strength, elongation, transverse rupture strength, compressive strength, flow stress and coefficient of thermal expansion, in addition to tribological behavior at ambient and elevated temperature. Properties obtained will be evaluated against microstructural features, phase analysis, matrix-reinforcement interfacial chemistry, effect of thermomechanical processing, matrix alloy and reinforcing fiber characteristics.

3.2 Salient Features of Aluminium Powder Metallurgy

i. Sintering of aluminium is only possible by disruption of nascent oxide layer covering the powder particles. Laboratory scale work was reported to rely on expensive canning and degassing methods, followed by hot pressing. Addition of elemental magnesium and sintering under dry nitrogen atmosphere is found to overcome this limitation by enabling direct press-sinter processing of aluminium powder.

ii. Evolution of transient liquid phases by early melting of eutectics (Al-Mg, Al-Cu, Al-Zn, Al-Si, Mg-Si, Mg-Zn) or trace additions of low melting point elements (Pb, Sn, Sb, Bi) are utilized for pore filling while the bulk compact sinters in solid state. Alloy design for such sinterable compositions is well reported in literature, with effects of other parameters like particle size, sintering temperature, cooling rates and heat treatment.

iii. Deformation processing of pre-sintered, green or raw aluminium (alloy) powders is a necessary requirement for achieving porosity free structures. Forging, extrusion and rolling are some of the processes that deliver components of equivalent strength, free of prior particle boundaries and a refined structure as wrought alloys.

iv. Controlling parameters include imposed strain- limited by desired shape; strain rate- rate of work hardening is reported to increase with strain rate; deformation temperature- flow softening is promoted by increasing working temperature- maximum working temperature bound by hot shortness; and complexity of shape. Development of powder forged automobile connecting rod and piston have been reported.

v. Deformation induced rupture of aluminium oxide is helpful in restraining grain growth by grain boundary pinning. Design of rapidly solidified non-equilibrium alloys, consolidated by deformation processes, for fatigue, elevated temperature, wear, creep and corrosive service environments have been reported.

3.3 Salient Features of P/M- Aluminium Matrix Composites

i. Limitations faced by liquid metallurgical fabrication of AMCs like inclusion and gas entrapment, reinforcement wettability, interfacial interaction, reinforcement agglomeration and degradation, and matrix alloy depletion are avoided in P/M on account of lower process temperature and solid-solid blending of constituents.

ii. Techniques for blending and uniform mixing of reinforcements (particulate/whisker/ short fiber) with aluminium based matrix powders are well developed.

iii. Vast numbers of P/M- AMCs have been developed for research and many industrial applications are noted.

iv. Ceramic particulate and whisker have been the dominant reinforcement in AMCs. Strength enhancements of the composites have been attributed to thermal stresses developed by differential in thermal coefficients of expansion of reinforcements and matrix alloys. Increase in dislocation density in the matrix alloy and development of a two phase microstructure. Shear-lag and effective load transfer to the higher modulus whisker or short fiber.

v. Tribological characteristics of ceramic reinforced AMCs have been investigated with respect to sliding distance, load and temperature under dry sliding conditions.

vi. Wear resistance is reported to increase with increasing reinforcement content against monolithic alloys. Wear regimes have been identified as mild and severe, reinforced compositions have generally resulted in expansion of mild regime and delay in onset of severe wear.

vii. Oxidative and adhesive wear have been reported for monolithic alloys; abrasive action of hard ceramics is known to offer better wear resistance at higher loads by formation of mixed tribo-layer at the contact zone.

viii. Resistance to grain boundary sliding provides effective strengthening at elevated temperature, as determined by tensile, compression and creep tests. Failure at high temperatures is largely due to opening up of cavitation voids at whisker/short fiber ends.

ix. Secondary consolidation processes have been employed in fabrication of AMCs, with superior fatigue and fracture toughness properties than those achieved by casting route.

x. Elimination of sintering step, direct deformation based consolidation of heated green compacts is reported to eliminate interfacial reaction between the reinforcement and matrix.

xi. Particle cracking, fiber fracture, loss of isotropy by reinforcement banding are some of the issues reported in P/M- AMCs, processed by deformation. The safe workability window, effective strain rate and temperature, is also narrowed in comparison to monolithic alloys.

xii. Extrusion induced alignment of alumina stringers, covering the deformed alloy particles, resists coalescence of voids against the extrusion direction during tensile tests.

3.4 Salient Features of Aluminium- Steel Interactions at Elevated Temperature

i. Presence of Fe_xAl_y intermetallics is noted from the Al-Fe phase diagram. Mechanism of formation of different intermetallic phases is discussed in literature. Fe_2Al_5 (η) is the dominant phase, having high hardness and is prone to brittleness.

ii. Studies have focused on liquid Al-solid Fe for determining growth mechanism of the intermetallics, which are reported to follow a reactive cum diffusion controlled growth kinetics.

iii. Limited literature is available for analysis of solid-solid interactions in this system. Effect of Si, from the Al-alloy is found to inhibit formation of the reaction interface

under liquid Al-solid steel system; fails to achieve the same effect under solid-solid interactions.

3.5 Salient Features of Aluminium- Steel MMC systems

i. Majority of the studies reported for development of steel (mild steel/stainless steel/alloy steel) reinforced aluminium (pure Al/Al-Mg/Al-Si) matrix composites focus on continuous reinforcement of steel wires in aluminium matrices, by spray forming, spray deposition, diffusion bonding, squeeze casting/squeeze infiltration, gravity casting and aluminium melt infiltration of cast iron inserts.

ii. P/M based development of the composite system is reported as vacuum hot pressing of continuous stainless steel fiber-aluminium powder blend and powder rolling of pure aluminium powder- stainless steel wire. Similarly, a single study, focused on short steel fibers vortex cast in Al-Mg alloy has been reported in literature.

iii. A well interfaced reinforcement will ensure efficient load transfer from the matrix, thereby improving upon the properties of the unreinforced matrix alloy. In the system being investigated, threshold values of reaction interface thickness have been reported, generally a few microns (7-10 μm) thick; beyond which a degradation in properties is observed resulting in premature failure of the brittle reaction interface.

iv. Several techniques have been suggested to control the reaction interface thickness namely: pre-aluminizing of the steel fibers, metallic coatings of Cu, Ni and Ti. Addition of the Si to the melt. Post-casting extrusion to eliminate porosity and disintegrate the intermetallics and finally lowering the processing temperature by spray deposition, P/M processing to limit constituent interaction. Patented work has explored carbonitriding of continuous steel wires prior to squeeze infiltration by aluminium alloy melt for optimal growth of the reaction interface.

v. Developed composites have been characterized for microstructure evolution, reaction interface chemistry, mechanical properties, damage evolution, coefficient of thermal expansion and tribological behavior.

vi. Secondary consolidation by rolling of cast short steel fiber reinforced composites has been reported.

3.6 Scope of the Proposed Research Work

Ceramic reinforced AMCs have been dominant in research and industrial applications. Metal reinforced AMCs have lacked predictable properties due to evolution of unstable intermetallics and hence received little attention by researchers.

Steel reinforced aluminium based AMCs, as detailed in literature, have been developed and characterized. However, the following areas for further research have been identified:

i. Short fiber morphology of steel reinforcement has not been explored as reinforcement in P/M based aluminium alloys - identification of intermetallic reaction products and their overall effect on composite characteristics has not been comprehensively evaluated.
ii. Low temperature fabrication of short steel fiber reinforced AMCs by P/M method has not been reported.
iii. Enhancements in mechanical properties has been reported by Cu coating of short steel fibers, ex-situ CVD based treatments for fiber surface modification and/or hardness increment has not been investigated.
iv. Fe_xAl_y types of intermetallics have found application in elevated temperature service environments. No study is available for elevated temperature physio-mechanical properties of Al-steel based composites.
v. Limited alloy formulations have been investigated for incorporation of steel as reinforcement. High strength, age hardenable aluminium alloy matrices have not been investigated.
vi. Comprehensive tribological characterization of the composite system is not available in literature.
vii. Deformation processing by forging, extrusion and rolling and their effect on overall composite characteristics has not been evaluated.

3.7 Objectives of the Research Work

Based on the scopes identified in the previous section, the following research objectives have been identified. The objectives are defined on the basis of two different matrix compositions namely pure aluminium and AA6061. Short steel fibers, commercially available as *dry-mix*; a reinforcement used in phenolic resin based brake pads, has been identified as the reinforcement.

3.7.1 Development of short steel fiber reinforced pure aluminium matrix composite

1. To determine the particle size distribution, as solidified microstructure, hardness and oxygen content of pure aluminium powder. To characterize the size distribution, microstructure and hardness of the short steel fibers.
2. To evaluate the Al-Fe reaction interface growth kinetics, under a controlled vacuum hot pressing process.
3. To carry out surface modifications by CVD cum heat treatment on the as-received steel fibers and to incorporate treated fibers in the aluminium matrix followed by characterization of the reaction interface.
4. To incorporate Mg powder as a sintering aid by in the base aluminium powder. To prepare green compacts of monolithic as well as reinforced compositions.
5. To sinter the compacts at temperatures determined by thermodynamic studies of pure aluminium powder. Determine the densification parameter, pore morphology, reaction interface chemistry and microhardness of sintered compositions.
6. To hot forge, roll and extrude the sintered composites and evaluate their mechanical properties and flow stress at elevated temperature.
7. To comprehensively evaluate room temperature and elevated temperature wear behavior of monolithic and composite specimens.
8. To determine the coefficient of thermal expansion of monolithic and composite specimens.

3.7.2 Development of short steel fiber reinforced AA6061 matrix composites

1. To determine the particle size distribution, as solidified microstructure, hardness and oxygen content of AA6061 prealloyed powder.
2. To prepare green compacts of monolithic as well as reinforced compositions.
3. To sinter the compacts at temperatures determined by thermodynamic studies of AA6061 prealloyed powder. Determine the densification parameter, pore morphology, reaction interface chemistry and microhardness of sintered compositions.
4. To hot forge the sintered composites and evaluate their mechanical properties and flow stress at elevated temperature.
5. To determine the ageing behavior of the compositions produced.
6. To comprehensively evaluate room temperature wear behavior of the composites.
7. To determine the coefficient of thermal expansion of monolithic and composite specimens.

3.8 Work Plan

For fulfillment of the research objects, a work plan is devised as follows:

i. **Procurement of raw materials**: Inert gas atomized, low oxygen content sinterable powders will be procured for pure aluminium and AA6061 compositions. Short steel fibers of appropriate size range will be procured.

ii. **CVD treatment of fibers**: It is proposed to carry out the surface modification of the fibers in a fluidized bed reactor. A appropriate gases (Ar, H_2, HCl, N_2) and precursor generating elements (aluminizing- Al powder; chromizing- Cr powder) will be procured.

iii. **Interface growth kinetics**: To be determined on Gleeble-3800^{TM}, thermomechanical simulator under high vacuum with data acquisition of time, preform contraction, stress and temperature.

iv. **Sintering**: Determination of sintering temperatures for different alloys will be done through thermodynamic studies using DSC (differential scanning calorimetary). Sintering of uniaxially cold compacted green preforms will be carried out on a self-designed tubular furnace with accurate temperature and environment control.

v. **Forging**: Forging of sintered compacts is proposed on a friction-screw press, under briquette shaped closed dies with floating platen arrangement.

vi. **Extrusion**: Set-up for extrusion will be self-designed. Extrusion of pre-sintered billets will be carried out on a vertical hydraulic press.

vii. **Rolling**: Hot rolling of pre-consolidated briquettes will be carried out on a laboratory scale 2-high rolling mill.

viii. **Characterization:** Density measurements will be done by water immersion technique, standard metallographic practice will be used for sample preparation to be examined under optical microscope and SEM. Phase analysis by XRD and elemental maps will be prepared by SEM-EDS. Tensile and compressive strength will be determined on a universal test rig. Coefficient of thermal expansion will be determined using a horizontal push-rod type dilatometer. Dry sliding wear tests are proposed to be conducted on both ball-on-disc and pin-on-disc tribometers. Flow stress will be determined at fixed temperature and strain rate on Gleeble-3800^{TM}, thermomechanical simulator. Effect of powder morphology on deformation behavior of monolithic alloys will be determined by EBSD (electron backscattered diffraction). Fig. 3.1 gives an overview of the methodology to be applied for the proposed research.

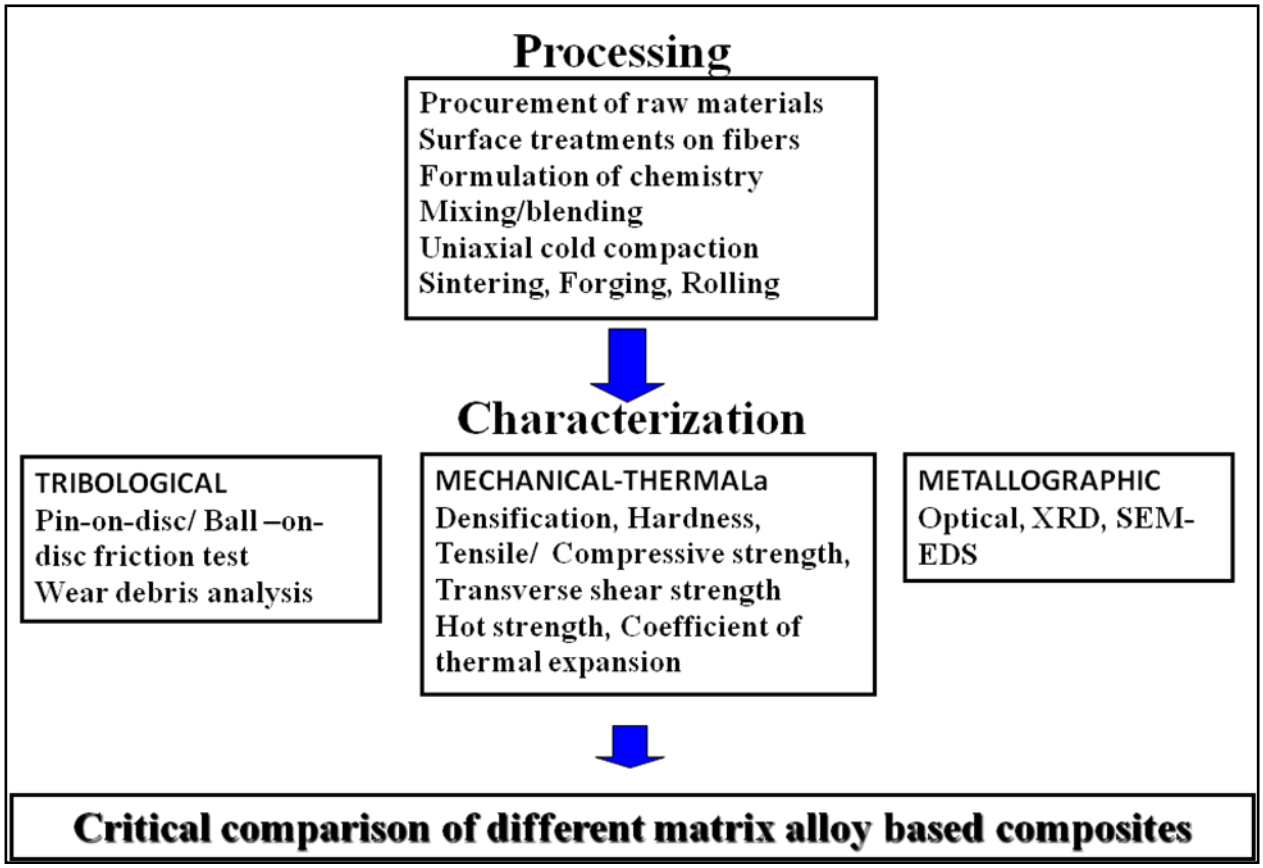

Fig. 3.1 Research methodology

Chapter 4

EXPERIMENTAL PROCEDURE

4.1 Introduction

The powder metallurgical processing of aluminium composites requires similar equipment and processing methodology as used in classical powder metallurgy, incorporating the steps of powder chemistry preparation, cold consolidation, sintering under controlled atmosphere and if required, secondary operations on the sintered body. In the introduction of fibrous reinforcements, for fabrication of composites, a blending step is added in the beginning to enable uniform reinforcement distribution in the matrix without altering the respective morphologies. Initial characterization starts from density measurements of green, sintered and secondary formed samples, correlation of macro and microstructural observations with mechanical and other attributes like, tribological behavior, flow at elevated temperature, phase analysis and fractography etc. This chapter will describe in detail about the starting materials, fabrication processes and characterization tools employed over the various stages of development of short steel fiber reinforced aluminium/aluminium alloy powder metallurgical (P/M) composites.

4.2 Materials

4.2.1 Pure aluminium, magnesium and pre-alloyed aluminium powders

Commercially pure, gas atomized, aluminium powder (-325 mesh), of nominal chemical composition (wt.%) as given in Table 4.1 was sourced from Atlantic Equipment Engineers, AEE^{TM}, Bergenfield, NJ, USA, (www.micronmetals.com). Pure magnesium metal powder (-325 mesh, 99.8% purity) was procured from Alfa Aesar (www.alfa.com). Gas atomized pre-alloyed AA6061 powder of nominal chemical composition as given in Table 4.2; was provided by United States Metal Powders Inc., Flemington, NJ, USA, under their brand name AMPAL^{TM} (www.ampal-inc.com). All compositions reported are as provided by the suppliers. The powders were free of any ad-mixed lubricants.

Table 4.1- Chemical composition of pure aluminium powder (wt. %)

Si	Fe	Ti	Zn	Cu	Mn	Al
0.05	<0.10	0.01	0.02	0.005	0.01	Bal.

Table 4.2- Chemical composition of AA6061 powder (wt. %)

Si	Fe	Cu	Mg	Cr	Al
0.68	0.19	0.30	1.10	0.30	Bal.

4.2.2 Short steel fibers

Short steel fibers, an industrial raw material, commercially known as *dry-mix* or *steel wool powder*, used as reinforcement in asbestos-free braking and friction elements like brake liners, brake pads, brake blocks and clutch plates, of nominal chemical composition as shown in Table 4.3, were sourced from Gurukripa Industries, New Delhi.

Table 4.3- Chemical composition of short steel fibers (wt. %)

C	Mn	Si	S	P	Fe
0.38	0.52	0.10	<0.02	<0.024	Bal.

4.2.3 Powders used for chromizing and aluminizing treatments on steel fibers in fluidized bed reactor

The fluidizing bed was composed of spherical Al_2O_3 particles (purity > 99.9%; Fisher Scientific^{TM}) having an average size of 125 µm. For chromizing treatment, pure chromium metal powder (purity > 99.5%; Sigma Aldrich^{TM}) of average particle size 100 µm was added to the fluidizing medium (Al_2O_3) in required proportion. Aluminizing treatment involved addition of pure aluminium powder of average size 200 µm (purity > 99.8%; Sigma Aldrich^{TM}) to the fluid bed.

4.2.4 Lubricant for cold compaction of monolithic and composite powder-fiber blends

Stearic acid ($CH_3(CH_2)_{16}CO_2H$) flakes (RANKEM^{TM}) were dissolved in acetone (technical purity; Fisher Scientific^{TM}) by heating upto 50ºC, followed by continuous stirring. A clear liquid resulting after complete dissolution of stearic acid was used as die wall/punch-plug face lubricant during cold consolidation of matrix powders and composite powder-fiber blends.

4.2.5 Hot working lubricant and release agent

Molybond 122L^{TM} (ITW Polymers and Fluids), MoS_2 based, quick drying, dry film, aerosol spray (Molybond 122L, 2006) was used to coat the inside walls and punch faces of hot pressing die-punch set-up.

GE Momentive^{TM} (GE, USA), boron nitride aerosol spray, effective upto 850ºC, (Boron nitride coatings, n.d.) was used as the die/punch/briquette lubricant in hot forging and container/dummy block/die/billet lubricant during extrusion.

4.2.6 Gases

For chromizing and aluminizing treatments an active HCl (hydrogen chloride) gas (BOC, technical grade) was used alongwith technical grade argon gas (all supplied by A-Gas^{TM}, Australia). Anhydrous ammonia (NH_3) was used for nitriding was supplied by Air Liquide^{TM}, Australia. Prior to surface treatment, fibers were de-oxidized with pure hydrogen gas. Sintering of green monolithic and composite powder-fiber compacts was conducted under pure nitrogen gas (technical grade, purity > 99.999%).

4.3 Processing

4.3.1 Surface modification of steel fibers by chemical vapour deposition (CVD) using fluidized bed reactor (FBR)

The as-received short steel fibers were sieved to remove any fines, dust and solid impurities. They were ultrasonically agitated in acetone to dislodge adherent impurities like oxide scale and fine dust, organic substances like metal working lubricants and oils. The surface treatments incorporated nitriding, chromizing and aluminizing of the short steel fibers by chemical vapour deposition (CVD) using a fluidized bed reactor (FBR) at the Institute for Frontier Materials, Deakin University, Waurn Ponds Campus, Geelong, Australia. Fig. 4.1 shows an image of the fluidized bed heat treatment-cum-CVD system. A schematic representation of the FBR-CVD

Fig. 4.1 Image of fluidized bed reactor at the Institute for Frontier Materials, Deakin University, Australia

system for chromizing of short steel fibers is shown in Fig. 4.2. The system was composed of a vertical 90 mm diameter stainless steel retort placed inside a resistance heating furnace of 4.5 kW rating, producing a vertical hot zone of 200 mm length with a maximum operating temperature of 1200^{o}C; controlled to an accuracy of 1^{o}C by Chromel/Alumel (K-type) thermocouple interfaced with a EUROTHERM 2116^{TM} PID (proportional-integral-derivative) controller. A gas bank located outside the laboratory was connected via overhead gas manifold. Gas flow rate could be controlled to an accuracy of 1 SCCM (standard cubic centimetre). A hydrogen/oxygen detector-cum-burner was placed in the path of the flowing gas above the retort to ensure controlled combustion of flue gases. The gas flow terminated into a scrubber; filled with caustic soda solution, to neutralize any residual HCl (active) gas. A sintered stainless steel disc (upto 60% porosity) placed at the bottom mouth of the retort, ensured homogeneous diffusion of gases into the alumina packed bed of the reactor. The top of the reactor was equipped with a view-port and pneumatic cylinder for loading and retraction of solid steel samples from the bed.

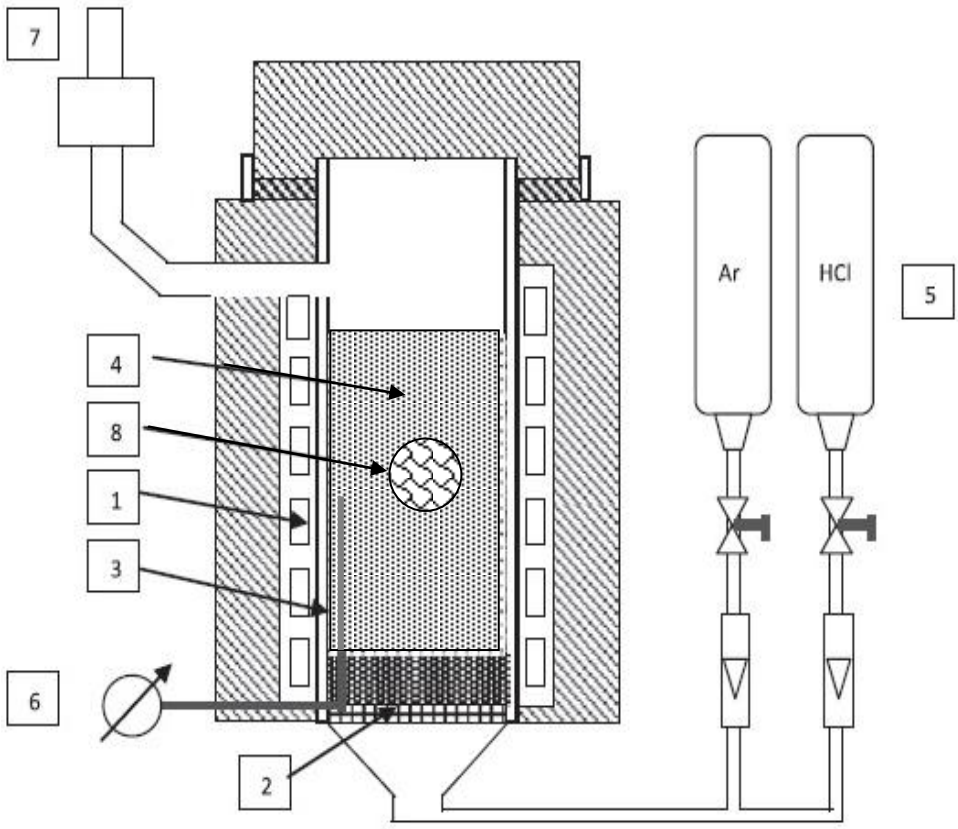

Fig. 4.2 Schematic diagram of the fluidized bed reactor (Ralston, et.al, 2011): (1) Heating elements, (2) Sintered metal disc, (3) Metal retort, (4) Al_2O_3 bed with Cr (Al) powder, (5) Gas source, (6)Thermocouple, (7) Scrubber system, and (8) Steel fibers

4.3.1.1 Nitriding

The nitriding process of short steel fibers in the fluidized bed reactor involved dispersion of 50 g of pre-cleaned fibers in about 1.8 Kg of alumina powder (average size 300 μm) at 525^{o}C for 90, 30 and 5min durations under 35% NH_3-65% N_2 atmosphere.

4.3.1.2 Chromizing

Chromizing treatment involved the addition of 50g of pure Cr powder to the fluidizing bed and carried out at 935^{o}C for 50 and 7 min durations under 99% Ar-1% HCl gas atmosphere.

4.3.1.3 Aluminizing

The aluminizing process of short steel fibers in the fluidized bed reactor involved dispersion of 50 g of pure aluminium powder to the fluidizing bed and carried out at 535^{o}C for 45 min duration under 99% Ar-1% HCl gas atmosphere.

Upon completion of the above mentioned treatments, the fibers were furnace cooled to room temperature while remaining in the fluidized bed, sieved and magnetically separated from the alumina powder.

4.3.2 Incorporation of magnesium as sintering aid in pure aluminium powder

Pure magnesium powder (0.5 wt.%) and pure aluminium powder, weighed to an accuracy of 1.0 mg, were ball milled together in a 4-jar planetary RETSCH PM-400^{TM} high energy ball mill, using 500 ml jars, to produce Al-0.5 wt.% Mg matrix powder blend. The milling intensity was maintained at 200 rpm for 1 h duration. Cr-steel balls, conforming to AISI 52100, of 16 mm diameter were the grinding media, with a ball to charge ratio of 5:1.

4.3.3 Blending of short steel fibers with aluminium matrix powders

Cleaned short steel fibers and matrix powders, weighed to an accuracy of 1.0 mg, were blended together in a 4-jar planetary RETSCH PM-400^{TM} high energy ball mill using 500 ml jars, to produce composite blends with 5, 10, 15, 20, 25 and 30 wt.% short steel fibers. The milling intensity was maintained at 80 rpm for 1 h duration. Cr-steel balls, conforming to AISI 52100, of 16 mm diameter were the grinding media, with a ball to charge ratio of 2:1.

4.3.4 Uniaxial cold compaction of monolithic and composite powder blends

Monolithic and composite powder blends, in weighed batches, were uniaxially cold compacted in hardened steel dies using a hydraulic press of 40 kN capacity (HEMCO^{TM}, Mumbai, India); the load was set with an accuracy of 1 kN, the press was equipped with a pressure regulating

valve, capable of delivering a dwell at maximum load, which was limited to 30 s. The compaction tooling consisted of circular cross-sectioned dies (13, 16 and 20 mm diameter) and flat bars of 40 mm × 8 mm for transverse rupture strength specimens, (KIMAYA^{TM}, Mumbai, India), having a rigid body, top punch, dummy disc and bottom plug; all polished to < 1μm mirror finish and hardness ≥ 53 HRC (Rockwell C-scale). Ejection of the pressed green compact was affected by inverting the top punch to lightly push-out the bottom plug, green body and top dummy disc into a spacer, provided with the die-set. Aspect ratio (*h*/*d*) of cylindrical compacts was always maintained below 0.5, to overcome density gradients associated with uniaxial cold compaction. Compaction stress was proportioned in MPa; consequently, press tonnage in kN was set as the product of compaction stress (MPa) with projected area of the die cavity (mm^2). Compacts for forging were in the shape of briquettes of size 23 mm x 48 mm x *h* mm; prepared by filling a floating platen type die cavity (Precision Engineering Works, Delhi), set between a bottom and top punch (pressing plane- 23 mm x 48 mm), made from HCHCr of mirror finish and hardness ≥ 52 HRC. The height of the green briquettes thus formed was dependent on the amount of filling and compaction pressure; with an upper bound of $h/d < 0.5$; imposed by considering the projected area of the pressing plane as a circle of 38 mm diameter. In practice, the height of the briquettes was limited to a maximum of 15 mm. Billets for extrusion were uniaxially pressed in a die of 29 mm diameter (locally fabricated), of similar finish and hardness as dies of smaller diameter. Dies were cleaned with acetone followed by liberal application of lubricant (*Section 4.2.4*) on die walls and punch/plug faces prior to loading. Dies were lightly tapped after filling to obtain charge packing upto apparent density with a flat meniscus. During months of high ambient humidity, the powder-fiber blends were warm compacted, by roasting the charges, wrapped in aluminium foil, in a laboratory oven at 60 ^{o}C.

4.3.5 Hot pressing

Composite powder blends based on Al-0.5wt.% Mg matrix were hot pressed in a uniaxially to ascertain the effect of low temperature consolidation on the fiber-matrix reaction interface. In the first instance, conventional radiant heating was applied; to enable a more detailed study of Fe_xAl_y reaction interface growth kinetics; green preforms were vacuum hot pressed at different temperatures and time periods in a specially designed punch and die set-up using GLEEBLE 3800^{TM} thermomechanical simulator.

4.3.5.1 Conventional uniaxial hot pressing

A 20 mm diameter die was loaded with monolithic and composite blends based on Al-0.5 wt.% Mg matrix powder. MoS_2 based lubricant, as described in *Section 4.2.5*, was applied on the die wall, punch and plug faces, prior to loading. The loaded die was enclosed in clamshell type radiant heating furnace under a MTS ™ 100 kN compression test frame. Hot pressing temperature was recorded by a Chromel/Alumel (K-type) thermocouple embedded in the outer wall of the die. Die temperature was ramped up at a rate of 25°C/min to the pressing temperature of 475°C, maintained for 5 min prior to compression under 70 MPa constant stress for a total of 20 min, as shown in Fig.4.3. A protective flow of Ar gas was maintained inside the clamshell heater till the die with the hot pressed sample cooled to room temperature. The hot pressed pellets, 20 mm in diameter and about 5 mm in height, were cleaned with acetone to remove any dry film lubricant.

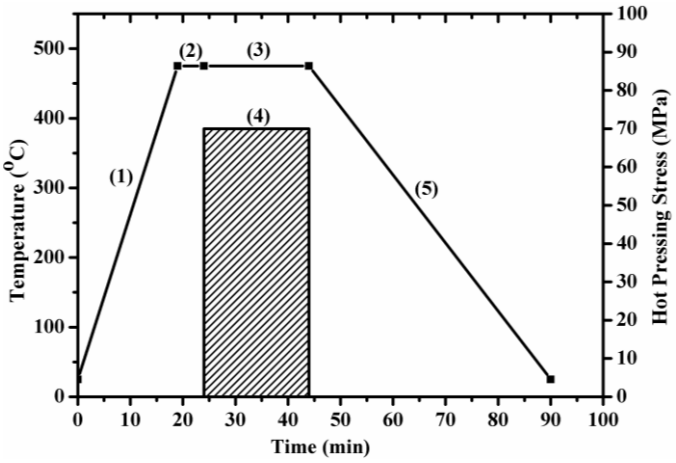

Fig. 4.3 Time synchronous plot of hot pressing cycle: (1) Ramp-up to 475°C/25°Cmin^{-1}, (2) 5 min dwell at 475°C, (3) Pressing duration at 475°C (4) Hot pressing stress (70 MPa) (5) Cooling of pellet in die under Ar gas

4.3.5.2 Vacuum hot pressing using GLEEBLE 3800™ thermomechanical simulator

The composite blends, conforming to pure Al- 5, 10 and 15 wt.% short steel fiber, were uniaxially cold compacted using a hardened steel die in a hydraulic press of 25 kN capacity at 375 MPa to prepare cylindrical green preforms of 16 mm diameter and 32 mm length. The green compacts of pure aluminium and all reinforced compositions were hot pressed in 10^{-3} torr vacuum, at 450°C, 500°C and 550°C for 5, 10 and 15 min durations, under 50 MPa maximum axial stress on GLEEBLE 3800™ thermomechanical simulator (www.gleeble.com; DSI Inc., Poestenkill, USA) using a set of custom fabricated cylindrical die and 2 punches, made of H13 hot die steel, as shown in Fig.4.4. GLEEBLE 3800™ system utilizes the resistance of the specimen for heating by controlling the flow of current through the specimen,

to an accuracy of ±1 ^{o}C across the specimen cross-section. The stem portion of the punches was held in water cooled copper jaws (Fig. 4.5), called pocket jaws for flow of current to enable heating of the green compact encased in the die, utilizing resistive heating ($H = I^2Rt$); where H is the heat evolved (J), I is the current (Amp), R is the resistance (ohm) of the die/green compact and t is the time (s). Chromel/Alumel (K-type) thermocouple was welded to the outer wall of the die for temperature measurements. Heating rate was maintained at 5^{o}C s^{-1}. A representative plot of the hot pressing cycle is shown in Fig. 4.6. A linearly increasing stress was applied with maximum stress attained at the end of hot press cycle. The sintered compacts were allowed to cool in vacuum. The die allowed for a 0.25 % diametric expansion of the green compact during hot pressing. MoS_2 based aerosol spray was used as the parting agent. A LVDT (linear variable differential transformer) was used to measure the axial contraction of the green compact to an accuracy of ±0.001 mm; all parameters were logged at a 100 s^{-1} data acquisition rate.

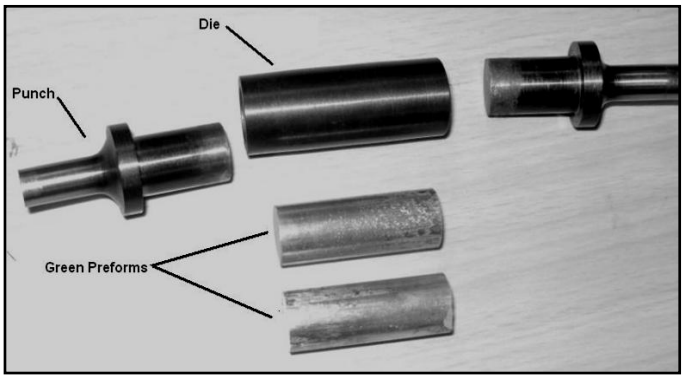

Fig. 4.4 Die and punches used for VHP on GLEEBLE 3800^{TM} thermomechanical simulator

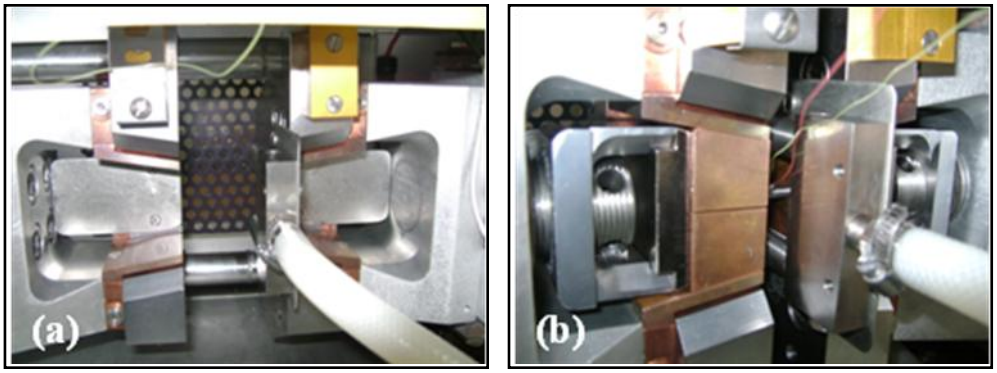

Fig. 4.5 (a) Pocket jaws **(b)** Pocket jaws with compression platens for vacuum hot pressing on GLEEBLE 3800^{TM} thermomechanical simulator

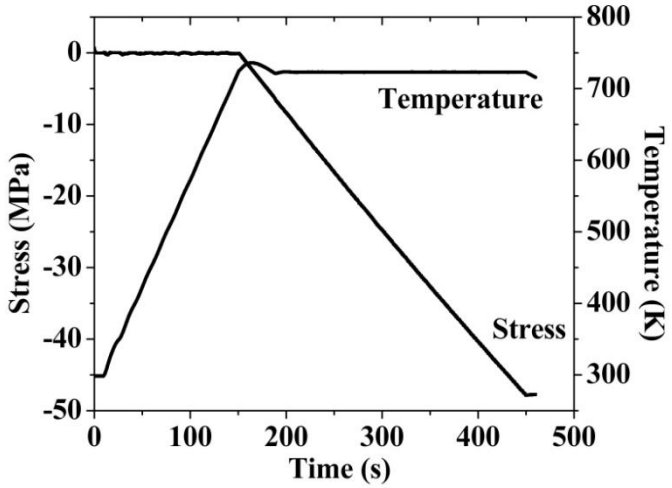

Fig. 4.6 Time synchronous plot of heating and hot pressing stress for vacuum hot pressing cycle on GLEEBLE 3800^{TM}

4.3.6 Sintering

4.3.6.1 Equipment and cycle

Monolithic and composite green compacts of different geometries were sintered using a self-assembled tubular furnace having a 99% recrystallized alumina tube of 75 mm outer diameter and 1 m length. The tube was fitted with custom machined end caps of AISI 304 stainless steel, having ball valve controlled ports for gas inlet, vacuum pump and tube pressure readout gauge (+760 to -760 mm Hg). Heating was affected by KANTHAL-A1^{TM} coil wound over the alumina tube, with a rated load of 2.5 kW. Maximum operating temperature was limited to 1150^{o}C, with a heating rate limitation of 40^{o}Cmin^{-1}. The hot zone of the furnace was 200 mm in length, extending 100 mm from the geometric center of the tube on either side, as verified by calibration against a standard thermocouple. Control of the ramp-up rate, degassing and sintering dwells and shut-down was accomplished by a programmable PID, WEST6400^{TM} make (± 1^{o}C accuracy, 1 min sensitivity, 8 segment programmable cycle, 4 memory stored programs) , interfaced with a Chromel/Alumel (K-type) thermocouple, placed at the center of the tube, in positive contact with the tube outer wall. A typical sintering cycle, as shown in Fig. 4.7, consisted of loading the green compact in the furnace hot zone, sealing of end caps, evacuation of the tube by a mono-block vacuum pump, (1) ramp-up to the degassing temperature, (2) holding at the de-gassing temperature, introduction of technical grade nitrogen in the tube, re-evacuation and back-filling of nitrogen (3-4 times), filling-up and constant flow of the gas at a desired flow rate (± 0.20 lmin^{-1}), (3) ramp-up to the sintering temperature, (4) dwell at the sintering hold and finally (5) shutdown of power to enable furnace cooling of samples to room temperature.

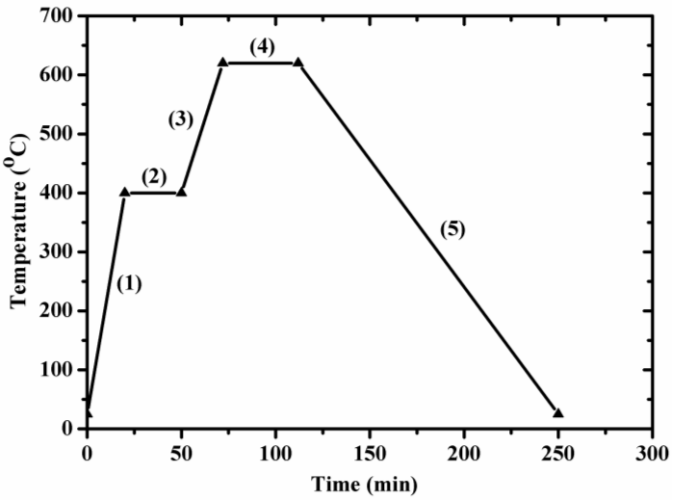

Fig. 4.7 A typical sintering cycle

4.3.6.2 Sintering temperatures

Green compacts based on different matrices with/without reinforcing fibers were solid-state sintered to enable solid-solid diffusion based sintering for Al-0.5wt.% Mg based formulations. Supersolidus liquid phase sintering was enabled by presence of upto 10 vol.% liquid phase for AA6061. Methodology for estimation of liquid volume fractions by thermodynamic investigations of pre-alloyed powders is described in *Section 4.4.5*.

4.3.6.3 Gas conditioning

Purity alongwith dryness of the sintering atmosphere is of utmost importance in sintering of aluminium powder. To ensure dry and oxygen free nitrogen gas for sintering, an online gas purification station was fabricated, it included the passage of gas through an air tight desiccant column of silica gel, followed by a stainless steel tube filled with copper turnings and pure magnesium chips, radiantly heated to 500^{o}C, for onward flow to the sintering furnace. The turnings and chips were visually inspected for excessive oxidation, if required, were recharged by stripping in 38% H_2SO_4.

4.3.7 Forging of sintered briquettes

Sintered briquettes of monolithic and reinforced compositions were hot forged in a spring loaded, floating platen type die of cavity size 25 mm x 50 mm x 35 mm; slightly bigger than cold compaction cavity, made of H13 hot die steel of average hardness ≥ 53 HRC and polished to < 1µm mirror finish, (Precision Engineering Works, Delhi). The die consisted of a top punch- moving with the press ram and a stationary bottom punch- resting on the die base plate. Sintered specimens were loaded onto the die cavity, resting on the bottom punch with top punch in its retracted position. The bottom punch also served as the ejector for forged

briquettes during the ejection cycle, wherein spacer blocks placed between the top punch and floating platen allowed for easy retrieval of the forged briquettes. Die-punch clearance was maintained at 0.05 mm. Sintered briquettes, spray coated with hot working boron nitride aerosol based lubricant (*Section 4.2.5*); were held at forging temperature for 30 min in a muffle furnace, without any protective atmosphere; quickly transferred to the die cavity for forging in a manually operated Weingarten-type friction-screw press of 100 kN capacity, 15 kW prime mover, as shown in Fig. 4.8; (BIRSON^{TM}, Ludhiana, India). Average ram velocity was maintained in the range of 250 - 275 mm s^{-1}; digital readout of ram velocity was enabled by interfaced proximity sensors placed at stroke extremities on the press pillar, coinciding with TDC- top dead center/ BDC- bottom dead center positions of the ram (sensitivity ± 1ms^{-1}). Floating platen of the die assembly, containing the H13 hot die steel insert cavity, was heated by 2 nos. rod type resistance heaters. Temperature of the die cavity was measured by a hand held non-contact infrared digital IR temperature sensor (-50^{o}C to +380^{o}C range, ± 1^{o}C accuracy, sensing distance 150 mm; XINZHIBAO- GM 300^{TM}, China). The forging plane for sintered briquettes was the long side of the short rectangular cross-section (48 mm x 15 mm) to enable constrained die upset forging, yielding forged specimens of 25 mm x 50 mm x *h* mm dimension (Fig. 4.9). Forged specimens upon ejection from the die cavity were immediately quenched in cold water and ground on 600 grit SiC paper to de-flash and remove residual lubricant. Compositions based on AA6061 were preserved in a freezer maintained at -18^{o}C for further characterization. Die cavity was cleaned with a wire brush for any flash or lubricant residue.

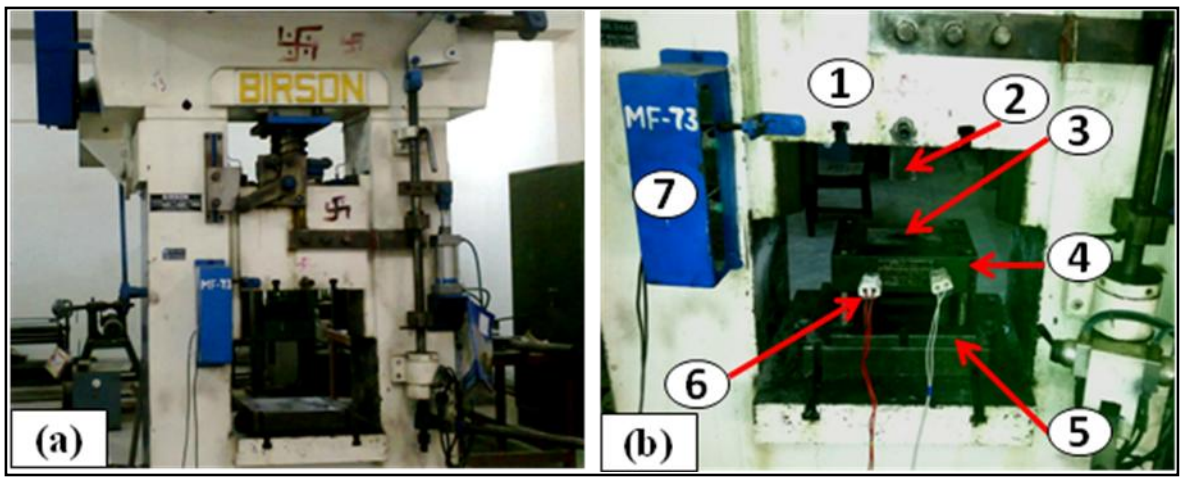

Fig. 4.8 Images showing (a) Friction screw forging press (b) Major components of forging set-up (1) Ram, (2) Top Punch (3) Die cavity (H13 hot die steel) (4) Moving platen (EN-8 alloy steel) (5) Die base (EN-8 alloy steel) (6) Heating element (7) Proximity sensors

Fig. 4.9 Image of sinter-forged briquettes

4.3.8 Rolling of sinter-forged briquettes

Hot rolling of sinter-forged briquettes with 25 mm x *h* mm as the leading face, was performed in a 2-high laboratory scale rolling mill (roll diameter 65 mm; roll length 200 mm; 5 kW prime mover). Briquettes were soaked at the rolling temperature in a muffle furnace; quasi-thermal condition of the rolling stock was maintained by re-heating and soaking at same temperature after each pass. Initial roll gap was maintained to an accuracy of 0.1 mm by a set of feeler gauges; successive reductions were attained by screw setting the roll gap to an accuracy of 0.2 mm. A reduction of 10% was achieved in the first pass, followed by 3 passes of 20% successive reductions each. Initial and final thicknesses t_i and t_f were recorded (±0.02 mm). As-rolled strips were annealed to room temperature from the rolling temperature.

Fig. 4.10 Image of hot rolled strips

4.3.9 Direct extrusion of sintered billets

Sintered billets of monolithic and reinforced compositions, as cylinders of 29 mm diameter and upto 40 mm height, were direct extruded in a resistance heated container as schematically shown in Fig. 4.11. Extrusion set-up was self designed and fabricated by Precision Engineering Works, Delhi.

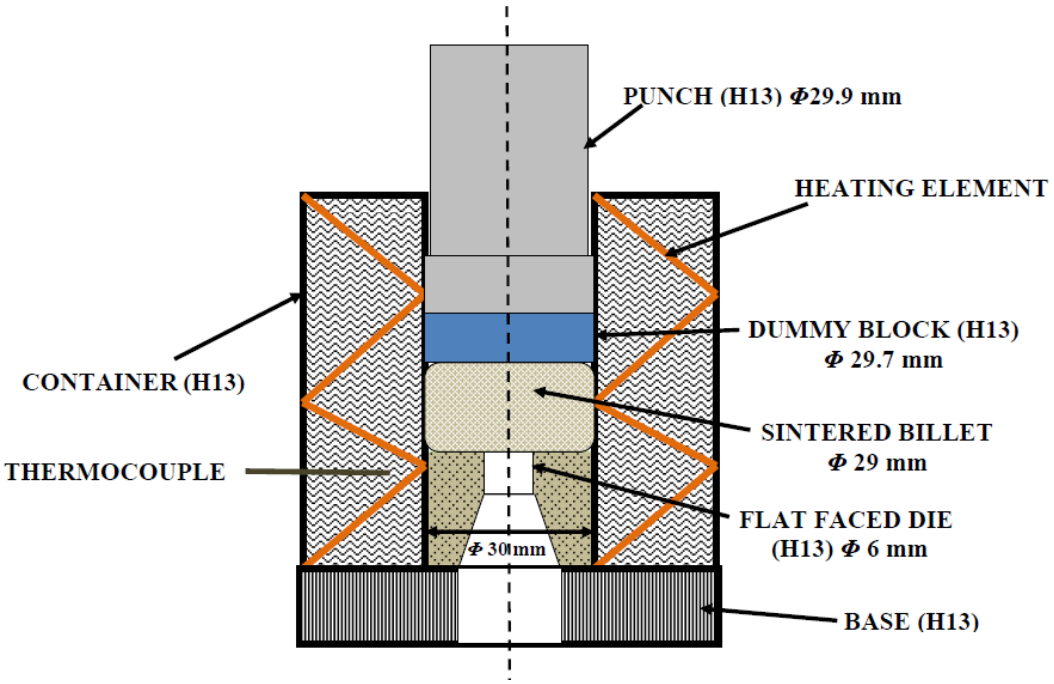

Fig. 4.11 Schematic representation of direct extrusion set-up

Extrusion is a hot working process that entails exposure of hot working temperatures for longer durations by the tooling, in comparison to forging or rolling, consequently H13 hot die steel (AISI Type H13 Hot Work Tool Steel, n.d.) was chosen as the material for fabrication of all major components, as shown in Fig. 4.11, on account of hardenability, hot strength and high temperature tribological characteristics; with average apparent hardness ≥ 55 HRC and a hard chrome surface finish < 1µm. Extrusion die of 30 mm outer diameter and 25 mm height, consisted of a flat faced entry, leading to a straight 4 mm long die-land of 6 mm diameter, thereafter tapering to a 3º included angle. A reduction ratio of 25:1 was thus achieved. Heating of the container and die was achieved by resistance heating elements (1.2 kW) radially embedded in the container wall. Container temperature was controlled by a Chromel/Alumel (K-type) thermocouple placed at a distance of 5 mm from the inner wall of the container, near the top face of the flat faced die. Thermocouple was interfaced with a WEST 6400^{TM} PID controller, having a sensitivity of 1^{o}C. Billets were pre-coated with boron nitride based aerosol coating and heated separately in a laboratory muffle furnace to extrusion temperature, with a 60 min soaking period. Pre-coated container wall, dummy block and die were also heated to extrusion temperature and maintained for 3 h prior to loading of the heated billet. Extrusion was performed under a 60 kN vertical hydraulic press, having a 35 mm circular opening in the base plate to enable uninterrupted downward flow of extrudate. Downward ram movement was maintained till about 80% of billet height, resulting in about 20% of billet as discard in the container. Extrudate was allowed to cool to room temperature, alongwith the container.

Container base was unfastened; extrudate cut at the die base by a hand hacksaw, die, dummy block and billet discard were slowly pushed out under hydraulic load and released from the container. All components were de-flashed by overnight dipping in (10%) caustic soda solution.

4.3.10 Solutionizing and ageing

Compositions (as-sintered/sinter-forged, rolled, extruded) based on AA6061 were solution treated in a laboratory muffle furnace at 515ºC for 2 h and artificially aged (T6) at 177ºC for different durations. Samples were quenched in ice-cold water and quickly transferred to an oil bath (EIE Instruments Ltd., Ahmedabad, India), filled with about 20 l of silicone oil, for ageing. The oil bath was equipped with an agitating fan, Platinum/Rhodium thermocouple (±1ºC sensitivity), and a programmable timer based PID controller (±1 min, upto 99 h cycle).

4.4 Characterization

4.4.1 Determination of particle size of as-received powders

Particle size distribution of aluminium and pre-alloyed powders was determined using Malvern Mastersizer 2000^{TM} (Malvern Mastersizer 2000, n.d.), equipped with Hydro 2000S^{TM} ultrasonic dispersion unit, capable of analysing particles in size range of 60 nm to 1000 µm. The system employs the technique of laser light beam scattering through a dispersed particulate sample. The scattering data is then analysed by the instrument software package to measure size of the the dispersed particles to an accuracy of 1%, as defined by the mean size of a relatevely sharp log-normally distributed powder sample. A known mass of powder sample was ultrasonically dispersed in a 5 ml glass vial with iso-propyl alcohol. The vial was loaded into the analysis chamber of the detector. Particle sizes were reported in µm as D_{10}, D_{50} and D_{90} representing the volume fractions corresponding to percentage distributions, i.e. D_{10} particle size value represents the particle diameter corresponding to 10% cummulative volume of particle size distribution, similarly D_{50} shows the size value for the median (50%) cummulative volume and D_{90} the 90% cummulative volume of overall particle size distribution within the given powder sample.

4.4.2 Sieve analysis of short steel fibers

Short steel fibers were sieved in a tower type motorized sieve shaker, utilizing ASTM E-11 standard sieves of No. (Size of opening): 16 (1.19 mm); 25 (707 µm); 60 (250 µm); 100 (149 µm) and 325 (44 µm). Known weight of cleaned fibers was sieved for 30 min. Size distribution based on weight fraction (%) retained (+) / weight fraction passed (-) was reported as: +16; -16 +25; -25 +60; -60 +100; -100 +325 and -325 (pan).

4.4.3 Powder and fiber morphology

Thin layer of powders was dabbed on conductive carbon stubs to ascretain the shape and morphology of the powders by scanning electron microscopy using ZEISS SUPRA 55VP^{TM} SEM, operated in secondary electron imaging mode with 20 kV accelerating voltage. Cleaned fibers were viewed at higher magnifications for surface morphology and aspect ratio. Powders and fibers were mixed with cold setting phenolic resin (Chennai Metco, 2012); ground and polished as per standard metallographic practice, for imaging of as-solidified sub-structure of powders and as-received as well as surface treated fibers, etched with 2.5% Nital. Polished mounts were imaged at different magnifications using OLYMPUS-D50^{TM} metallurgical microscope.

4.4.4 Determination of oxygen content in powders

Powders were cold pressed into pellets of 10 mm diameter and about 2 g weight. Pellets were cut into 4 roughly equal parts for determination of oxygen content using TC236^{TM} (Leco, USA) oxygen/nitrogen analyzer, equipped with EF-100^{TM} (Leco, USA) electrode furnace, for complete combustion of samples loaded in a graphite crucible. Oxygen content is determined using infra-red detection of CO_2 gas, liberated on crucible and sample combustion; referenced against CO_2 gas liberated on combustion of empty crucible. Electrode current was maintained at 1050 Amp for electric arc melting under a protective cover of pure argon carrier gas, flow maintained at 625 cm^3 min^{-1}. Powder samples, of approx 0.5 gm weight were analyzed and results recorded in ppm (parts per million).

4.4.5 Thermodynamic analysis of powders

Powders were analyzed by DTA (differential thermal analysis) to determine the melting point and onset of liquid formation. Studies were conducted on EXSTAR 6300^{TM}, using approximately 10 mg of powder samples, referenced against 10 mg alumina standard, heated under nitrogen (100 ml min^{-1}) at 10ºC min^{-1} upto 700ºC. Heat flow was recorded in µV.

Heat flow trace in the L+S region was used to determine the appropriate sintering temperature, to enable pre-determined transient liquid volumes for super-solidus liquid phase sintering.

4.4.6 Density

4.4.6.1 Nominal densities of matrix alloys

The inverse rule of mixtures was used to calculate the nominal theoretical densities (ρ_m) of the matrix alloy by converting the given chemical composition in (mass) weight (%) fraction to volume (%) fractions and adding the respective volume fractions of the constituents, using the formula:

$$\rho_m = \frac{100}{(\frac{M_1}{\rho_1}) + (\frac{M_2}{\rho_2}) + (\frac{M_3}{\rho_3}) + ... + (\frac{M_x}{\rho_x})} \qquad \text{(Eq. 4.1)}$$

where (M_1, M_2, M_3….M_x) and (ρ_1, ρ_2, ρ_3… ρ_x) represent (mass) weight fractions and elemental densities of the constituents respectively.

4.4.6.2 Theoretical composite density

The inverse rule of mixtures was extended to compute the theoretical composite density (ρ_c) from the respective weight fractions (%) and theoretical densities of the matrix and reinforcing fibers, using the formula:

$$\rho_c = \frac{100}{(\frac{M_m}{\rho_m}) + (\frac{M_f}{\rho_f})} \qquad \text{(Eq. 4.2)}$$

where (M_m, ρ_m) and (M_f, ρ_f) represent weight fractions (%) and density of matrix and reinforcing fibers respectively.

4.4.6.3 Density of green compacts

Green densities (ρ_g) of cold consolidated green compacts, were estimated by weighing to an accuracy of 0.1 mg using AUW120^{TM} (Shimadzu, Japan) electronic weighing balance (120 g weighing capacity) and dimensional measurements to accuracy of 0.01 mm using MITUTOYO^{TM} (150 mm measuring range) digital vernier caliper. Measurements were repeated on at least 2 identically processed compacts, and average weight and volume values were used to report green densities.

4.4.6.4 Density of sintered compacts

Sintered densities (ρ_s) were determined by water displacement technique (Archimedes's method). Compacts were weighed in air (M_a) and distilled water (M_w) by immersion of the compacts placed on a stainless steel pan, freely suspended by a wire attachment provided at the bottom of the weighing machine (±0.1 mg, AUW120^{TM}, Shimadzu, Japan) in a glass beaker filled with distilled water. Water level in the beaker and depth of immersion of the compact holding pan were kept constant. Measurements were repeated on at least 2 identically processed compacts, and average weights were used to report sintered densities, by using the formula:

$$\rho_s = \frac{M_a}{M_a - M_w} \qquad \text{(Eq. 4.3)}$$

All densities were reported in gcm^{-3}.

4.4.6.5 Densification parameter

Densification parameter (ψ) is a dimensionless parameter, expressed as a percentage number, useful in capturing the effect of net density progression activated by sintering alone, thereby isolating the density gain achieved during prior cold consolidation. Positive values are indicative of density enhancement by sintering, negative values point towards compact expansion. It is calculated as:

$$\psi = \left(\frac{\rho_s - \rho_g}{\rho_t - \rho_g}\right) \qquad \text{(Eq. 4.4)}$$

where ρ_s and ρ_g are sintered and green densities respectively; theoretical density ρ_t corresponds to ρ_m and ρ_c for monolithic alloys and composite formulations respectively.

4.4.7 Microstructure

4.4.7.1 Sample preparation

Sintered and secondary processed compositions were sectioned along required planes by precision cutting saw, ISOMET 4000^{TM} (Buehler, USA), sections were mounted in 20 mm diameter cold setting phenolic resin based quick hardening compound (Chennai Metco, 2012). Mounted samples were hand ground on 240, 600, 800, 1200, 1500 and 2000 standard grit SiC papers (3M^{TM}, India). Grinding lay was turned over by 90º after each paper. Care was taken to frequently dip the ground surface in kerosene oil, to ensure release of SiC particles from the

soft aluminium matrix. Ground samples were ultrasonically cleaned in distilled water for manual polishing using an aqueous suspension of fine magnesium oxide (heavy) (99% purity, Loba Chemie, Mumbai, India) on open-nap (rough) billiards cloth, followed by another polishing cycle on closed-nap (fine) billiards cloth, mounted on 8" diameter aluminium discs, rotating at 150-200 rpm. Mounts were finally cleaned ultrasonically in distilled water.

4.4.7.2 Etchants and optical micrography

As- sintered compositions were examined without application of any etchant, for better resolution of pore size, distribution and morphology. To enable resolution of prior particle boundaries (PPB's) of the aluminium based matrices, different etchants were employed. Keller's reagent (95 ml H_2O, 2.5 ml HNO_3, 1.5 ml HCl, 1.0 ml HF) applied by a cotton swab, was most effective in revealing PPB's and sub-particle grains for Al-0.5 Wt.% Mg based compositions. Modified Poulton's reagent (50 ml solution of HCl, HNO_3, HF and H_2O in ratio 12:6:1:1 respectively, mixed with 12 g Chromic acid solution in 25 ml HNO_3 and 40 ml H_2O) was used for AA6061. Optical microscopy was performed on DMI5000M^{TM} (Leica, Germany) and D50^{TM} (Olympus, Japan) metallurgical microscopes, having 1000X and 2000X maximum compound magnifications respectively with facility for image digitization and capture. Samples etched with modified Poulton's reagent were viewed under polarized light with color sensitive tint.

4.4.7.3 Analysis of reaction interface

A more detailed evaluation of the morphology and chemistry of the interfacial region between the aluminium matrix and steel fibers was carried out using LEICA S440^{TM} and ZEISS SUPRA 55VP^{TM} scanning electron microscopes equipped with Oxford EDAX^{TM} (energy dispersive X-ray- EDS) detector. An accelerating voltage of 20 kV was applied for both secondary and back scattered electron modes, suitable delay and bias was adjusted for elemental mapping over selected areas or along linear trajectories. As required, similar regions were scanned and average values were reported.

4.4.7.4 Analysis of recrystallization by EBSD

As-forged monolithic composition of AA6061 were analyzed for PPB dissolution, grain orientation and estimation of number fraction of grains attaining complete or partial recrystallization by EBSD (electron backscattered diffraction). EBSD analysis was performed on FEI, Quanta 200F^{TM} FESEM (field emission scanning electron microscope) using TSL-OIM^{TM} (orientation imaging microscopy) analysis version 4.6 software (TEXSEM laboratories

Inc., USA). Polished samples, developed by standard metallographic practice (*Section 4.4.5.1*) were electropolished at -15ºC in a 80-20 (vol.%) solution of methanol and perchloric acid at 11 V DC potential, for sufficient time to strip the mechanically polished layer. EBSD scans employed a step size of 0.1 μm.

4.4.8 Analysis of phases by X-ray diffraction

Phases evolved by surface modification of short steel fibers and interfacial reaction products formed during sintering of different composites were identified by X-ray diffraction (XRD) analyses using a Panalytical X'Pert Pro™ diffractometer. Samples were exposed to CuK_{α} radiation (λ=1.5406 Å) at 40 kV and 30 mA settings, employing a step size of 0.02° per step, over a 2θ range of 20-120º. Diffraction patterns based on inter-planar spacing (*d* values) and relative intensities (I/I^o) for respective 2θ values were analysed by X'Pert HighScore™, desktop based analysis package, against standard ICDD™ (International Centre for Diffraction Data) version PDF-4™ (powder diffraction file) database.

4.4.9 Mechanical behavior

4.4.9.1 Hardness

Microhardness measurements were conducted on as-received and surface modified short steel fibers. To determine the effect of reinforcement content on the different matrices, hardness of matrix, unreacted reinforcement and the reaction interface was systematically measured for the composites using FutureTech FM-700™ (Japan) Vickers microhardness tester at 10-50 g load for 15 s dwell time. Average of 5 measurements was reported for each zone in VHN. Apparent hardness (Vickers) values for monolithic and composite samples were recorded at 5 Kg load for 15 s dwell time using VM50™ (FIE Instruments, India) hardness testing machine. Average of 5 measurements was reported for each composition in VHN. Standard hardness test block (RTA™, India) was used to calibrate the instruments prior to testing of samples. Test surfaces were parallel and polished to 2000 grit finish by using SiC grinding papers. Distance between successive indents was maintained at more than 5 times the indent diagonal.

4.4.9.2 Compression

In order to ascertain the damage evolution and failure mechanism as a function of reinforcement content at room and elevated temperature, 20 mm x 5 mm (h/d = 0.4) as-sintered discs of Al-0.5wt.% Mg based compositions were tested in compression at room temperature and 250°C using MTS ™ 385kN and MTS ™ 100 kN compression test frames respectively. Specimens were heated at 25°C min^{-1} with a clamshell type infrared heating attachment and

held at test temperature for 10 min prior to loading at a crosshead velocity of 1mm min^{-1}. Tested specimens were prepared along the pressing plane for metallographic examination. Cylinders of size 6 mm diameter x 9 mm height (*h/d* = 1.5) were machined out of forged briquettes of Al-0.5wt.% Mg and AA6061 compositions for room temperature compression tests on H25K-S^{TM} (Housnfield) 25kN universal test frame at a cross head velocity of 1mm min^{-1}. Test samples were wrapped in PTFE tape, to ensure a uniform coefficient of friction between the sample and compression platens. Load (*P*) in N and ram displacement (Δh) in mm, logged for compression tests was converted to true stress (σ) MPa and true strain (ε) using the following relations, (Cavaliere, 2007):

$$\sigma = \frac{P(h_O - \Delta h)}{A_O . h_O} \qquad \text{(Eq. 4.5)}$$

$$\epsilon = \ln\left(\frac{h_O}{h_O - \Delta h}\right) \qquad \text{(Eq. 4.6)}$$

where, where A_O and h_O denote the initial cross-sectional area and the height of the sample, in mm^2 and mm and respectively.

Flow stress behaviour in compression for monolithic and reinforced compositions, of cylindrical specimens 6 mm diameter x 9 mm height (*h/d* = 1.5), machined out of forged briquettes, was characterized on GLEEBLE 3800^{TM} thermomechanical simulator (*Section 4.3.5.2*) at a constant true strain rate of 0.01 s^{-1} for 0.5 true strain at 250ºC, between tungsten-carbide platens. True-stress and true-strain was logged alongwith axial contraction of the specimens (±1 µm sensitivity) at 100 s^{-1} data acquisition rate. Chromel/Alumel thermocouple was welded to the center of the specimens for temperature control (ramp-up rate 5ºCs^{-1}, 5 min hold before compression). Tested specimens were sectioned along the longitudinal axis for metallographic examination.

4.4.9.3 Flexure

Flexure strength of as-sintered and sinter-forged compositions based on Al-0.5wt.% Mg matrix was determined by 3-point bend test on centrally loaded 40 mm × 8 mm × 3 mm flat specimens against roller supports, 25 mm apart, on H25K-S^{TM} (Housnfield) 25kN universal load frame, operated at a crosshead speed of 0.001mms^{-1}. Load-displacement data was reported.

4.4.9.4 Tension

Tensile specimens of dumbbell shape, as shown in Fig. 4.12, were machined from sinter-forged briquettes conforming to different matrices and heat treated conditions. Nominal gauge dimensions were fixed at 25 mm length x 6 mm diameter. Samples were polished to remove any tool markings. Flat specimens of nominal gauge dimension 20 mm x 4mm x 2 mm, as shown in Fig. 4.13, were punched out from rolled strips using a shaped die, operated in a hand press.

Dumbbell type tensile test pieces were extracted by machining from extruded rods, having nominal gauge dimensions of 25 mm length x 4 mm diameter. All tests were conducted by secure placement of test pieces in suitable grips, to avoid any slippage, using H25K-S^{TM} (Housnfield) 25kN universal load frame, at a constant crosshead velocity of 1 mm min^{-1}.

Fig. 4.12 Tensile test pieces machined from sinter-forged briquettes

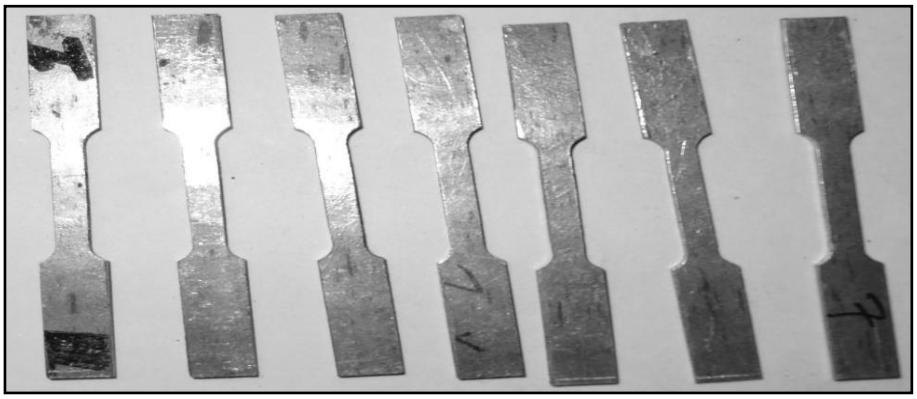

Fig. 4.13 Tensile test pieces punched-out from rolled strips

Load (N) and displacement (mm) logged by the interfaced computer was converted to engineering stress-strain. At least 2 samples were tested for a given composition and processing condition. Analysis of fracture surfaces was conducted using ZEISS SUPRA 55VP^{TM} scanning electron microscope for surface topology and matrix-reinforcement interactions.

4.4.10 Wear behavior

4.4.10.1 Ball-on-disc test configuration

The 20 mm diameter x 5 mm thick sintered discs, conforming to Al-0.5wt.% Mg based compositions with 0, 10, 20 and 30 wt. % steel fibers were ground to 1200 grit and ultrasonically cleaned with ethanol for room temperature and 250°C wear tests on CSM Instruments ^{TM} (www.csm-instruments.com, Switzerland) high temperature tribometer, using ball-on-disc configuration. AISI 52100 Cr-steel ball of 6 mm diameter having a hardness of 60 HRC was held against sample disc under 1N normal load, as shown in Fig.4.14. The disc was rotated at 0.1 ms^{-1} relative to the ball, creating a circular wear track. All tests were conducted unlubricated, in air, at 20-25°C ambient temperature; 45-55% relative humidity, for a 500 m sliding distance. A soaking period of 20 min was given, for samples to attain thermal equilibrium prior to commencement of tests at 250°C. The tribometer was equipped with a data acquisition system capable of time synchronous logging of coefficient of friction (±0.1 N), ball penetration depth (±1 µm) and disc temperature (±0.1°C) at 1 s^{-1} acquisition rate. Cross sectional surface scanning of the wear scars was performed using Talysurf-50^{TM} (Taylor Hobson, UK) profilometer, having a 2µm tip-radius, conisphere diamond stylus, which sampled data at 1 µm intervals. The line scan data was used to calculate the area of the wear scar using ORIGIN Pro-8^{TM}, from which wear volume was determined.

Weight loss was determined to an accuracy of 0.1 mg. For understanding of wear mechanism, wear debris were preserved and wear tracks were analyzed by scanning electron microscopy (ZEISS SUPRA 55VP^{TM}).

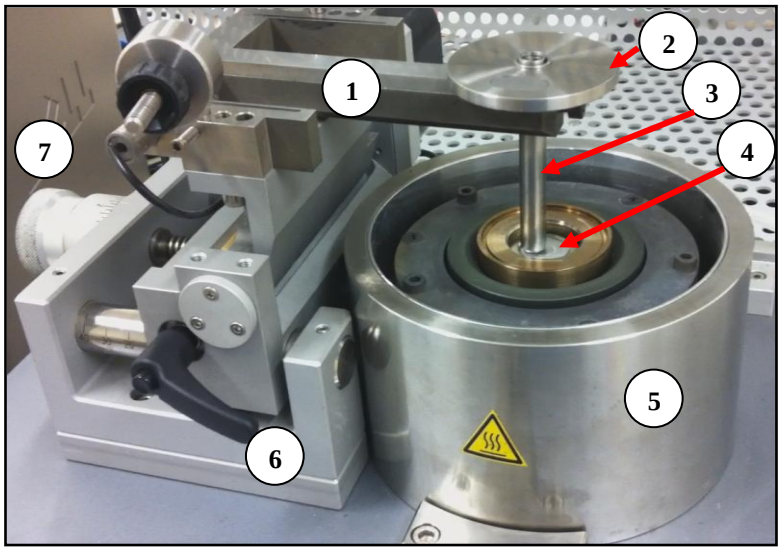

Fig. 4.14 Image showing CSM^{TM} high temperature tribometer test arena (1) Arm (2) Weight (3) Ball holder (4) Sample disc (5) Heating pot (6) Locking lever and (7) Track radius set screw

4.4.10.2 Pin-on-disc test configuration

Test pins of 6 mm diameter x 25 mm height, with hemispherical ends (3 mm diameter) were machined out of sinter-forged Al-0.5wt.%Mg, AA6061 and AA7075 based compositions for dry sliding wear tests against hardened steel counterface disc (58 HRC), using TR-201E-M2^{TM} (Ducom, Bangalore, India), pin/ball-on-disc tribometer, as shown in Fig. 4.15. Specifications of the tribometer are detailed in Table 4.4.

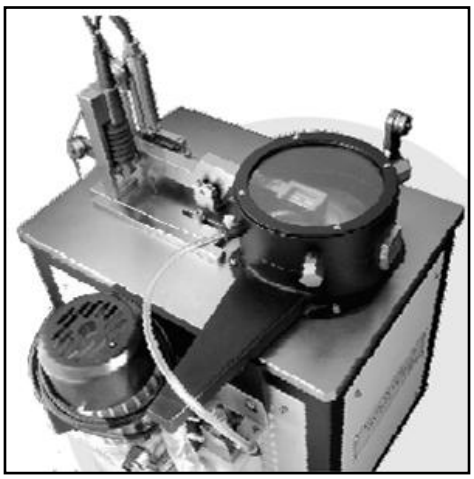

Fig. 4.15 Ducom TR-201E-M2^{TM} tribometer

Table 4.4 Specifications of Ducom TR-201E-M2™ tribometer

Attribute	Value
Diameter of wear disc	100 mm
Pin/ball diameter	3-10 mm
Pin/ball holder length	20-30 mm
Wear track diameter	0-80 mm
Disc rotation speed	200-2000 rpm (± 1%)
Normal load	10-100 N (in steps of 5N)
Friction force limit	0-100 N (resolution 0.1N, ± 1%)
Timer	99/59/59 (h/min/s)
Wear range	2000 µm (resolution 1 µm, ± 1%)

Wear tests were conducted at 10, 20 and 30 N normal loads and 1 m s^{-1} sliding velocity. To ascertain the effect of sliding speed on wear behavior, pins were tested at 20 N and 2 m s^{-1}. Sliding distance was fixed at 1500 m for all test runs. The tribometer was interfaced with a continuous data logging software, WINDUCOM-2000™, (Ducom, Bangalore, India); which logged frictional force and pin height loss at 1 s^{-1} frequency. Cumulative wear volume loss was determined in accordance with ASTM G99-05 (2010); standard test method for wear testing with a pin-on-disc apparatus. The standard specifies the calculation of pin volume loss as below:

$$Pin\ volume\ loss\,(mm^3) = (\pi \frac{h}{6})[3\frac{d^2}{4} + h^2]$$
$$where:$$
$$h = r - [r^2 - d^2/4]^{1/2}$$
$$d = wear\ scar\ diameter\,(mm)$$
$$r = pin\ end\ radius\,(mm) \qquad \text{(Eq. 4.8)}$$

Wear scar diameter was measured by a travelling microscope (Radical Instruments, India), equipped with a 10X eyepiece, to an accuracy of 0.01 mm. Wear rate (volumetric) was reported in (mm^3 m^{-1}). Weight loss was determined to an accuracy of 0.1 mg. For analysis of wear mechanism, wear debris were preserved for analysis and wear tracks were analyzed by scanning electron microscopy (ZEISS SUPRA 55VP™) equipped with OXFORD EDAX™ energy dispersive x-ray spectroscopy (EDS) detector.

4.4.11 Coefficient of thermal expansion (CTE)

CTE of cylindrical pins (6 mm diameter x 9 mm length) machined from sinter-forged briquettes was determined in 25-350°C temperature range, under a linear 10°C min^{-1} heating rate using horizontal push rod type L76-PLATINUM^{TM} (Linseis, Germany) dilatometer. Pure argon gas flow rate was maintained at 1 $lmin^{-1}$ (±0.2 $lmin^{-1}$). Specimens were loaded in between an alumina piston and back support, at 300 mN contact load. A correction cycle for eliminating dimensional changes in the sensor probe was run and subtracted from experimental outputs. Absolute and relative changes in sample length were logged with time and temperature at $1s^{-1}$ intervals. The expansion curve was linearly fitted to evaluate the CTE using ORIGIN Pro-8^{TM} plotting and data analysis package.

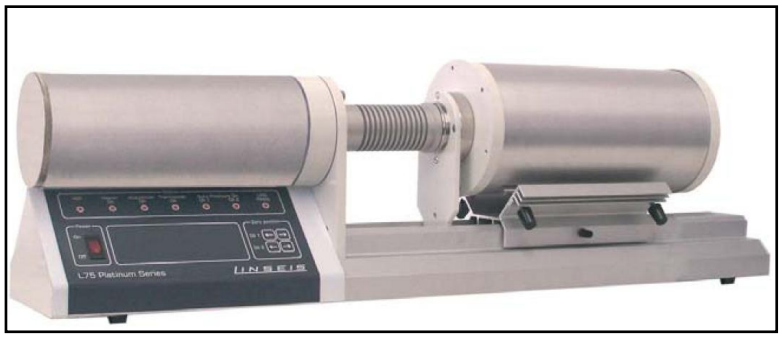

Fig. 4.16 L76-PLATINUM^{TM} (Linseis, Germany) horizontal push rod type dilatometer

4.4.12 Process Flow Charts

The detailed flow charts, including major processing steps as well as characterization tools employed at various stages of the research work are shown in Fig. 4.18 (pure aluminium matrix) and Fig. 4.19 (AA6061 matrix).

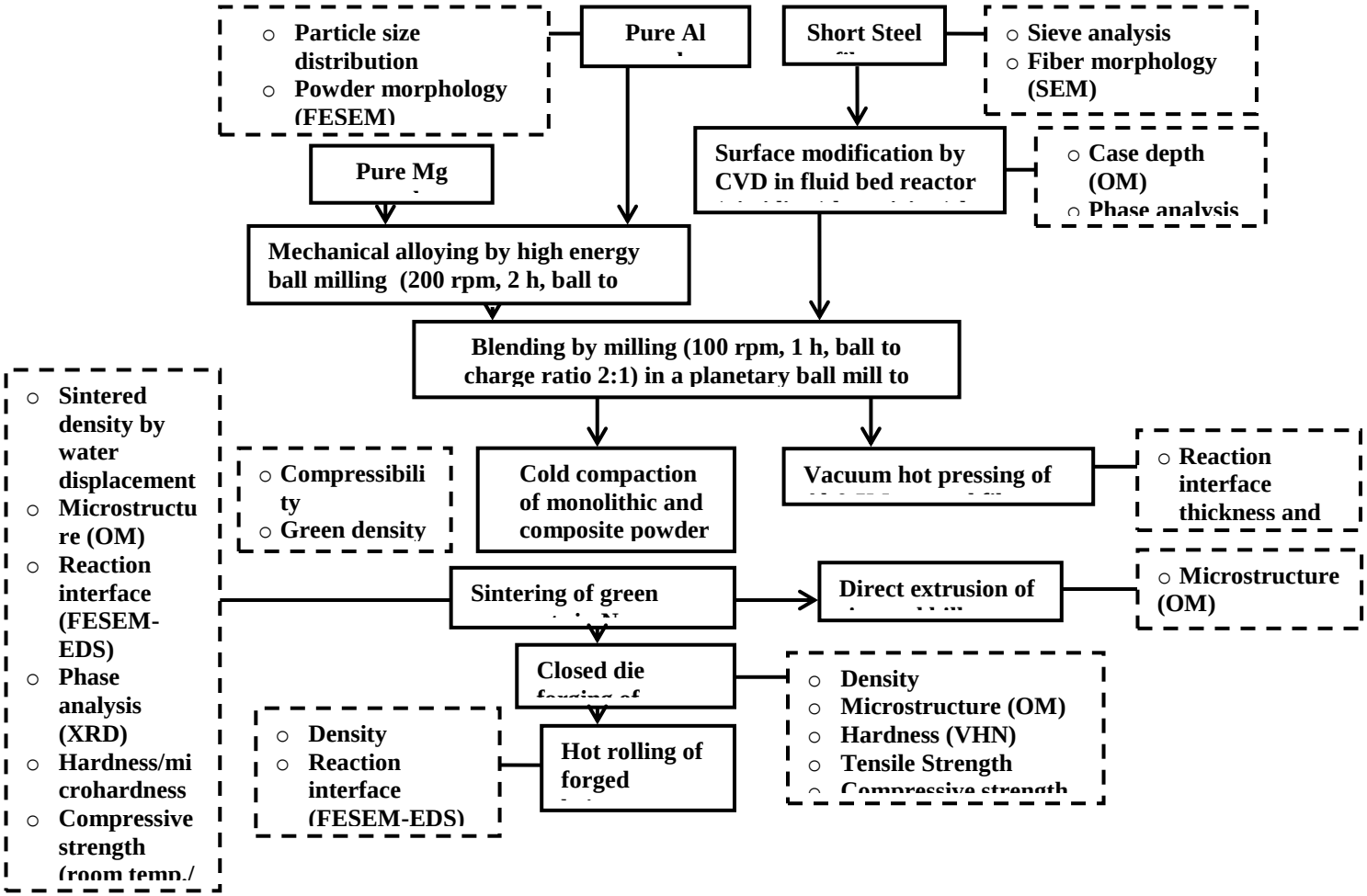

Fig4.17 Research methodology for pure aluminium based composites

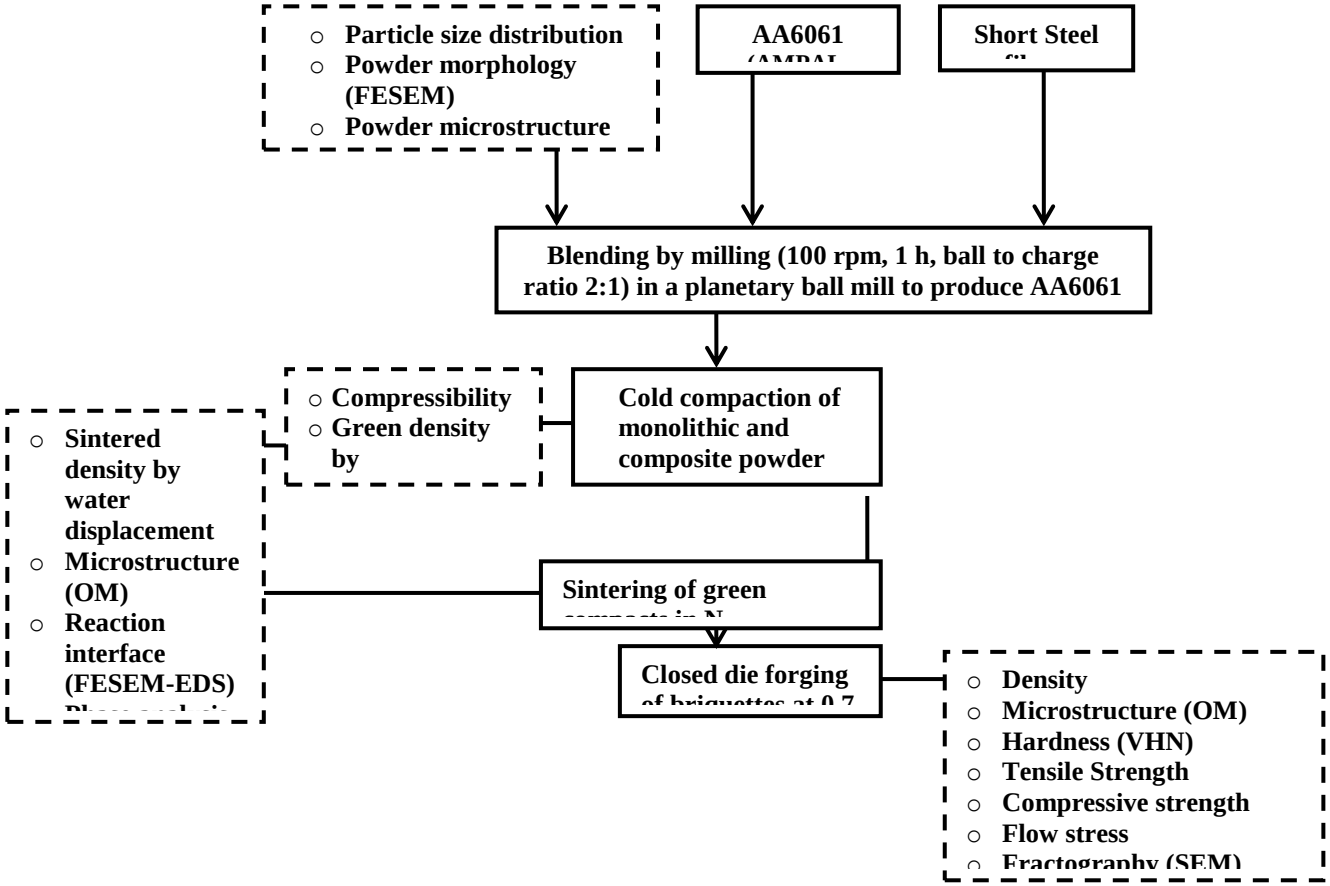

Fig. 4.18 Research methodology for AA6061 based composites

Chapter 5
RESULTS AND DISCUSSIONS

5.1 Introduction

Characterization of as-received short steel fibers is presented first, followed by determination of interface growth kinetics under simulated hot pressing conditions. Effect of surface modification of short fibers on fiber properties and characterization of reaction interface formed with aluminium matrix is investigated. Development and characterization of composites based on pure aluminium and AA6061 matrices, covering sintering and secondary consolidation by forging, rolling and extrusion is covered separately for respective matrix alloy system. Comparison of critical properties of matrices and their composites is made at the end of the chapter.

5.2 Characterization of As-received short Steel Fibers

5.2.1 Morphology, microstructure and hardness

Short steel fibers of nominal chemical composition as described in *Section 4.2.2*, Table No. 4.3, are generally used as a reinforcement and coefficient of friction modifier in phenolic resin based automobile brake pads (Jang, et al., 2004). The 0.38 wt.% C steel fibers are manufactured on an industrial scale by machining of steel blocks (Nakagawa et al., 1980) or by melt spinning (Markaki, et al., 2003). Both the fabrication methods result in a "kidney" like near semi-circular cross section, with slight variation along the fiber length. By the metallographic examination of the fiber sub-structure, the fabrication method can be ascertained. Fine equiaxed microstructure is obtained by melt spinning; whereas an excessively cold-worked chip like morphology results from machining. Fibers are batch classified as coarse or fine according to nominal diameter and length.

Fine fibers having a nominal diameter of 50 μm and upto 1.50 mm length (average aspect ratio 30) were selected for the present study, as shown in Fig. 5.1 (a). The outer surface was convex, Fig. 5.1 (b), with a concave inside surface, Fig. 5.1 (c), having chip like features. On close examination of the inside surface, striations were visible, Fig. 5.1 (d). This roughness, generated by machining, is preferred to provide extra "ancourage" of short fibers in the matrix.

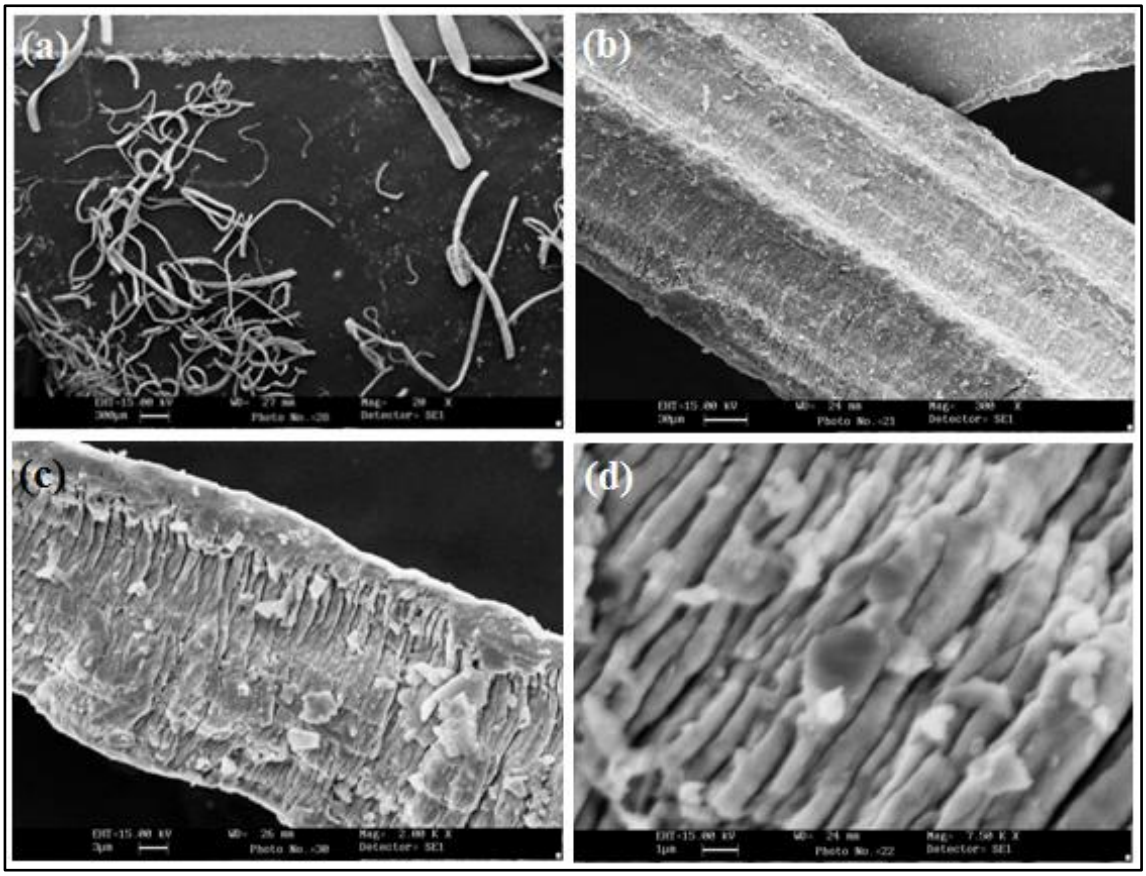

Fig. 5.1 Scanning electron micrographs of short steel fibers

A schematic representation of the "kidney" shaped fiber cross-section is shown in Fig. 5.2(a). To facilitate mathematical evaluation of fiber cross-sectional area (Pemberton et al., 2011) have suggested a transformation of the "kidney" shape to a regular circle of radius *R* of equivalent cross-sectional area as shown if Fig. 5.2 (b).

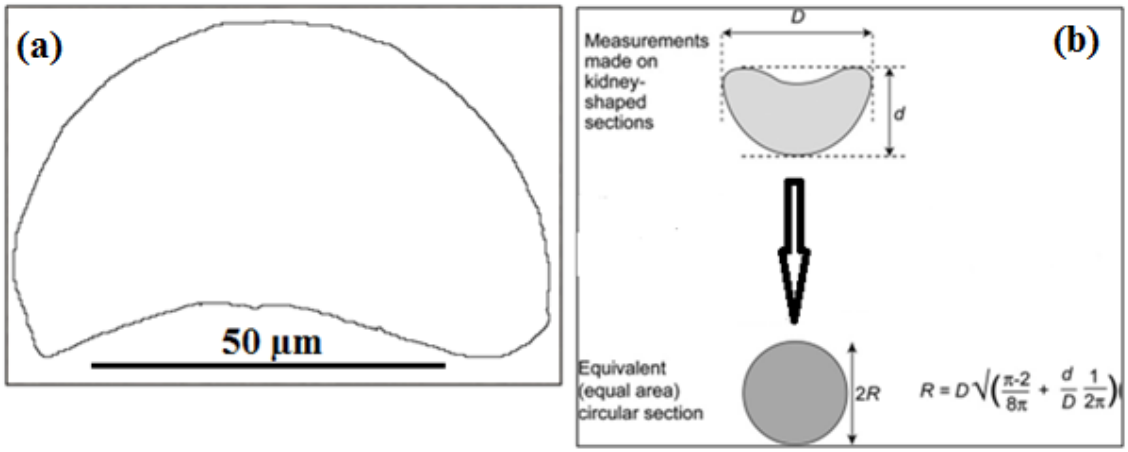

Fig. 5.2 (a) Schematic outline of the short fiber cross-section and (b) representation of fiber cross-section with an equivalent circle (Pemberton et al., 2011)

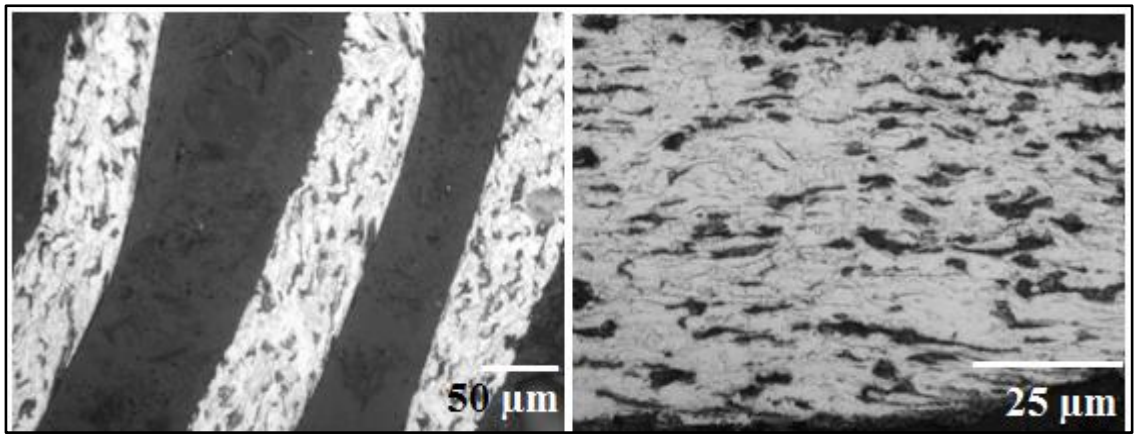

Fig. 5.3 Microstructure of short fibers, etched with 2.5% Nital

Fiber microstructure revealed by etching with 2.5% Nital, was found to be composed of cold worked, largely ferrite matrix with pearlite grains Fig. 5.3. Wavy features, a result of high strain rate shear, indicative of machining process, were visible in the fiber sub-structure. Microhardness of as- received fibers was determined to be 235±10 HV.

5.2.2 Size distribution of short steel fibers

Analysis of short fiber size and overall size distribution is difficult using standard sieving methods, shortcomings of sieving fibers have been enumerated upon by (Bath, 2003). Standard sieve analysis method for asbestos fibers has been promulgated by ASTM under D2947/D2947M-88 (ASTM International, 2006). The same procedure was followed using standard ASTM: E-11 sieves for 30 min duration. The results are presented in Table 5.1. Sieve-wise separation was also used to segregate large fibers retained upto +100 (250 µm), which were discarded.

Table 5.1 Sieve analysis of as-received short steel fibers

ASTM Sieve Number	Size (µm)	% retained (30 min)
+16		Nil
-16 +25	1190	2
-25 +60	707	3
-60 +100	250	15
-100 +325	149	35
-325 (Pan)	44	45

5.2.3 Physical and mechanical properties of short steel fibers

As per the nominal chemical composition provided by the manufacturer, short steel fibers conform to AISI 1035 grade steel. Some characteristic physical properties of AISI 1035 steel are tabulated as below.

Table 5.2 Physical and mechanical properties of short steel fibers (ASM International, 1990)

Theoretical density (ρ_t)	7.85 g cm^{-3}
Coefficient of thermal expansion (20-300ºC)	11.9 x 10^{-6} C^{-1}
Elastic modulus	200 GPa
Poisson's ratio	0.29
Ultimate tensile strength	565 MPa
Yield strength	370 MPa

5.3 Characterization of Pure Aluminium Powder

5.3.1 Particle morphology, size distribution and substructure

Pure aluminium powder of nominal chemical composition as shown in *Section 4.2.1*, Table No. 4.1 was used. Particle morphology of pure aluminium powder was composed of large ligamental and small spherical particles, as shown in a representative micrograph (Fig. 5.4).

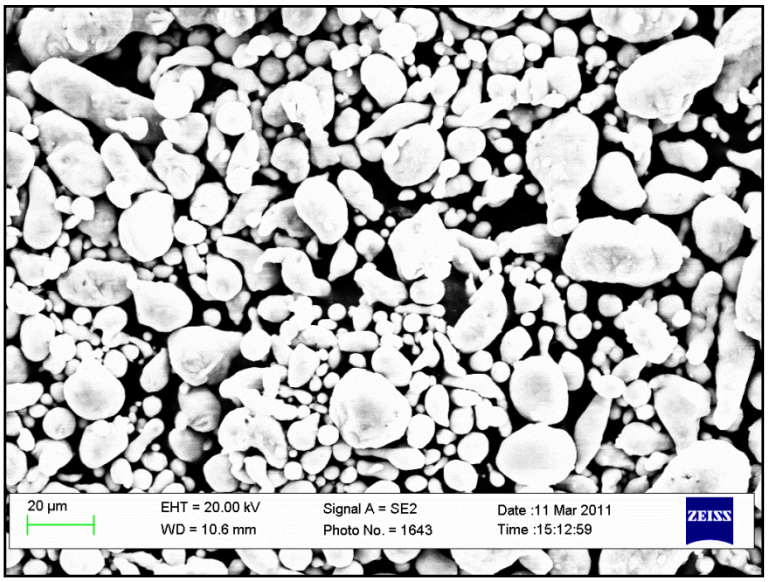

Fig. 5.4 Scanning electron micrograph of pure aluminium powder

Particle size distribution, as determined by laser scattering technique, was D_{10} -5.4 µm, D_{50} -20.4 µm and D_{90} -50.3 µm. Volume fraction-wise particle size distribution is shown in Fig. 5.5. The required average particle size was 45 µm, which was satisfied by the range of the sample (D_{90}- D_{10} = 45.8 µm); however, a certain level of bi-modality observed under SEM was confirmed by calculating the span (D_{90}- D_{10}/ D_{50}) of the given sample. A span value of unity, signifies a perfectly unimodal particle size distribution. In the present case, a span value of 2.2 does indicate sufficient bi-modality in the sample. Some degree of bi-modality is found to be favorable in particle packing during cold compaction of ductile powders. For mildly bi-modal powders, higher green densities are achieved by filling-up of interstitial sites between large particles by smaller particles, at relatively lower compaction pressures (Oberacker, 2011).

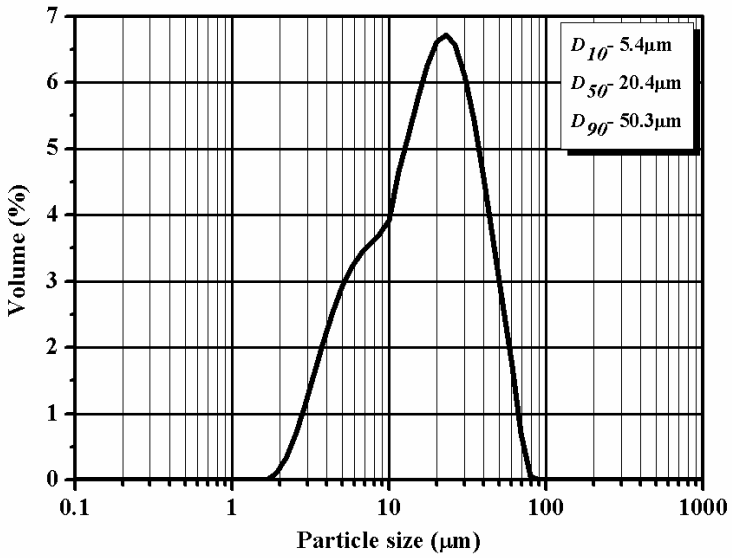

Fig. 5.5 Particle size distribution of pure aluminium powder

Powder particle sub-structure was revealed after metallographic examination under light optical microscope (LOM), as shown in **Fig. 5.6**. Powder particles displayed a characteristic rapidly solidified, fine grained structure. Aluminium powder is produced by inert gas atomization of a melt stream; generally nitrogen is preferred, helium and argon based atomization is also reported. Typical cooling rates range upto 10^{-3} K s^{-1}(Lavernia & Srivatsan, 2009). A small amount of oxygen is also bled into the atomizing chamber to chemically stabilize the otherwise highly reactive freshly formed aluminium powder particles (Ünal, 1990). Oxygen helps in forming an oxide covering (maximum 10 nm thick) on the powder particle, rendering it safe for storage and handling.

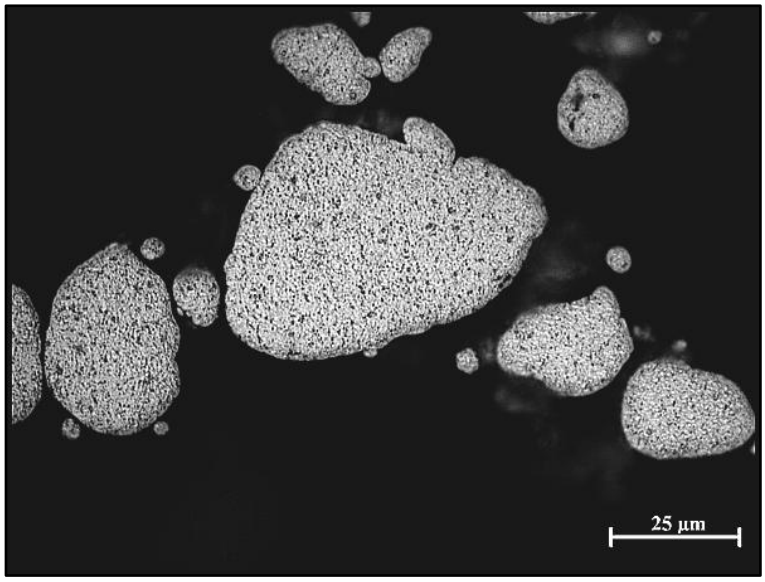

Fig. 5.6 Optical micrograph of aluminium powder particles

5.3.2 Oxygen content

Oxygen content was determined as 1647±57 ppm (~ 0.16 wt.%). Oxygen content is an important factor in determining the sinterability of the aluminium powder. Evidently, gas atomized powders have lower oxygen content than air atomized powders, which translates to a thinner oxide layer over the powder particles. (Ünal, et al., 1998) have shown that air atomized samples can contain upto 1.0 wt.% of oxygen with upto 10 nm thick oxide layer, compared to a maximum of 0.2 wt.% of oxygen and 4 nm thick layer for inert gas atomized aluminium powders of the same size. Sphericity of the powder particle is also a function of total oxygen content and thereby dependent on atomizing environment. Inert gas systems generate more spherical particles in contrast to air atomization which produces irregular shape of particles, having a higher specific surface area (Ünal, 1990).

Commercial powder production technologies are proprietary in nature, and not easily available in open literature. Based on the oxygen content of the powder sample, it can be said with confidence that the batch analyzed was inert gas atomized.

5.3.3 Microhardness

As-received powder particles had a microhardness of 29±2 HV. Degassing treatment in a vacuum oven (10^{-2} torr) at 250ºC for 2 h duration, followed by annealing to room temperature under vacuum, resulted in softening of the particles to 24±1 HV.

5.3.4 Physical properties of pure aluminium powder

Some important physical properties of inert gas atomized pure aluminium powder have been tabulated as below:

Table 5.3 Physical properties of pure aluminium powder (Ünal, et al., 1998)

Theoretical density (ρ_t)	2.70 g cm^{-3}
Melting point	660ºC
Apparent density	0.80-1.30 g cm^{-3}
Tap density	1.20-1.50 g cm^{-3}
Oxygen content	< 0.2 wt.%
Coefficient of thermal expansion	22.2 x 10^{-6} C^{-1}

5.4 Vacuum Hot Pressing (VHP) of Pure Aluminium based Compositions

5.4.1 Blending

The short steel fibers were cleaned with acetone, dried in an oven, and hand-mixed with aluminium powder. The mixture of aluminium powder with 5, 10 and 15 wt.% short steel fibers was further blended in a horizontal tumble jar mill, using ceramic balls of 16mm diameter, with a ball to composite weight ratio of 1:1. A low ball to charge ratio was maintained to avoid fiber damage; a uniform distribution of de-agglomerated fibers was obtained after 2 h of milling at 80 rpm. As received, aluminium powder was also subject to the same milling cycle. Details of further processing steps i.e. cold consolidation followed by vacuum hot pressing are presented in *Section 4.3.5.2*.

5.4.2 Green density

Effect of compaction pressure on relative green density (ρ_g/ρ_t), where ρ_g, denotes the absolute green density, for pure aluminium powder is shown in Fig. 5.7. A typical compaction curve for ductile metal powders, which is characteristic of higher density gradient at low compaction pressures, followed by flattening out of green density with increasing compaction pressures is observed. Particle rearrangement and release of entrapped air at low compaction pressures followed by shear deformation and formation of outer retaining skin under the effect of die wall friction leading to particle-particle mechanical interlocks at intermediate pressures and finally attainment of quasi-hydrostatic stress conditions at higher pressures, is reported to be responsible for distinct density regimes observed in uniaxial compaction of ductile metal powders (Oberacker, 2011).

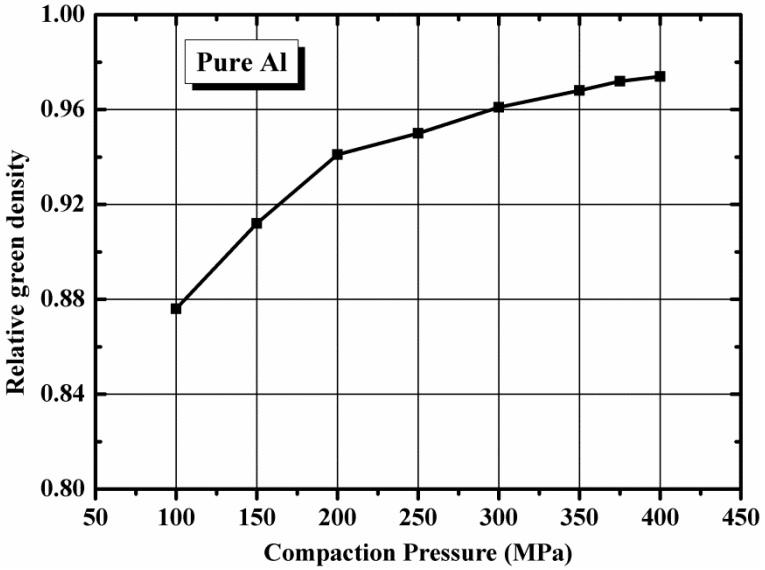

Fig. 5.7 Effect of compaction pressure on relative green density of aluminium powder

Effect of compaction pressure on relative green density of Al-5wt.% steel fiber composite blend has been shown in Fig. 5.8. Uniaxial cold compaction can be described as a two-stage process wherein compaction is followed by relaxation on account of elastic recovery. The high elastic modulus of short steel fibers relative to aluminium matrix aids in relaxation due to higher elastic recovery. At the targeted compaction pressure of 375 MPa, almost a 4% deficit in relative green density of the composite was observed against pure Al. The fibers also act as barriers to formation of inter-particle bonds between aluminium powder particles (ter Haar & Duszczyk, 1992). However, the higher specific hardness of the fibers may have promoted particle rupturing and thereby shearing of hard alumina layer on irregular aluminium particles during cold compaction.

Similarly, an increase in porosity is observed with increasing reinforcement content (*R*) from 5- 15 wt.% at 375 MPa as shown in Fig. 5.9. A near-linear fit was obtained for decreasing relative green density, given by equation (5.1):

$$(\rho_g / \rho_t) = 0.97114 - 0.0106(R) \quad \ldots\ldots\ldots\ldots\ldots (5.1)$$

In the present case, the effect of steel fibers in hindering powder particle packing under applied consolidation pressure could be the major factor in increased porosity level with increasing short fiber content. The aspect ratio (*l/d*) of the green compacts was targeted as 2; density gradients that usually exist in uniaxially cold compacted preforms, which could also be a contributing factor for increased porosity.

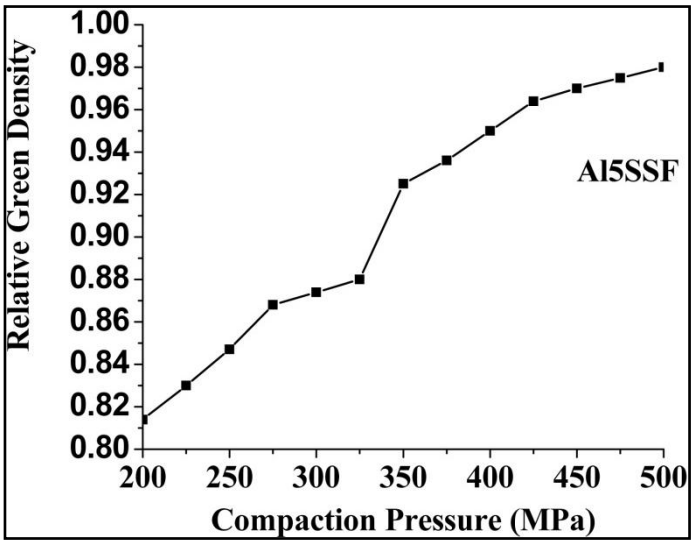

Fig. 5.8 Cold compaction behavior of Al-5wt. % short steel fiber composite blend

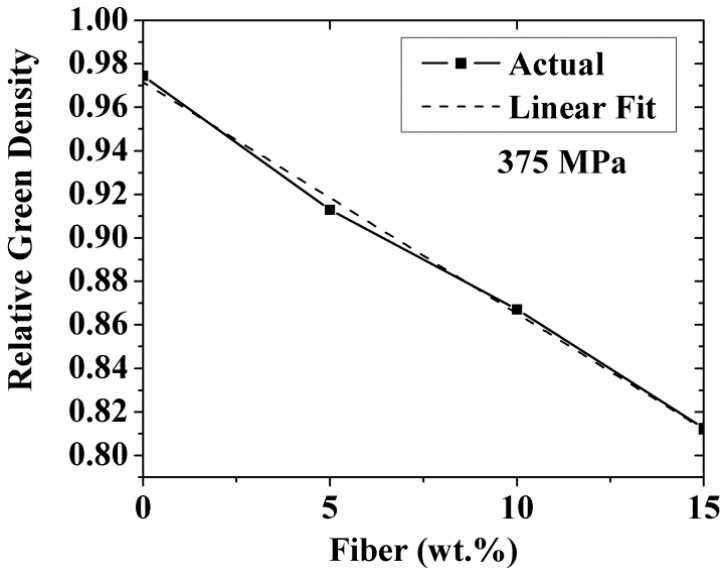

Fig. 5.9 Effect of reinforcement content on relative green density of compacts

5.4.3 Vacuum hot pressed density

The cylindrical green specimens, conforming to unreinforced and reinforced compositions were vacuum hot pressed along the major axis of the cylinder, bi-axially. The ram stroke displacement was used to determine the expansion or contraction events during the complete cycle. During initial period of the VHP cycle, the specimen was heated at $5^{o}C\ s^{-1}$, a net thermal expansion was observed for the heating duration followed by a net contraction of the specimen under hot pressing stress which reached a maximum value of 50 MPa at the end of the cycle. As shown in Fig. 5.10, for Al-5wt.% short steel fiber composite**.** The net contraction of the

green compact was higher than the initial thermal expansion; hence, a net densification of the green compact was aided by VHP.

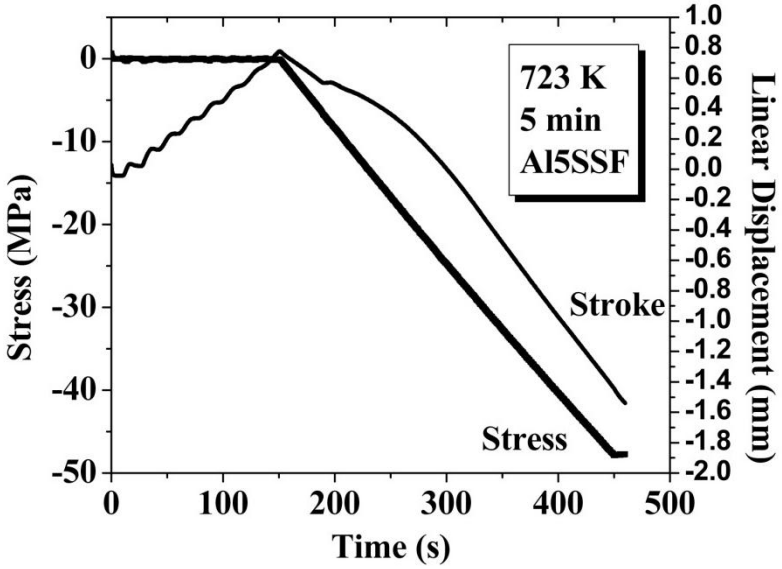

Fig. 5.10 Linear contraction of the specimen under hot pressing stress

Density increments for VHP compacts were dependent on initial green density, which was a function of short fiber content. Diffusion, plastic flow, and power-law creep have been reported as the dominant mechanisms for densification by hot pressing (Kim, 2008). Relative hot pressed density (ρ_s/ρ_t), where ρ_s denotes the absolute hot pressed density, decreased with increasing fiber weight fraction, as shown in Fig. 5.11. Relative hot pressed density was found to follow a linear dependence on short fiber content, given by equation (5.2):

$$(\rho_S / \rho_t) = 0.99162 - 0.00832(R) \quad \text{.....(5.2)}$$

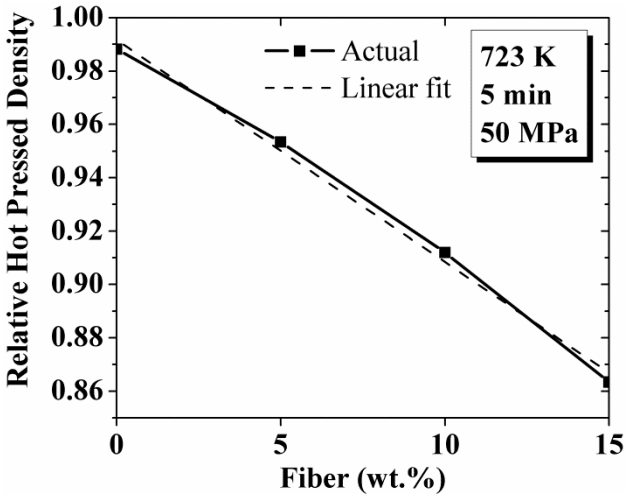

Fig. 5.11 Effect of reinforcement content on relative VHP density

The effect of VHP on densification of green monolithic and composite preforms has been evaluated by densification parameter, as shown in Fig. 5.12, for all compositions.

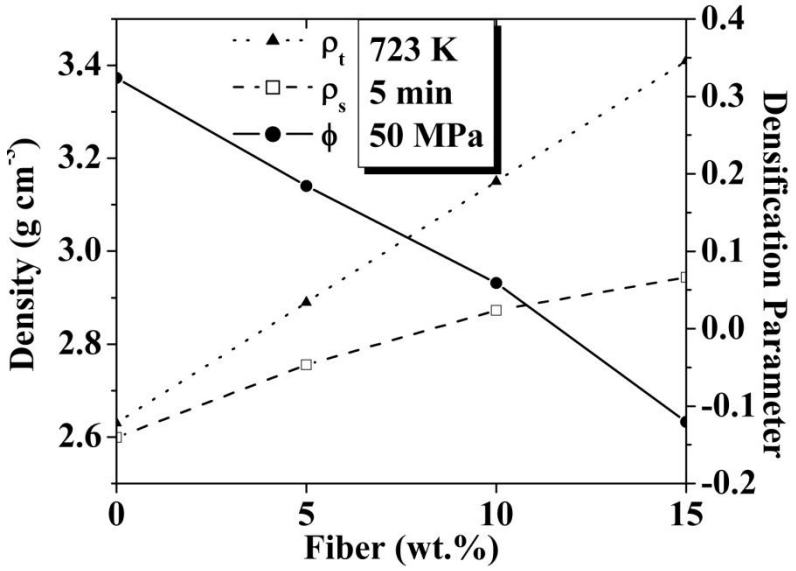

Fig. 5.12 Dependence of densification parameter on fiber wt.%.

Positive values of densification parameter (ϕ) are indicative of increment in green density. VHP aided densification was obtained for unreinforced, 5 wt.% and 10 wt.% reinforced compacts, whereas a negative value for 15 wt.% reinforced composition, is attributed to higher starting green porosity of the compacts and likely reduced inter-particle contacts due to hindrance imposed by the short steel fibers. Increase in porosity with increasing short steel fiber content (2.5 to 10 wt.%) has also been reported by (Mandal, et al., 2008) for vortex cast Al-2 Mg based composites on account of fiber agglomeration and air entrapment, that could have created areas where the melt did not penetrate. Similarly, in the present investigation, voids may have formed between agglomerated short fibers, leading to formation of isolated spots devoid of aluminium powder particles during die filling and cold compaction stage. Densification parameter was characterized for 5 min duration of VHP; increasing the hot pressing duration may result in increased plastic flow of the particles and hence result in better densification.

5.4.4 Matrix hardness

Addition of a hard reinforcing phase in soft aluminium based matrices is reported to generate dislocations in the matrix due to coefficient of thermal mismatch. Movement and dissolution of these dislocations is pinned by the hard reinforcing phase and hence the increased dislocation density results in hardening of the matrix (Shahani & Clyne, 1991). Presence of voids or

interparticle porosity is reported to have the opposite effect, i.e. voids result in decreasing the net effective area for load transfer and hence cause stress relaxation. For the VHP steel fiber reinforced composites under investigation, microhardness estimations of the aluminium matrix has been considered an important parameter for optimizing the weight fraction of the reinforcement and determination of optimum processing parameters like hot pressing time and temperature. Fig. 5.13 shows the dependence of sintering time and temperature on matrix hardness of unreinforced and all reinforced compositions. There is an increase in hardness as a result of reinforcement for all temperatures and hot pressing durations. The maximum hardness of 51 HV is achieved for Al-10 wt.% short fiber composite hot pressed at 823K for 15 min duration.

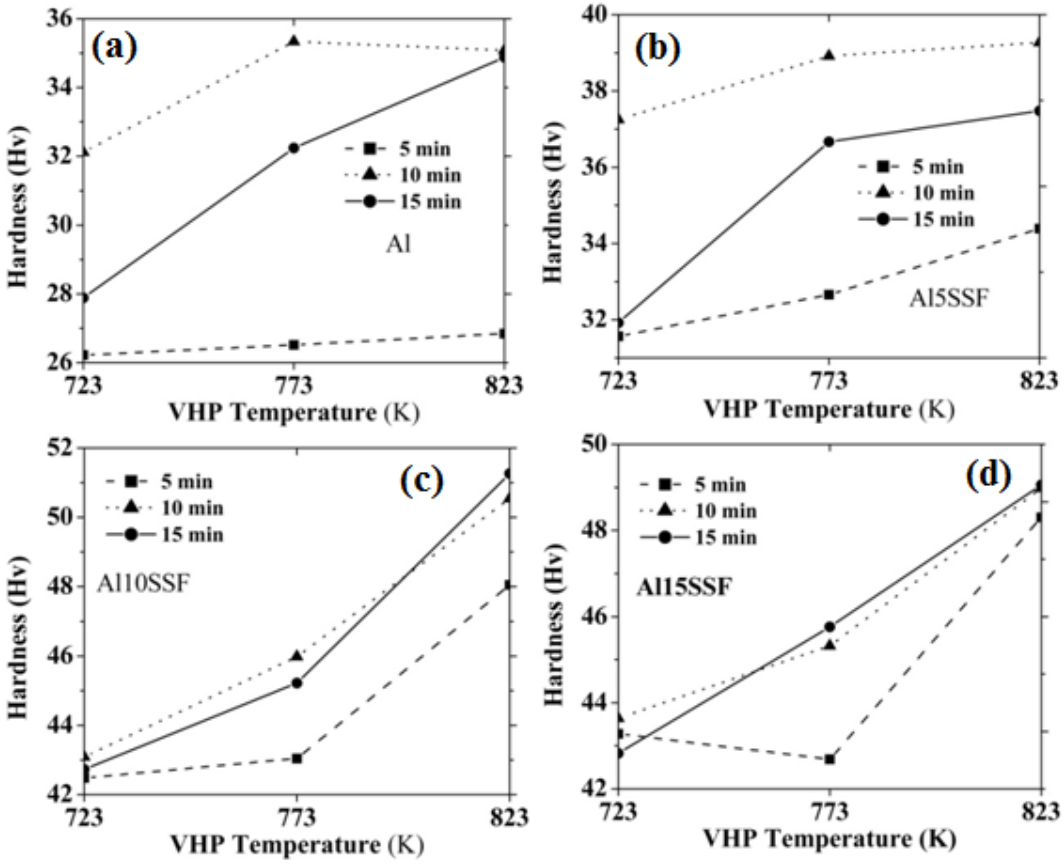

Fig. 5.13 Effect of VHP time and temperature on matrix hardness for (a) Al (b) Al-5wt% (c) Al-10 wt.% and (d) Al-15 wt.% short steel fiber reinforced composites

The densification rate of a porous composite has been reported to be directly proportional to the rate of matrix plastic flow and inversely proportional to the void fraction (Kim, 2008). Decrease in matrix hardness following increased short fiber content from 10 wt. % to 15 wt.% could be attributed to lower starting green density and retention of voids post hot pressing.

5.4.5 Characterization of reaction interface

A steady growth of the reaction interface was observed in Al-10 wt.% composite vacuum hot pressed at 823K under 50MPa stress. The hot pressed compacts were sectioned in a plane perpendicular to the axis of the cylindrical specimen for characterization of the reaction interface by scanning electron microscope equipped with energy dispersive X-ray spectroscopy (EDS).

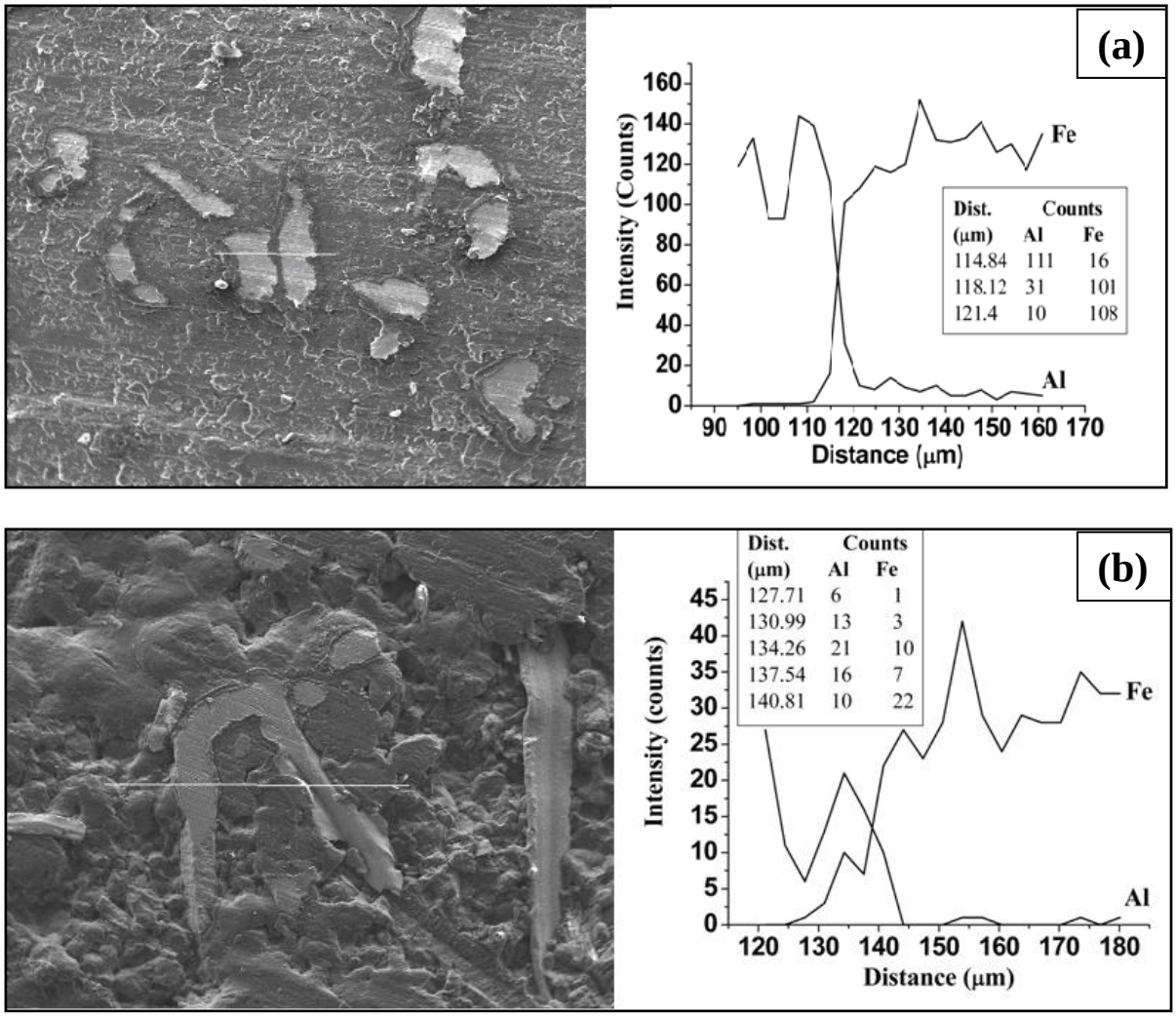

Line scans along the steel fibers confirmed the presence of a reaction interface formed as a result of interdiffusion of Fe and Al. Fig. 5.14 shows the line scans for Fe and Al. From the intensity counts, it is possible to establish the presence of Fe_3Al (Fig. 5.14(a)), $FeAl_2$ and Fe_2Al (Fig. 5.14(b)), Fe_3Al and Fe_4Al (Fig. 5.14(c)), Fe_2Al_5 and FeAl (Fig. 5.14(d)), and other non-stoichiometric intermetallics.

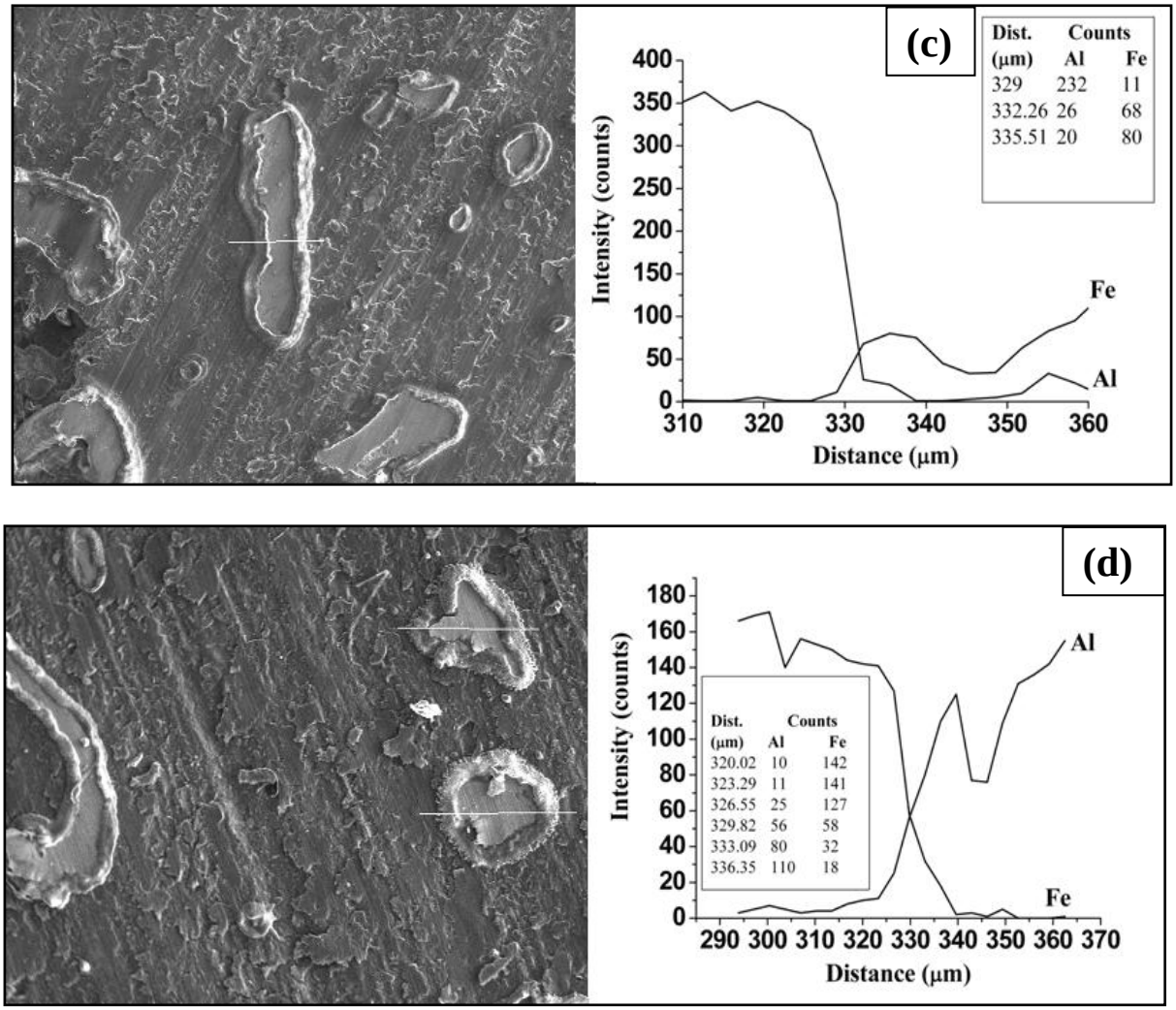

Fig. 5.14 SEM micrographs with corresponding EDS line scans of VHP Al-10 wt.% compacts for (a) 5 min, (b) 10 min, (c) 15 min, and (d) 20 min pressing durations

To evaluate the reaction interface growth kinetics, thickness d of the interface was plotted against square root of hot pressing time $t^{1/2}$, as shown in Fig. 5.15. Straight line in the central portion of the curve indicates that the growth of the interface follows a parabolic law ($d^2 = kt$); which is indicative of a diffusion controlled mechanism; where k is the temperature depended parabolic rate constant (Hwang, et al., 1997). The value of k, determined from slope of the straight line portion of the curve was 1.41×10^{-12} m^2 s^{-1} at 823 K. This value was about 10 times higher than that obtained by (Hwang et al., 1997) for vacuum hot pressing of aluminium foil-stainless steel wire composite at 873K, 70 MPa, and about 4 times higher than that obtained by (Bhagat, 1989) for stainless steel wire-P/M aluminium composite vacuum hot pressed at 800K, 140 MPa.

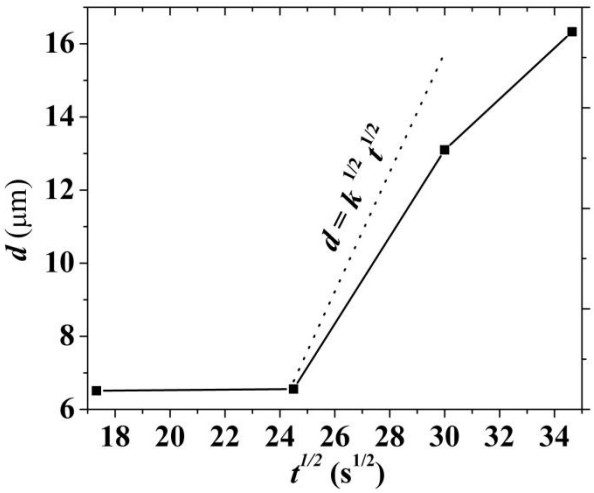

Fig. 5.15 Variation of interface thickness d (μm) with (time) $t^{1/2}$ at 823 K

Discussion: Two temperature regimes are operative for formation of Fe-Al intermetallic phases namely, (793-922 K) and (1003-1673 K), the present investigation falls in the former range, wherein, aluminium diffuses into iron (Kobayashi and Yakou, 2002). Investigators have reported the dominance of Fe_2Al_5 (η), for both the temperature ranges. More recently, (Springer, et al., 2011) have reported the formation of Fe_2Al_5 (η) and thin interlayers of AlFe (β)/$AlFe_3C$(κ) for solid- solid (873 K) interdiffusion. Phases detected in the present work start from iron rich species and progress to aluminium rich intermetallics with increasing VHP duration. Generally iron-rich phases are difficult to detect due in spite of their thermodynamic stability and lower free energy of formation in comparison to Fe_2Al_5 (η) due to diffraction peak overlap of iron rich reaction products in XRD. However, following the preferential growth of Fe_2Al_5 (η), absence of other iron rich intermetallics cannot be ignored (Shahverdi, et al., 2002). Lower temperature processing, in the present case, would have promoted formation of iron rich phases, which from a composite standpoint would be considered favorable, as aluminium rich intermetallics have been reported to be excessively hard and prone to embrittlement (Stoloff, 1998). Higher value of the rate constant in present work could be attributed to:

1. Modification suggested by (Hwang et al., 1997) to the planar diffusion boundary was found to be dependent on wire radius, for stainless steel wires of uniform cross-section hot pressed within layers of pure aluminium foil. Short steel fibers, with a kidney shaped cross-section, would offer a larger equivalent planar interface for diffusion.
2. Absence of any heavy alloying elements like Ni and Cr in short steel fibers against comparative studies, wherein, stainless steel wire-aluminium couples have been investigated; form complex ternary intermetallics which are known to retard reaction interface growth (Bhagat, 1989; Mannan, et al., 1983; Hwang et al., 1997).

3. Inherent surface roughness of the short steel fibers would have provided other diffusion paths in addition to the cross-sectional boundary.
4. Intermittent rupture of the oxide film over aluminium particles by hard steel fibers during cold compaction could promote better contact between Al-short steel fibers and hence accelerate the interdiffusion process.
5. The present study was done in a simulated environment wherein the green compacts were resistively heated by current flowing axially through the compacts. Steel fibers of higher specific resistivity than aluminium matrix, could have led to development of localized hot spots dispersed evenly within the compact; against comparative studies which have been conducted in radiant heating environments.

5.4.6 Conventionally hot pressed Al-10 wt.% steel short fiber composites

Al and Al-10 wt.% steel short fiber composites were fabricated by conventional hot pressing (*Section 4.3.5.1*), which involved direct loading of the charges, without prior cold consolidation. Hot pressing temperature was maintained at 748 K for 20 min under 70 MPa constant stress. Near full density was achieved for the unreinforced composition with no visible porosity, however, un-dissolved prior particle boundaries remained, as shown in Fig. 5.16. Since the process temperature was below 793 K, minimum required temperature for Fe-Al interdiffusion, no reaction interface was formed between the short fibers and Al matrix, as shown in Fig. 5.17. Hot pressed relative density values of 99.2% and 98.6% were recorded for Al and Al-10 wt. % short steel fiber compositions respectively.

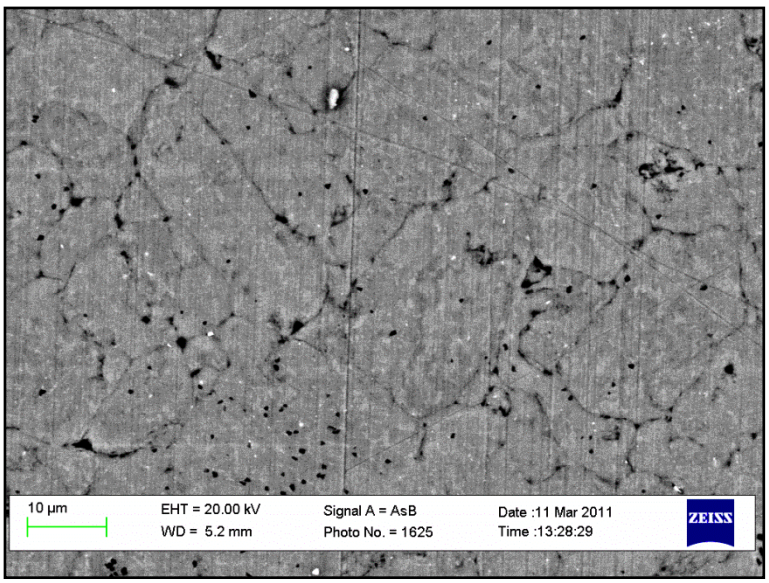

Fig. 5.16 SEM micrograph (BSE mode) of conventionally hot pressed Al powder

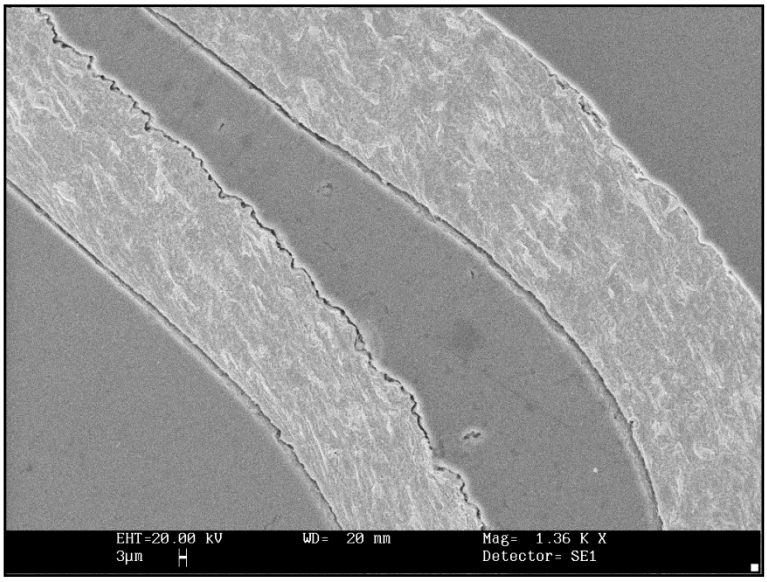

Fig. 5.17 SEM micrograph of Al-10 wt.% short steel fiber conventionally hot pressed composite

Higher hot pressed densities for both monolithic and composite compacts by conventional hot pressing in comparison to VHP, resulted due to increased plastic flow of the matrix powder through the inter fiber regions. However, a slight detachment of the short fiber from the matrix at the interface is observed. This phenomenon has been explained by (Springer, et al., 2011) as Kirkendall voids, which develop at the boundary of faster diffusing element (Al), due to coalescence of vacancies at the Al-side migrating in the direction opposite to that of diffusion.

With reference to both the fabrication methods discussed above namely VHP and hot pressing , it is important to note that the thickness of the reaction interface is an important consideration for metal-metal MMC systems; a well interfaced composite can give much superior properties by synergistic effects arising from effective load transfer from the weak matrix to the strong reinforcement (Pai, et al., 1999); however, the intermetallic nature of the reaction interface leads to excessive hardness, low ductility, susceptibility to crack propagation, and environmental embrittlement. Patented work for manufacture of steel wire mesh reinforced cast aluminium automobile connecting rods (Kim & Yoon, 1996) has reported an optimum interface thickness of 2–10 ?m, achieved by carbonitriding treatment of wire mesh prior to melt infiltration. Vortex cast short steel fiber reinforced aluminium based composites investigated by (Mandal, et al., 2007) have suggested Cu coating of the fibers for improved wetting and inhibition of reaction interface growth. Avoidance of intermetallic products by spray deposition of aluminium melt over steel wire interconnected preforms as reported by (Gupta, et al., 2005) could be due to low interaction temperature of disintegrated melt droplets impinging on steel wire.

The present work achieves a near optimum reaction interface thickness by P/M based processing and vacuum hot pressing technique without any pretreatment of the steel fibers.

5.5 Surface Modification of Short Steel Fibers

Surface modification of short steel fibers by chemical vapor deposition (CVD) using fluidized bed reactor (FBR) was conducted as per methodology and process parameters described in *Section 4.3.1*.

5.5.1 Nitriding

As shown in Fig. 5.18, the untreated fibers have a cold worked structure composed of ferrite and pearlite with a microhardness of 235±10 HV. Nitriding treatments for 90min and 30min, resulted in a through nitrided structure which extended to the core of the fiber, uniform microhardness of about 761±6 HV was obtained for both the durations. Reducing the nitriding time to 5min resulted in a case of about 1.5µm having a microhardness of 650±3 HV to a softer core of 194±4 HV. Controlled nitriding was possible by shortening the process time. For higher nitriding times, the equilibrium growth kinetics for growth of compound layer were not observed, primarily on account of very small diameter of the fibers.

The XRD patterns as shown in Fig. 5.19, confirm the development of γ'-Fe_4N and ε-$Fe_{2-3}N$ phases with respect to nitriding durations.

Discussion: Nitriding of alloy steels is reported to form a hardened case of upto 30 µm thickness composed of γ'-Fe_4N and ε-$Fe_{2-3}N$ (Alsaran, et al., 2005). Nitrogen is also reported to form a solid solution interlayer (composed of metal nitrides (AlN, TiN, CrN etc.) as small particles that provide hardening of the underlying Fe matrix (Cavaliere, et al., 2009). Plain carbon steel (0.38 wt.% C) used as substrate in the present study would only have formed the case hardened layer due to absence of alloying elements like Cr etc. Therefore, for higher nitriding durations of 90 and 30 min, a through hardening of the short fiber was achieved as revealed by XRD analysis of treated fibers, where a decrease in α-Fe peak intensity counts was detected with increasing nitriding duration.

In the present work, fluidization of short fibers in a packed alumina particle bed ensured uniform deposition of reactive gas vapour throughout the fiber surface, however, non-uniformity of the fiber cross-section, especially at fiber ends, may have led to formation of zones with excessive deposition and degradation of the fiber sub-structure.

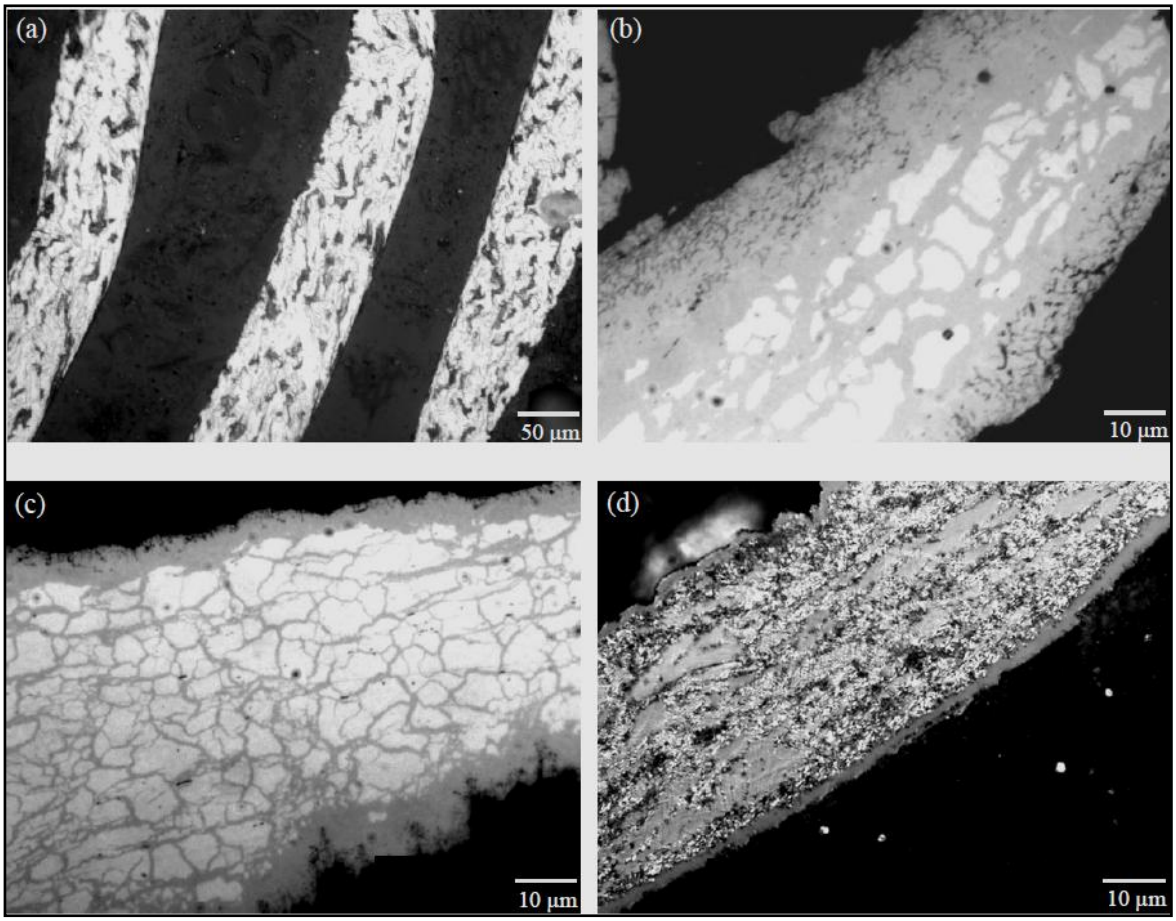

Fig. 5.18 Optical micrographs of short steel fibers (a) untreated (etched by 2.5% nital) nitrided for (b) 90min (c) 30min and (d) 5min duration

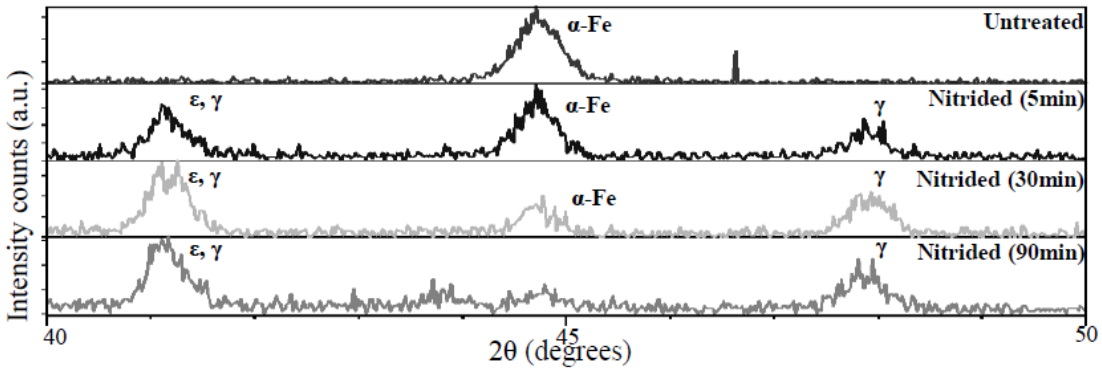

Fig. 5.19 XRD patterns of untreated and nitrided short steel fibers

5.5.2 Chromizing

Compounds formed by chromizing treatment were detected by XRD and phase studies from Cr-Fe binary phase diagram using Thermocalc^{TM} TCFE-3 database. Fig. 5.20 shows the representative micrographs of chromized fibers, the 50 min cycle resulted in formation of $Cr_{1.07}Fe_{18.93}$ and $Cr_{1.36}Fe_{0.52}$ type of solid solutions of average microhardness 234±8 HV; the 7 min cycle formed $CrFe_4$ of average hardness 164±3 HV with a completely decarburized structure, composed of large ferrite grains. The fibers had a stainless steel like appearance.

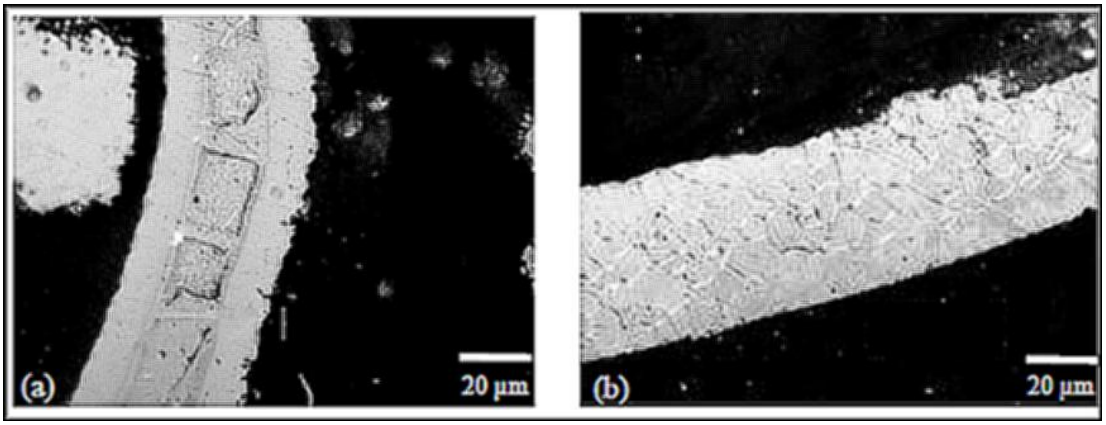

Fig. 5.20 Optical micrographs of short steel fibers chromized for (a) 50min and (b) 7min durations

Discussion: Decrease in substrate hardness from as-received hardness of 235 HV was indicative of soft-chromizing. A threshold carbon content of 0.3 wt.% is reported to form complex hard Cr-carbides by chromizing treatment of low alloy or plain carbon steels (Ralston, et al., 2011); instead a decarburized structure made up of Fe-Cr solid-solution over large α- Fe grains was observed. Fig. 5.21 shows a part of Cr-Fe binary phase diagram for upto 20 wt.% Cr. Fe-Cr solid solution is formed between 11.2 and 13.4 wt.% Cr and separates γ-Fe from α-Fe (ASM International, 1992). The anomaly in the present case, wherein, soft-chromizing resulted even with sufficient C in the fibers can be explained by the diffusion of C, which has high affinity for Cr, occurs in the outward direction, to form complex carbides. Formation of an optimum thickness of hard carbide layer is dependent on treatment duration, which was limited to just 7 min in the present case. Longer treatment times are reported to cause depletion of C from the ferrite-pearlite matrix at 935ºC (Jongbloed, 1994). Probable concentration of Cr lying between 11.2 and 13.4 wt.% would have resulted in formation of Fe-Cr solid-solution of compositions as reported above. The treated fibers were found to be magnetic, implying that Mn (0.52 wt.%) reported to enlarge the γ-Fe zone during chromizing (Jongbloed, 1994), was not sufficient enough to completely austenitize the fiber sub-structure.

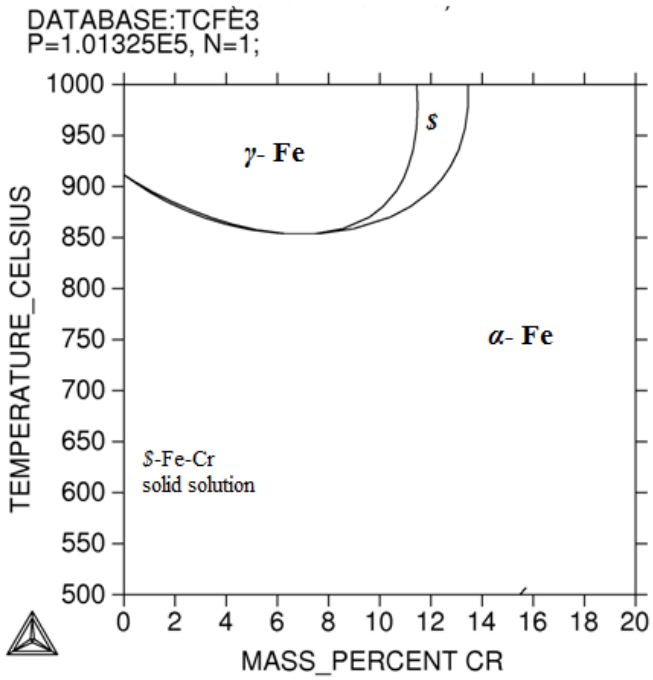

Fig. 5.21 Section of Cr-Fe binary phase diagram

5.5.3 Aluminizing

Aluminizing treatment of short steel fibers, carried out for 45 min duration, resulted in formation of a strongly adherent layer composed of $FeAl_3$ (θ), as determined by XRD (**Fig. 5.23**), of about 7 µm thickness, as shown in Fig. 5.22**.** The deposited intermetallic layer had a serrated morphology, characteristic of Fe-Al interdiffusion products. An average microhardness of 890 ±12 HV was obtained for the coated zone.

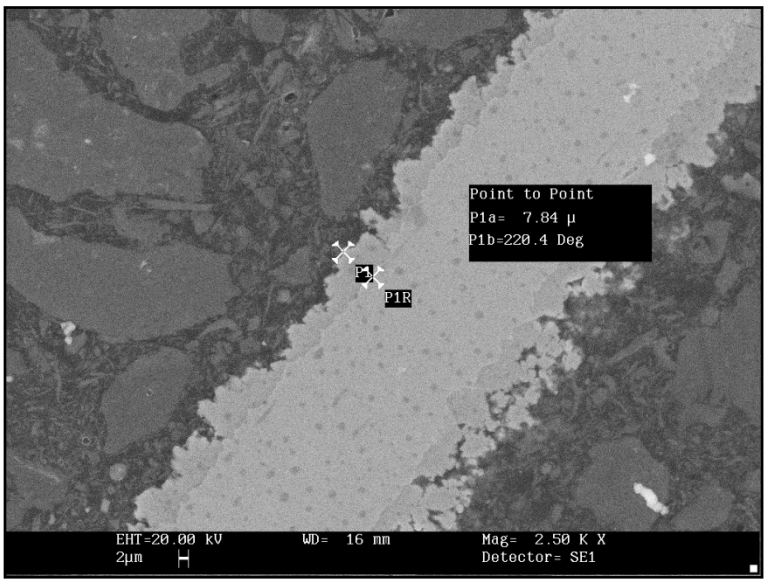

Fig. 5.22 SEM micrograph of a short steel fiber aluminized for 45 min

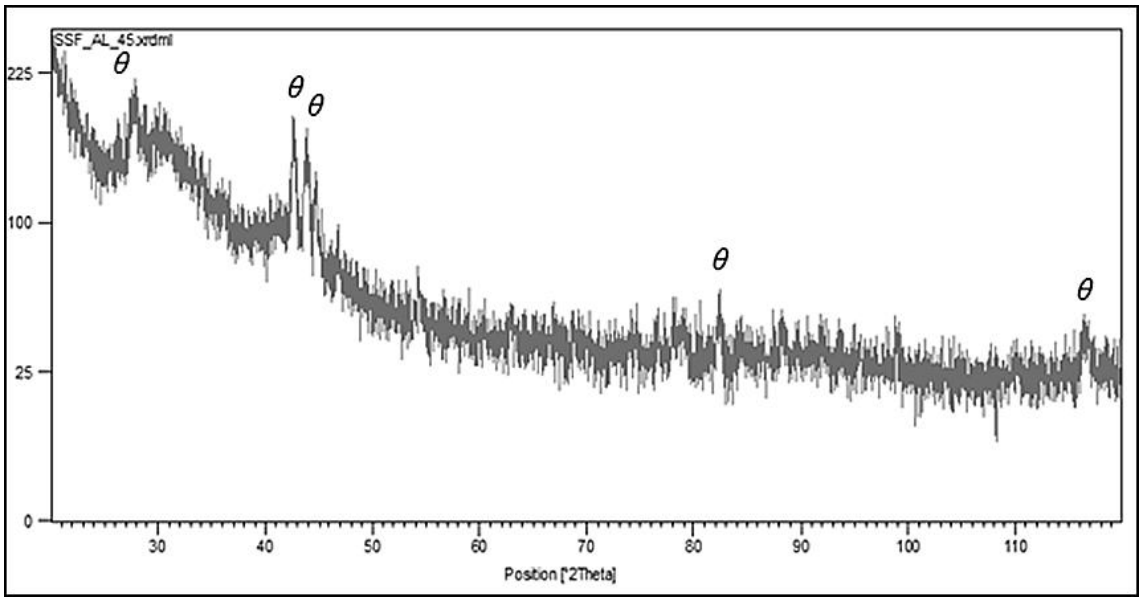

Fig. 5.23 XRD scan of aluminized short steel fibers showing (θ) - $FeAl_3$

Discussion: Effect of pre-aluminizing on continuous stainless steel wire for AMC application has been investigated by (Patankar et al., 1985); they have reported formation of both Fe_2Al_5 (η) and $FeAl_3$ (θ) phases. Formation of $FeAl_3$ (θ) against the more aluminium rich phase Fe_2Al_5 (η) is observed in the present study. Fe_2Al_5 (η) has been reported as the more dominant phase with faster growth kinetics (Springer, et al., 2011) in comparison to other intermetallics. A lower processing temperature (535ºC) in the present case could be the factor for inhibited growth of Fe_2Al_5 (η). An equivalent hardness range of 900-1000 HV has been reported for $FeAl_3$ (θ) against 890 HV achieved in the study; which was considerably higher than Fe_2Al_5 (η) (700-800 HV); thereby limiting the toughness, as can be seen in the representative micrograph (Fig. 5.22); wherein, fragmentation of the deposited layer has been caused by metallographic grinding and polishing. For FBR based CVD of Al, it was not possible to further increase the retort temperature. Choking of the porous gas distributor located at the bottom of bed limited the maximum temperature to 590ºC.

5.6 Effect of Surface Treatment on Reaction Interface

The composite blend of Al-0.5 wt.% Mg-10wt.% treated fibers was uniaxially cold compacted using a hardened steel die in a hydraulic press of 15 kN capacity at 375 MPa to prepare cylindrical green preforms of 20mm diameter × 5 mm height. The green compacts were sintered at 620^{o}C in N_2 atmosphere for 60 min. Effect of surface treatment on reaction interface formed by sintering was determined by optical microscope, SEM, XRD and microhardness measurements.

5.6.1 Nitrided fibers

Representative micrographs of Al-0.5wt.%Mg-10wt.% nitrided steel fiber composites for various nitriding times are shown in Fig. 5.24. Reaction interfaces of Fe-Al type were formed for all nitrided short fibers, irrespective of nitriding durations or starting fiber microstructure. A porous interface was observed for the 90 min nitrided fibers, with an aluminized core, similarly for the 30 min nitrided fibers the fiber core was almost completely composed of Fe-Al intermetallics. In the case of fibers nitrided for 5 min, a limited reaction layer was observed. These fibers had a well defined 1.5 µm thick case of γ'-Fe_4N and ε-$Fe_{2-3}N$ compounds, which are reported to be thermally stable upto 550ºC (Usta, et al., 2004). The lower limit for Fe-Al interdiffusion is reported to be 520ºC; upto which the hardened case could have inhibited fiber-matrix interaction. For the 5 min nitrided fiber composite, a 10 µm thick interface with peak hardness of 1560 HV was formed; core hardness of fiber was retained at 230 HV. The maximum hardness of 1596 HV corresponds to 5 min nitriding time with 1087 HV and 1119 HV for 30min and 90min durations. These excessive hardness values suggest the formation of Fe_xAl_y type of intermetallic reaction interface, but the same could not be detected by XRD analysis, presence of AlN was however confirmed.

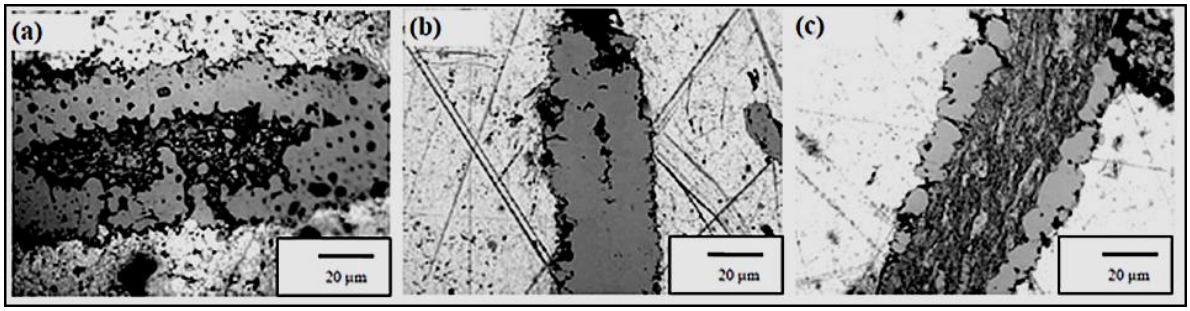

Fig. 5.24 Optical micrographs of reaction interface in sintered Al-0.5wt.%Mg-10wt.% (a) 90min (b) 30min (c) 5 min nitrided short steel fiber composites

Thermal stability of the case hardened layer over 5 min nitrided fibers was evaluated by low temperature hot pressing (475 ºC, 70 MPa, 20 min). A representative micrograph is presented in Fig. 5.25. The hot pressed compact was over etched with 2.5 % Nital solution to differentiate the compound layer. As can be seen, an effective barrier against Fe-Al interdiffusion was offered by the nitrided interlayer. A near optimum case thickness of 1.5 µm was sufficient to separate the composite constituents. Interface porosity developed by Kirkendall effect is also avoided, presumably by formation of AlN, therefore a smooth interface is obtained.

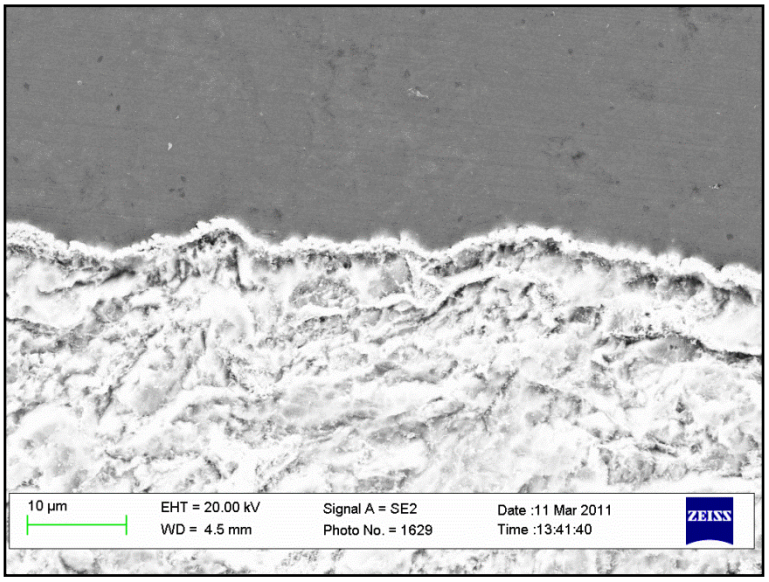

Fig. 5.25 Scanning electron micrograph of reaction interface in hot pressed Al-0.5wt.%Mg-10wt.% 5 min nitrided short steel fiber composite

5.6.2 Chromized fibers

Reaction interfaces around chromized short steel fibers have been shown in Fig. 5.26.

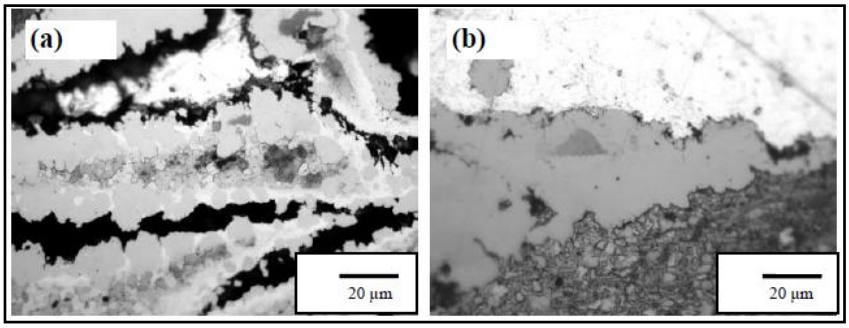

Fig. 5.26 Optical micrographs of reaction interface in sintered Al-0.5wt.%Mg-10wt.% (a) 53 min (b) 7 min chromized short steel fiber composites

A peak hardness of 1225 HV was obtained for 53 min chromized fiber and 989 HV for 7 min, with the reaction interface being composed of $Al_{0.983}Cr_{0.017}$ intermetallic, detected by XRD, in both the compositions. The soft chromized, carbon depleted fiber core in both the treated fibers, was unable to provide an effective barrier against growth of the reaction interface.

5.6.3 Aluminized fibers

Sintering of composite containing pre-aluminized fibers was found to be successful in controlling the growth of intermetallic reaction interface, beyond the preformed diffusion coating thickness, as shown in **Fig. 5.27**. Slight reduction was noted in the interface hardness,

which reduced from 890 HV to 790 HV following sintering. Chemistry of the reaction interface remained unchanged. However, the serrated gaps, Kirkendall voids, formed during pre-aluminizing treatment remained unfilled.

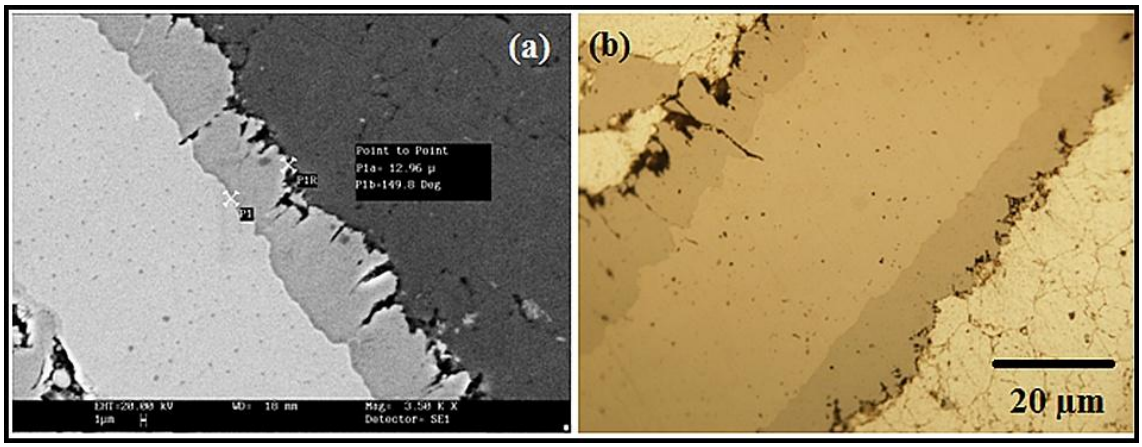

Fig. 5.27 (a) SEM and (b) optical micrograph of reaction interface in sintered Al-0.5wt.%Mg-10wt.% aluminized short steel fiber

5.7 Development of Al-0.5 wt.% Mg based Composites by Press-Sinter Route

Pure aluminium powder was blended with 0.5 wt.% magnesium powder, used as a sintering aid, as described in *Section 4.3.2*. Untreated short steel fibers (10, 20 and 30 wt.%) were dispersed in the Al-0.5 wt.% Mg matrix powder blend (*Section 4.3.3*). Monolithic and composite powder mixes of Al-0.5 wt.% Mg-x wt.% short steel fibers (x = 0, 10, 20, 30), corresponding to reinforcement volume fractions of 0, 3.7, 7.9 and 12.8 vol.% , designated as C1, C2, C3 and C4 respectively were uniaxially cold compacted at 375 MPa into cylindrical green preforms (ϕ 20 mm × ~ 4 mm) and rectangular bars and flat bars of 40 mm × 8 mm × 3 mm for transverse rupture strength specimens as described in *Section 4.3.3*. Details of sintering process have been elaborated in *Section 4.3.6*. All compositions were sintered at 620ºC for 60 min duration under dry nitrogen atmosphere.

5.7.1 Green density

Green densities determined for matrix powder blend Al-0.5 wt.% Mg and composite blends of Al-0.5 wt.% Mg with 10, 20 and 30 wt. % short steel fibers against respective theoretical densities and residual green porosity have been tabulated in Table 5.4.

Table 5.4 Green densities of Al-0.5 wt.% based compositions

Composition	Short steel fibers wt.% (vol.%)	Theoretical density (g cm^{-3})	Green density (g cm^{-3})	Porosity (vol.%)
C1	0	2.69	2.46	8.55
C2	10 (3.7)	2.88	2.57	10.76
C3	20 (7.9)	3.10	2.69	13.22
C4	30 (12.8)	3.35	2.81	16.11

For the same compaction pressure, higher green porosity was attained with increasing reinforcement content, a trend observed earlier for compacts pressed for VHP. But from comparison of 10 wt.% reinforced composition, higher relative green density is obtained for press-sinter compact at 250 MPa on account of lower aspect ratio (h/d = 0.4) compared to about 2 for VHP pressed at 375 MPa. The hard short fibers hindered the flow of aluminium powder particles by either forming agglomerates during die filling or the pressing stage. Reinforcement agglomeration, especially in case of discontinuously reinforced short fiber composites, is reported to cause retained voids at fiber boundaries or at the center of fiber agglomerates (Rack, 1991).

5.7.2 Sintering temperature

Sintering cycle has been described in *Section 4.3.6.1*. Al-0.5 wt.% Mg based compositions were solid state sintered, due to absence of any transient liquid phase evolving element. Sintering temperature of 620ºC, was selected as the minimum temperature, based on similar studies reported in literature (Lumley, et al., 1999; Schaffer, et al., 2005), for maximum densification (Pieczonka, et al., 2008) in sintering of pure aluminium powder with elemental magnesium employed as sintering aid, heated under dry nitrogen atmosphere. At least three samples were identically processed for any given composition.

5.7.3 Effect of Mg and nitrogen on sintering of Al-0.5 wt.% Mg powder blend

Role of elemental Mg has been reported in Al-P/M as a sintering aid to disrupt the nascent oxide layer over aluminium powder particles (Lumley, et al., 1999). Elemental additions of Mg from 0.1 wt.% to 1.0 wt.% have been investigated (Kondoh, et al., 2001). (Schaffer, et al., 2001) have reported an optimum addition of 0.15 wt.% Mg alongwith elemental addition of Sn for simultaneous metallurgical bonding between Al powder particles due to rupture of oxide shell and pore filling aided by transient liquid Sn. In the present work, 0.5 wt.% elemental Mg was blended with pure Al powder without the addition of any low melting point additive. The heat flow traces obtained by differential scanning calorimetary (DSC) of Al-0.5 wt.% Mg

powder blend has been compared with pure Al powder, are shown in Fig. 5.28. Samples were heated at 10ºC s^{-1} to 700ºC under high purity nitrogen atmosphere. A slight shift in the melting point towards the lower side is observed, this can be due to the lower melting point of Mg (650ºC) compared to 660ºC for Al, upon bulk melting the Al-0.5 wt.% Mg powder blend behaves like an alloy, hence by ROM, lowering of bulk melting point takes place, with a narrower L+ S zone.

Heating of Al powder in nitrogen atmosphere does not form any reaction products, loss of adsorbed hydrogen and water vapor from the powder surface is reported under low oxygen partial pressures (vacuum) (Ünal, et al., 1998; Yamasaki & Kawamura, 2004). Accordingly a smooth heat flow curve is obtained for Al, followed by endothermic event of bulk melting, whereas, for Al-0.5 wt.% Mg powder blend, significant disturbances are noted in the heat flow trace from about 400ºC onwards, followed by a distinct exothermic event just after 500ºC. This observation can be attributed to reduction of Al powder surface by Mg (400-500ºC) and reaction of exposed Al surface and nitrogen gas to form AlN (500-550ºC).

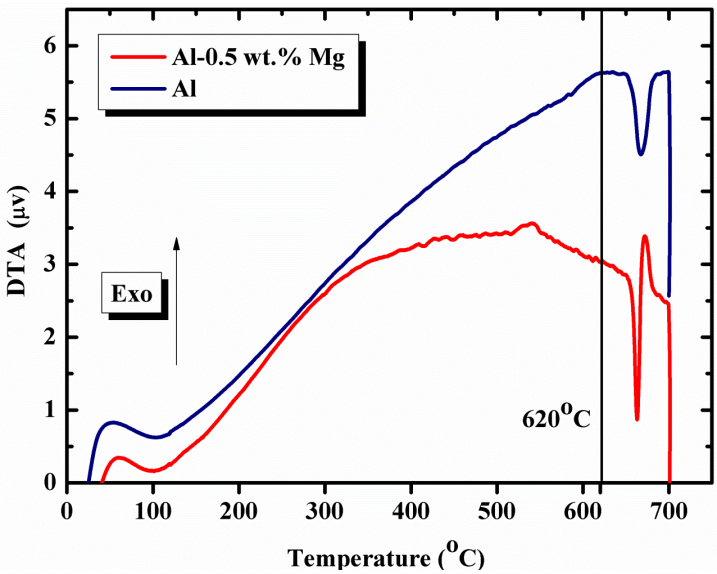

Fig. 5.28 Heat flow traces of Al powder and Al-0.5 wt.% Mg powder blend

Discussion: Effect of Mg in scavenging oxygen and setting-in a self gettering mechanism by formation of spinel ($MgAl_2O_4$), thereby exposing the aluminium powder particle surface has been described in literature by the equation: $3Mg + 4Al_2O_3 \rightarrow 3Al_2MgO_4 + 2Al$. Exposed and metallurgically clean (free from γ-Al_2O_3) Al powder surface is then free to react with nitrogen gas: $2Al + N_2 \rightarrow 2AlN$; to form aluminium nitride (Schaffer & Hall, 2002). Consumption of nitrogen to form AlN is reported to assist in pore closure by creating a negative pressure at the pore surface (Schaffer, et al., 2005). AlN has been synthesized by physical vapor deposition or

plasma nitriding on aluminium substrates with temperature in the 300-350ºC range. (Kent, et al., 2006) have reported on a novel processing technique for synthesis of AlN by heating (540ºC) of an encapsulated assembly composed of aluminium foil separated by a layer of Mg powder, under dry flowing nitrogen. Mg is reported to scavenge oxygen traces from nitrogen as well as expose aluminium under the alumina shell, leading to layer wise deposition of AlN on the foil substrate.

Heat flow traces for Al-0.5 wt.% Mg from the present work, point out to a similar mechanism being operative, wherein, Mg induced reduction of surface oxide over the aluminium powder followed by further formation of AlN, observed as distinct exothermic heat flow traces for the powder blend. Reduction of Al surface oxide commences after 400ºC, continues till 500ºC, after which, AlN is formed in the 500-550ºC range.

Formation of spinel $MgAl_2O_4$ and presence of AlN could not be conclusively detected by XRD; presumably owing to the low volume fractions (≤ 2%) of these compounds, hence the same was attempted by GDOES (glow discharge atomic emission spectroscopy) using LECO GDS850A^{TM}, which allows for quantitative elemental profiling of a surface by layer–wise uniform sputtering to known depths, operating at 40 mA, 1200 V, with a 10 s^{-1} data acquisition rate. Fig. 5.29 shows the elemental depth profile of elements in sintered (620ºC, 60 min) Al-0.5wt.% Mg, upper portion of the profile has been blanked to facilitate comparison of elements other than aluminium.

After an initial build-up of oxygen, present in an unsintered outer shell of approximately 5 µm thickness, a constant level of nitrogen and magnesium was observed. Mg was detected only after the outer oxygen rich layer was sputtered out, in an amount almost equal to that (0.5 wt.%) blended with Al powder. Formation of an outer unsintered layer has been observed by (Schaffer & Hall, 2002), on account of the oxygen content in dry nitrogen, that first interacts with the outer layer of the compact. This oxygen is reportedly consumed as nitrogen gas permeates through the porous green compact by a self sustaining mechanism as described earlier.

Metallographic examination of partially sintered samples, where, sintering was terminated after 15 min at 600ºC; as shown in Fig. 5.30 (a), revealed necking between neighboring powder particles. Inter-particle neck formation is the first step towards densification by pore closure. Uniformly distributed AlN particles, lighter in contrast, were detected by contrast adjustment in the BSE mode.

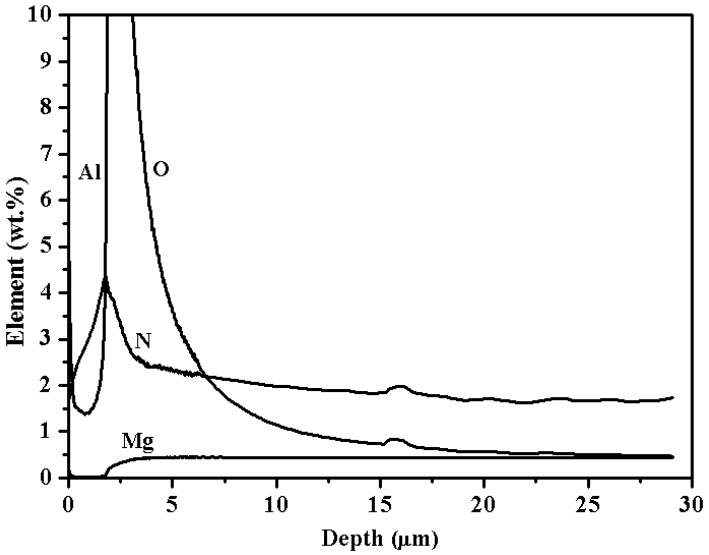

Fig. 5.29 Elemental depth profile analysis by GDOES of sintered Al-0.5wt.% Mg sample

The higher magnification micrograph (Fig. 5.30 (b)), shows that neck growth is prominent in areas which are in close vicinity of Mg rich areas. Dissolution of Mg over the Al particle surfaces is highlighted by arrows. The exothermic nature of AlN formation is also reported to promote bonding of Al particles by localized increase in temperature (Schaffer & Hall, 2002).

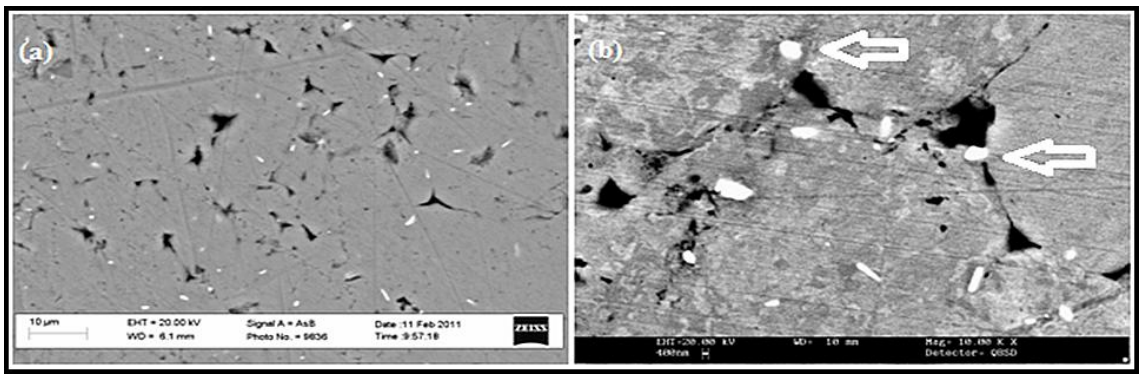

Fig. 5.30 SEM micrographs (BSE mode) of partially sintered Al-0.5 wt.% Mg compact at (a) low (b) high magnification

5.8 Characterization of Sintered Al-0.5 wt.% Mg based Compositions

5.8.1 Microstructure, density and densification parameter

Microstructures of sintered compacts for unreinforced Al-0.5 wt.% Mg (C1) and reinforced compositions (C2, C3 and C4) are shown in Fig. 5.31. C1 composition shows an uneven surface topology, this can be attributed to partial decomposition of Mg, which transforms to spinel $MgAl_2O_4$. Mg particles lying at Al powder particle boundaries aid in sintering densification, by mechanism discussed earlier, are not fully dissolved. By microscopic examination of unetched surfaces, no visible micro-porosity was detected. Increase in visible

macro-porosity (highlighted by arrows) is observed with increasing reinforcement content; however, from the examination of pore size and distribution, pores were found to be located in areas either enveloped by short fiber agglomerates, between two neighboring fibers or within cracks on a single fiber. Fibers were found to be plastically deformed into hook like shapes by imposed stress in the cold consolidation stage. Sintered densities of all the compositions are given in Table 5.5.

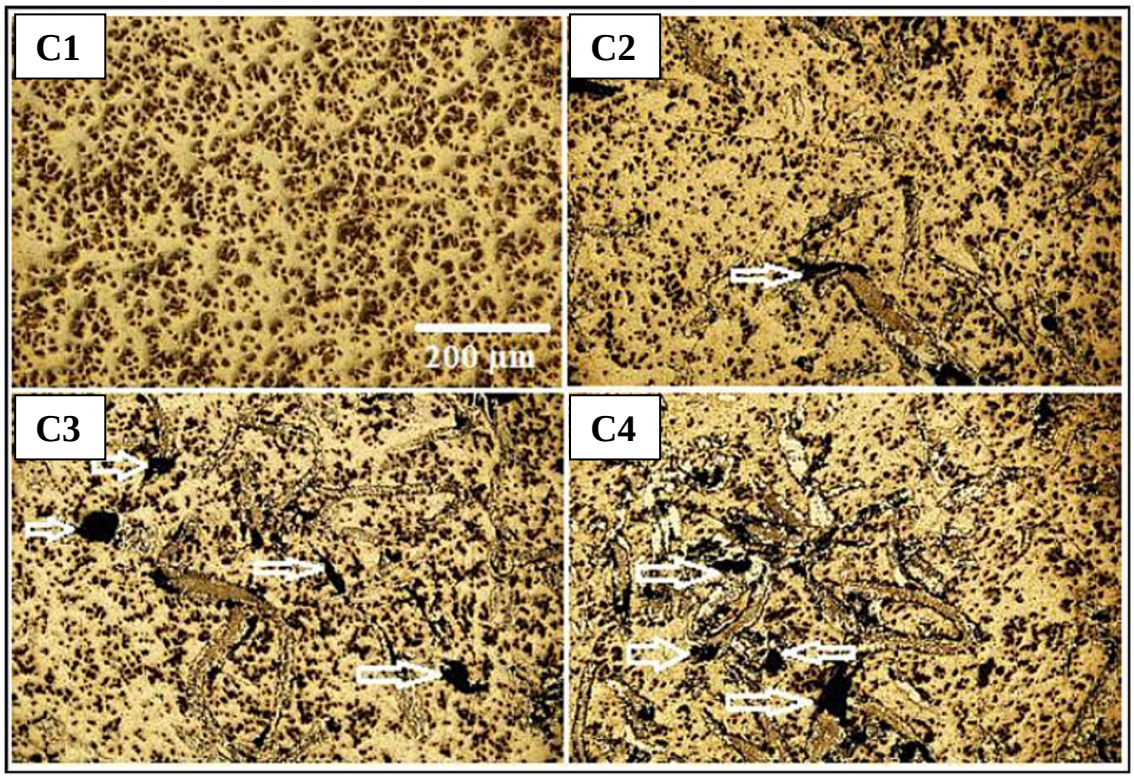

Fig. 5.31 Optical micrographs of sintered compositions

Table 5.5 Sintered densities of Al-0.5 wt.% based compositions

Composition	Short steel fibers wt.% (vol.%)	Theoretical density (g cm^{-3})	Sintered density (g cm^{-3})	Porosity (vol.%)
C1	0	2.69	2.59	3.71
C2	10 (3.7)	2.88	2.73	5.21
C3	20 (7.9)	3.10	2.91	6.13
C4	30 (12.8)	3.35	3.05	8.95

Sintered densities show similar behavior as green densities of starting preforms. Final porosity is found to be a function of reinforcement content, signifying the importance of initial green density in a fiber reinforced composite system. Closer scrutiny of sintered porosity values show a marginal increase in final porosity from C2 to C3 composition, against more than two-fold increment in reinforcement volume fraction. A better understanding of sintering induced densification is obtained from densification parameter (ϕ) (*Section 4.4.6.5*); which negates the

effect of starting green density such that the singular effect of sintering is reflected by way of a numerical value, represented on either a 0-1 scale or in terms of percentage. Densification parameter for the present AMC system alongwith sintered porosity has been shown in Fig. 5.32. Positive values are indicative of a net density increment by sintering (Upadhyaya, 1997). It can be seen that sintering has added to the green density for all compositions.

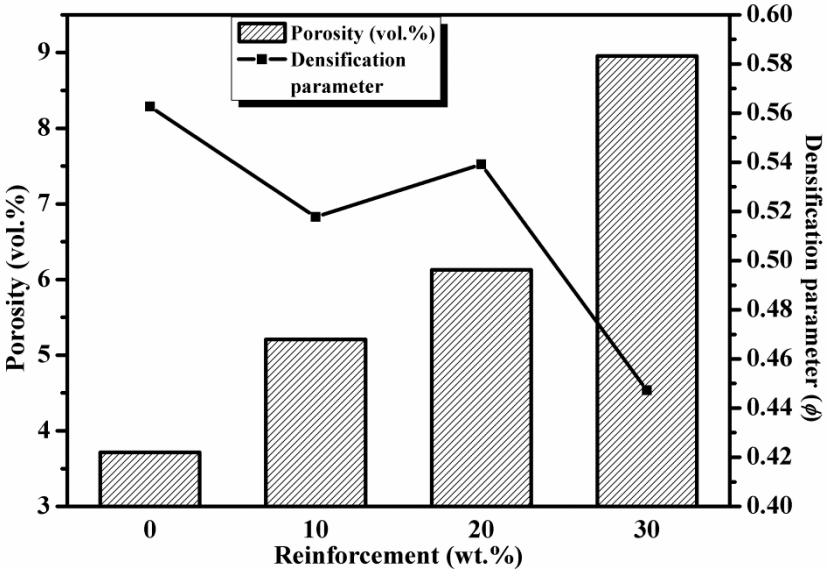

Fig. 5.32 Effect of reinforcement content on sintered porosity and densification parameter

Discussion: Cold pressing of ceramic short fiber or whisker powder blends, has been reported to cause fiber cracking, such that the aspect ratio of short fibers is sometimes found to be reduced by a factor of 10 or more, thereby affecting their load bearing capacity (Feest, 1994). Metallic short fibers, like steel, used in the current investigation, are far more ductile than ceramics and hence deformable. Cracking of the fibers can be attributed to fiber-fiber interaction leading to failure of fibers having pre-existing flaws. Sintering densification has been promoted by elemental Mg and nitrogen atmosphere; short fibers provide a discontinuity in the matrix by hindering powder particle packing in the pressing stage and retention of prior voids during sintering. Unlike casting, P/M is based on very short range mass transport; therefore it should not possible to fill up large stand alone voids by sintering. Rheology of the matrix-reinforcement powder-fiber blend is vital to blend flowability and subsequent packing during cold consolidation. Presumably the 10 wt.% (3.7 vol.%) composition lacked sufficient homogeneity at all the processing stages upto sintering. Size and morphology mismatch of the constituents, may have contributed to lower than expected densities for the highest loaded composition. Formation of a porous interface, owing to Kirkendall porosity, mechanism of which has been elaborated in literature (Springer, et al., 2011); would also lower the composite density, in an amount proportional to volume fraction of fibers.

5.8.2 Characterization of reaction interface

Reaction interface has been characterized by micrography, elemental analysis and hardness determination as shown in Fig. 5.33. Randomly distributed short fibers are observed, with both planar and embedded orientations against a flat polished viewing plane. Intermetallic reaction interface (RI) is observed as the darker phase, with some chipping, presumably due to mechanical grinding and polishing. Cloud like near continuous morphology of the RI is observed. Elemental analysis by EDS line scan is shown in Fig. 5.34. Reaction products formed were further analyzed by XRD, for all the sintered compositions, as shown in Fig. 5.35.

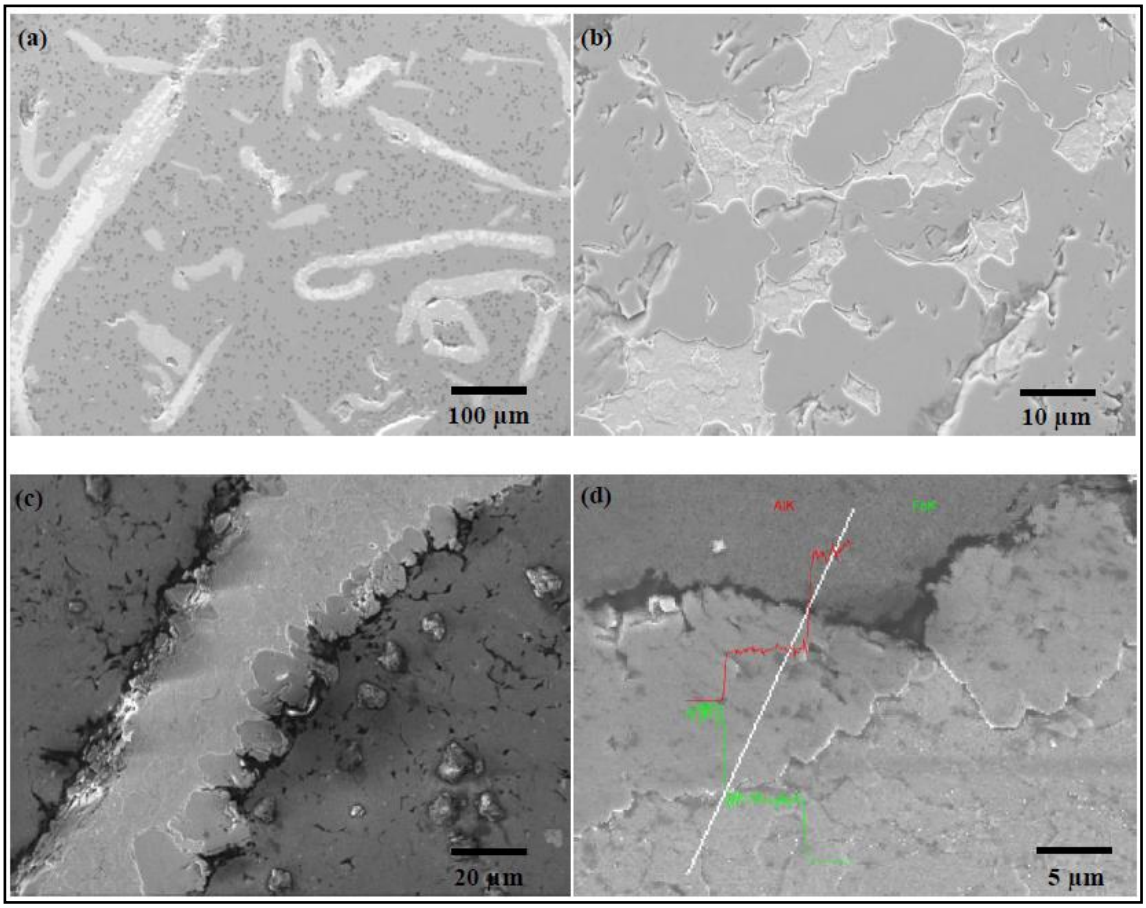

Fig. 5.33 Scanning electron micrographs showing (a) distribution of fibers (b-c) morphology of reaction interface and (c) EDS line scan through the interface

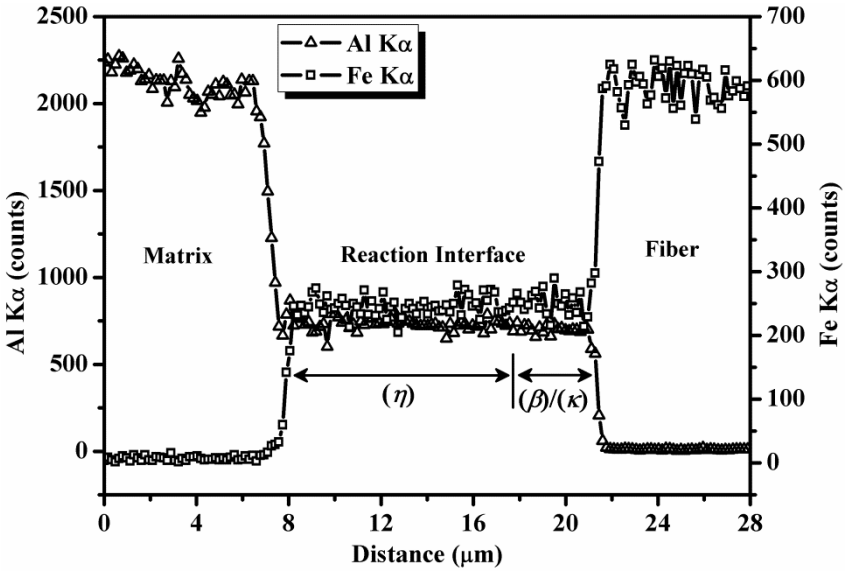

Fig. 5.34 Elemental profile along EDS line scan shown in Fig. 5.33 (d)

Average microhardness measurements from the matrix, through the RI and into the unreacted core of the fiber for all the compositions have been plotted against respective zones, as shown in Fig. 5.36, to determine the phases present as well as to establish an average value of the RI hardness for the composite, irrespective of the reinforcement content. Mean values of at least 3 readings at equal linear locations corresponding to the respective zones are plotted as a step function, rather than point specific values. Area under each step of the curve has been determined to estimate the average composite hardness.

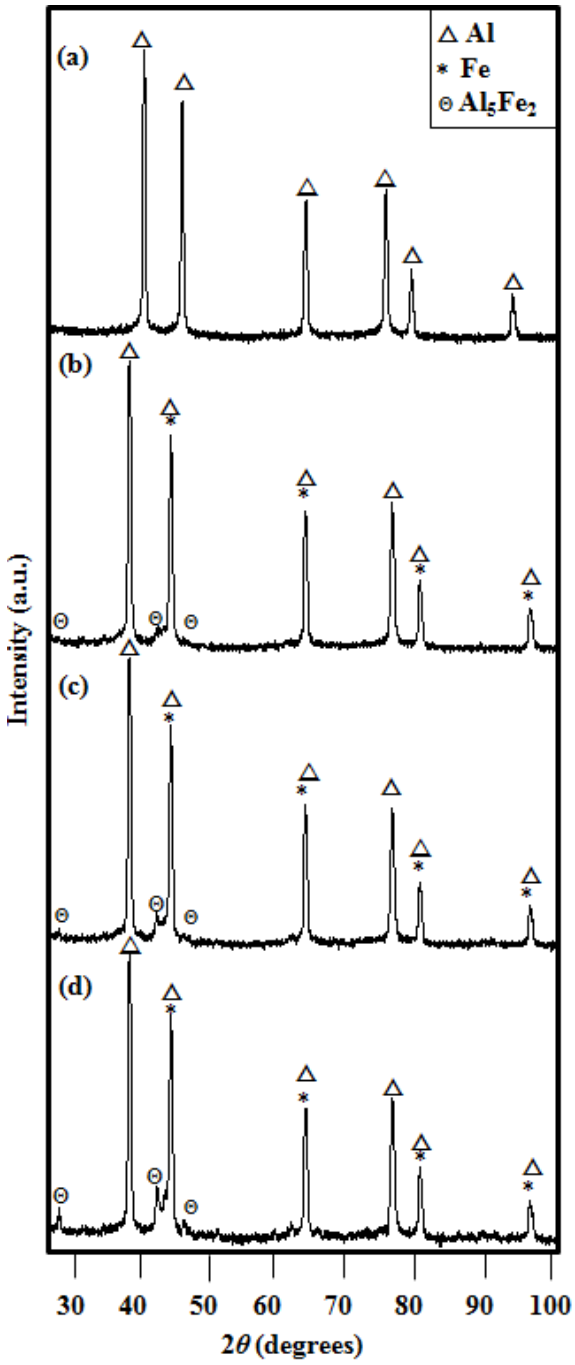

Fig. 5.35 XRD scans of (a) C1, (b) C2 (c) C3 and (d) C4 sintered compositions

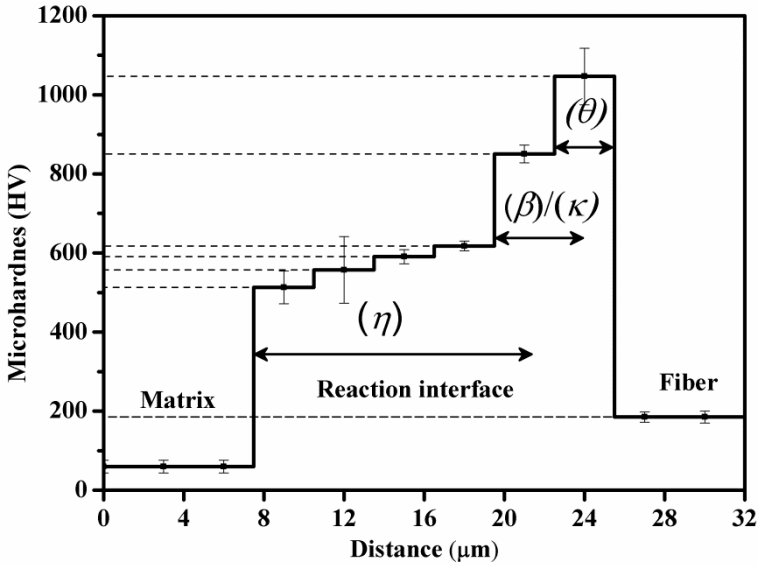

Fig. 5.36 Average microhardness across the interface for all compositions

Discussion: The interface is of a serrated morphology, as reported by (Shahverdi, et.al, 2002a) for iron coupons dipped in molten aluminium and (Springer et al., 2011) for aluminium-steel solid state interdiffusion at 600°C. EDS line spectra along the interface, alongwith x-ray diffractogram confirm the presence of Fe_2Al_5 (η) intermetallic phase. The microhardness profile along the reaction interface of approximately 15 μm, from the unreacted core of a fiber to the matrix, however, points towards the presence of other intermetallic products like $FeAl_3$(θ), but the same is undetected in XRD, presumably due to overlap in the peaks of highest intensities. Fe_2Al_5 (η) has a higher free energy than $FeAl_3$ (θ), but Fe_2Al_5 is reported to grow faster than $FeAl_3$ (Shahverdi, et.al, 2002a). From the detailed analysis of the reaction interface formed during solid-solid interdiffusion of low carbon steel-aluminium at 600°C; (Springer et al., 2011) have reported emergence of FeAl (β) and Fe_3AlC (κ) as thin interlayers on the steel side, abutting the dominant Fe_2Al_5 (η) intermetallic. In the present investigation, the reaction interface is found to be composed of steel fiber/ $FeAl_3$ (θ)/ FeAl (β) and Fe_3AlC (κ)/ Fe_2Al_5 (η)/ Al-0.5 wt.% Mg matrix. The same is conclusively established by microhardness measurements. As FeAl (β) and Fe_3AlC (κ) are reported to form as thin inter layers, an overlapping is observed in average hardness values, as shown by respective area dominance of the intermetallic phases in Fig. 5.36.

Considering the RI to be composed of three distinct components, the ROM for can be applied to estimate the RI hardness (H_{RI}) as:

$$H_{RI} = H_\theta V_\theta + H_\beta V_\beta + H_\kappa V_\kappa + H_\eta V_\eta \qquad \text{(Eq. 5.1)}$$

where H denotes the hardness and V is the volume fraction of respective components.

Similarly, the ROM can be extended to the composite as suggested by (Agarwala, et al., 1999) to predict the composite hardness:

$$H_C = H_M V_M + H_F V_F + H_{RI} V_{RI} + H_V V_V \quad \text{(Eq. 5.2)}$$

where the sub scripts *C*, *M*, *F* and *V* denote composite, matrix, fibers and voids respectively. H_V is equivalent to zero; therefore, Eq. 5.2 can be reduced to:

$$H_C = H_M V_M + H_F V_F + H_{RI} V_{RI} \quad \text{(Eq. 5.3)}$$

5.8.3 Mechanical properties

5.8.3.1 Matrix hardness

Effect of reinforcement content on matrix hardness is presented in Table 5.6.

Table 5.6 Matrix microhardness of sintered composites

Composition	Short steel fibers wt.% (vol.%)	Matrix microhardness (HV)	Porosity (vol.%)
C1	0	32	3.71
C2	10 (3.7)	41	5.21
C3	20 (7.9)	67	6.13
C4	30 (12.8)	74	8.95

Matrix microhardness is found to increase with increasing reinforcement content. But a linear correlation is not observed, rather, matrix hardness is found to be more closely dependent on sintered porosity. In comparison to ceramic reinforced AMCs, where a large difference in CTE (coefficient of thermal expansion) of about 5x for SiC and 3x for Al_2O_3 between the aluminium matrix and reinforcement, results in a higher dislocation density (Arsenault, 1988); only a two-fold difference in the present case will not generate the same level of mismatch strains upon cooling of the composite. Dislocations generated as a result would have piled up around the hard fibers; however, voids in the aluminium matrix will tend to act as sinks for annihilation these dislocations, thereby lowering the strengthening effect.

5.8.3.2 Damage evolution by compression

As-sintered compacts were compressed at room temperature and 250ºC; as described in *Section 4.4.9.2*. Since the aspect ratio of as sintered compacts was about 0.4, the compression data (load-displacement) was not converted to stress-strain. Purpose of the tests was to merely ascertain the damage evolution mechanism under both temperature regimes.

As shown in Fig. 5.37, brittle cracks develop in the reaction interface at room temperature compression, there is likewise a reduction in resistance to deformation offered by the

composite and consequently at approximately 50% nominal strain, to which the compacts were tested, the unreinforced compact show better load bearing ability Fig. 5.38.

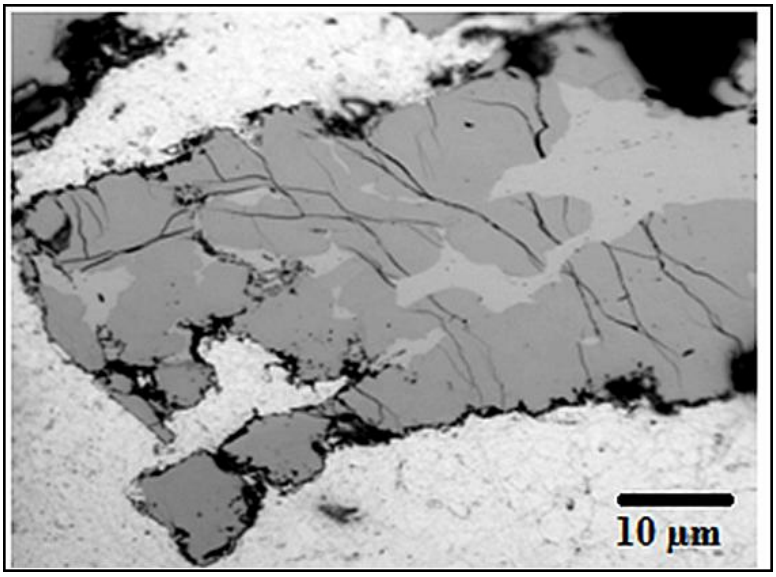

Fig. 5.37 Micrograph showing crack morphology after room temperature compression

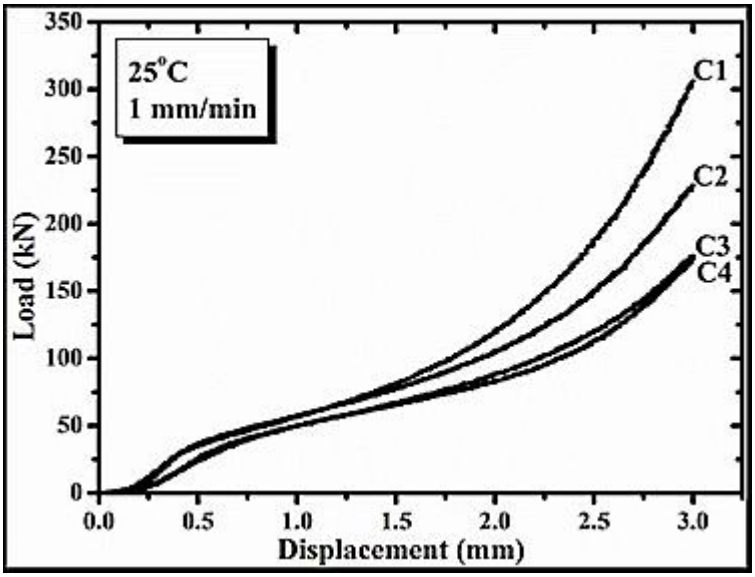

Fig. 5.38 Load-displacement curve for room temperature compression tests

(Friedrich, et al., 1974) have reported an increase in strength of the composite upto a critical RI thickness of about 6µm, beyond which rapid deterioration was observed. Since the system is composed of the matrix, RI and the reinforcement; the composite strength depends on the volume fraction of the RI, which in the present case is brittle (but stronger than the ductile matrix), hence lesser the RI volume fraction, higher the composite strength. An optimum RI thickness is modeled, based on the site of failure initiation (RI or reinforcement) according to

their relative volume fractions. In the first case, wherein, the RI volume fraction is below the optimum level, failure will start from the reinforcement and from the rule of mixtures, the RI will contribute in increasing the composite strength. In the second case, wherein, the RI volume fraction is higher than the optimal level, the crack initiation will commence from the RI at multiple points- causing reinforcement failure due to stress concentration at crack initiation sites- finally resulting in debonding between fiber and RI as the multiple cracks in RI act as stress raisers. Most of the deformation at room temperature is consumed in filling up of the retained porosity in C3 and C4 compositions. As observed in Fig. 5.37; the cracks converge and the intermetallic reaction interface develops fine isolated cracks, presumably from the hydrostatic stress generated through the soft matrix. Cracks grow into the unreacted steel fiber and finally cracks cause fiber splitting.

At 250°C the matrix is softened and starts to flow, resulting in opening up of previously developed cracks and shearing of the steel fibers is observed (Fig. 5.39) at regions where the intermetallic phase extends deep within the fibers. This flow of the matrix alongwith sheared fibers creates fiber-fiber interlocks, which resist further matrix flow, thereby increasing their load bearing capacity at elevated temperature as also observed by (Karpinos, et al., 1978)for composites with Fe-Al reaction interface of greater than the optimum range.

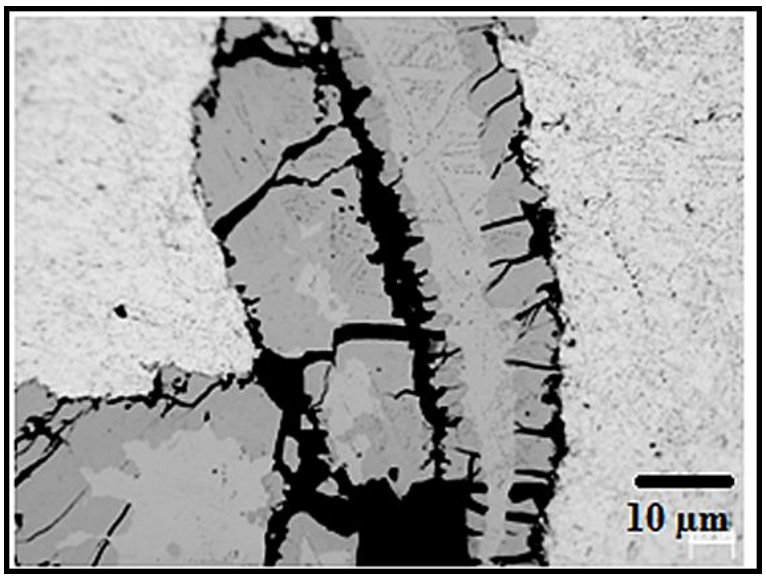

Fig. 5.39 Micrograph showing crack morphology after compression at 250ºC

In the present case, reinforcement morphology undergoes significant modification by cracking of fibers and deformation induced dispersion of cracked intermetallic rich particles in the ductile flowing matrix. This could have led to dispersoid strengthening of the matrix like

particle reinforced AMCs. Thereby, an increase in load carrying ability of the reinforced compositions is obtained (Fig. 5.40).

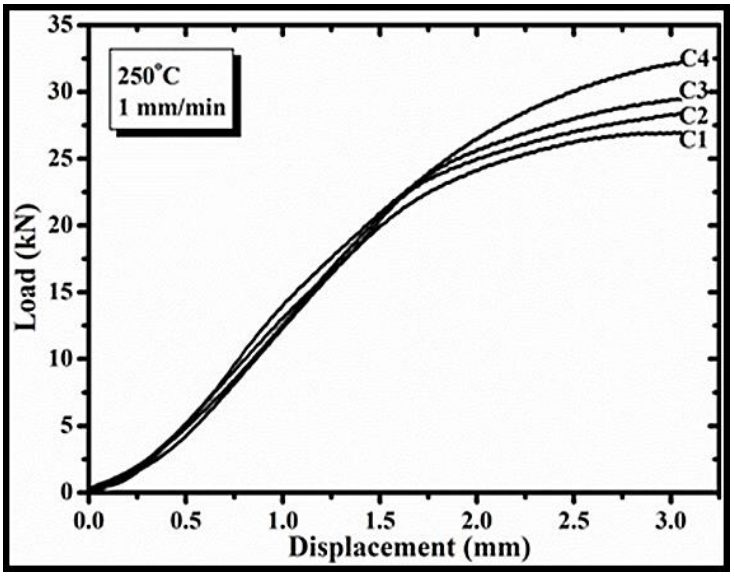

Fig. 5.40 Load-displacement curve for elevated temperature compression test

5.8.3.3 Flexure strength

Flexure behavior of the compositions was evaluated by 3-point bend tests of the monolithic as well as composite samples as per procedure described in *Section 4.4.9.3*. Strain to failure decreased with increasing reinforcement content.

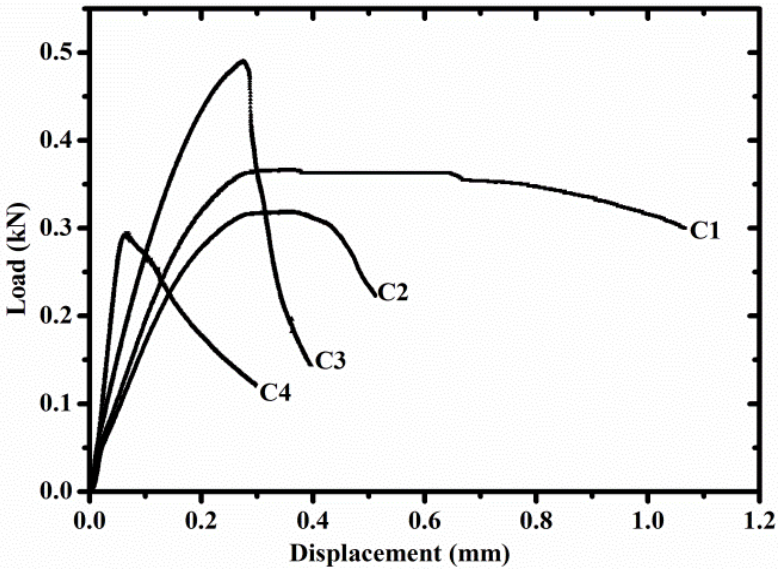

Fig. 5.41 Load-displacement curves from 3-point bend test

Stress relaxation did not lead to failure by rupture in case of C1 and C2 compositions, both samples displayed the ability to deform plastically. Rupture was observed for C3 and C4 compositions. As there is marked decrease in room temperature ductility on account of brittle failure of the intermetallic fraction of the reinforcement, the flexural rigidity also follows a similar behavior. The unreinforced specimen under 3-point bend test also has the lowest level of porosity, as evident from the displacement before stress relaxation occurs (Fig. 5.41). The reinforced compositions under the pure bending mode of loading, achieve a peak load for C3 composite, with C2 having a low reinforcement volume fraction whilst C4 fails prematurely on account of high retained porosity and excessive volume of brittle intermetallic phases.

5.8.4 Wear behavior

Compositions were characterized for wear resistance as per methodology described in *Section 4.4.10.1*, by ball-on disc tests.

Scanning electron micrographs of wear tracks and collected debris are shown in Fig. 5.42, for respective compositions. The room temperature wear behavior for the monolithic composition (C1) is characteristic of pure aluminium, wherein, the wear debris are mainly composed of large chip-like aluminium flakes scattered on both sides of the wear track. Flaky debris tend to dislodge as a result of delamination failure (Suh, 1977) leaving behind large craters, indicative of adhesive wear. As there is an increase in the reinforcement volume fraction, the morphology of the debris changes to a fine powder (C3-C4), mainly composed of Al and Fe oxides and intermetallics of type Fe-Al.

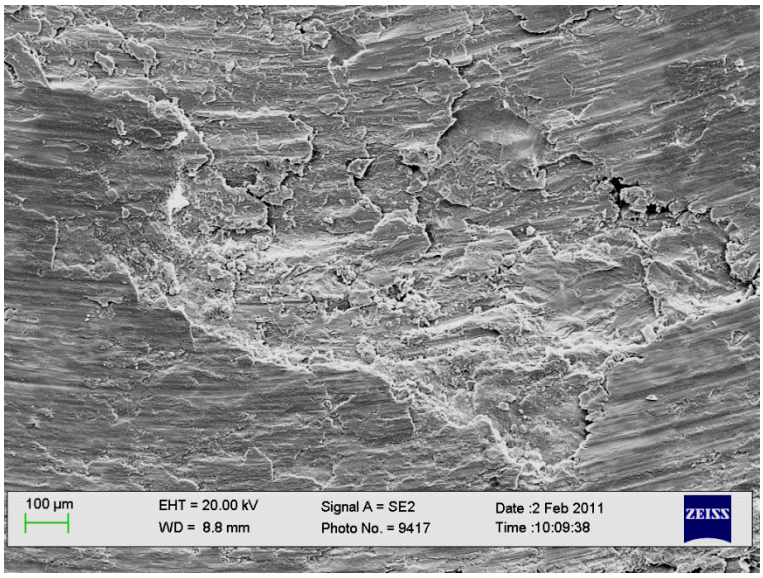

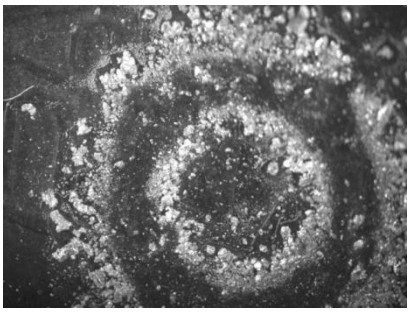

C1

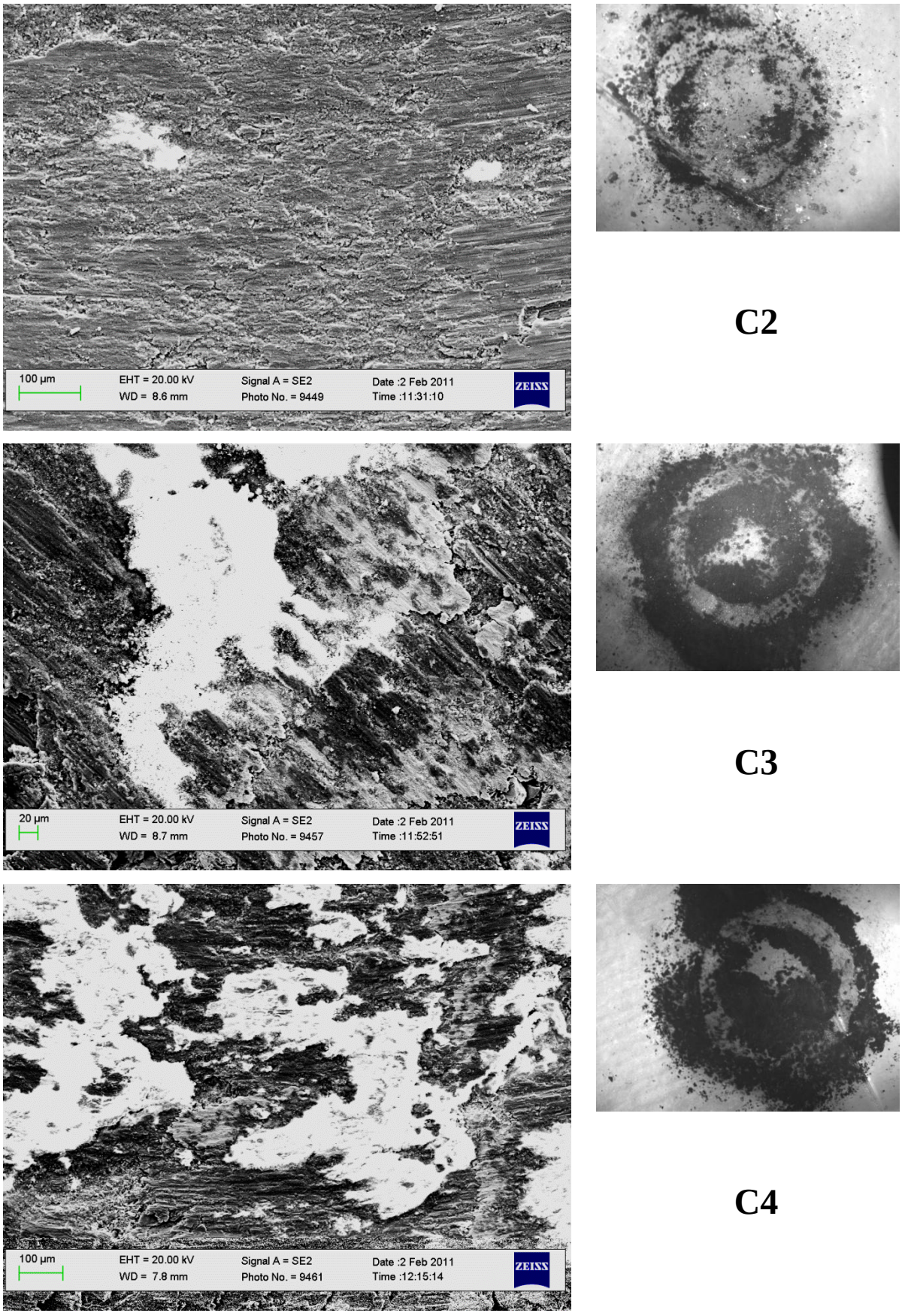

Fig. 5.42 Scanning electron micrographs of wear scar and optical macrographs of wear debris for Al-0.5 wt.% based compositions

Change in debris morphology and size can be attributed to the formation of a third body tribo-layer that causes grooving and micro-cutting. This tribo-layer is also reported to act as a solid lubricant **(**Singh & Alpas, 1995) thereby ensuring a more constant coefficient of friction (Fig.5.43). The increased hardness of the composites based on higher matrix hardness and presence of hard intermetallic phases results in lower groove depth thereby increasing the wear resistance. It can be seen the steel fibers flatten out and cover a larger area over the wear track, resulting in a mixed-mode contact of the counterface ball with the composite. Fiber fragmentation occurs as a result of excessive contact stresses between the composite and counterface ball; these fragments are larger initially but undergo a grinding action, resulting in fine dispersal of these ground oxides over the wear track.

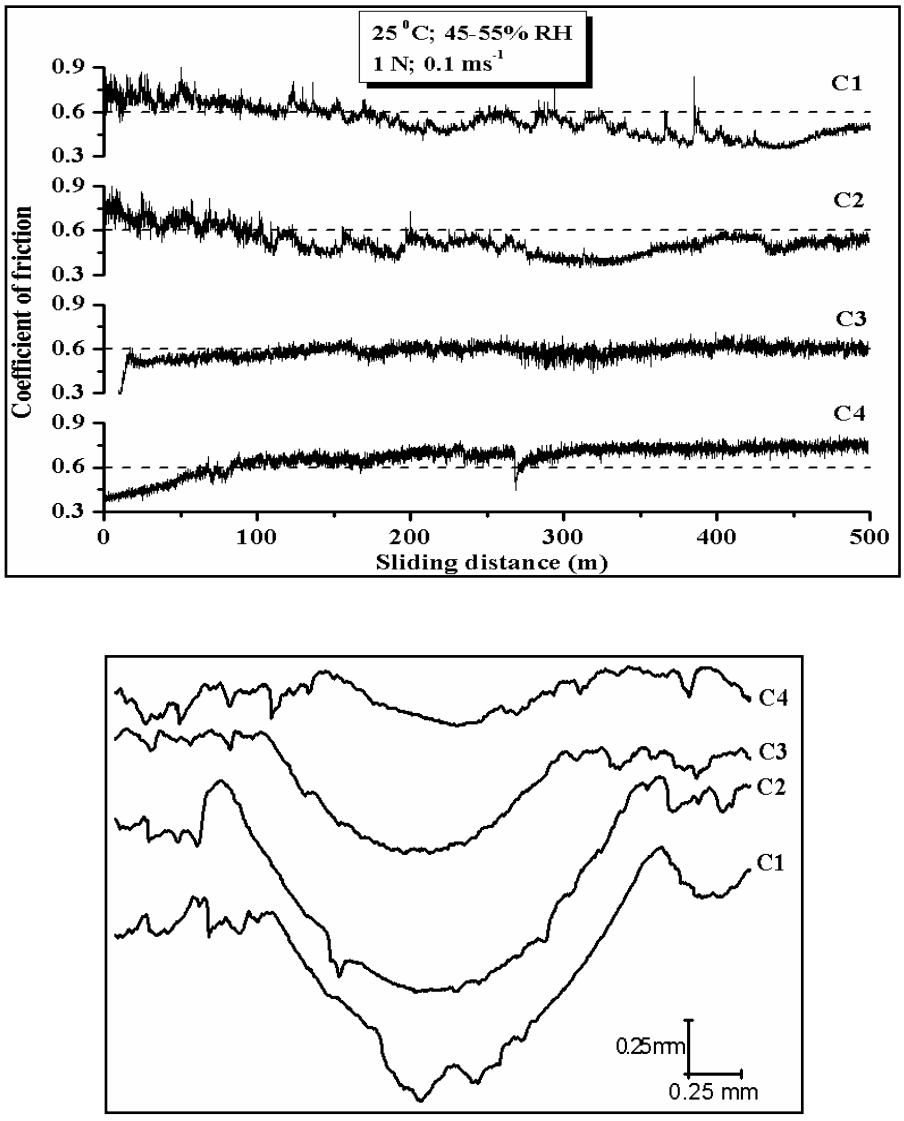

Fig. 5.43 Coefficient of friction and wear groove traces for room temperature wear tests

In the present study, a relatively smooth coefficient of friction plot is achieved for C3 and C4 compositions. Short steel fibers are commercially used in phenolic resin based automobile brake shoes/pads. They serve two major purposes, namely (1) act as a coefficient of friction stabilizer (2) enable a scrubbing action on the cast iron brake drum/disk counterface, ensuring removal of corrosion (rust) products and accumulated dirt (Jang et al., 2004). Formation of an abrasive tribolayer between the counterface Cr-steel ball and the composite disk, further ensures a stable coefficient of friction, against intermittent jumps in coefficient of friction, caused by exposure of fresh delaminated matrix surface which adheres to the ball for C1-C2 compositions. Delaminated debris of aluminium are oxidized by high contact plane temperature, forming Al_2O_3; which resists further delamination by forming an abrasive tribolayer, thereby decreasing coefficient of friction (Mandal, et al., 2004). These two wear processes (delamination-oxidation), proceeding in tandem, generate fluctuations in coefficient of friction.

The wear tracks from elevated temperature (250°C) tests for all compositions are shown in Fig. 5.44. No debris were generated during this test.

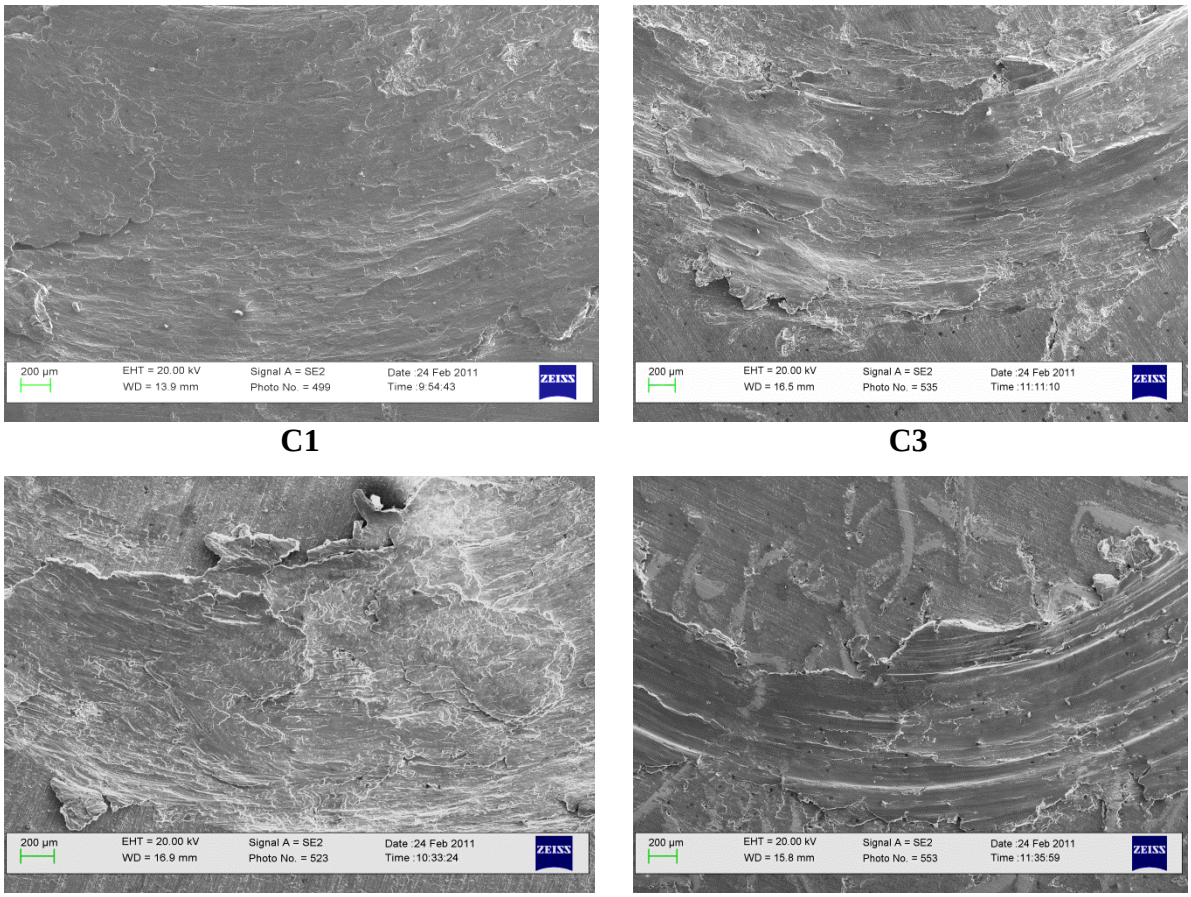

Fig. 5.44 SEM micrographs of wear tracks for wear tests at 250°C

A decrease in wear scar width is observed for increasing reinforcement content, as shown in Fig. 5.42. Wear scar width is reportedly used as a direct indicator of wear resistance, broader the scar lower is the wear resistance. For C1 composition, the test was aborted midway on account of excessive build-up of aluminium, akin to seizure, on the counterface ball. Such phenomenon has been well reported by (Singh & Alpas, 1995) for high temperature wear of AA6061 and AA6061/Al2O3 composites, wherein a transition temperature of about 150°C is found to establish the onset of severe wear by delamination failure. The present study at 250°C is above the generally accepted transition temperature for aluminium alloys and composites and hence in composition C2 similar behavior is observed, with coefficient of friction larger than unity (Fig. 14), signifying sticking rather than sliding.

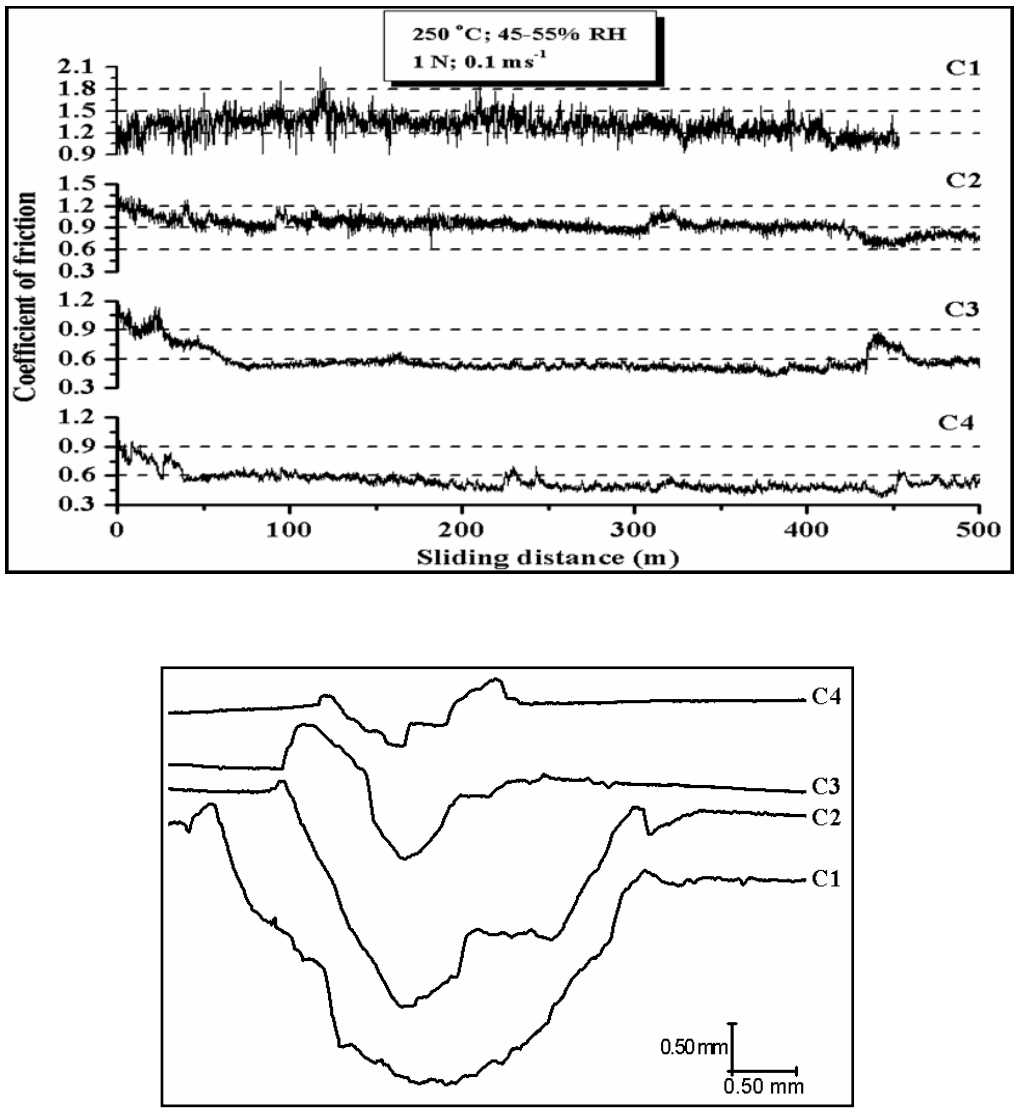

Fig. 5.45 Coefficient of friction and wear groove traces for elevated (250ºC) temperature wear tests

For C3 and C4; a reversal in friction coefficient is observed, wherein, sliding resumes after a short initial run-in period. From the analysis of wear tracks, it is also found that there is a continuous decrease in wear groove width and shallowing out of the groove depth with increasing reinforcement content. The short steel fibers act as a reinforcing bed over which soft a layer of soft aluminium is found to be smeared. Smearing of aluminium matrix over the steel fibers can also be seen to reduce the wear scar width, as shown in (Fig. 5.46).

The protrusion of aluminium from in between the reinforcing fibers will further lead to oxidation and thereby generate fine aluminium oxide which would have countered the sticking effect and hence stabilized the coefficient of friction. Such behavior can be deemed to be anti-frictional (Prasad, 1992).

.

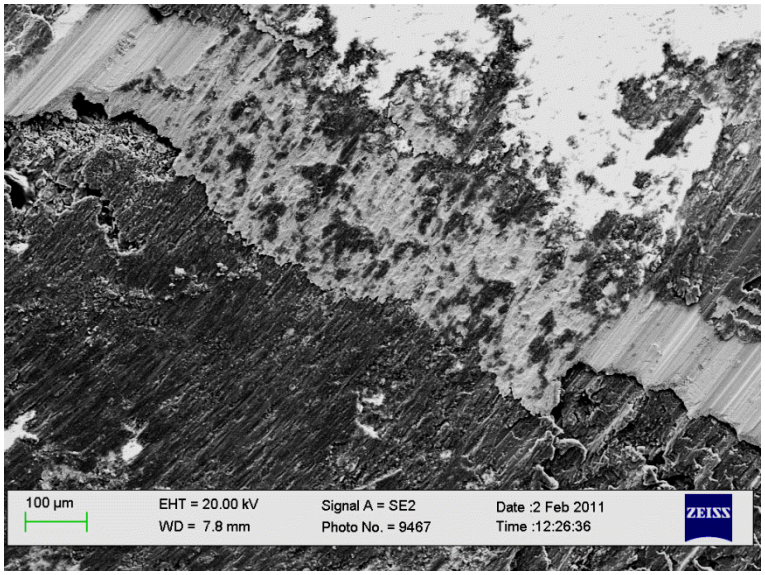

Fig. 5.46 Fiber-matrix interaction under dry sliding wear test (250º)

The wear volume loss for room temperature and elevated temperature dry sliding has been summarized in Fig.5.47. Notably there is a decrease in material volume loss with increasing reinforcement content for both the categories of tests. However, the smearing of aluminium and mixed-mode contact of the matrix and reinforcing fibers with counterface ball results in equivalent or even higher wear resistance for C3 and C4 compositions.

Wear studies by (Mandal et al., 2004) using pin-on-disc configuration have reported specific wear rates for a similar cast AMC composite in the range of 4- 20 x 10^{-3} mm^3 m^{-1} at 10 N/1.8 ms^{-1} normal load for 500 m dry siding conducted at room temperature. In comparison, the present work yields a magnitude of difference (10^{-3}) for ball-on-disc configuration wear test at 1 N/0.1 ms^{-1} normal load for the same distance. Assuming the comparative study was conducted using flat-flat contact, the present work utilized ball-flat contact, which despite the

lower load (1 N against 10 N) develops equivalent Hertzian contact stresses at the contact plane.

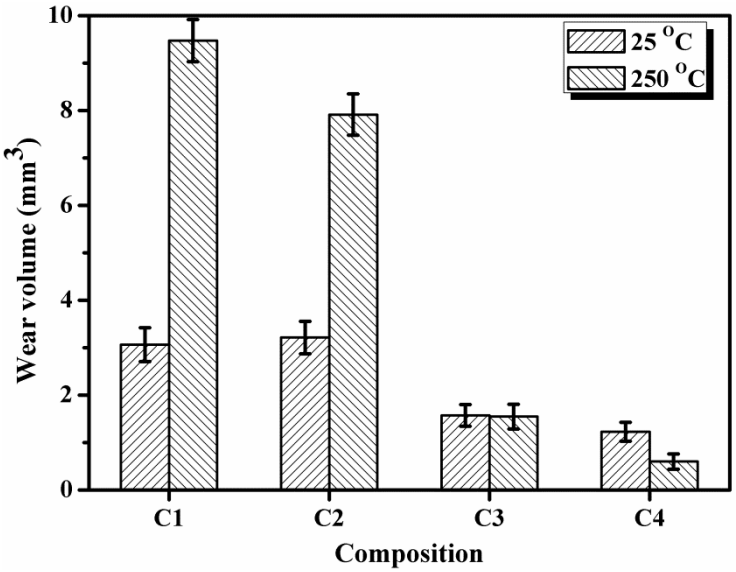

Fig. 5.47 Wear volume loss for dry sliding wear tests at room temperature and 250ºC

5.8.5 Sinter-forging of Al-0.5 wt.% Mg based compositions

Pre-sintered briquettes of Al-0.5 wt.% Mg based compositions were hot forged in a constrained die, as described in *Section 4.3.7*. Forging temperature was optimized by extensive experimentation conducted between 0.2 T_m to 0.7 T_m (melting point of the matrix alloy on absolute scale K); optimal processing temperature was found to be 0.7 T_m (375ºC) as the maximum permissible temperature to achieve a deformed sub-structure with dissolution of prior particle boundaries whilst avoiding Fe-Al interdiffusion. Forging was carried out on a manually operated Weingarten-type friction-screw press of 100 kN capacity, with ram speeds maintained in the 250 - 275 mm s^{-1} range. (Venugopal, et al., 1990) have reported on average strain rates (actual strain rates depend upon specimen temperature), attained by Weingarten friction screw-type presses to be in the 10 s^{-1} range. Imposed deformation strain, strain rate and temperature are reported to be critical in hot consolidation of sintered Al-P/M preforms (Greasley and Shi, 1993; Shi and Greasley, 1992; Iwata, et al., 1989). Particularly in the case of aluminium P/M, wherein, elimination of sintered porosity and a homogeneous microstructure free from prior particle boundaries (PPBs) is an essential requirement for increments in mechanical properties equivalent to wrought counterparts (Mann, et al., 2011). Forged briquettes were immediately quenched in cold water after ejection.

5.8.5.1 Estimation of strain in closed die constrained forging

It was important to quantify the imposed strain, for which a commercial FEM program, ABAQUS 6.3.10^{TM} was used. Geometry of the developed tooling was modeled alongwith a deformable aluminium briquette of similar dimensions using Ramberg-Osgood material behavior. A mesh of 2-D, plain strain, quadratic elements was simulated for a single step deformation cycle at 10 s^{-1} strain rate, equal to the average strain rate from the present work. Fig. 5.48 shows the FEM modeled forging set-up, with simulated positions of the top punch and deforming briquette.

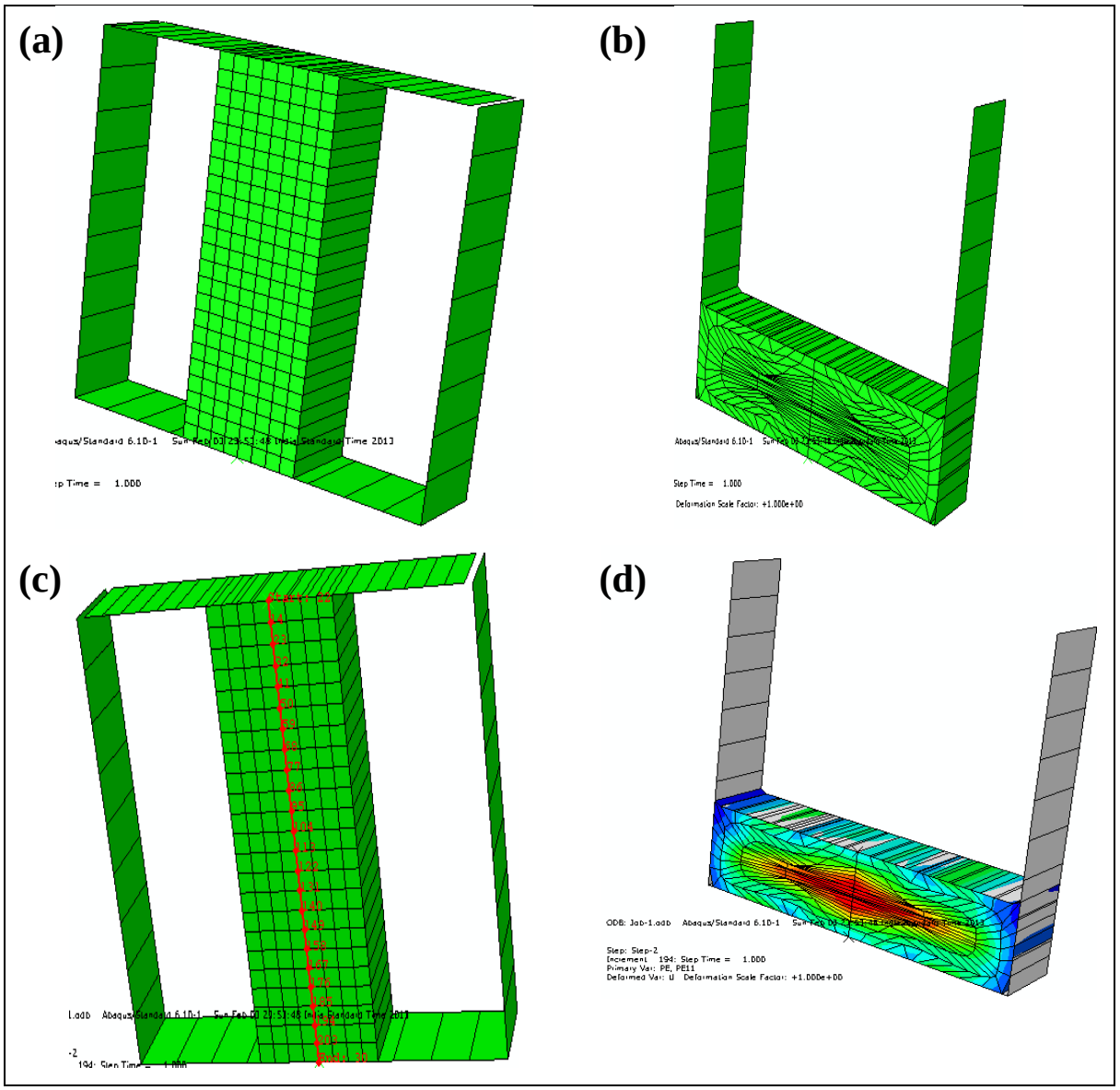

Fig. 5.48 FEM plots showing (a) TDC of punch (b) BDC of punch (c) path along briquette for estimation of plastic strain (d) equivalent plastic strain map over deformed briquette

Plastic strain distribution over the briquette centerline is shown in Fig. 5.49. As expected, a non-uniform deformation regime is observed for material elements based on their respective locations. It can be assumed that an effective mean true strain of 1.2 was delivered by constraints on the briquette, imposed by tooling employed in the present work. Threshold limits of strain, strain rate and deformation temperature have been established for PPB dissolution in Al-P/M systems by (Greasley and Shi, 1993). The present employed combination of strain, deformation temperature and strain rate 1.2, 0.7 T_m, and 10 s^{-1} lies in-between 0.8, 0.7 T_m (insufficient) and 1.6, 0.7 T_m (sufficient)- insensitive to strain rate; is less than the sufficient strain to form a completely recrystallized microstructure by annihilation of PPB's; only a partial dissolution could be expected. The same is also confirmed by Fig. 5.48 (d), where strain intensity over the briquette is mapped by varying colors; red-maximum to blue-minimum.

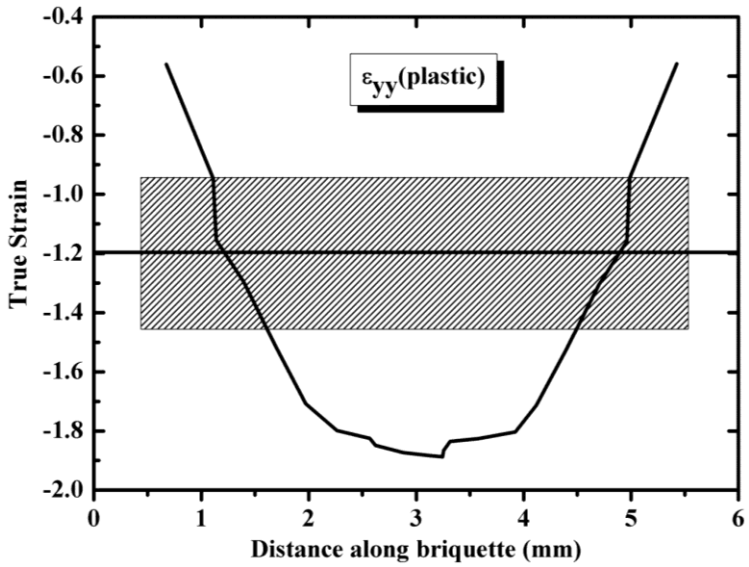

Fig. 5.49 Plastic strain along path shown in Fig. 5.48 (c)

5.8.5.2 Microstructure, reaction interface, density and hardness of Al-0.5 wt.% Mg based sinter-forged compositions

Micrographs of short-transverse section (S-T) from sinter-forged briquettes of monolithic Al-0.5 wt.% Mg have been shown in Fig. 5.50 as: (a) fully deformed high strain region (b) semi-deformed intermediate strain region and (c) largely underfomed low strain region-forging direction is vertical. Establishment of strong metallurgical bonds between neighboring particles by disruption of oxide layer, with characteristic "pancaking" of particles is observed for high strain regions, compared to retention of an almost as-sintered microstructure for zones experiencing limited lateral flow during deformation.

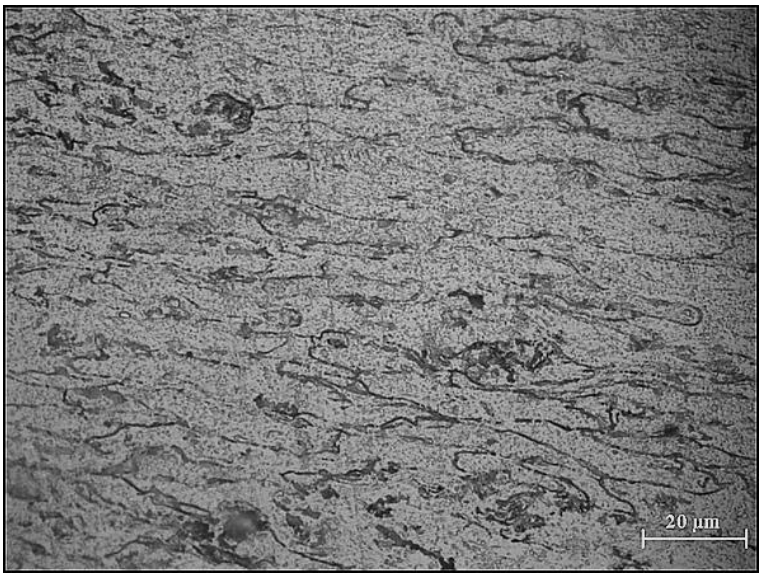

(a)

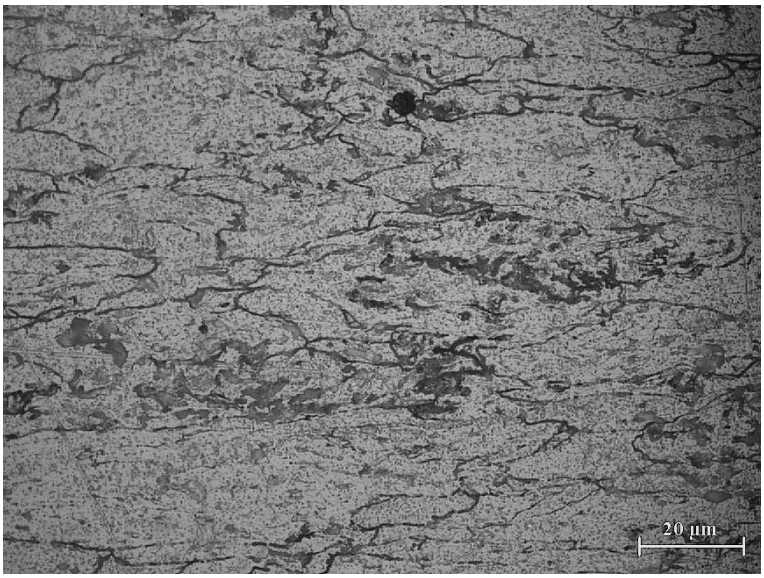

(b)

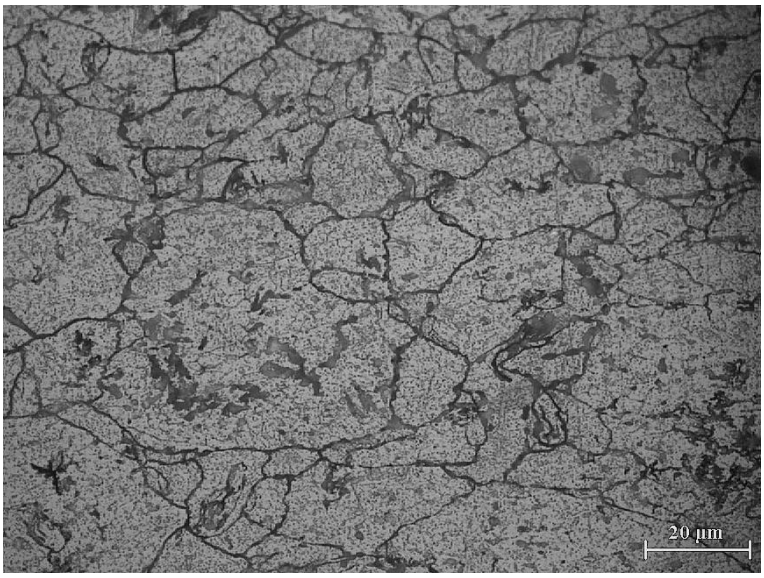

(c)

Fig. 5.50 Short-transverse (S-T) section optical micrographs (etched) of sinter-forged Al-0.5 wt.% Mg briquettes

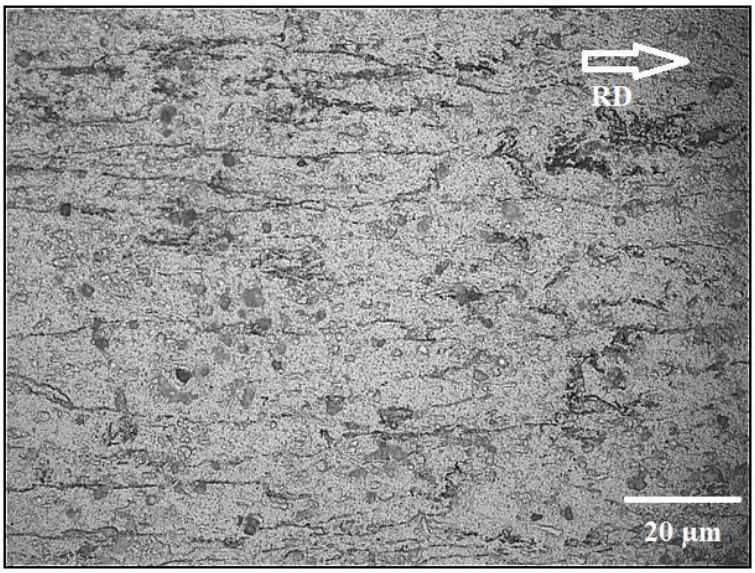

Fig. 5.51 L-T (long-transverse) section optical micrograph (etched) of sinter-forged and rolled Al-0.5 wt.% Mg strip

Sinter- forged briquettes of Al-0.5wt.% Mg unreinforced composition were hot rolled at 300ºC as per details given in *Section 4.3.8.* Smaller initial reduction of 10 % was given to avoid crack formation; subsequently 3 further reductions of 20 % were tolerated without any visible surface cracking. Microstructure of rolled strip in the L-T (long transverse) plane is shown in Fig. 5.51. It can be seen that the relatively low strain rate deformation process helped achieve a homogeneous microstructure throughout the strip thickness. Few PPBs were visible, thereby resulting in finer dispersion of the cracked surface oxide covering the powder particles.

Scanning electron micrograph of Al-0.5 wt.% Mg- 20 wt.% (C3) short steel fiber sinter-forged briquettes from the S-T plane is presented in Fig. 5.52 (a). Fiber cracking and dispersion is observed as a result of deformation induced flow of the soft matrix. Reinforcement banding as reported by (Chawla, et al., 2002) for sinter-forged SiC particulate reinforced AMC, is not clearly established in the present work. This can be attributed to: (1) bi-directional deformation of the sintered briquette- horizontal lateral flow with vertical compression, achieved in a single step (2) higher loss in aspect ratio of starting fibers due to fiber cracking, in comparison to smaller reductions for particulate reinforcements.

Fig. 5.52 (b) shows the fiber-matrix interface, it was found to be composed of two distinct layers of Fe-Al intermetallic reaction products. The average thickness was about 5 µm as determined from EDS line scan through the interface (Fig. 5.52 (c)).

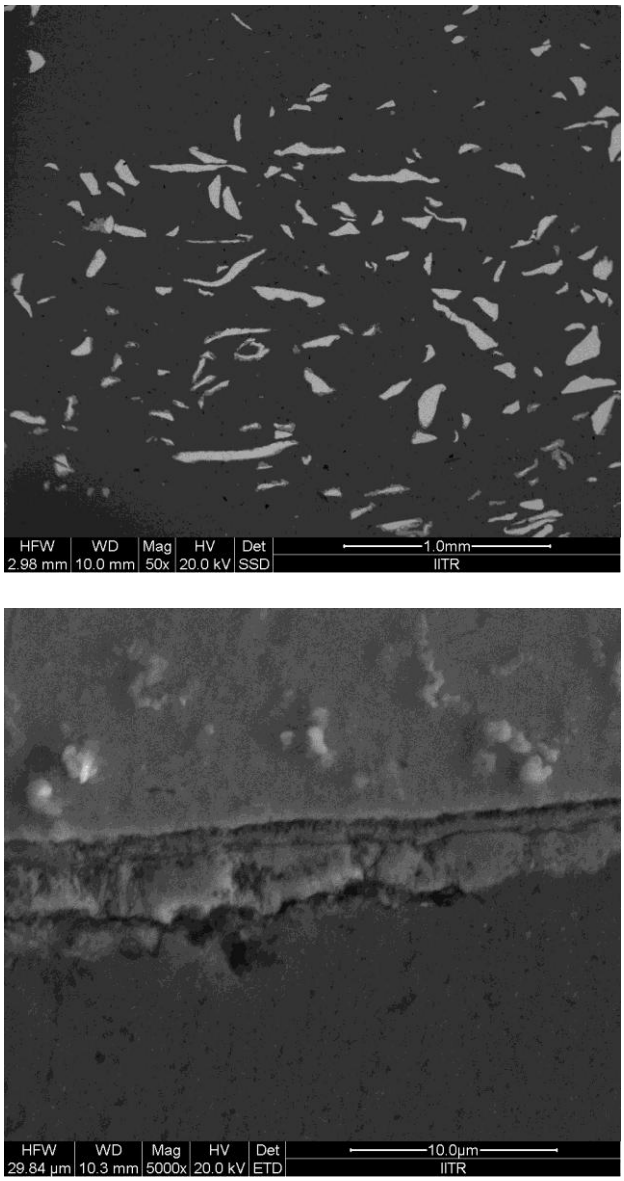

(a)

(b)

(c)

Fig. 5.52 Scanning electron micrographs of (a) Al-0.5 wt.% Mg- 20 wt.% short steel fiber sinter-forged composite (b) reaction interface (c) EDS line scan through reaction interface

Microhardness of the thin reaction interface could not be conclusively determined. Kirkendall porosity at the Al-RI interface, observed in sintered specimens was almost non-existent after forging, resulting in a well faceted joint. Compressive stress generated by immediate quenching of the forged briquette could be responsible for elimination of interfacial porosity; also suggested by (Springer, et al., 2011) for Fe-Al weldments, where avoidance of 660-400ºC temperature range after welding is reported to result in a sound joint.

From the elemental counts detected by EDS as shown in Fig. 5.53, the presence of $FeAl_3$ (θ) could be established. However, Fe_2Al_5 (η), the dominating phase which should have developed during sintering at 620ºC, was not detected post forging of sintered briquettes. The brittle Fe_2Al_5 (η) could have entered the solution (matrix) after causing extensive fiber cracking- as observed during hot compression tests of sintered compositions. (Agarwala et al., 1999) have also reported on similar solid –solutionizing of reaction products for cast wire reinforced AMCs. Hence, a considerable volume fraction of reaction products should offer dispersoid strengthening to the ductile matrix.

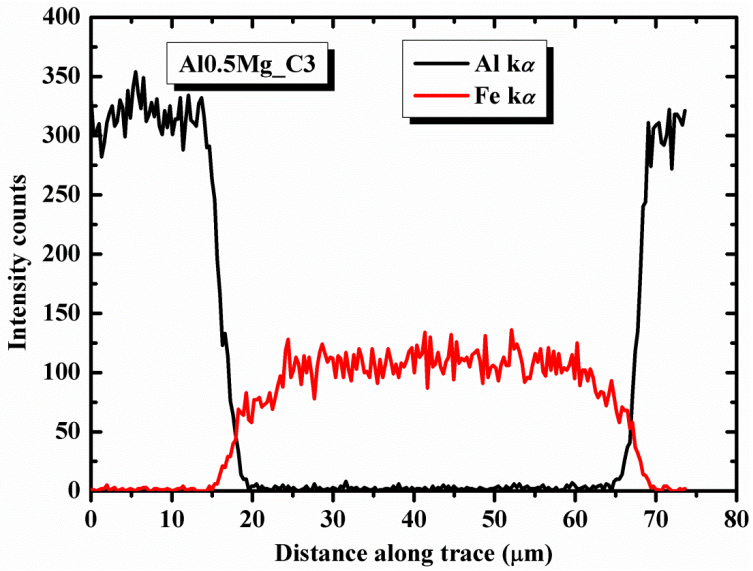

Fig. 5.53 Elemental profile along EDS line scan shown in Fig. 5.50 (c)

Density values for sinter-forged composites have been presented in Table 5.7, as determined, very low values (< 1 vol.%) of final retained porosity, characteristic of a fully consolidated material are obtained. Deformation strain employed was sufficient to cause disruption of the oxide layer leading to better bonding between powder particles. Some porosity was observed as surface cracks on the briquette surface, however, effect of intermetallic particles dispersed in the matrix and disruption of oxide, which also would have gone into the matrix, have not been considered for determining final density.

Effect of forging based consolidation on as-sintered matrix microhardness has been reported in Table 5.8, similar to increments in composite density, the matrix also experiences hardening due to: (1) thermal mismatch stresses are retained around steel fibers, creating a higher dislocation density in a near fully dense matrix, without any voids (2) uniform dispersion of disrupted alumina and $Fe_2Al_5(\eta)$ intermetallic in the matrix, causing dispersoid and solid-solution strengthening.

Table 5.7 Sinter-forged densities of Al-0.5 wt.% based compositions

Composition	Short steel fibers wt.% (vol.%)	Theoretical density ($g\ cm^{-3}$)	Sintered density ($g\ cm^{-3}$)	Forged density ($g\ cm^{-3}$)	Porosity (vol.%)
C1	0	2.69	2.59	2.68	0.37
C2	10 (3.7)	2.88	2.73	2.86	0.69
C3	20 (7.9)	3.10	2.91	3.08	0.65
C4	30 (12.8)	3.35	3.05	3.29	0.90

Table 5.8 Matrix microhardness of sinter-forged compositions

Composition	Short steel fibers wt.% (vol.%)	Matrix microhardness (as-sintered) (HV)	Matrix microhardness (sinter-forged) (HV)
C1	0	32	54
C2	10 (3.7)	41	63
C3	20 (7.9)	67	84
C4	30 (12.8)	74	92

5.8.5.3 Mechanical properties of sinter-forged compositions

Tensile behavior (as per *Section 4.4.9.4*) of sinter-forged and sinter-forged-rolled, unreinforced Al-0.5 wt.% Mg is shown in Fig. 5.54. UTS of 167 MPa was achieved by the forged specimen with 18% elongation to failure; in comparison to the rolled and annealed specimen which failed at UTS of 116 MPa, but with 28% elongation. UTS values of P/M processed pure aluminium processed from cast or wrought routes is considerably lower than values determined in the present investigation. Disrupted oxide layer is reported to provide dispersion strength to the ductile aluminium matrix (Abouelmagd, 2004), such that the aluminium actually behaves like an in-situ Al- Al_2O_3composite, which fails at higher stress in comparison to counterparts processed by other routes. Higher elongation to failure for rolled specimens, which were annealed from 300ºC, to remove residual stress effects from punching out on flat tensile specimens; could be attributed to recovery of strain induced dislocations in the matrix. Moreover, from microstructural examination of rolled strip, lower retained PPB's would have contributed to enhanced metallurgical bonding between powder particles. This is further

confirmed by higher volume of small sized rounded dimples for rolled samples in comparison to uneven sized dimples with cleavage formation for forged samples; observed from fractographs of the respective fracture surfaces of the samples, as shown in Fig. 5.55.

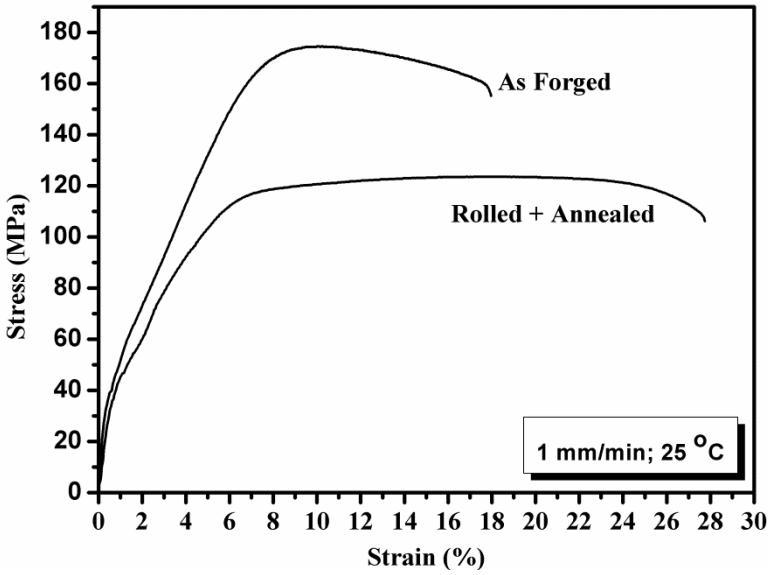

Fig. 5.54 Stress-strain curve from tensile tests of unreinforced sinter-forged and sinter-forged-rolled Al-0.5 wt.% Mg

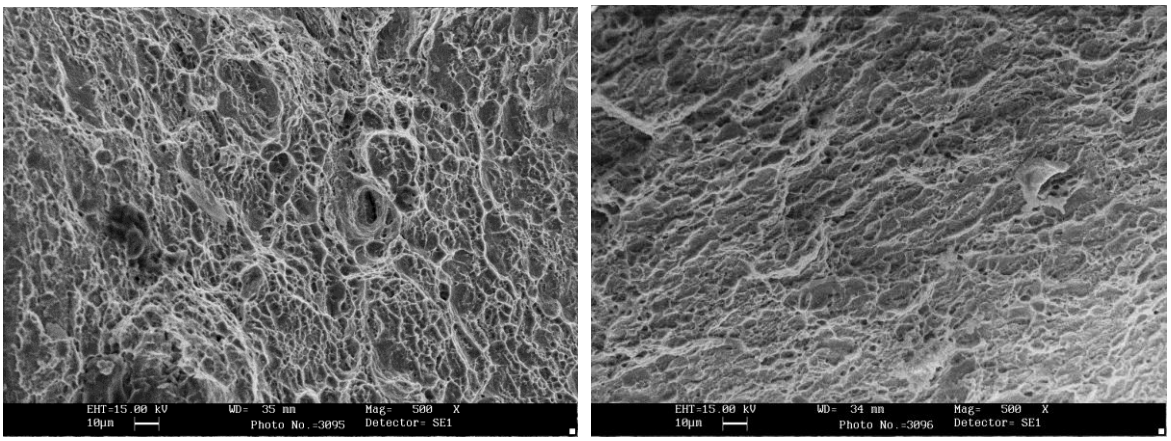

(a) **(b)**

Fig. 5.55 Scanning electron micrographs showing tensile fracture surfaces for unreinforced (a) sinter-forged (b) sinter-forged-rolled Al-0.5 wt.% Mg

Room temperature compression strength was determined as per methodology described in *Section 4.4.9.1*. True-stress vs true-strain curves for both as-forged and forged-annealed conditions are shown in Fig. 5.56. After an initial work hardening, flow softening was observed for both the specimens, without any cracking of the test pins. Higher initial slope and flow stress observed for forged composition could be due to grain pinning by undisloved surface oxide in comparison to a more ductile behavior observed after annealing at 300ºC,

wherein dissolution of dislocations could have led to recovery and thereby softening of the matrix.

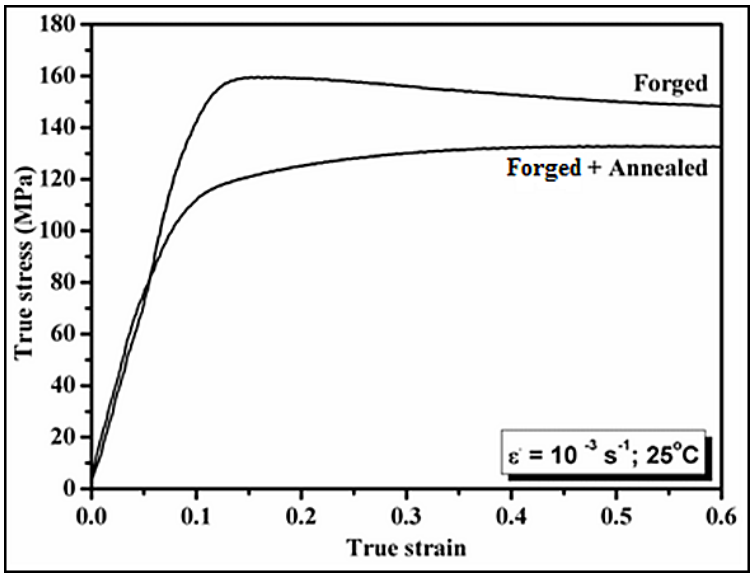

Fig. 5.56 True stress- true strain curves from compression test of unreinforced sinter-forged Al-0.5 wt.% Mg

Tensile behavior of as-forged Al-0.5 wt.% Mg based composites is shown in Fig. 5.57, UTS values with corresponding stains to failure are tabulated in Table 5.9. Inadequate strengthening of the matrix (UTS 167 MPa) is seen with even higher deterioration in elongation to failure. Such failure is characteristic of premature debonding of the reinforcing fibers from the matrix. As confirmed from fractographs, shown in Fig. 5.58.

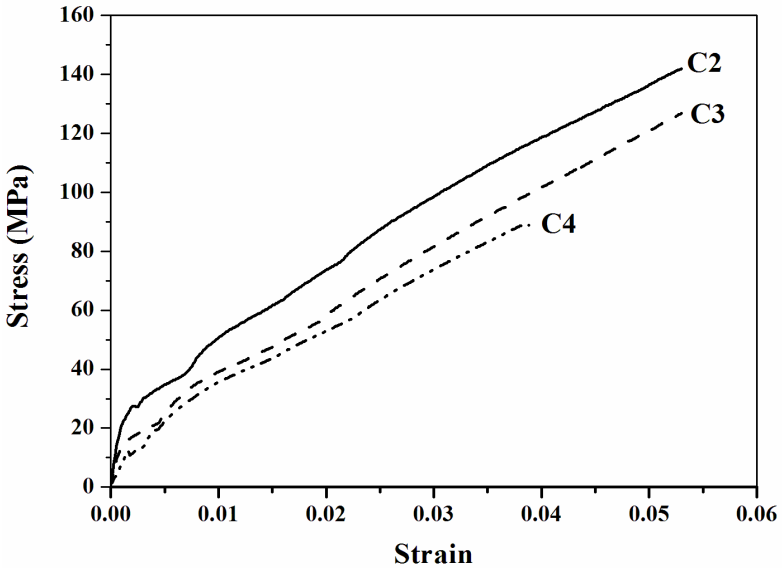

Fig. 5.57 Stress-strain curves from tensile tests of reinforced sinter-forged Al-0.5 wt.% Mg based composites

Table 5.9 UTS and elongation for Al-0.5 wt.% Mg based as-forged composites

Composition	Short steel fibers wt.% (vol.%)	UTS (MPa)	% Elongation
C2	10 (3.7)	141	5.7
C3	20 (7.9)	127	5.5
C4	30 (12.8)	87	3.9

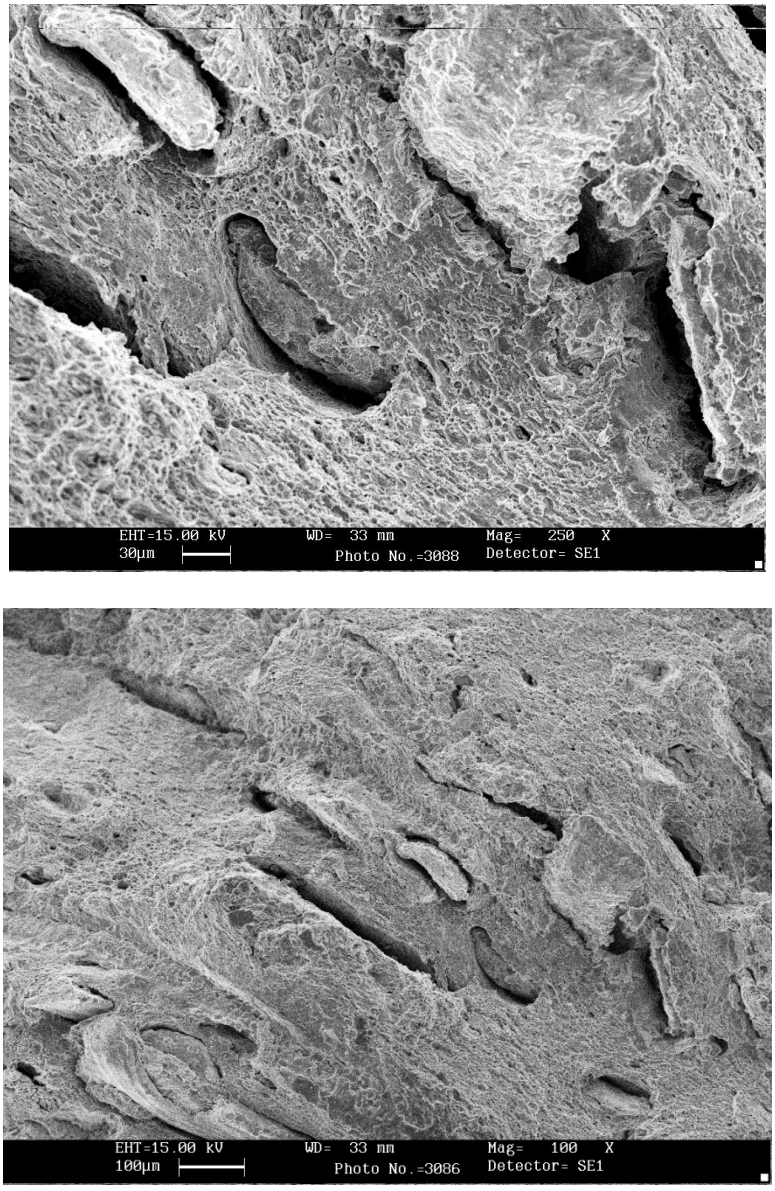

Fig. 5.58 Scanning electron micrographs showing tensile fracture surfaces for as-forged Al-0.5 wt.% Mg based composites

Shallow dimples are observed, indicative of insufficient straining of the matrices. Predominant failure mechanism was fiber-matrix interfacial debonding, indicated by elongated cavities in the matrix. For improving the overall failure characteristics of the reinforced compositions, the forged briquettes were rolled, followed by annealing from 300ºC. Tensile behavior of rolled composites is shown in Fig. 5.59.

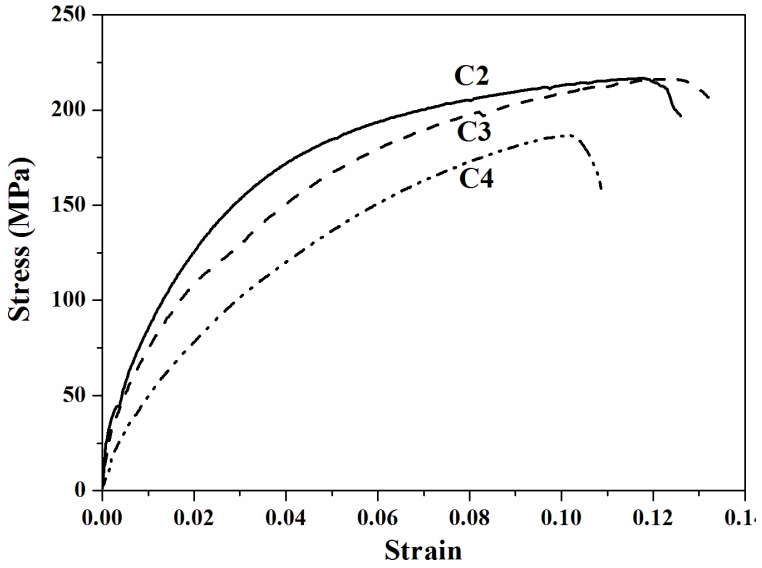

Fig. 5.59 Stress-strain curves from tensile tests of sinter-forged-rolled Al-0.5 wt.% Mg based composites

Increments in UTS and elongation to failure were determined after rolling and annealing treatment, as tabulated in Table 5.10.

Table 5.10 UTS and elongation for Al-0.5 wt.% Mg based forged-rolled and annealed composites

Composition	Short steel fibers wt.% (vol.%)	UTS (MPa)	% Elongation
C2	10 (3.7)	213	13.7
C3	20 (7.9)	212	12.9
C4	30 (12.8)	176	10.9

Increments in UTS and elongation of the rolled and annealed composites could be attributed to the following effects of rolling on as-forged composites: (1) particle fracture, elongation and dispersion of oxide in the matrix (2) attainment of a homogeneous microstructure by better bonding within the matrix (3) fiber cracking and brittle failure of intermetallic phases, which provide dispersoid strengthening of the matrix (4) low strain rate deformation by rolling resulted in strong embedding of the fibers, intermetallics and oxide particles into the soft matrix.

As observed in Fig. 5.60 (a), wherein, sites for fiber pull-out are of a serrated morphology against smooth cavities observed for as-forged composites; implying that rolling was responsible for creating strong fiber-matrix bonding and sufficient ancourage was available to the fibers, before matrix failure- as evident by higher density of smaller dimples. In Fig. 5.60 (b) failure of fibers is also observed, which is an evidence of stress transfer from the loaded matrix to the reinforcing fibers.

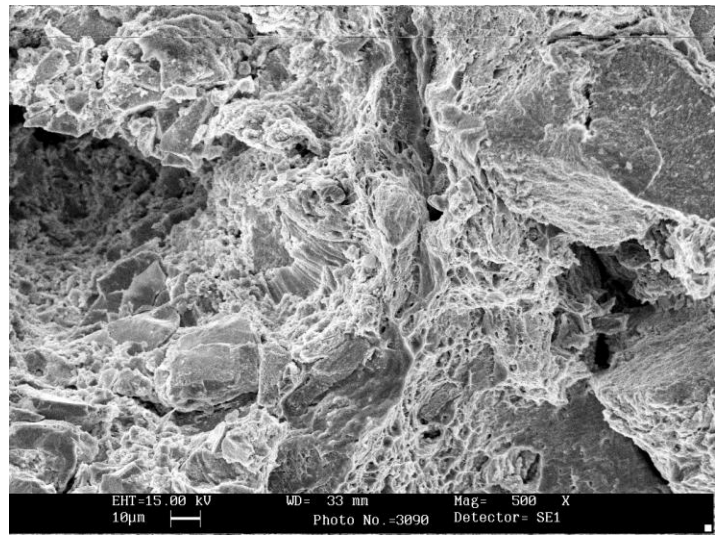

(a)

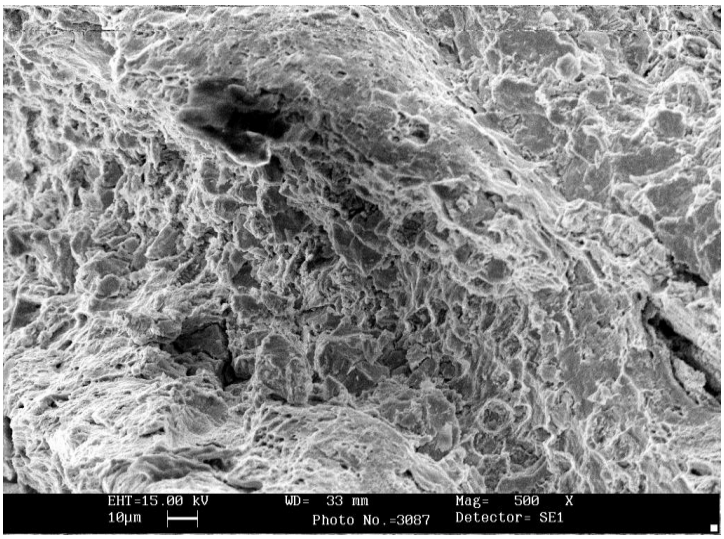

(b)

Fig. 5.60 Scanning electron micrographs of rolled and annealed composite fracture surface

Discussion: Considering ROM for theoretical UTS (σ), we have from the following equation:

$$\sigma_c = \sigma_m V_m + \sigma_f V_f + \sigma_v V_v \qquad \text{(Eq. 5.4)}$$

where, subscripts *c*, *m* and *v*, denote composite, matrix and voids respectively. V represents their respective volume fractions. From density measurements, assuming $V_v = 0$; for both as-forged and rolled composites. UTS for short steel fibers, from table 5.1, can be taken as 565 MPa. UTS for Al-0.5 wt.% Mg matrix, as determined for rolled and annealed specimens was 116 MPa. Short fiber core was found to loose about 15 % hardness during sintering, 235 HV for as-received fibers, dropped to 200 HV after sintering. A similar reduction in fiber UTS, gives a value of 480 MPa. Applying Eq. 5.4, the ROM values for composite UTS have been tabulated in Table 5.11 as below:

Table 5.11 Comparison of as-forged and rolled UTS with ROM

Composition	Short steel fibers wt.% (vol.%)	UTS- forged (MPa)	UTS- rolled (MPa)	UTS- ROM (MPa)
C2	10 (3.7)	141	213	129
C3	20 (7.9)	127	212	145
C4	30 (12.8)	87	176	163

From Table 5.11, it can be seen that, as-rolled strengths are consistently better than those predicted by ROM for all reinforcement volume fractions. For as-forged compositions 10 wt.% loaded composition has higher strength than ROM value. In a multi-component system, composed of fibrous reinforcement of varying morphology, a ductile matrix and a significant volume of intermetallic phases with different chemistries, the ROM may not be directly applicable; at best the values predicted through ROM can be used as benchmarks. In the present case, continuity and homogeneity of the matrix component is found to be the dominant factor in realizing composite properties, rather than proportional characteristics of constituent phases. Rolling of pre-forged briquettes was able to ensure better matrix continuity, resulting in higher elongation to failure; as a consequence load was shared by the short fibers, enabling the composite to fail at higher strength than that predicted by ROM.

5.8.5.4 Effect of forging on flexural strength

Flexural behavior under 3-point bending for sinter-forged composites is shown in Fig. 5.61.

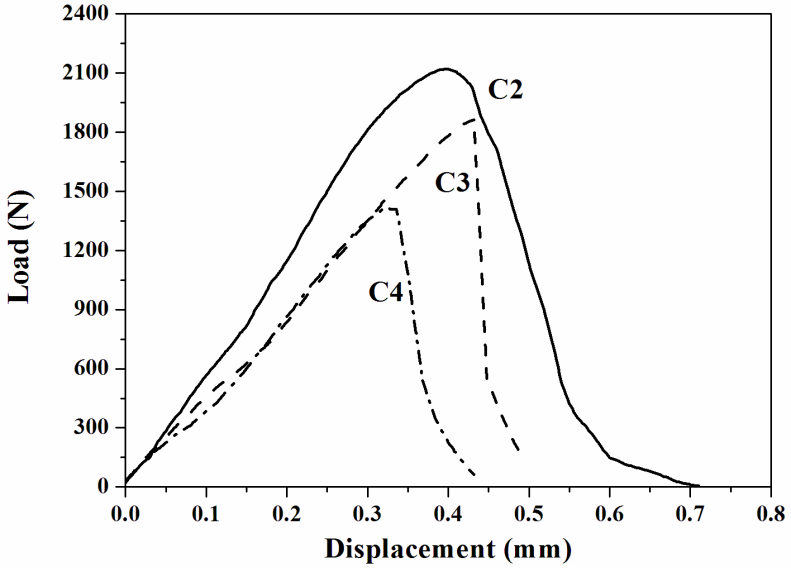

Fig. 5.61 Load-displacement curves from 3-point bend test of as-forged Al-0.5 wt.% Mg based composites

In comparison to the flexural strength of as-sintered composite specimens, maximum load attained increased to about 4-fold for the as-forged composites. Elimination of sintered porosity by forging is attributed as the principal reason for increase in flexural resistance of the composites.

5.8.5.5 Flow stress

Flow stress of sinter-forged unreinforced (C1); C3 and C4 reinforced compositions was determined as described in *Section 4.4.9.2*. Flow stress plots obtained for constant strain rate compression at 250ºC are shown in Fig.5.62. Higher work hardening is observed for C3 and C4, in comparison to C1, which shows monatomic flow softening behavior, characteristic of dynamic recrystallization (DRX) (Jabbari et al., 2012). C3 and C4 show higher flow stress due to initial work hardening, by obstruction to matrix flow posed by short fibers or Fe-Al intermetallic particles. Plastic flow of the composites is observed after about 0.25 strain; wherein flow softening is activated by opening up of cavitation voids in the matrix, near fiber or intermetallic agglomerates, as shown in Fig. 5.63 (b).

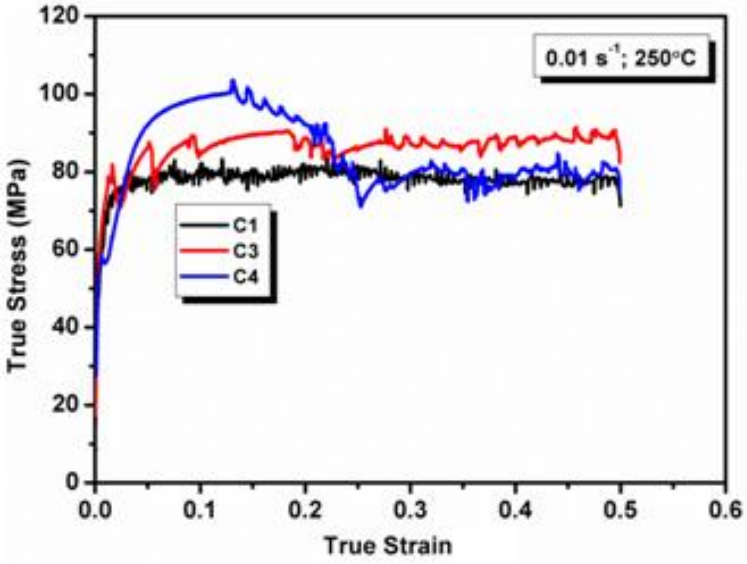

Fig. 5.62 Flow stress of Al-0.5 wt.% Mg based C1, C3 and C4 compositions

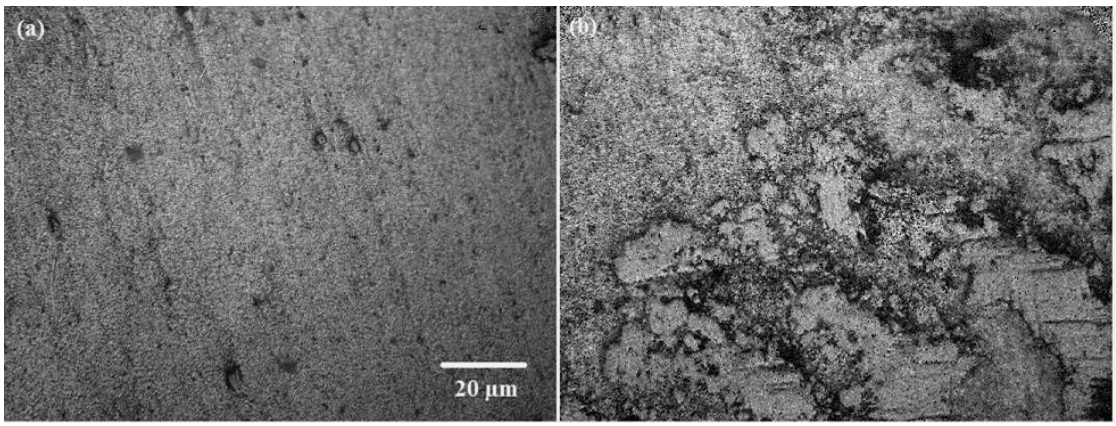

Fig. 5.63 Optical micrographs of (C1) and (C3) from mid plane of deformed pins (compression direction is horizontal)

5.8.5.6 Coefficient of thermal expansion (CTE)

CTE by measurement of linear expansion of cylindrical specimens, machined from sinter-forged briquettes, was determined as per procedure detailed in *Section 4.4.11*. Values obtained have been tabulated in Table 5.12, as below. As a standard, CTE was also determined for a 0.4 wt.% plain C steel specimen. CTE values for the composite have been compared with ROM (Eq. 2.7) and Schapery equation (Eq.2.8).

Table 5.12 CTE of Al-0.5 wt.% based compositions

Composition	Short steel fibers wt.% (vol.%)	CTE (x 10^{-6} $^{o}C^{-1}$)	CTE (ROM)	CTE (SE)
C1	0	23.0	--	--
C3	20 (7.9)	21.3	22.1	20.7
C4	30 (12.8)	19.6	21.5	19.6
0.4 wt.% C Steel	--	11.4	--	--

Incorporation of steel fibers in Al-0.5 wt.% Mg matrix, results in decrease of CTE. ROM and Schapery equation are used to predict CTEs of multi component systems; presenting the upper and lower limits respectively (Ganesh, et.al, 2002). CTE values obtained for sinter-forged C3 and C4 composite formulations were found to lie within these limits.

5.8.5.7 Wear behavior of sinter-forged compositions (pin-on-disc test regime)

Dry sliding wear tests at room temperature, utilizing pin-on-disc configuration, were conducted on cylindrical pins with hemispherical ends, as per the test regimen described in *Section 4.4.10.2*. Effect of reinforcement content on wear rate is shown in Fig. 5.63.

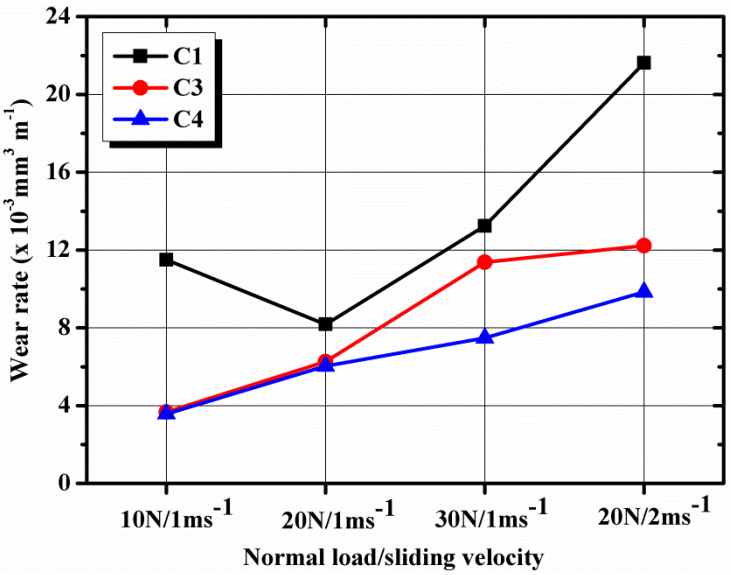

Fig. 5.64 Effect of composition on wear rate

It can be seen that wear rate increases with increasing load or sliding velocity. C3 and C4 are less sensitive to increase in load, in comparison to C1. Relatively, C3 and C4 exhibit lesser sensitivity towards changes in sliding conditions, due to the friction stabilizing effect of short steel fibers (Jang et al., 2004) and formation of a mechanically mixed tribolayer at the contact plane, composed of Al and Fe oxides, is reported to act as a solid lubricant (Wang and Rack, 1991b). Similar behavior was noted for ball-on-disc tests of sintered compositions, the tribolayer changed the wear mechanism from adhesive to abrasive, thereby lowering material loss.

Fig.5.65 shows the effect of test conditions on average coefficient of friction for different compositions. It can be seen that for the given load range (10-30N) there is a steady increase in COF. COF is found to decrease with increase in sliding velocity (1 to 2 ms^{-1}).

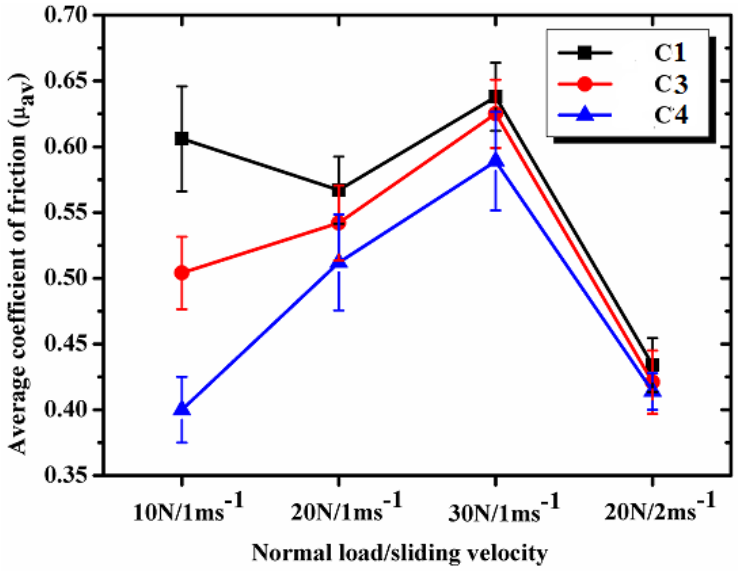

Fig. 5.65 Effect of normal load and sliding velocity on average coefficient of friction

From the analysis of wear tracks, as shown in Fig. 5.66, it can be seen that, excessive grooving leading to delamination type removal of material from C1; transitions to micro-cutting with decreasing groove width from C3 to C4. Material removal by ploughing is observed for C1 at 20 N load (Fig. 5.67), large debris are deposited on the wear track; for C3 at 20 N, shallow plough marks with plastically deformed ridges are observed. For C4 composition at 20 N, uniformly spaced shallow grooves are visible. This transition can be explained by the presence of an underlying hard layer of fibers that are found to flatten out under load and cover a larger area of the contact plane. These flattened fibers support the ductile matrix by sharing the contact load; resulting in shallower, smoother wear tracks in comparison to rough and uneven surfaces of the unreinforced material.

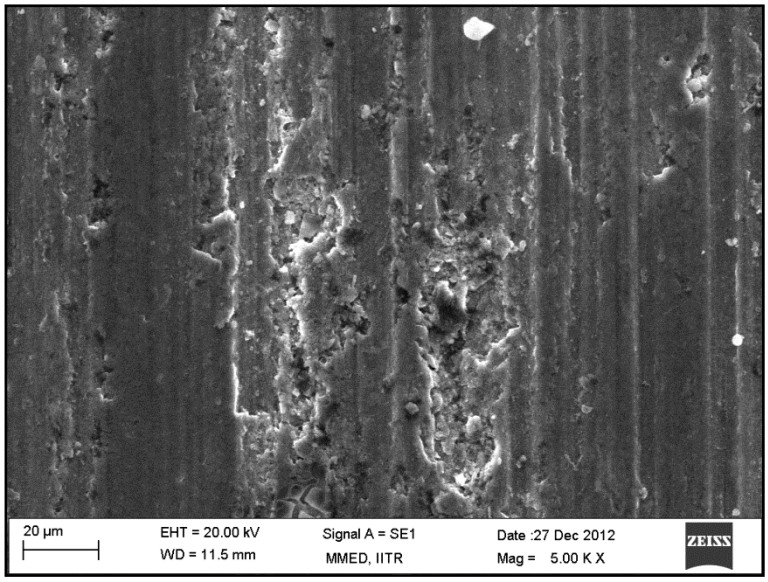

(a)

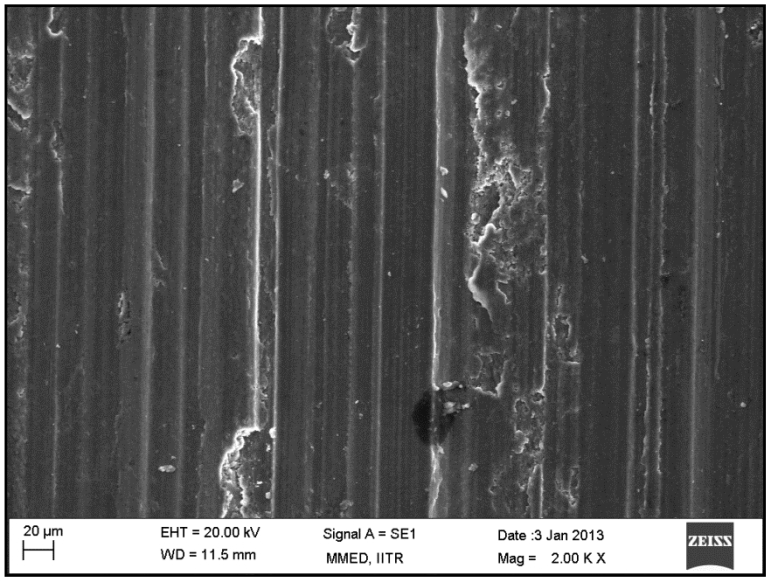

(b)

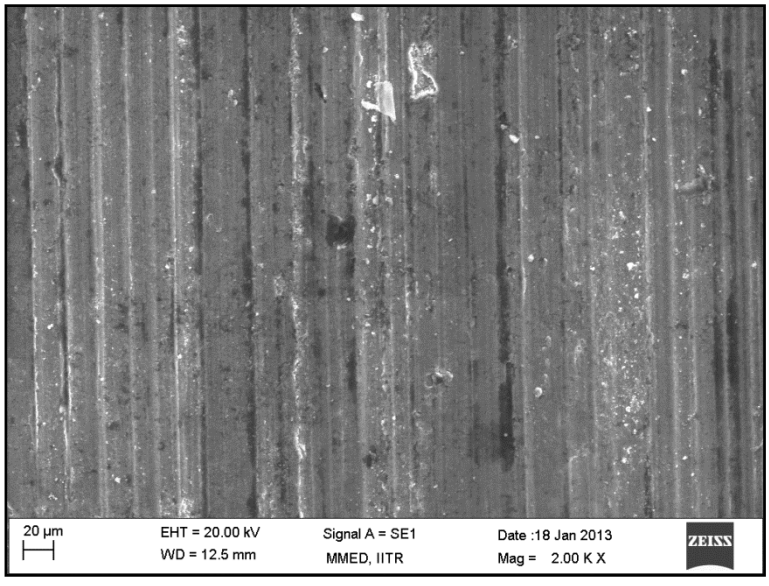

(c)

Fig. 5.66 Scanning electron micrographs of wear tracks formed at 10N/1ms^{-1} for (C1), (C3) and (C4) (sliding direction is vertical)

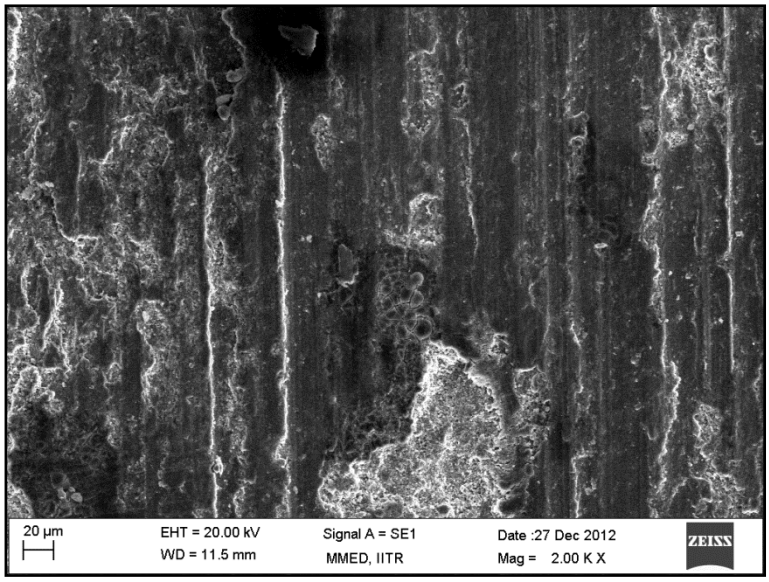

(a)

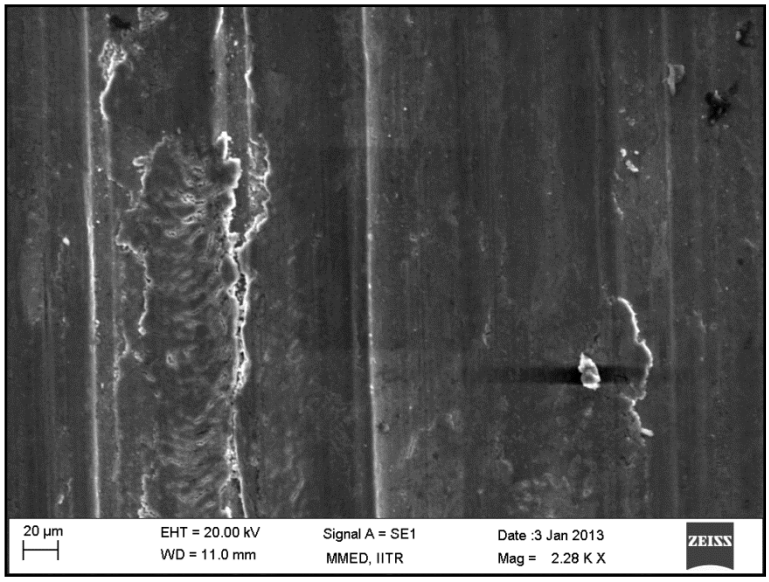

(b)

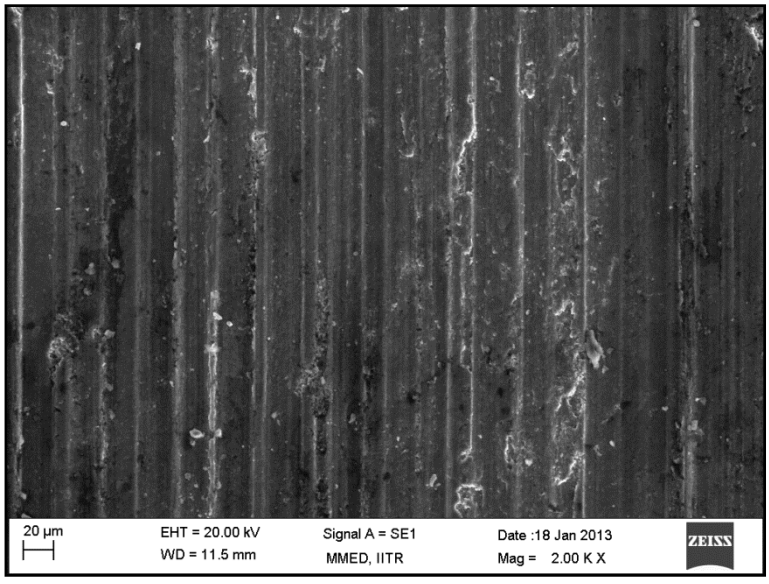

(c)

Fig. 5.67 Scanning electron micrographs of wear tracks formed at 20N/1ms^{-1} for (C1), (C3) and (C4) (sliding direction is vertical)

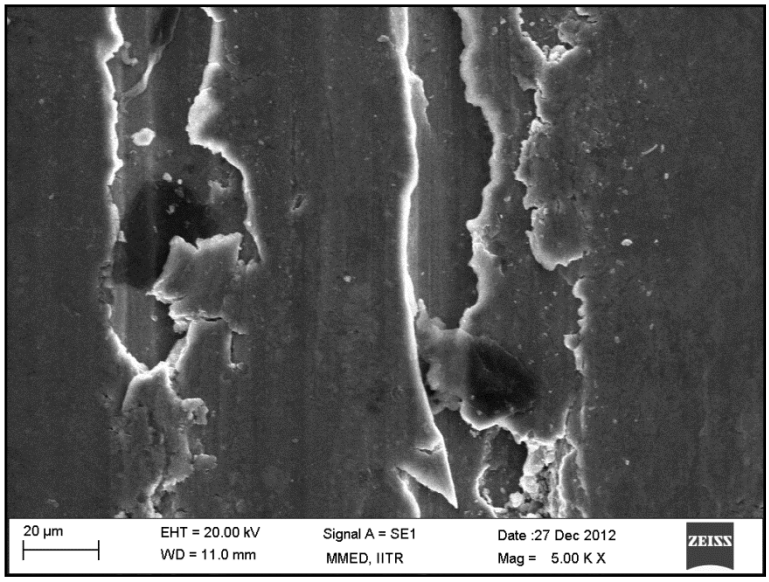

(a)

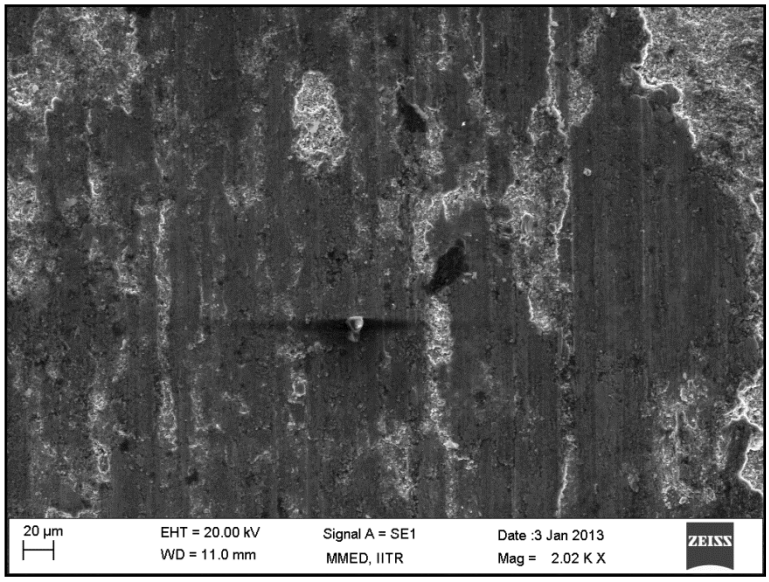

(b)

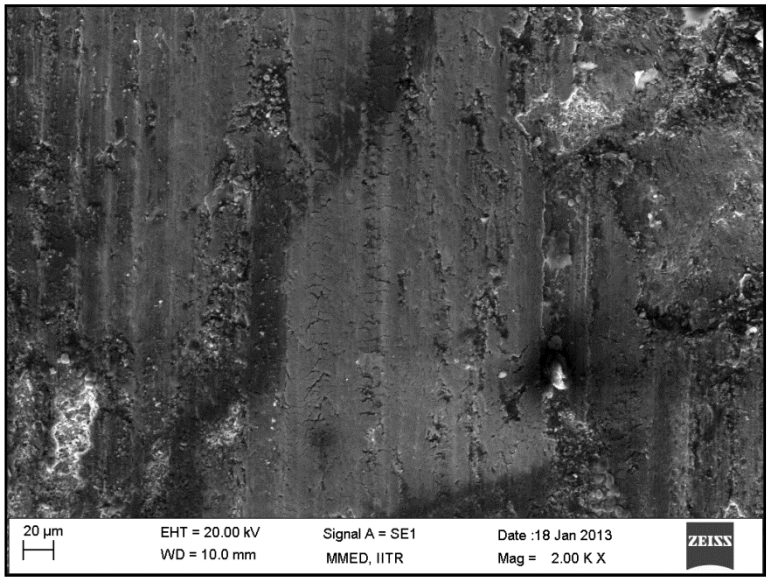

(c)

Fig. 5.68 Scanning electron micrographs of wear tracks formed at 30N/1ms^{-1} for (C1), (C3) and (C4) (sliding direction is vertical)

Effect of increasing the normal load to 30 N, is shown in Fig. 5.68. Delamination of the wear surface is observed for C1, indicative of severe wear, wherein, plate like flaky morphology of the wear debris can be expected. Delamination of the test material is indicative of adhesive wear. With increasing reinforcement content, a transition to ploughing and grooving is observed for C3 and C4. Higher apparent hardness of the matrix for reinforced compositions, also creates microcracking of the ploughed furrows.

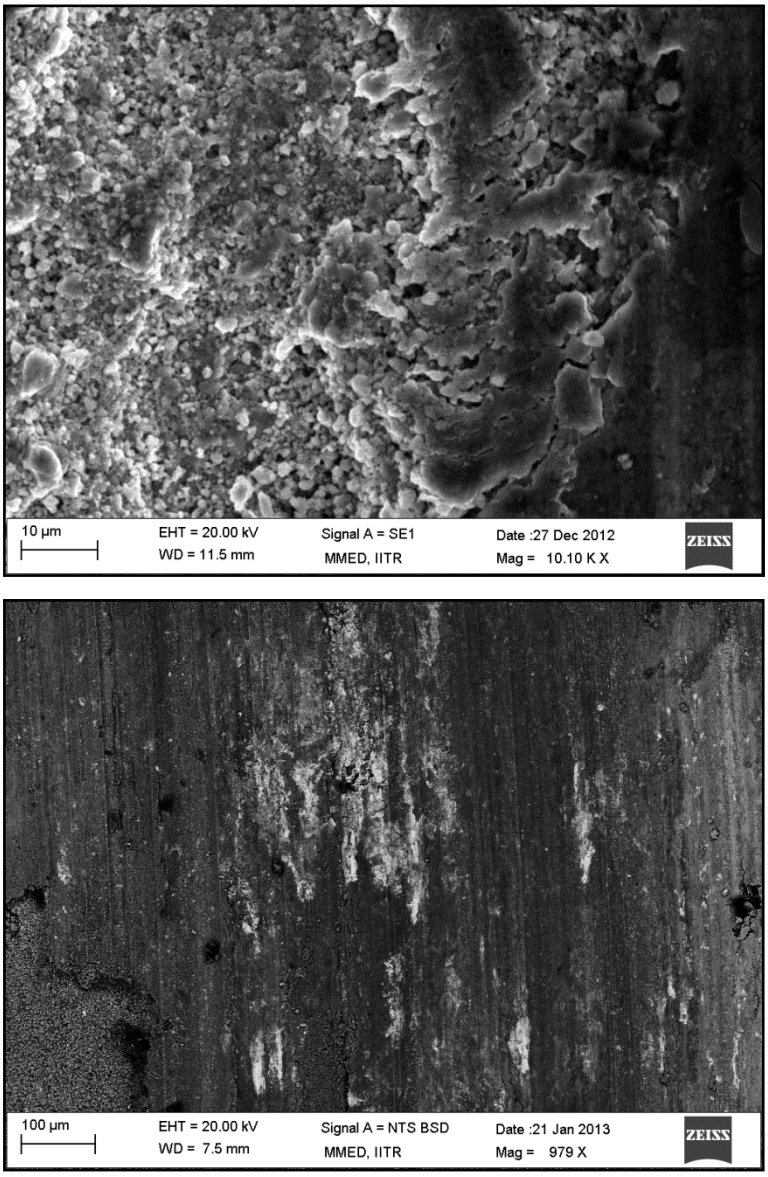

(a)

(b)

Fig. 5.69 Scanning electron micrographs of wear tracks formed at 20N/2ms^{-1} for (C1) and (C4) (sliding direction is vertical)

Short steel fibers can be seen to flatten out and increase their specific coverage over the wear track, as shown in Fig. 5.69 (b); formation of a crater by delamination of material can be observed for C1 at 2 m s^{-1} (Fig. 5.69 (a)). At the increased speed, C1 undergoes the transition to severe wear (Fig. 5.64), however, COF was found to be reduced. This could be attributed to

formation of an interlayer, mainly composed of fine Al_2O_3, which undergoes a grinding action to a fine size and gets embedded in aluminium, thereby changing the mode to abrasive wear, hence reduction in sticking causes a likewise drop in COF.

From the above investigation the likely modes for wear induced material loss are: oxidation-grooving-delamination forunreinforced composition, whereas for reinforced counterparts-microgrooving-ploughing-microcracking are observed. Presence of steel fibers is found to avoid the onset of severe wear by delamination failure of pin surface.

5.8.6 Sinter-extrusion of Al-0.5 wt.% Mg based compositions

Sintered billets were direct extruded as per details provided in *Section 4.3.9*. As a reference, to study the flow behaviour and microstructure evolution, an as-cast billet of AA1100- pure aluminium (99.8% purity, Hindustan Aeronautics Ltd., Bangalore) was hot extruded using the same set-up at 360^{o}C, with container maintained at 350^{o}C.

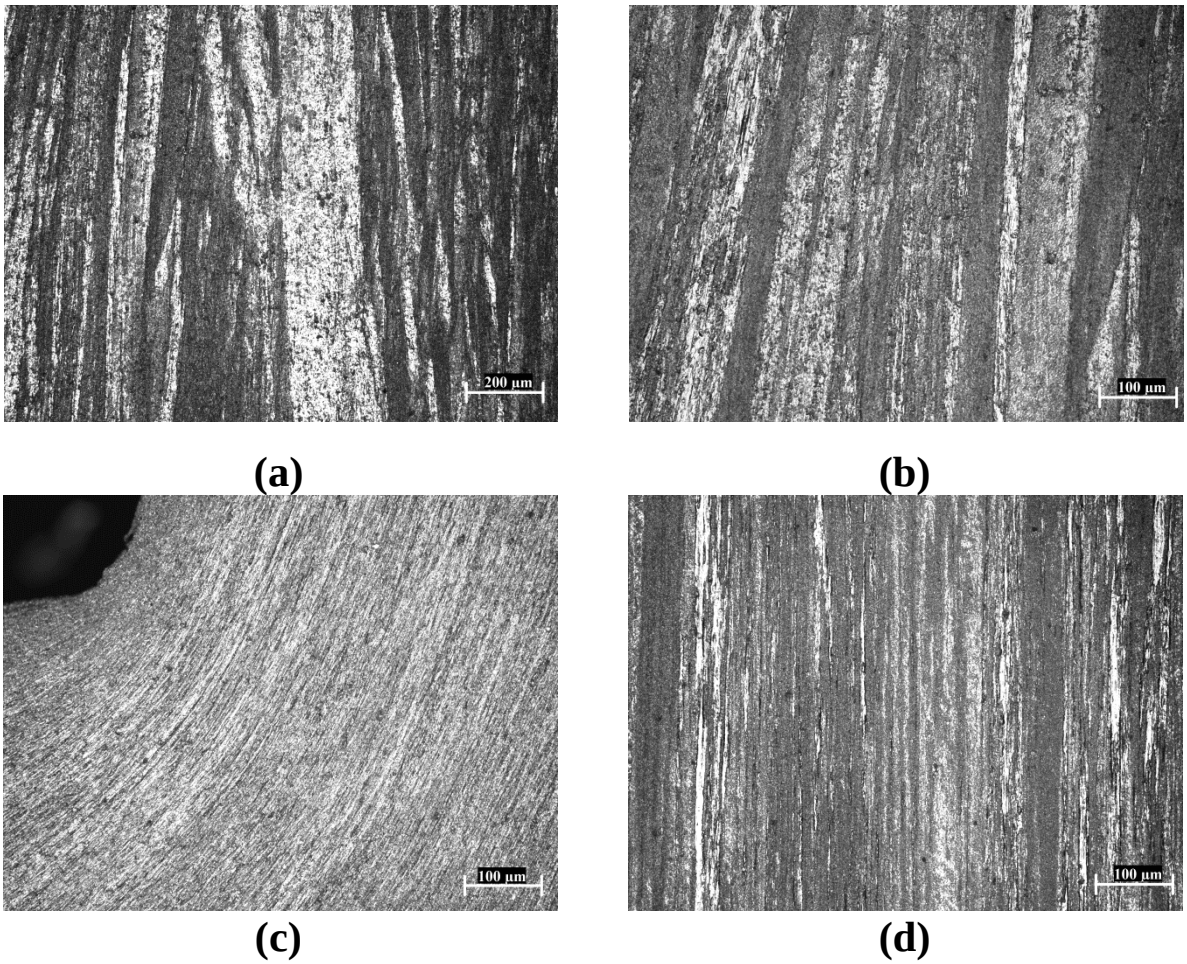

Fig. 5.70 Optical micrographs (etched) of extruded AA1100: (a) before die (b) near die (c) at die corner and (d) extrudate after die exit (LS)

As shown in Fig. 5.70, different zones are formed during hot extrusion of aluminium, based on local strain fields, train rates and friction namely: shear intensive zone (Fig. 5.70(a-b)) - breakdown of the as-cast structure starts; inflow zone at die corner (Fig. 5.70(c)) and fully deformed zone (Fig. 5.70(d)) (Güzel et al., 2012). From the microstructural examination of different zones, a steady decrease in grain width is observed; simultaneously there is emergence of fine equiaxed secondary grains within the large fibrous ligaments by dynamic recrystallization.

Pre-sintered billets of Al-0.5 wt.% Mg (C1) and C3 (20 wt.% short steel fiber) composite were extruded under 25:1 reduction (equivalent true strain of 3.22) at 450ºC billet temperature and container maintained at 375ºC through a flat faced die. Fig. 5.71 shows the microstructures representing the different deformation zones of sinter-extruded C1. As can be seen, a fibrous structure is developed by elongation of powder particles along the extrusion direction; small dark spots observed in between grains could be of disrupted oxide, $MgAl_2O_4$ or MgO formed during sintering.

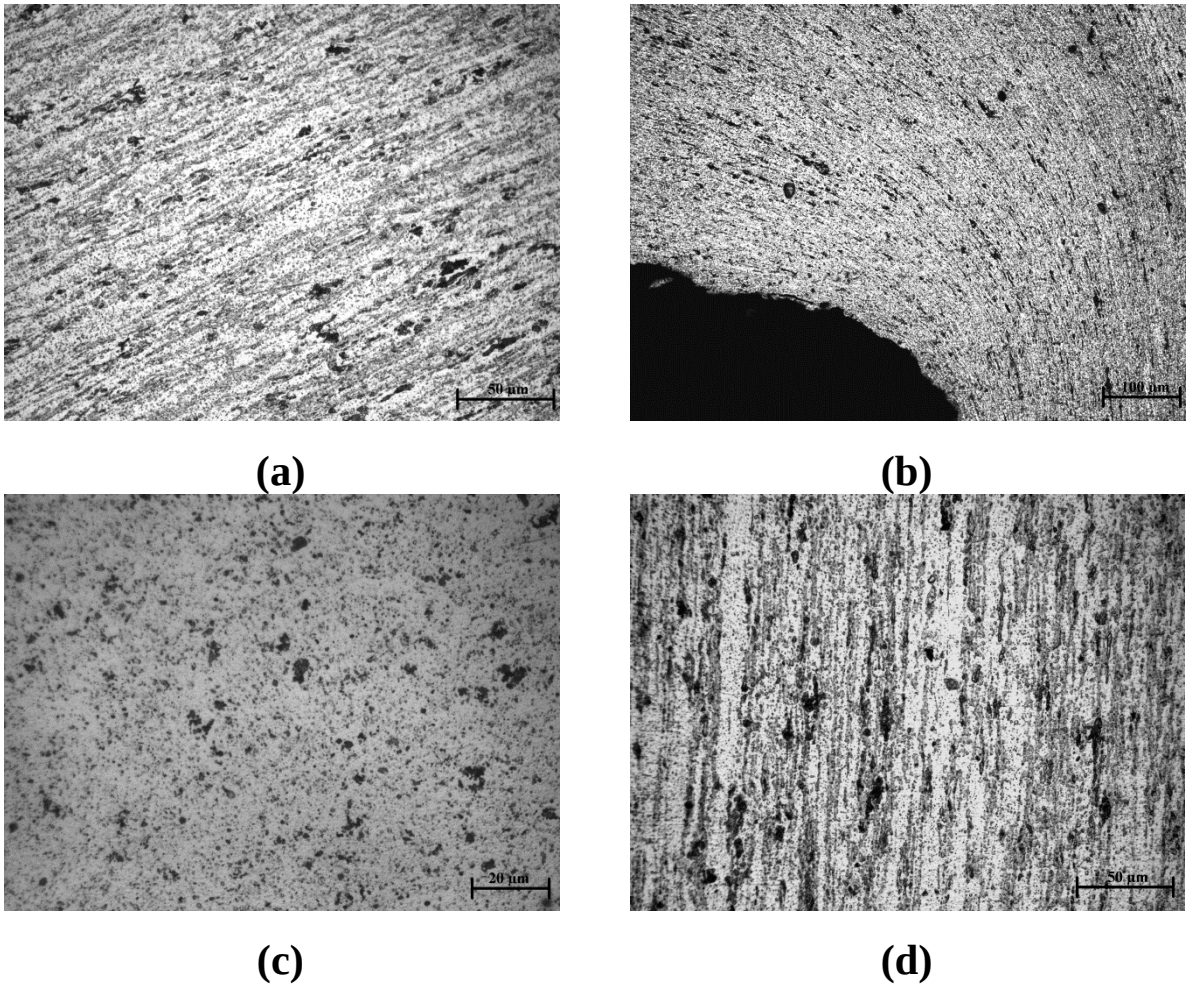

Fig. 5.71 Optical micrographs (etched) of extruded sintered Al-0.5 wt.% Mg: (a) before die (b) at die corner (c) transverse section and (d) extrudate after die exit (LS)

Extrusion ratio of 25:1 employed in the present work is sufficient to cause disruption of the oxide layer and thereby ensure sound metallurgical bonding between powder particles (Greasley & Shi, 1993). Sintered billet of C3 composite was hot extruded at 475ºC billet temperature, with container at 425ºC. Optical micrographs of sinter-extruded C3 composite are shown in Fig. 5.72. Fiber shortening and dispersion of particulate like broken fibers, preferentially aligned along the extrusion direction was observed. Uniform dispersion of randomly oriented short fibers was visible in the transverse section.

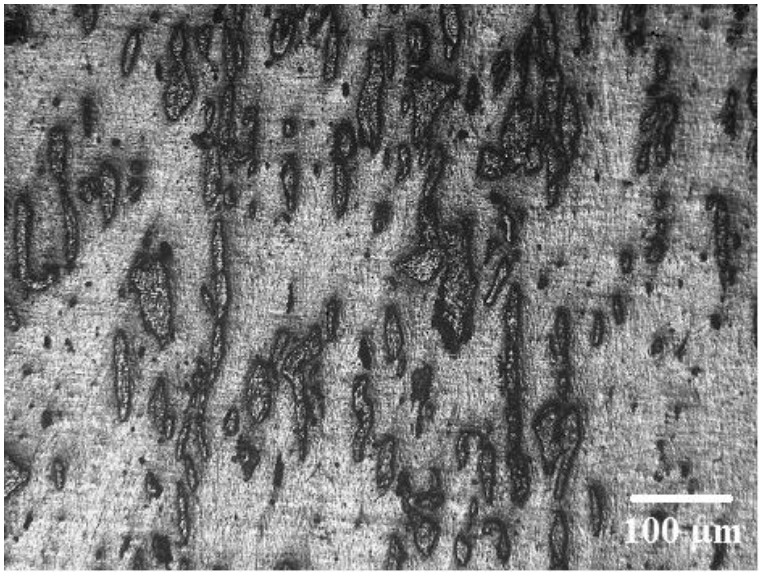

(a)

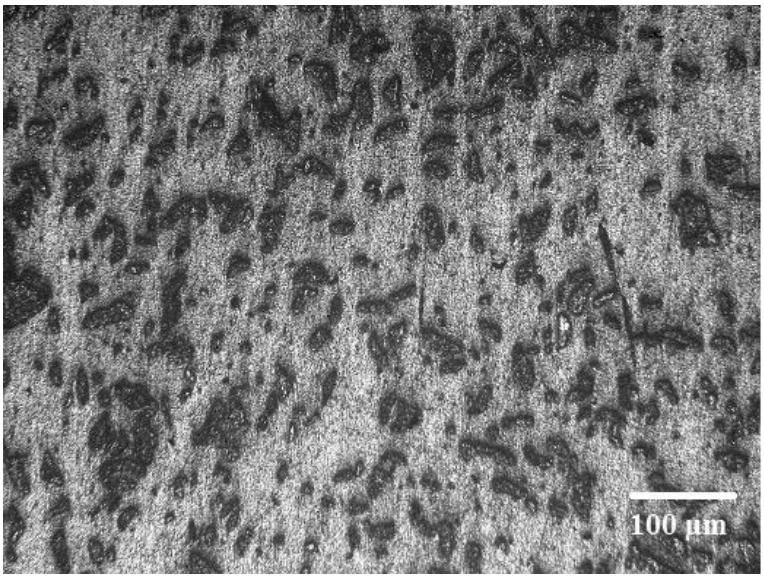

(b)

Fig. 5.72 Optical micrographs of extruded sintered C3 composite (a) LS (b) TS

5.8.6.1 Mechanical properties

As-extruded microhardness of 63 HV and 55 HV were recorded for C1 and C3 compositions. Unreinforced composition (C1) showed a higher elongation that forged samples, as shown in Fig. 5.73, due to greater disruption of the surface oxide (Sheppard, et al., 1983; Chawla et al., 2002) in comparison to forging. Considering the average strain imposed on during the two consolidation routes, a true strain of 3.22 by extrusion was considerably higher than 1.2 achieved in forging.

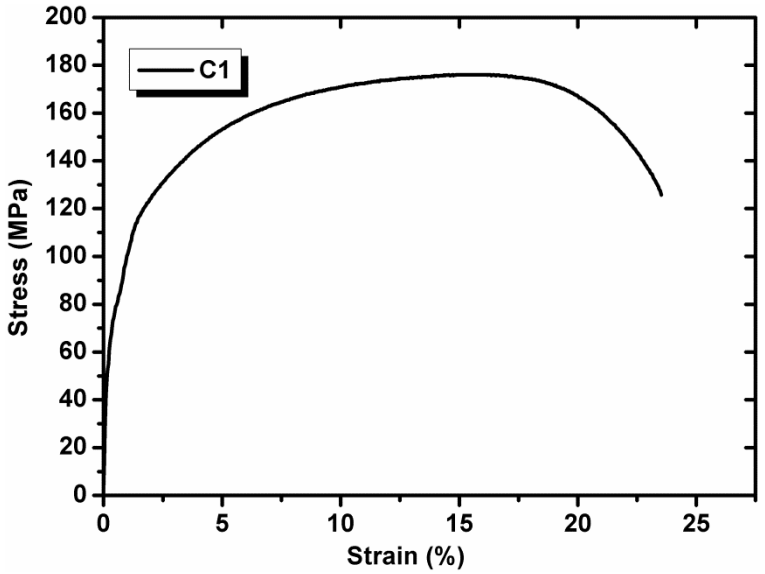

Fig. 5.73 Stress-strain curve from tensile tests of sinter-extruded Al-0.5 wt.% Mg

Tensile behavior of extruded (C3) composite is shown in Fig. 5.74. Comparison of mechanical properties determined from different processing routes has been presented in Table 5.12.

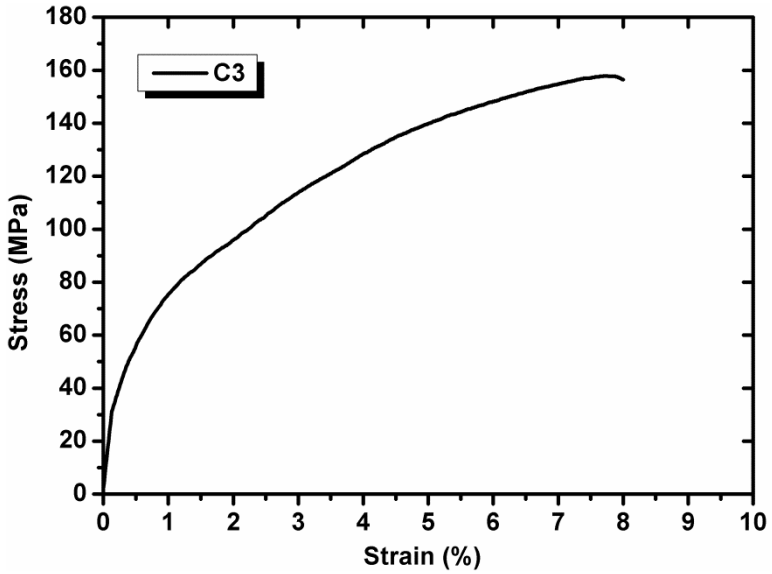

Fig. 5.74 Stress-strain curve from tensile tests of sinter-extruded C3 composite

Table 5.13 Comparison of as-forged, rolled and extruded UTS with ROM

Composition	Short steel fibers wt.% (vol.%)	UTS-forged (MPa)	UTS-rolled (MPa)	UTS-extruded (MPa)	UTS- ROM (MPa)
C1	0	167	116	176	--
C3	20 (7.9)	127	212	158	145

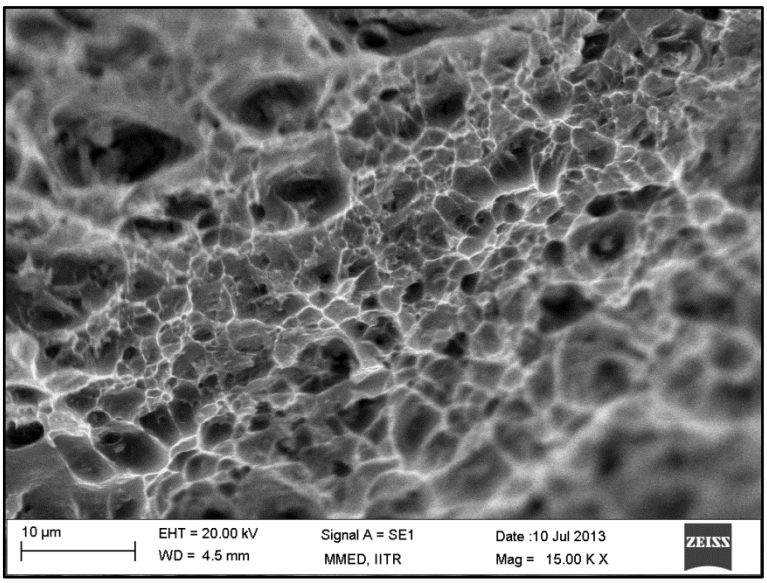

(a)

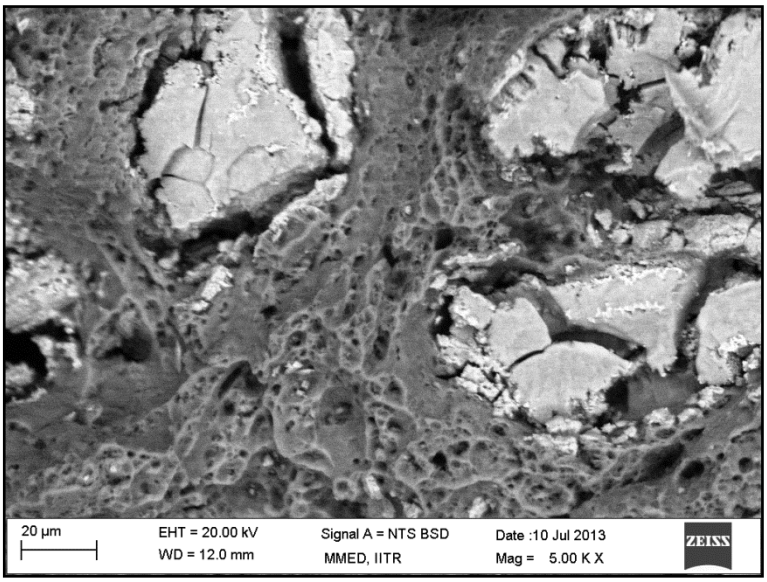

(b)

Fig. 5.75 Scanning electron micrographs showing tensile fracture surfaces for sinter-extruded (a) C1 and (b) C3 compositions

Small sized dimples, with lesser cleavage like features are visible for sinter-extruded fracture surface, in comparison to sinter-forged samples. Thereby, an increase in UTS with higher

elongation to failure is achieved. In-situ incorporation of surface oxide and spinel is also reported to offer composite like characteristics in Al-P/M extrusions, thereby strength increments are possible by pinning of grains against applied loads. Finer sub-grain structure is also retained after extrusion due to arrest of grain growth by oxide stringers (Topping, et al., 2013). Fractograph for sinter-extruded C3 shows fiber splitting and presence of an intermittent reaction interface, fiber agglomeration is also observed. Lower strength for the C3 extruded composite can be attributed to: (1) retention of intermetallic layer during extrusion, unlike rolling where it is dispersed in the matrix, (2) fracture initiation from the reaction interface (Friedrich et al., 1974) leading to fiber splitting and brittle failure of the fibers without any necking, (3) decreased inter-fiber spacing, generating unfilled voids.

5.9 Development of AA6061 based Short Steel Fiber Composites

5.9.1 Characterization of AA6061 prealloyed powder

AA6061 prealloyed powder of nominal chemical composition as shown in *Section 4.2.1,* Table No. 4.2 was used. Particle morphology of the powder was composed of large and small spherical particles, as shown in a representative micrograph (Fig. 5.76).

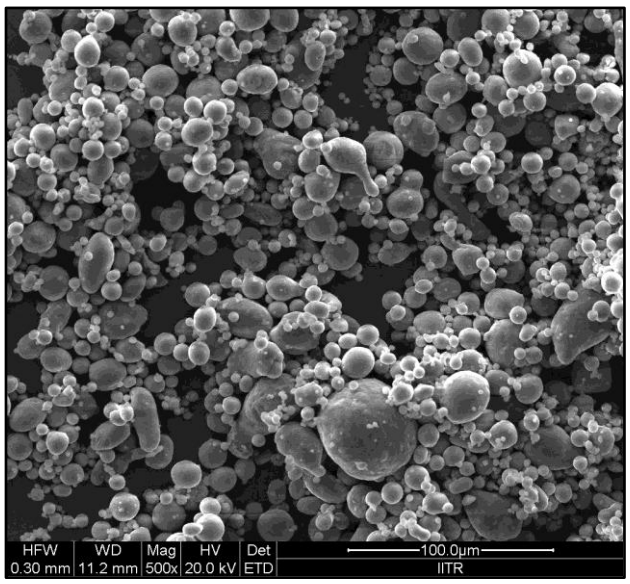

Fig. 5.76 Scanning electron micrograph of AA6061 powder

Prealloyed powders are produced by atomization of aluminium alloy melts under air or inert gas environments, exact processes are guarded and little information is available in published literature. However, by analysis of particle morphology and oxygen content, atomizing environment can be identified. (Ünal, 1990) has attributed the evolution of sphericity of atomized droplets combined with satelliting of fine particles around large spherical particles, as

observed in Fig. 5.76, to the use of inert gas atomizing medium. Irregular, ligamental shapes are generally evolved by air atomization, where shape of droplets is distorted by surface oxidation. Particle size distribution, as determined by laser scattering technique, was D_{10} -11 µm, D_{50} -59 µm and D_{90} -190 µm; with a span value of 3.03, suggestive of a bi-modal size distribution.

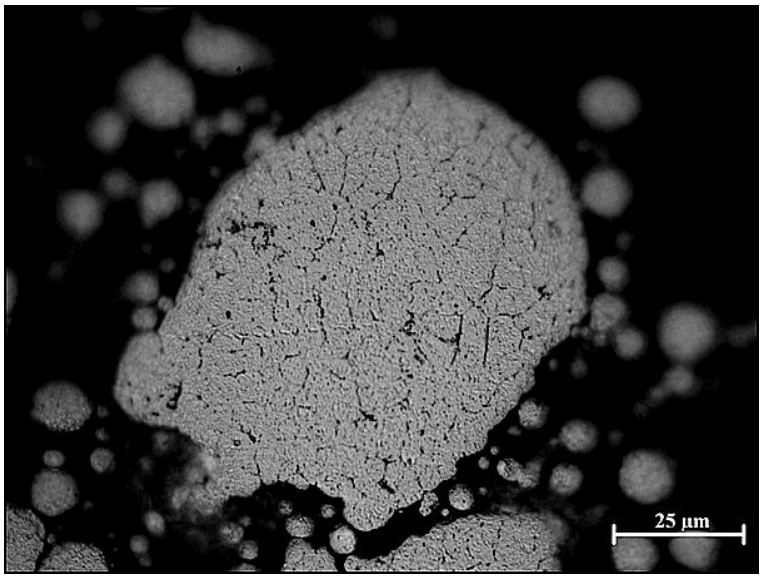

Fig. 5.77 Optical micrograph of AA6061 powder sub-structure

Nominal theoretical density, determined by inverse ROM, as given by Eq. 4.1 (*Section 4.4.6.1*) was 2.69 g cm^{-3}. Low oxygen content of the powder sample, 567± 23 ppm, was a further confirmation of inert gas atomization.

5.9.2 Cold compaction and sintering

AA6061 attained reasonable green strength at relatively low compaction, pressures, as shown in Fig.5.78, due to particle re-arrangement and filling up of interstitial spaces between large diameter particles by smaller spheres (Oberacker, 2011). Compaction at higher pressures led to "capping" phenomena, wherein, top face of the consolidated briquettes dislodged on ejection from the die. 200 MPa (92% relative density) was chosen as the green consolidation pressure for AA6061.

Sintering temperature was determined from the heat flow characteristics of the powder, as shown in Fig. 5.79. AA6061 displayed a singular phase change, with only bulk melting of the alloy at 646°C detected. Supersolidus liquid phase sintering was conducted at 625°C under pure nitrogen atmosphere, to ensure presence of at least 10 vol.% of liquid phase at the sintering temperature, as per the general sintering cycle described in *Section 4.3.6.1*.

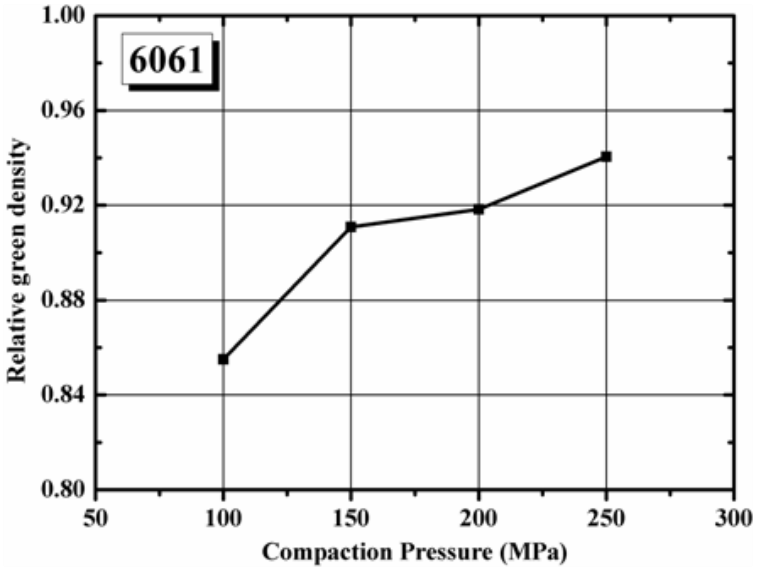

Fig. 5.78 Relative green density as function of compaction pressure

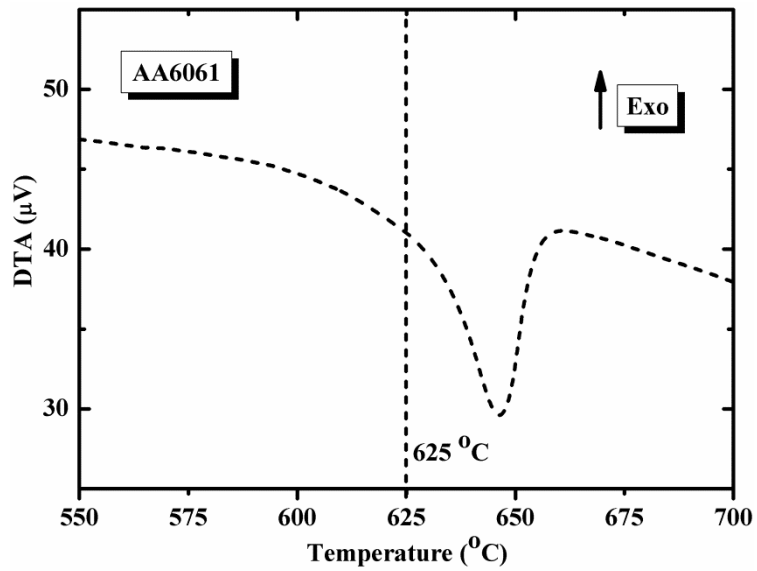

Fig. 5.79 Heat flow data from thermodynamic analysis of AA6061and sintering temperature

Sintered microstructure is shown in Fig. 5.80, both localized large voids and smaller interparticle porosity is observed, with negligible neck growth; starting with a 92 % relative green density, sintered density value of 93 % theoretical was recorded.

Discussion: Supersolidus liquid phase sintering (SLPS) is the preferred method of achieving densification in single component P/M systems, i.e. where no additional sintering aids, like elemental Mg, are ad-mixed. However, SLPS is found to be very sensitive to heating and cooling rates (German, 1997), due to re-solutionizing of the active liquid (Mg_2Si), which precipitates out of the powder particles, if sufficient time is made available at the sintering hold or slow cooling rates. Large Kirkendall voids are reported by (Youseffi and Showaiter, 2006)

for slow cooling rates during sintering of prealloyed AA6061; similar to the present work. Sintered microstructure obtained here was indicative of emergence of the SLPS phase followed by its re-homogenization with the α-Al bulk. Control of cooling rates was not possible with the equipment available. For disruption of surface oxide, irregular or ligamental shape of particles is reported to be more favorable in comparison to rounded or spherical particles, so that the thermal mismatch stresses between alumina layer and aluminium base aid in cracking the oxide shell (Liu, Sercombe, & Schaffer, 2007).

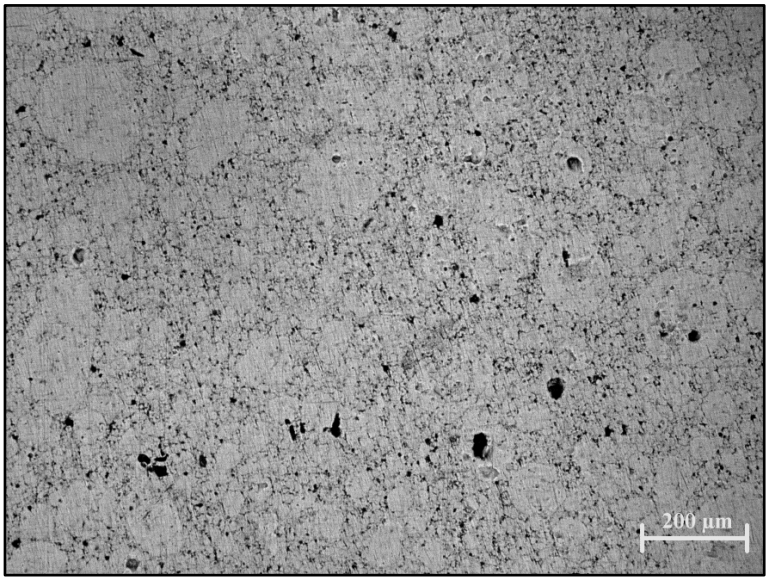

Fig. 5.80 Optical micrograph of sintered AA6061

5.9.3 Sinter-forging of monolithic AA6061

Sintered compacts, in the form of cylindrical pins (ϕ 6 mm x 9 mm) were put through simulated hot compression at 370ºC (~0.7T_m) under 10 s^{-1} strain rate, to determine the flow behavior and effect of imposed deformation on densification. As shown in Fig. 5.80.

Peak flow stress of about 60 MPa was observed from a characteristic monotonic flow curve for the sintered compact. Such behavior is indicative of work hardening in the initial low strain regime, followed by DRX induced flow softening (Mosher, et al., 2011). Density of deformed compacts was measured to be 98.6 ± 0.3 % of theoretical density. Based on this finding, it was proposed to consolidate the porous sintered AA6061compacts by forging.

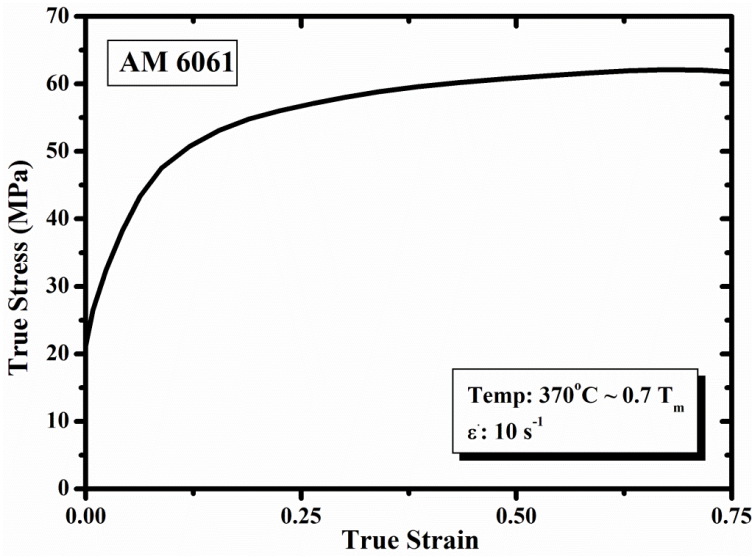

Fig. 5.81 Flow stress behavior of sintered AA6061

Constrained die hot upset forging of pre-sintered briquettes was performed as per details given in *Section 4.3.7* and explained earlier. Temperature of sintered billets was maintained at 515ºC, to coincide with the solutionizing temperature of the alloy. The maximum hot working limit is bound by onset of hot shortness of age hardenable aluminium alloys and segregation, coarsening or cracking of hardenable precipitates (Bishop, et al. 2011; MacAskill, et al., 2009). These deleterious events can be avoided by keeping the hardening phases in solution; moreover, a completely recrystallized-wrought like structure can be obtained by utilizing flow softening of the material. Optical micrograph of sinter-forged AA6061 is shown in Fig. 5.82.

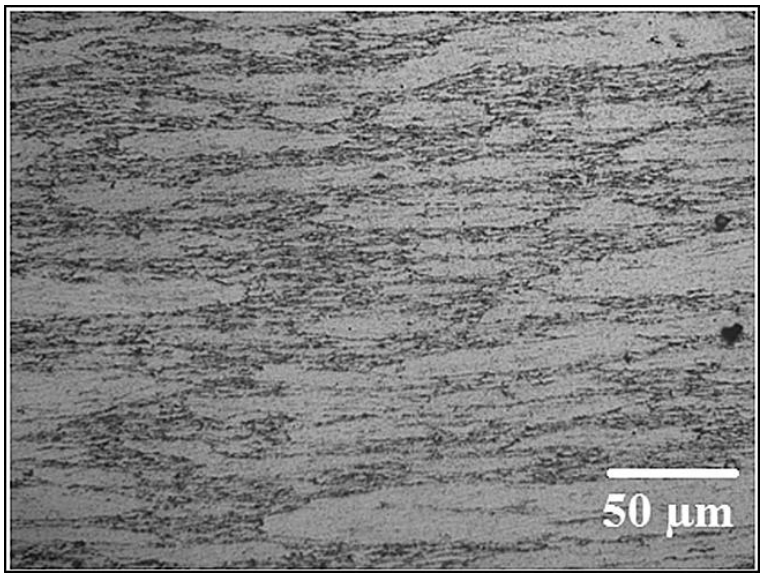

Fig. 5.82 Optical micrograph of sinter-forged AA6061 (S-T section)

Near- full theoretical density was obtained after forging. Bi-modality of the starting microstructure was however retained; pancaking of large powder particles was observed in a network of small particles. Contrary to literature, wherein a refined microstructure is reported by selection of deformation conditions as described above, retention of PPB's as shown in Fig. 5.81, was further investigated by EBSD (electron backscattered diffraction- ref. *Section 4.4.7.4*). Fig. 5.83 shows the central region, corresponding to maximum strain, of sinter forged AA6061.

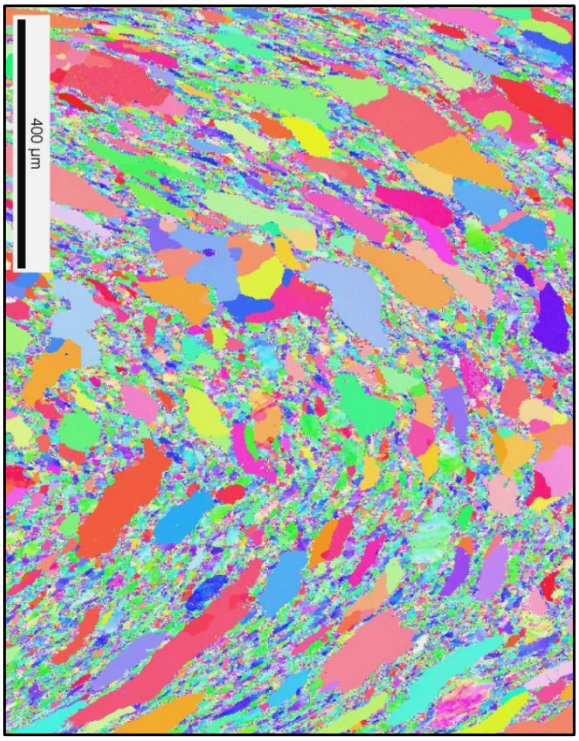

Fig. 5.83 EBSD micrograph of sinter-forged AA6061
(forging direction is vertical)

From the EBSD micrograph, bi-modality of the microstructure was revealed; and the large difference in size between the constituent powder particles was found to be responsible for causing a flotation like movement of larger particles within a matrix of small powder particles. As a consequence, the smaller particles, with their high specific surface area and consequently higher surface friction, were able to absorb a larger fraction of deformation energy, leaving the larger particles mildly pancaked.

5.9.3.1 Mechanical properties of sinter-forged AA6061

Hardness values of monolithic sinter-forged composition in as-forged, solutionized and peak aged conditions are tabulated as below:

Table 5.14 Microhardness of AA6061

Condition	Microhardness (HV)
As- forged (T1)	82±4
Solutionized (515ºC- 2 h)	61±11
T6 aged (177ºC- 8 h)	129±3

Tensile behavior of AA6061 tested in the as-forged condition is shown in Fig. 5.84.

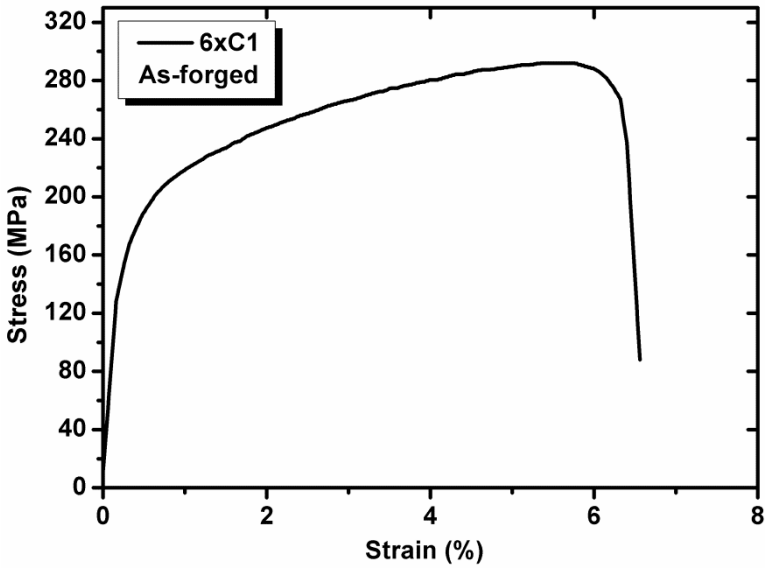

Fig. 5.84 Stress-strain curve from tensile tests of sinter-forged AA6061

Sintered briquettes were forged at the solutionizing temperature (515ºC), followed by cold water quench immediately after ejection from the die; inadvertently there was a time gap of upto 2 days between forging and testing of the samples; this may have contributed to natural ageing of the tensile test pieces. Microhardness determined from the grip section of the dumbbells, after testing, reported values within the 61±11 range.

Increase in UTS was observed for samples tested after artificial ageing (T6) treatment, as shown in Fig. 5.85. A slight increase in elongation to failure is also noted (6.37% to 7.48%), which can be attributed to recovery of dislocations by solutionizing.

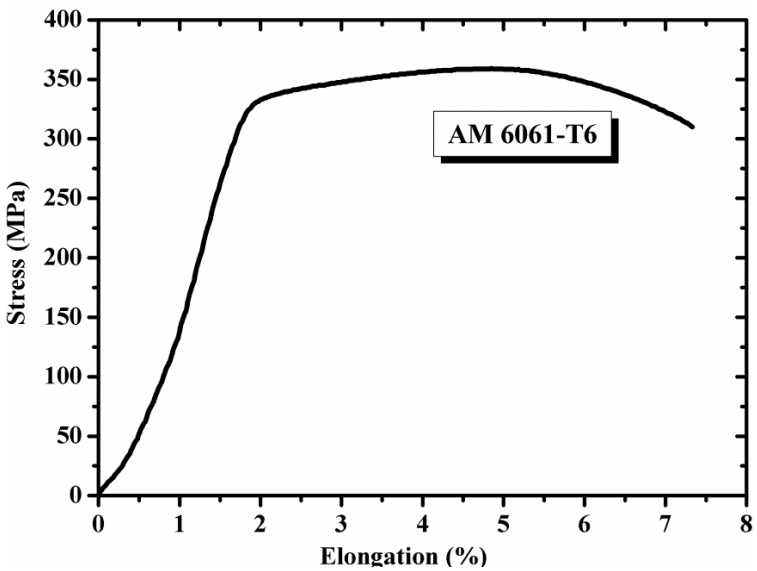

Fig. 5.85 Stress-strain curve from tensile tests of sinter-forged AA6061 (T6)

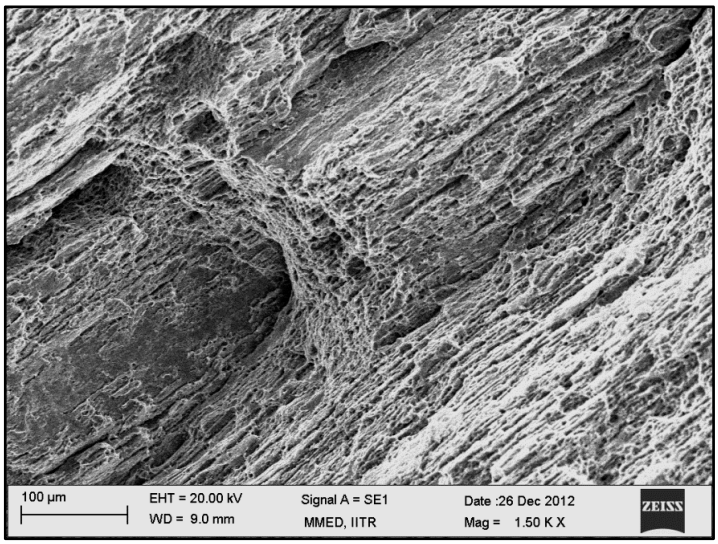

(a)

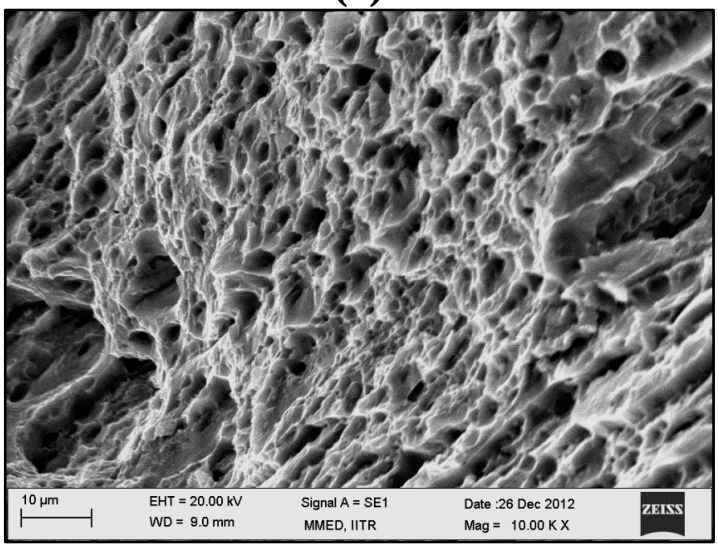

(b)

Fig. 5.86 Scanning electron micrographs showing tensile fracture surfaces for sinter-forged AA6061 (T6)

Powder morphology, found to be composed of two distinct sized components, was manifest in the fractographs as well. Small particles were seen to be well bonded with small sized dimples, indicative of ductile failure. Larger particles, far apart, showed evidence of tearing with cleavage like features.

5.9.4 Sinter-forging of AA6061 based short steel fiber composites

5.9.4.1 Microstructure and mechanical properties

Composite formulations with 10, 20 and 30 wt.% (designated as 6061C2, 6061C3 and 6061C4 respectively) short steel fibers were cold compacted into briquettes at different pressures to obtain 90-92 % theoretical density and sintered at a lower temperature (550ºC) for 40 min under nitrogen atmosphere. Without cooling from the sintering temperature, they were directly transferred to the hot forging die. Fig. 5.87 shows the representative micrographs of sinter-forged 6061C1 and 6061C3 compositions.

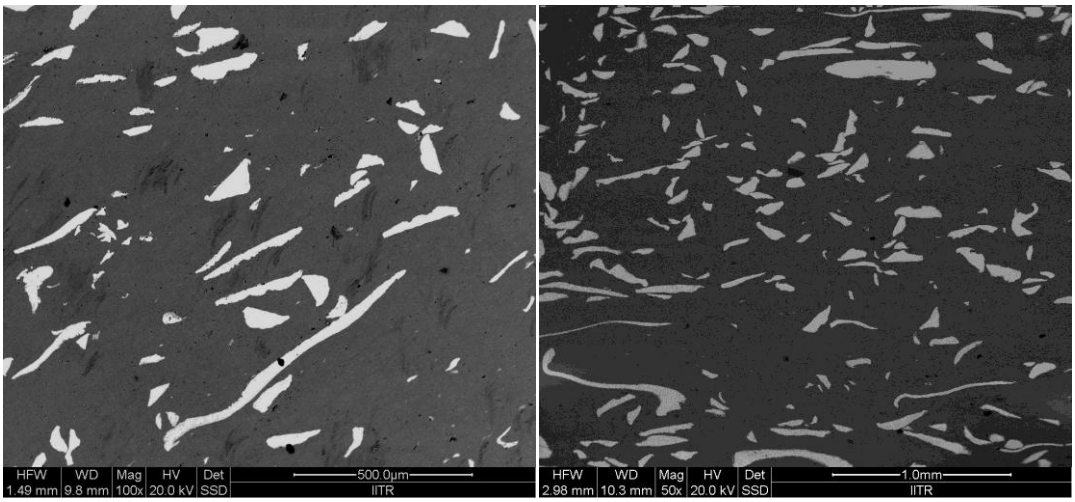

Fig. 5.87 Scanning electron micrographs of sinter-forged 6xC1 and 6xC3 composites (S-T section)

Reinforcement banding was observed for 6061C4 composite, with fiber breakage and shortening; however no apparent agglomeration of short was observed. Low temperature processing of the composites resulted in absence of a reaction interface. Solutionizing followed by artificial ageing treatment (T6) of the composites resulted in formation of an intermittent reaction interface, as shown in Fig. 5.88.

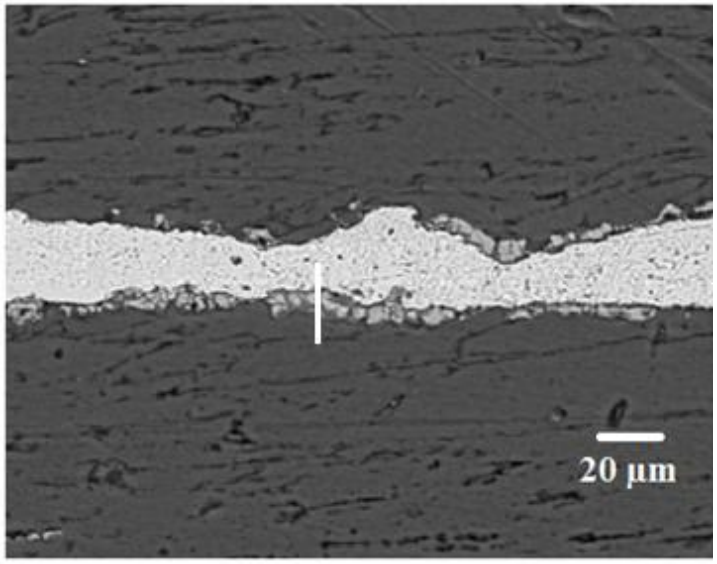

Fig. 5.88 Scanning electron micrograph of 6xC3 (T4) fiber-matrix interface

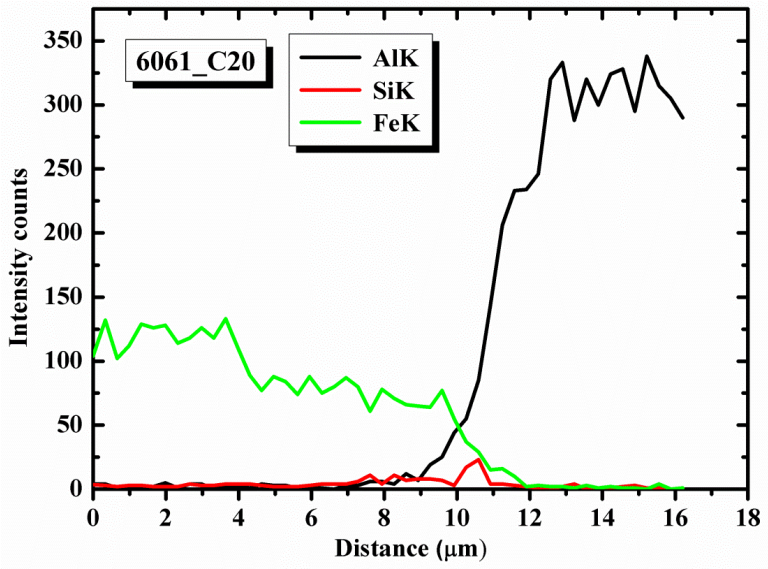

Fig. 5.89 Elemental profile by EDS line scan through interface shown in Fig. 5.88

Reaction interface of about 3 µm was formed (Fig. 5,89), from the elemental profile; presence of ternary AlFeSi intermetallic can be detected.(Springer, et al., 2011) have reported similar growth of the ternary intermetallic phase during solid-solid interdiffusion between Al-Si alloy and plain carbon steel, where a Si peak is found to separate Fe_2Al_5 (η) from $FeAl_3$ (θ) (Baron, et al., 1997). Composite specimens did not respond to T6 heat treatment, rather, a loss in matrix hardness was observed with increasing aging duration or reinforcement content. The major hardening phase in 6000 series aluminium alloys is Mg_2Si; Si content of the alloy investigated was 0.68 wt.%, any loss in Si content is bound to deteriorate the ageing characteristics and thereby impact the strength of the composites.

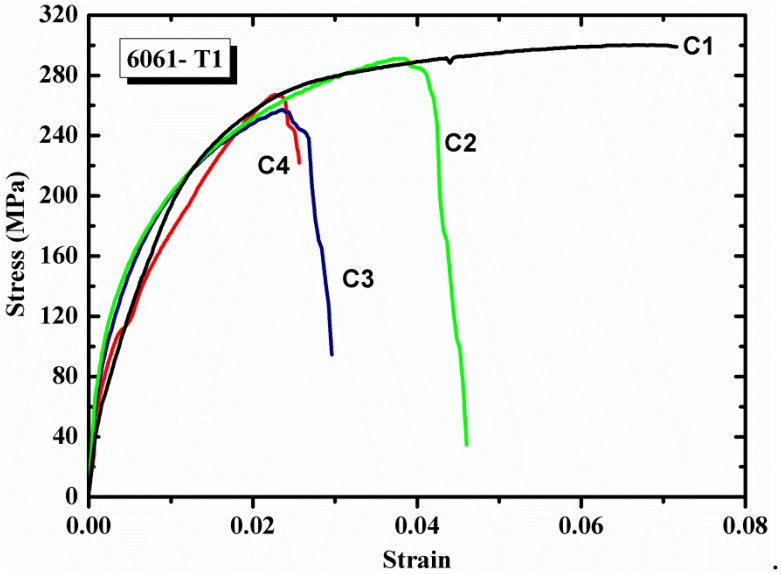

Fig. 5.90 Stress-strain curves from tensile tests of as-forged AA6061 based compositions

Elongation to failure of the composites is found to be more sensitive to increasing reinforcement content than UTS, as seen in Fig. 5.90. Evidence of premature composite failure by fiber pull-out (Fig. 5.91 (a)), interfacial debonding (Fig. 5.91 (b)) and precipitate coarsening (Fig. 5.91 (c)) is observed.

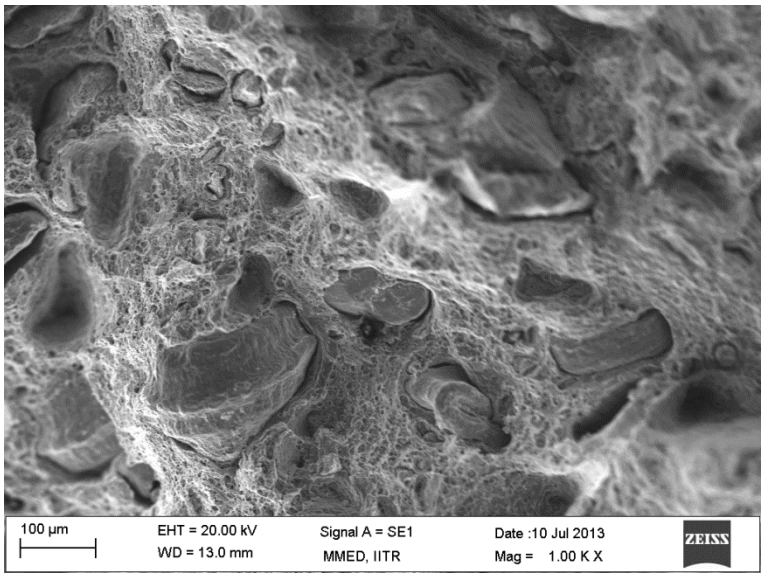

(a)

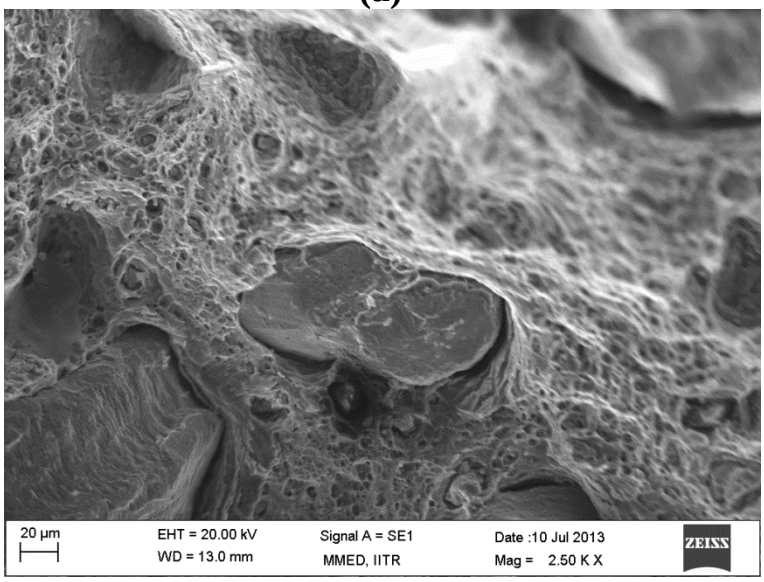

(b)

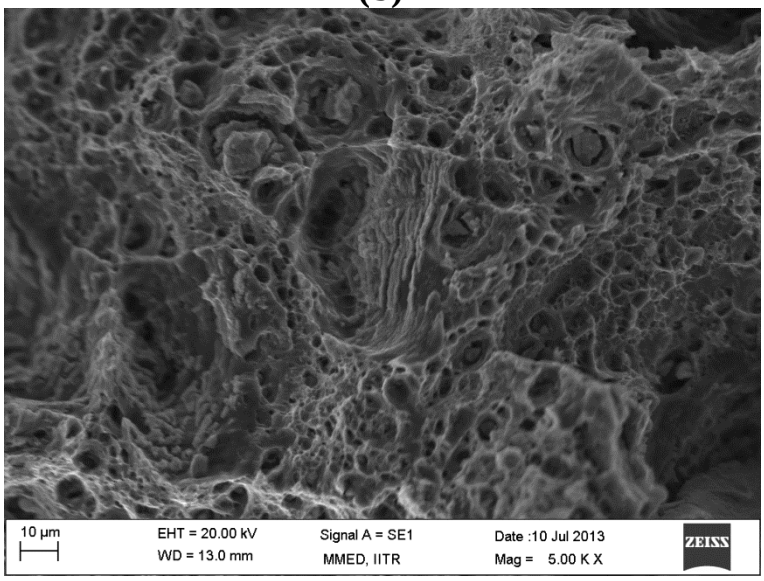

(c)

Fig. 5.91 Scanning electron micrographs showing tensile fracture surfaces for as-forged AA6061 based composites

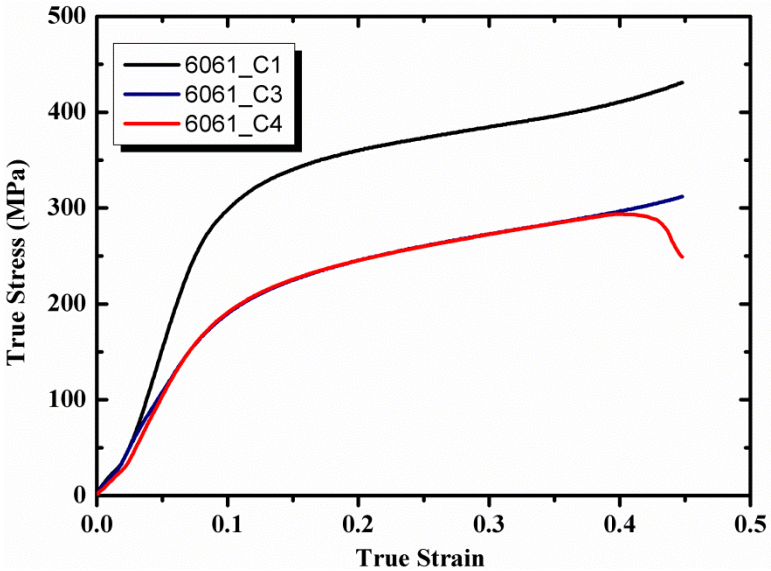

Fig. 5.92 True stress- true strain curves from room temperature compression tests for sinter-forged AA6061 based compositions

Room temperature compression test results for sinter-forged compositions are shown in Fig. 5.92; decrease in strength is seen with increasing reinforcement content. Effect of increase in reinforcement from 10 to 20 wt.% is found to cause external cracks on the test cylinder surface.

Flow stress behavior is shown in Fig. 5.93. Work hardening is observed in all the compositions; however, the initial work hardening rate is higher for reinforced compositions in comparison to monolithic alloy which shows monatomic flow softening with a constant flow stress; indicative of work hardening followed by dynamic recovery (DRV) and finally recrystallization by DRX. For the composites, as has been observed by fractographic analysis, coarse precipitate particles and hard steel fibers delay the onset of constant flow by DRX, thereby DRX commences only upon dissolution of the precipitates or formation of cavitation voids at fiber ends. Higher volume fraction of the reinforcement is reported to provided more sites for precipitate nucleation by higher dislocation density around fibers on account of coefficient of thermal mismatch stresses in the matrix (Williams, et al., 2002). Increment in flow stress at higher temperature for the composite is in contrast to lower elongation to failure and UTS observed at room temperature. Such behavior can be attributed to brittle failure of both the reinforcement and coarse precipitates; whereas at elevated temperature the flow of a softening matrix is effectively resisted by coarse precipitates and fiber interlocks, as shown in Fig. 5.94.

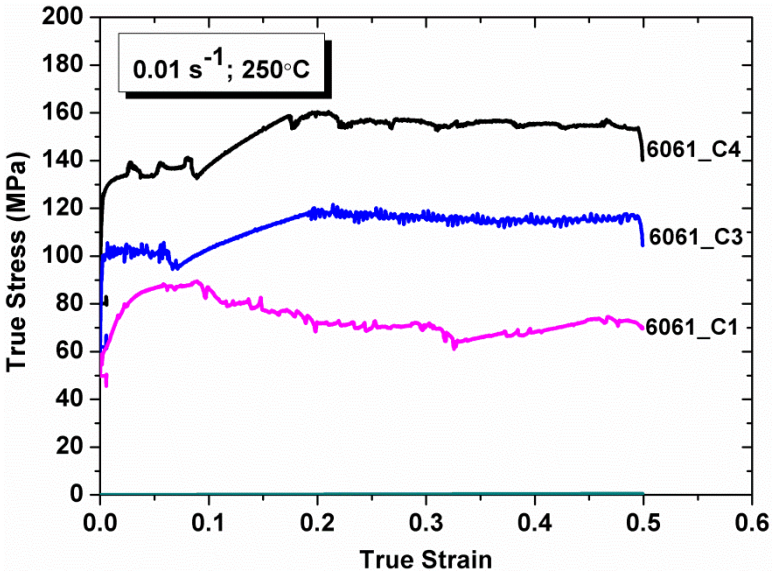

Fig. 5.93 Flow stress of AA6061 based compositions

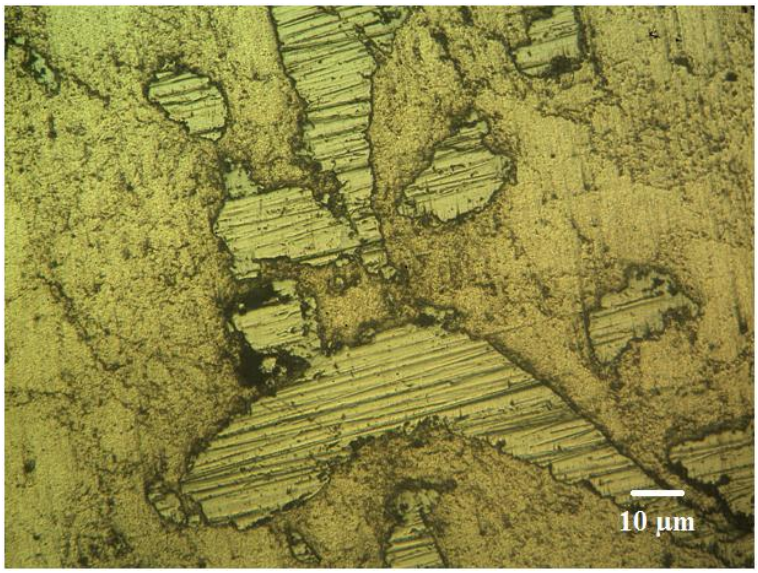

Fig. 5.94 Optical micrographs of 6061_C3 from mid plane of deformed pins (compression direction is vertical)

5.9.4.2 Wear behavior

Effect of reinforcement content on wear rate is shown in Fig. 5.95. Higher wear rates are obtained for reinforced composition in comparison to monolithic. Similarly, average COF is lower for unreinforced composition (Fig. 5.96). Expected increase in wear resistance by incorporation of a hard second phase, was not observed. It has been reported, from dry sliding wear tests of large particulate reinforced AMCs, by abrasive wear is attributed to sudden dislodgement of large reinforcement particles, which consequently leads to a larger loss of surrounding matrix material (Wang & Rack, 1991a). From the analysis of wear tracks, Fig.

5.97, a relatively smooth, shallow grooved surface is observed for AA6061, compared to a rougher, cracked and chipped appearance of wear tracks for composites, which is indicative of continuous material loss at the contact plane. The large size of material lost as debris would require a longer sliding distance to transform into oxides by grinding. In the present case, these large debris would further counteract with the test pin leading to increase in COF and wear volume loss. As observed in the previous study, wherein enhanced wear resistance was attributed to flattening out of short steel fibers at the contact plane, is not found to be a sufficient criterion for AMCs with a narrow hardness difference in the reinforcement and matrix.

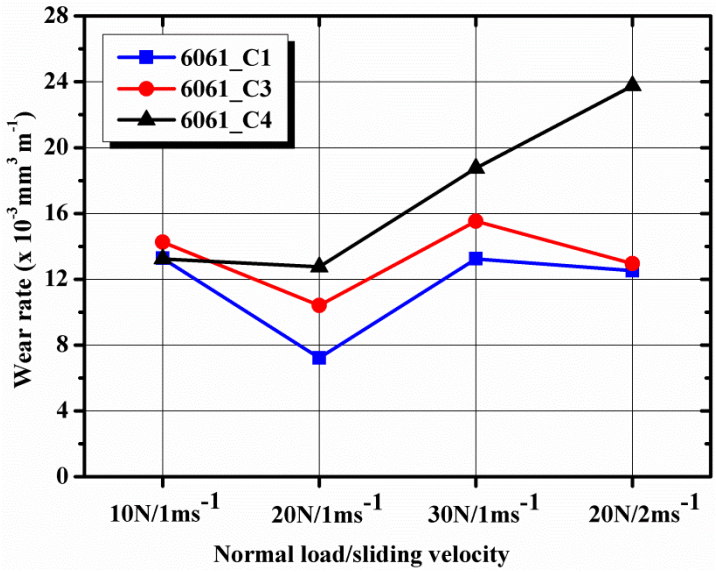

Fig. 5.95 Effect of composition on wear rate

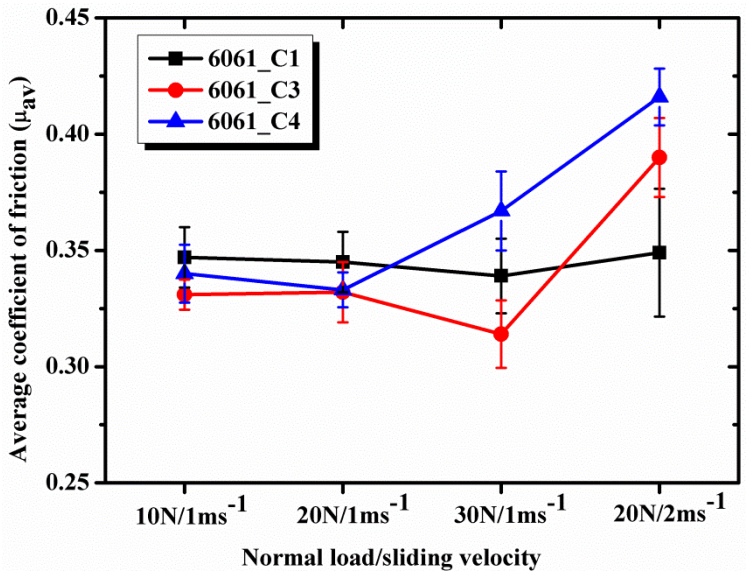

Fig. 5.96 Effect of normal load and sliding velocity on average coefficient of friction

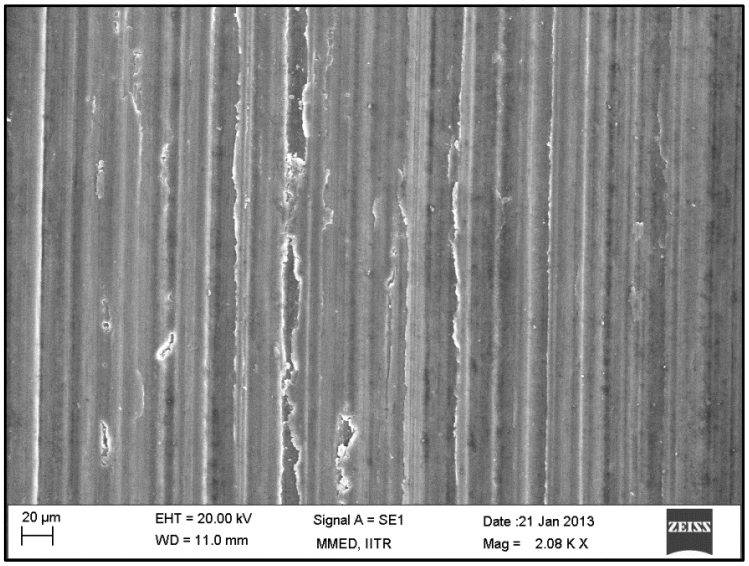

(a)

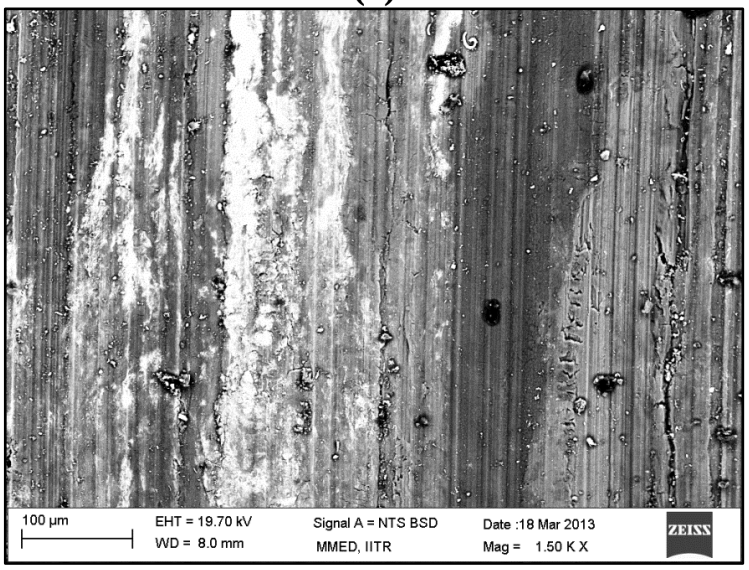

(b)

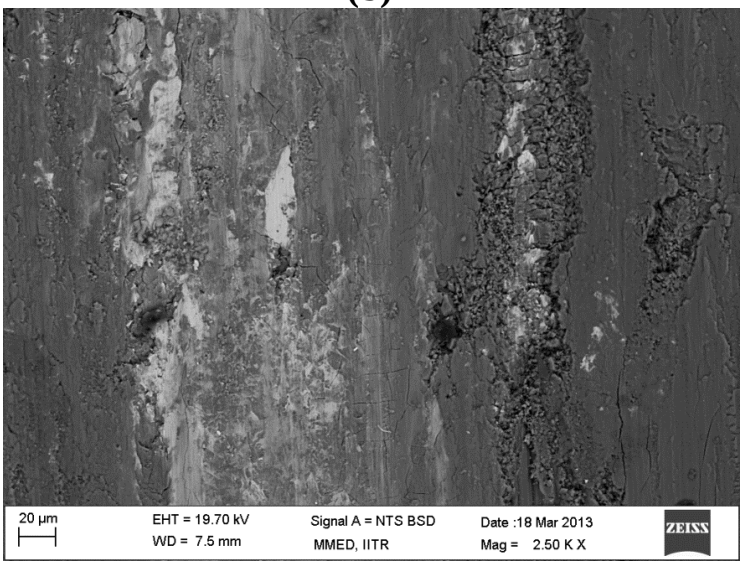

(c)

Fig. 5.97 Scanning electron micrographs of wear tracks formed at (a) 6061_C1 at 20N/1ms^{-1}, (b) 6061_C3 at 10N/1ms^{-1} and 6061_C3 at 20N/1ms^{-1} (sliding direction is vertical)

5.9.4.3 Coefficient of thermal expansion

Values obtained have been tabulated in Table 5.14, as below. CTE values for the composite have been compared with ROM (Eq. 2.7) and Schapery equation (Eq. 2.8).

Table 5.15 CTE of AA6061 based compositions

Composition	Short steel fibers wt.% (vol.%)	CTE (x 10^{-6} $^{o}C^{-1}$)	CTE (ROM)	CTE (SE)
6061_C1	0	24.6	--	--
6061_C3	20 (7.9)	22.8	23.5	22.0
6061_C4	30 (12.8)	20.5	22.9	20.7
0.4 wt.% C Steel	--	11.4	--	--

Incorporation of short steel fibers is found to reduce the linear CTE for the composites.

CTE values for sinter-forged AA6061 based composites are found to lie within the limits proposed by ROM and Schapery equations.

In addition to the two matrix materials, namely pure aluminium and AA6061 investigated for development of short steel fiber reinforced composites. AA7075 prealloyed powder, provided by United States Metal Powders Inc., Flemington, NJ, USA, was investigated for sintering behavior and a trial composition of AA7075- 20 wt.% short steel fiber prepared by blending and cold pressing for further sintering and characteriation of reaction interface.

5.10 Development of AA7075 based short steel fiber composites

5.10.1 Characterization of AA7075 prealloyed powder

The powder sample of nominal chemical composition given in Table 5.14; was composed of elongated, ligamental particles with a dendritic substructure (Fig. 5.98). Oxygen content of the sample was determined to be 1689±23 ppm; elongated shape and high oxygen content was indicative of air atomization. AA7075 powder sample had a particle size distribution of D_{10} 43: D_{50} 88: D_{90} 165 (µm) yielding a span value of 1.38- suggestive of a near unimodal particle size distribution; apparent density 1.26 gcm^{-3} and the nominal theoretical density, calculated by inverse ROM, was 2.78 gcm^{-3}.

Table 5.16 Nominal chemical composition of AA7075

Si	Fe	Cu	Mg	Cr	Zn	**Al**
0.05	**0.09**	**1.60**	**2.50**	**0.30**	**5.30**	**Bal.**

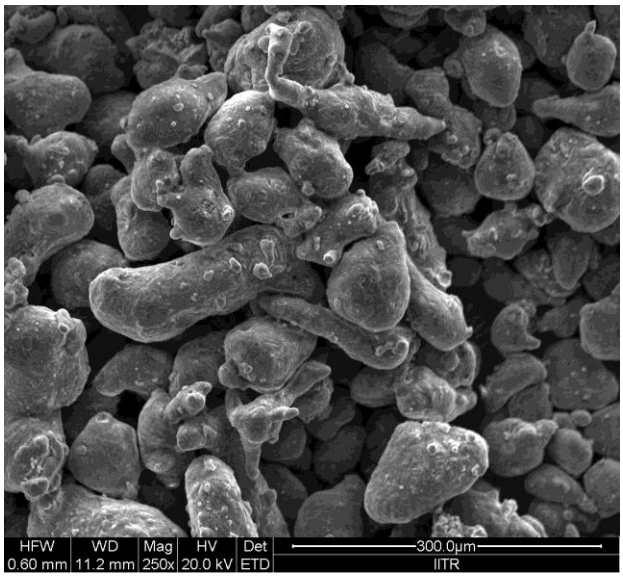

(a)

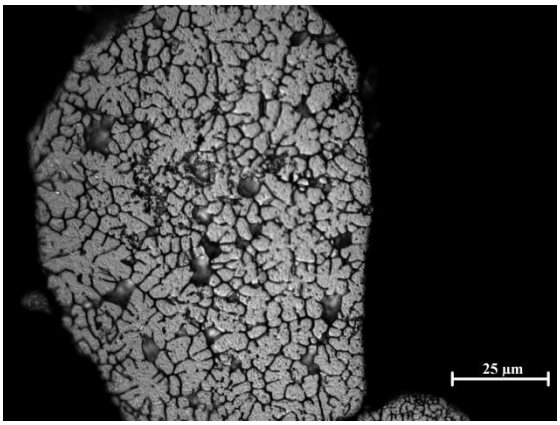

(b)

Fig. 5.98 (a) Scanning electron micrograph of AA7075 powder and (b) optical micrograph showing powder sub-structure

5.10.2 Cold compaction and sintering of AA7075

Effect of compaction pressure on green density is shown in Fig. 5.99. Elongated particles are known to deform and create particle-particle interlocks; green density is reported to follow a linear growth with increasing compaction pressure.

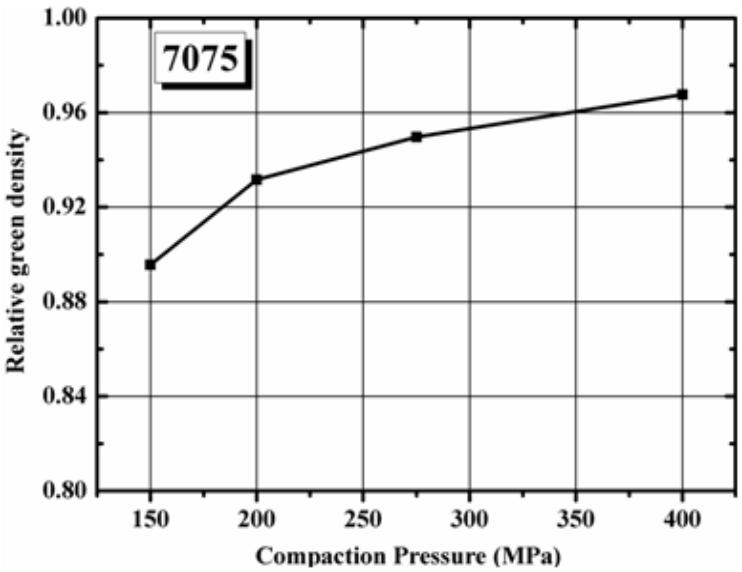

Fig. 5.99 Effect of compaction pressure on relative green density of AA7075

Based on the above compaction curve, 275MPa was selected as the compaction pressure to yield about 95% relative theoretical density.

Selection of sintering temperature was estimated from the heat flow trace of the powder, ensuring at least 10 vol.% liquid fraction for supersolidus liquid phase sintering. As shown in Fig. 5.100, a small endothermic event between 550-575ºC is observed. This is attributed to emergence of a low temperature eutectic phase Al_2Cu, which is reported to aid in sintering densification by wetting the powder particles (LaDelpha, et al., 2009). A sintering temperature of 605ºC was selected to enable sufficient liquid formation, necessary to wet the powder particles and aid in sintering densification. Fig. 5.101 shows a particle junction, which upon sintering is found to be filled with the eutectic. Surface features within the particles were coarse precipitates. A 4% density increment was attained by sintering, yielding a nearly fully dense sintered compact.

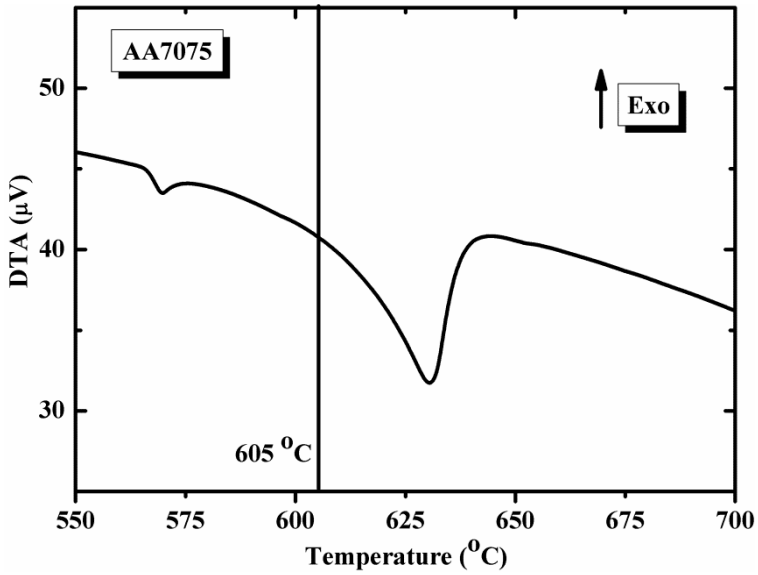

Fig. 5.100 Heat flow trace of AA7075

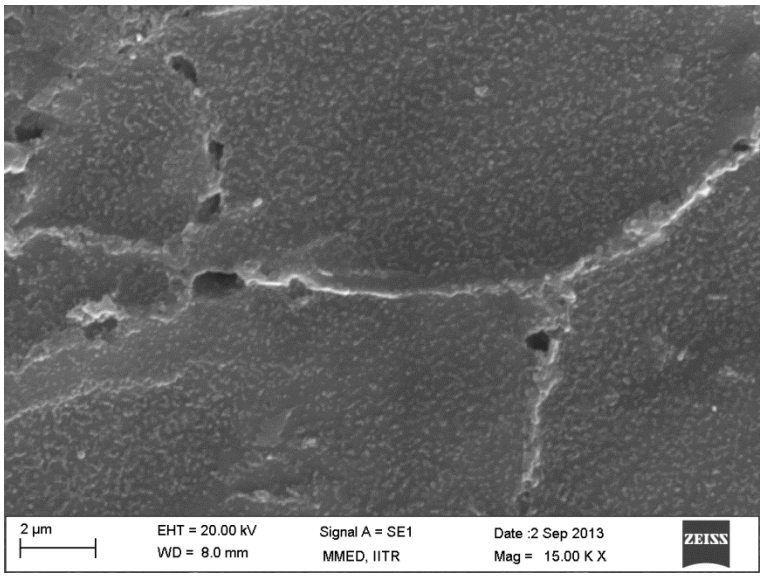

Fig. 5.101 Scanning electron micrograph of sintered AA7075

5.10.3 Sintering of AA7075 - 20 wt. % short steel fiber composite

Composite blend of 20 wt.% steel fibers in AA7075 powder matrix was cold compacted to about 90 % theoretical density and sintered at 605ºC for 40 min under pure nitrogen. The composite compact after sintering was found to have highly porous, foam like structure that extended to the core of the compact. Due to high porosity, density after sintering could not be determined. Fig. 5.102 shows the optical micrographs and EDS area map of sintered compact. The fibers were seen to be coated with a light gray element; huge voids were visible near the fibers.

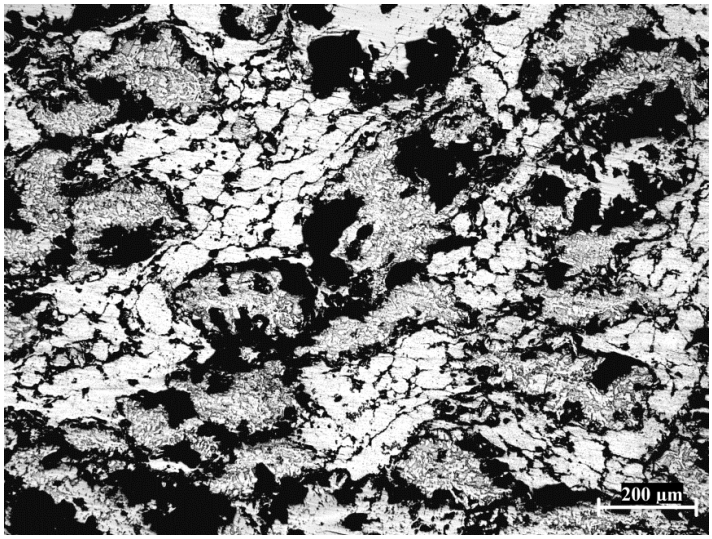

(a)

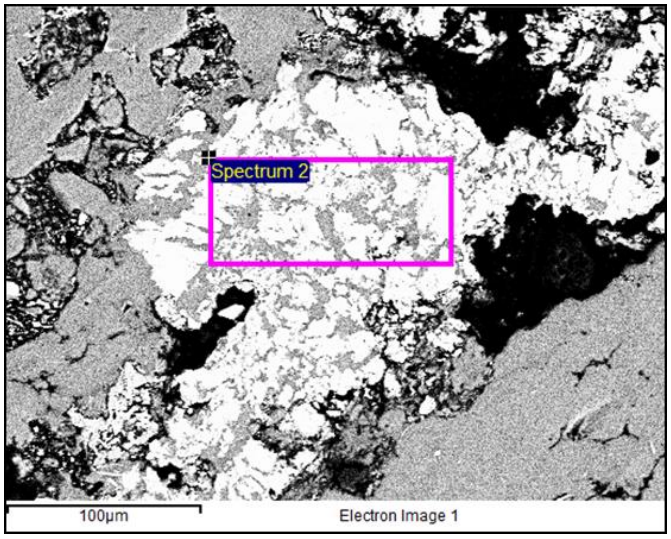

(b)

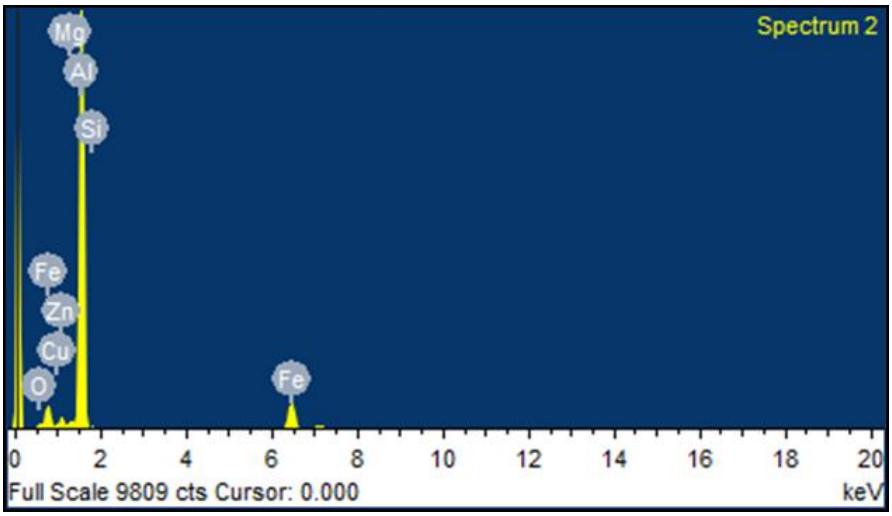

(c)

Fig. 5.102 (a) optical micrograph (b) EDS area map (c) elemental profile from sintered AA7075- 20 wt.% short steel fiber composite

The elemental profile was unable to conclusively establish the presence of any specific element (Fig. 5.102(c)), however it appeared that one or more alloying elements from the AA7075 matrix had leached out reacted with the steel fibers.

Discussion: It is reported that Zn forms a low temperature eutectic (380ºC) with aluminium, which exists as a persistent liquid phase at the sintering temperature (Delgado, et al., 2005). However, Zn is not used as a sintering aid in Al-P/M, in-spite of the liquid forming capability, due to its limited solid-solubility in Al.

As per the Zn-Fe-Al ternary diagram at 460ºC, shown in Fig. 5.103, Zn is seen to form complex intermetallics with Fe.

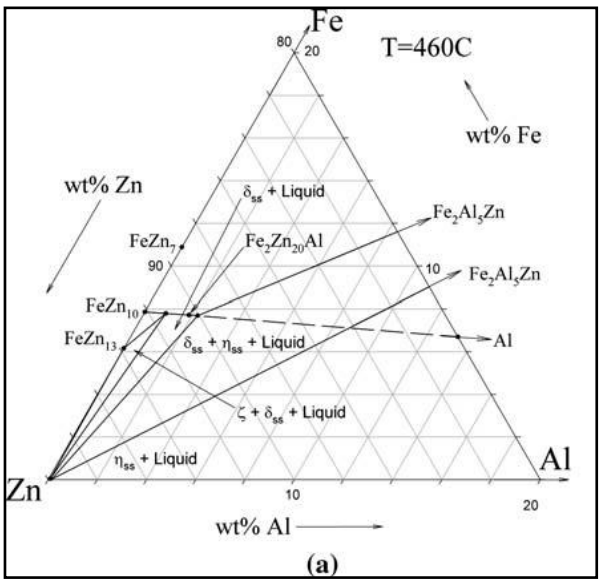

Fig. 5.103 Zn rich part of the Zn-Fe-Al ternary diagram (McDermid, et al., 2007)

The most probable explanation for the observed phenomena could be that Zn leached out of AA7075 matrix at 380ºC; reacted with Fe from short steel fibers to form Fe-Zn intermetallic phases; leading to either an aluminothermic reduction of Fe-oxides by α-aluminium or some other reaction by which volumetric expansion of the compact occurred, creating large voids.

In light of the above observations, it was proposed to limit the development of AA7075 based short steel fiber composites at this stage.

Chapter 6

CONCLUSIONS

6.1 Conclusions

The aim of the present investigation was focused on the development of short steel fiber reinforced aluminium matrix composites by powder metallurgical processing. Matrices based on pure aluminium and AA6061 were investigated. For development of the composites, it was necessary to first understand the salient features of aluminium powder metallurgy, characterize the starting materials, develop a processing methodology and evaluate the mechanical, elevated temperature and tribological behavior of the developed unreinforced and composite materials.

The significant achievements of the research have been listed as below, in accordance with the stated objectives:

i. As- received powders were characterized for morphology, size distribution, sub-structure and oxygen content. Powders were inert gas atomized, determined on the basis of oxygen content.

ii. Short steel fibers were composed of a ferritic-pearlitic substructure with a "kidney" shaped cross-section.

iii. Fe-Al type of intermetallic reaction products were analyzed by simulated vacuum hot pressing. Growth of reaction interface was diffusion controlled and found to obey a parabolic law, for which the rate constant was evaluated.

iv. Low temperature conventional hot pressing resulted in avoiding the growth of reaction interface.

v. Surface modification and heat treatment by nitriding, chromizing and aluminizing of short fibers was successfully achieved in a fluidized bed reactor.

vi. Uniform deposition was observed over the fiber surface, thickness was controlled by varying heat treatment duration.

vii. Nitriding resulted in formation of a hardened case, composed of γ'-Fe_4N and ε-$Fe_{2-3}N$, which was able to provide a barrier against Fe-Al interdiffusion.

viii. Soft chromizing resulted in formation of Fe-Cr solid-solution layer over the steel fibers.

ix. Aluminizing treatment provided a strong $FeAl_3$ (θ) layer over the fiber surface, which prevented further growth of brittle reaction interface during sintering of composites.

x. Role of elemental Mg as sintering aid was evaluated by DSC, SEM and optical emission spectroscopy. Disruption of oxide layer and sintering densification was achieved for pure aluminium.

xi. Positive sintering densification was achieved for all compositions. Fiber-matrix reaction interface of 15 µm thickness was composed of $FeAl_3$ (θ)/ FeAl (β) and Fe_3AlC (κ)/ Fe_2Al_5 (η) intermetallic compounds.

xii. Significant increase in as-sintered matrix hardness (32 HV) for pure aluminium to 74 HV for 30 wt.% reinforced composite was achieved.

xiii. Flow stress at elevated temperature was found to increase with increasing reinforcement content.

xiv. Elevated temperature wear behavior was studied. Wear rate and COF were found to decrease with increasing fiber content. Increased temperature had no effect on wear volume loss of 20 and 30 wt.% reinforced composites.

xv. Constrained die hot upset forging after sintering yielded near-full density composites with a controlled reaction interface thickness of 5 µm. Effect of deformation strain on microstructure and reinforcement distribution was evaluated.

xvi. 4-fold increase in flexural strength was achieved by forging.

xvii. Highest UTS, significantly higher than ROM, and elongation to failure was achieved by rolling.

xviii. Lower wear rate and stable COF was recorded for composites from room temperature dry sliding tests.

xix. UTS and elongation to failure for sinter-forged AA6061 were comparable to wrought alloy.

xx. Increase in flow stress (2-fold) at elevated temperature was achieved for AA6061 based composites in comparison to monolithic alloy.

xxi. Decrease in matrix hardness was observed for AA6061 composites, thereby deterioration in wear resistance was observed.

xxii. Reduction in CTE was achieved for all the compositions investigated.

6.2 Suggestions for future work

Some of the points that emerged during the present investigation need to be further investigated in detail, these are as follows:

i. To achieve preferential alignment of short fibers for functionally specific applications.

ii. To further investigate the reaction of fibers with AA7075 and develop barrier coatings which inhibit fiber-matrix interactions.

iii. To evaluate fracture toughness and elastic moduli of the developed composites by NDT.

iv. To characterize the developed composites for ballistic impact applications.

REFERENCES

1. Abdel-Rahman M., and El-Sheikh, M. (1995). Workability in forging of powder metallurgy compacts. *Journal of Materials Processing Technology*, (54), 97–102.
2. Abouelmagd, G. (2004). Hot deformation and wear resistance of P/M aluminium metal matrix composites. *Journal of Materials Processing Technology*, (155-156), 1395–1401.
3. Agarwala, R. C., Agarwala, V. and Garg, L.M. (1998) production of reinforced castings containing stainless steel wires in Aluminium alloy *BergUndHuttenmannischeMonatshefte*, . (143) 3 86–.89
4. Agarwala, V., Satyanarayana, K. G., and Agarwala, R. C. (1999). Studies on the development of aluminium alloy–mild steel reinforced composite. *Materials Science and Engineering: A*, *270*(2), 210–218.
5. Aghajanian, M., and Rocazella, M. (1991). The fabrication of metal matrix composites by a pressureless infiltration technique. *Journal of Materials Science*, (26), 447–454.
6. Alahelisten A., Bergman F., Olsson M. and Hogmark S. (1993). On the wear of aluminium and magnesium metal matrix composites. *Wear*, 165(April), 221–226.
7. Alsaran, A., Çelik, A., and Karakan, M. (2005). Structural, mechanical and tribological properties of duplex-treated AISI 5140 steel. *Materials Characterization*, 54(1), 85–92.
8. Alpas, T., and Zhang, J. (1994). Effect of microstructure (particulate size and volume fraction) and counterface material on the sliding wear resistance of particulate-reinforced aluminium matrix composites. *Metallurgical and Materials Transactions A*, 25(5), 969–983.
9. Arsenault, R. J. (1988). Relationship between strengthening mechanisms and fracture toughness of discontinuous SiC/Al composites. *Journal of Composites Technology and Research*, 10(4), 140–145.
10. Asgharzadeh H., and Simchi, A. (2008). Hot deformation of PM Al6061 alloy produced by sintering and powder extrusion. *Powder Metallurgy*, 51(4), 354–360.
11. ASM International. (1990). *ASM Handbook–Volume 1: Properties and Selection: Irons, Steels, and High Performance Alloys*. *ASM International*. ASM International, Materials Park, OH, USA
12. A S M International. (1992). *ASM metals handbook volume 3 Alloy Phase Diagrams*. ASM International, Materials Park, OH, USA
13. Kumar Ashok, Jain P. C., and Mehta M. L. (1982). Aluminium powder extrusion through wedge-shaped dies as an effective use of energy. *Journal of Mechanical Working Technology*, (6), 235–251.
14. ASM International. (1991). *ASM Metals Handbook, Vol.4: Heat Treating* (pp. 1064–1066). ASM International, Materials Park, OH.
15. Pai B. C., Pillai R. M., and Satyanarayana K. G. (1999). Interfaces and Structure Property in Metal Matrix Composites. In R. S. Agarwala, R.C., Agarwala V., Kumar S. (Ed.), *Institute Industry Interaction Meet, University of Roorkee*, 25–31.
16. Bader, M. G., Clyne, T. W., Cappleman, G. R., and Hubert, P. A. (1985). The fabrication and properties of metal-matrix composites based on aluminium alloy

infiltrated alumina fibre preforms. *Composites Science and Technology*, 23(4), 287–301.

17. Badini, C., Vecchia, G. La, Fino, P., and Valente, T. (2001). Forging of 2124/SiC p composite: preliminary studies of the effects on microstructure and strength. *Journal of Materials Processing Technology*, (116), 289–297.

18. Baker, T., Gorton, A., and Song, Y. (1996). Powder processing of AA 6061 aluminium metal matrix composites using hot forging as means of consolidation. *Powder Metallurgy*, 39(3), 223–229.

19. Baron, R., Wert, J., Gerard, D., and Wawner, F. (1997). The processing and characterization of sintered metal-reinforced aluminium matrix composites. *Journal of Materials Science*, (2), 6435–6445.

20. Bath, F. (2003). Fine Tuning Sieve Analysis.(Unpublished work) *Chemical Engineering*. Retrived from http://www.retsch.dk/pdf/pdf_applikationer/fine_tuning_sieving_analysis_en.pdf

21. Bhagat, R. (1988). High pressure squeeze casting of stainless steel wire reinforced aluminium matrix composites. *Composites*, 19(5), 393–399.

22. Bhagat, R. B. (1985). The effects of hot pressing parameters on the strength of aluminium/stainless steel composites. R.B. Bhagat. *Metallurgical Transactions A*, 16(April), 623–628.

23. Bhagat, R. B. (1989). Growth kinetics of interface intermetallic compounds in stainless steel fibre reinforced aluminium matrix composites. *Journal of Materials Science*, 24(4), 1496–1502.

24. Bishop, D. P., Cahoon, J. R., Chaturvedi, M. C., Kipouros, G. J., and Caley, W. F. (2000). On enhancing the mechanical properties of aluminium P/M alloys. *Materials Science and Engineering: A*, 290(1-2), 16–24.

25. Bishop, D. P., Caley, W. F., Kipouros, G. J., Hexemer, R. L., and Donaldson, I. W. (2011). Powder metallurgy processing of 2xxx and 7xxx series aluminium alloys. *Canadian Metallurgical Quarterly*, 50(3), 246–252.

26. Bouche, K., Barbier, F., and Coulet, A. (1998). Intermetallic compound layer growth between solid iron and molten aluminium. *Materials Science and Engineering: A*, (249), 167–175.

27. Boron nitride coatings. (n.d.). Retrieved December 01, 2013, from www.momentive.com/Products/Main.aspx?id=22816

28. Campbell, F. C. (2006). Chapter 2 - Aluminium. For A. S. M. Campbell (Ed.), *Manufacturing Technology for Aerospace Structural Material*, 15–92.

29. Cavaliere, P., Zavarise, G., and Perillo, M. (2009). Modeling of the carburizing and nitriding processes. *Computational Materials Science*, 46(1), 26–35.

30. Cavaliere, P. (2007). Flow curve prediction of an Al-MMC under hot working conditions using neural networks. *Computational Materials Science*, 38(4), 722–726.

31. Carvalho, M. H., Carvalhinhos, H., and Sellars, C. M. (1990). Extrusion and Properties of 7075 Ingot and Particulate. *Powder Metallurgy*, 33(4), 339–348.

32. Chaturvedi, A. K., Chandra, K., and Mishra, P. S. (2009). Wear Characterization of Al/Ingredients MMFC. *Journal of Tribology*, 131(4), 0416011–0416017.

33. Chawla, N., Williams, J. and Saha, R. (2002). Mechanical behavior and microstructure characterization of sinter-forged SiC particle reinforced aluminium matrix composites. *Journal of Light Metals*, *2*(4), 215–227.

34. Chennai Metco. (2012). Retrieved from http://www.chennaimetco.com/consumables-catalogue.pdf

35. Chinh, N. Q., Lendvai, J., Ping, D. H., and Hono, K. (2004). The effect of Cu on mechanical and precipitation properties of Al–Zn–Mg alloys. *Journal of Alloys and Compounds*, 378(1-2), 52–60.

36. Choi, N., and Takahashi, K. (1992). Stress fields on and beneath the surface of short-fiber-reinforced composites and their failure mechanisms. *Composites Science and Technology*, 43(3), 237–244.

37. Clyne, T. (2000). An introductory overview of MMC systems, types, and developments. In A. K. and C. Zweben (Ed.), *Comprehensive composite materials*, Elsevier B.V., 821–842.

38. Clyne, T. W. (2001). Metal Matrix Composites : Matrices and Processing. In A. Mortensen (Ed.), *Encyclopaedia of Materials: Science and Technology* (1–14). Elsevier B.V.

39. Clyne, T., and Watson, M. (1991). Interfacial mechanics in fibre-reinforced metals. *Composites Science and Technology*, (42), 25–55.

40. Karpinos, D M. et al., (1978). Role of brittle layers in the behavior of fiber composite materials at elevated temperatures. *Institute of Materials Science, Academy of Sciences of the Ukrainian SSR. Translated from Porosh- Kovaya Metallurgiya*, 3(183)(3), 44–50.

41. Karpinos D. M. et al., (1974). Preparation of an aluminium-base composite material reinforced with steel fibers using the plasma spray deposition technique. *Institute of Materials Science, Academy of Sciences of the Ukrainian SSR. Translated from Porosh-Kovaya Metallurgiya*, 8(140)(8), 636–638.

42. Kim, M., and Yoon, B. (1996). Reinforced material for an automobile connecting rod. *US Patent 5,523,171*.

43. Das, S. K., Gilman, P. S., and Raybould, D. (1990). Applications of Rapidly Solidified High Temperature Aluminium Alloys. *Key Engineering Materials*, (38-39), 367–392.

44. Dashwood, R., and Schaffer, G. (2002). Powder forging of a sintered Al–3.8Cu–1Mg–0.8Si–0.1Sn alloy. *Materials Science and Engineering: A*, 323(1-2), 206–212.

45. Davies, C. H. J. (1995). Critical issues in the extrusion of particle reinforced metal matrix composites. *Key Engineering Materials*, (104-107), 447–458.

46. Delannay, F., Colin, C., Marchal, Y., Tao, L., Boland, F., Cobzaru, P.,Dellis, M.A. (1993). Processing and properties of metal matrix composites reinforced with continuous fibres for the control of thermal expansion, creep resistance and fracture toughness. *Le Journal de Physique IV*, 03(C7), 1675–1684.

47. Delgado, M. L., Ruiz-Navas, E. M., Gordo, E., and Torralba, J. M. (2005). Enhancement of liquid phase sintering through Al–Si additions to Al–Cu systems. *Journal of Materials Processing Technology*, (162-163), 280–285.

48. Deuis, R. L., Subramanian, C., and Yellup, J. M. (1997). Sliding of aluminium composites-a review. *Composites Science and Technology*, 57(96), 415–435.

49. Durrant, G., Gallerneault, M., and Cantor, B. (1996). Squeeze cast aluminium reinforced with mild steel inserts. *Journal of Materials Science*, (31), 589–602.

50. Eggeler, G., Auer, W., and Kaesche, H. (1986). On the influence of silicon on the growth of the alloy layer during hot dip aluminizing. *Journal of Materials Science*, (21), 3348–3350.

51. Eksi, A., Veltl, G., Petzoldt, F., Lipp, K., and Sonsino, C. M. (2004). Tensile and fatigue properties of cold and warm compacted Alumix 431 alloy. *Powder Metallurgy*, 47(1), 60–64.

52. Fabijanic, D. M. and Hodgson, P. D. (2010). Surface alloying of metals using fluid bed reactor, International heat treatment and surface engineering. *International Heat Treatment and Surface Engineering*, 4(3), 103–104.

53. Feest, E. (1994). Interfacial phenomena in metal-matrix composites. *Composites*, 25(2), 75–86.

54. Feng, Y. C., Geng, L., Zheng, P. Q., Zheng, Z. Z., and Wang, G. S. (2008). Fabrication and characteristic of Al-based hybrid composite reinforced with tungsten oxide particle and aluminium borate whisker by squeeze casting. *Materials and Design*, 29(10), 2023–2026.

55. Fogagnolo, J., Ruiz-Navas, E., Simón, M., and Martinez, M. (2003). Recycling of aluminium alloy and aluminium matrix composite chips by pressing and hot extrusion. *Journal of Materials Processing Technology*, (143-144), 792–795.

56. Friction, Lubrication and Wear Technology. (1992). In *ASM Handbook vol. 18* (p. 340). ASM International, Materials Park, OH.

57. Friedrich, E., Pompe, W., and Kopjov, I. M. (1974). The influence of brittle boundary layers on the strength of fibrous metallic composites. *Journal of Materials Science*, 9(12), 1911–1916.

58. Friend, C. (1987). The effect of matrix properties on reinforcement in short alumina fibre-aluminium metal matrix composites. *Journal of Materials Science*, (22), 3005–3010.

59. Galanty, M., and Kazanowski, Pawel, Panya Kansuwan, W. Z. M. (2002). Consolidation of metal powders during the extrusion process. *Journal of Materials Processing Technology*, (125-126), 491–496.

60. Ganesh, V., and Gupta, M. (2001). Effect of the extent of reinforcement interconnectivity on the properties of an aluminium alloy. *Scripta Materialia*, 44(2), 305–310.

61. Ganesh, V., Lee, C., and Gupta, M. (2002). Enhancing the tensile modulus and strength of an aluminium alloy using interconnected reinforcement methodology. *Materials Science and Engineering: A*, 333(1-2), 193–198.

62. Ganesh, V., Tan, P., and Gupta, M. (2001). Development and characterization of an aluminium alloy containing interconnected-wires as reinforcement. *Journal of Alloys and Compounds*, 315(1-2), 203–210.

63. German, R. (1997). Supersolidus liquid-phase sintering of prealloyed powders. *Metallurgical and Materials Transactions A*, 28(July), 1553–1567.

64. Ghomashchi, M. R., and Vikhrov, A. (2000). Squeeze casting : an overview, *Journal of Materials Processing Technology*, *101*(May 1998), 1–9.

65. Ghosh, P., and Ray, S. (1987). Effect of porosity and alumina content on the high temperature mechanical properties of compocast aluminium alloy-alumina particulate composite. *Journal of Materials Science*, 22(11), 4077–4086.

66. Girot, F., Quenisset, J., and Naslain, R. (1987). Discontinuously-reinforced aluminium matrix composites. *Composites Science and Technology*, (30), 155–184.

67. Goswami, R. K. et al., (1999). Extrusion characteristics of aluminium alloy / SiC metal matrix composites, *Materials Science and Technology* 15(April), 443–449.

68. Greasley, A., and Shi, H. (1993). Microstructural development during hot working of powdered aluminium alloy. *Powder Metallurgy*, 36(4), 288–292.

69. Griffiths, T., Davies, R., and Bassett, M. (1976). Compatibility equations for the powder-forging process. *Powder Metallurgy*, (4), 216–220.

70. Güley, V., Ben Khalifa, N., and Tekkaya, A. E. (2010). Direct recycling of 1050 aluminium alloy scrap material mixed with 6060 aluminium alloy chips by hot extrusion. *International Journal of Material Forming*, 3(S1), 853–856.

71. Gupta, M., Lai, M., and Lim, C. (2006). Development of a novel hybrid aluminium-based composite with enhanced properties. *Journal of Materials Processing Technology*, (176), 191–199.

72. Gupta, M. et al., (2005). On the use of interconnected reinforcements to enhance the performance of monolithic aluminium. *Current Science*, (1050), 1419–1425.

73. Güzel, A. et al., (2012). A new method for determining dynamic grain structure evolution during hot aluminium extrusion. *Journal of Materials Processing Technology*, 212(1), 323–330.

74. H. Akbulut, M. D. F. Y. (1998). Dry wear and friction properties of t -Al2O3 short fiber reinforced AI-Si (LM 13) alloy metal matrix composites. *Wear*, (215), 170–179.

75. Hansen, N., Bay, B. (1972). The effect of particle content, particle distribution and cold deformation on the recrystallization of low oxide Al-Al203 products. *Journal of Materials Science*, (7), 1351–1362.

76. Hendrickson, Machmeier, P. M., and Smith, D. W. (2000). Impact forging of sintered steel preforms. *Powder Metallurgy*, *43*(4), 327–344.

77. Hodiamont, S., Peter, M., and Bunk, W. (1991). Extrusion and swaging of rapidly quenched aluminium powders: microstructure and mechanical properties. *Materials Science and Engineering: A*, (133), 270–273.

78. Huda, D., El Baradie, M. a., and Hashmi, M. S. J. (1993). Metal-matrix composites: Materials aspects. Part II. *Journal of Materials Processing Technology*, 37(1-4), 529–541.

79. Humphreys, F., and Kalu, P. (1987). Dislocation-particle interactions during high temperature deformation of two-phase aluminium alloys. *Acta Metallurgica*, 35(12), 2815–2829.

80. Hunt, W. J. (2000). New directions in aluminium: Based P/M materials for automotive applications. *Society of Automotive Engineers*, (2000-01-03), 1–8.

81. Hunt, Jr., W. H. (2000). Aluminium metal matrix composites today. *Materials Science Forum*, (331-337), 71–84.

82. Hutchings, I. (1994). Tribological properties of metal matrix composites. *Materials Science and Technology*, 10(June), 513–517.

83. Hwang, Y.H., Horng, C.F., Lin, S.J., Liu, K.S., and Jahn, M.T. (1997). Interface study for stainless steel fibre-reinforced aluminium matrix composite. *Journal of Materials Science*, (32), 719–725.

84. Ichikawa, J., and Morita, K. (2010). Manufacturing method of sinter forged aluminium parts with high strength. *US Patent 7,651,659*.

85. Iwai, Y., Yoneda, H., and Honda, T. (1995). Sliding wear behavior of SiC whisker-reinforced aluminium composite. *Wear*, (181-183), 594–602.

86. Iwata, Y., Mae, S., Urai, Y., and Tsunoda, T. (1989). Aluminium alloy having an excellent forgiability. *US Patent 4,889,557*.

87. Yang J., D. D. L. C. (1989). Casting particulate and fibrous metal-matrix composites by vacuum infiltration of a liquid metal under an inert gas pressure. *Journal of Materials Science*, (24), 3605–3612.

88. Karwan-baczewska J., Dymkowski T. and Sobiecki J.R., (2010). Processing and surface properties of based on iron sintered alloys after plasma nitriding treatment. *Archives of Metallurgy and Materials*, 55(2), 383–389.

89. Jabbari Taleghani, M. A., Ruiz Navas, E. M., Salehi, M., and Torralba, J. M. (2012). Hot deformation behaviour and flow stress prediction of 7075 aluminium alloy powder compacts during compression at elevated temperatures. *Materials Science and Engineering: A*, (534), 624–631.

90. Jabbari Taleghani, M. A., Ruiz Navas, E. M., and Torralba, J. M. (2014). Microstructural and mechanical characterisation of 7075 aluminium alloy consolidated from a premixed powder by cold compaction and hot extrusion. *Materials and Design*, (55), 674–682.

91. Jang, H., Ko, K., Kim, S., Basch, R., and Fash, J. (2004). The effect of metal fibers on the friction performance of automotive brake friction materials. *Wear*, 256(3-4), 406–414.

92. Jones, H. (2004). Gas-atomised aluminium alloy powders and their products: an update 1996–2001. *Materials Science and Engineering: A*, (375-377), 104–111.

93. Jongbloed, R.C. (1994). Chromizing. *Materials Science Forum*, (163-165), 611–618.

94. Kaczmar, J. W., Pietrzak, K., and W, W. (2000). The production and application of metal matrix composite materials. *Journal of Materials Processing Tchnology*, (106), 58–67.

95. Kainer, K. U. (2006a). Basics of metal matrix composites. In *Metal Matrix Composites* (1–54). Wiley-VCH Verlag GmbH and Co. KGaA.

96. Kainer, K. U. (2006b). Metal matrix composites: custom-made materials for automotive and aerospace engineering. In K. U. Kainer (Ed.), *Metal Matrix Composites. Custom-made Materials for Automotive and Aerospace Engineering*. WILEY-VCH Verlag GmbH and Co. KGaA, Weinheim.

97. Kang, C., Kim, N., and Kim, B. (2000). The effect of die shape on the hot extrudability and mechanical properties of 6061 Al/Al2O3 composites. *Journal of Materials Processing Technology*, 100(1-3), 53–62.

98. Karwan Baczewska, J., Dymkowski, T., Sobiecki, J. R., and Bonarski, J. T. (2011). Structural Investigations of Iron-Based Sintered Alloys after Plasma Nitriding. *Materials Science Forum*, (674), 121–128.

99. Kato, K. (2000). Wear in relation to friction - a review. *Wear*, 241(2), 151–157.

100. Kato, K. (2002). Classification of wear mechanisms/models. *Proceedings of the Institution of Mechanical Engineers, Part J: Journal of Engineering Tribology*, 216(6), 349–355.

101. Kent, D., Schaffer, G. B., Sercombe, T. B., and Drennan, J. (2006). A novel method for the production of aluminium nitride. *Scripta Materialia*, 54(12), 2125–2129.

102. Kevorkijan, V. (2004). Mg AZ80/SiC composite bars fabricated by infiltration of porous ceramic preforms. *Metallurgical and Materials Transactions A*, 35(February), 11–14.

103. Kim, T.W. (2008). Determination of densification behavior of Al–SiC metal matrix composites during consolidation processes. *Materials Science and Engineering: A*, (483-484), 648–651

104. Kipouros, G., Caley, W., and Bishop, D. (2006). On the advantages of using powder metallurgy in new light metal alloy design. *Metallurgical and Materials Transactions A*, (37 A), 3429–3436.

105. Kobayashi, S., and Yakou, T. (2002). Control of intermetallic compound layers at interface between steel and aluminium by diffusion-treatment. *Materials Science and Engineering: A*, 338(1-2), 44–53.

106. Kondoh, K., Kimura, A., and Watanabe, R. (2001). Effect of Mg on sintering phenomenon of aluminium alloy powder particle, 44(2), 161–164.

107. Kuhn, H. A. (1978). Chapter 4 - Deformation Processing of Sintered Powder Materials. In H. A. KUHN and A. LAWLEY (Eds.), *Powder Metallurgy Processing* (99–138). Academic Press.

108. Kumar, A., Jain, P., and Mehta, M. (1987). Hot extrusion of aluminium powder at low reduction ratios: Analytical and metallographic studies. *Metallurgical Transactions B*, 18(December), 703–711.

109. Kumar, A., Jha, S., Jain, P., and Mehta, M. (1985). An investigation into product defects in the hot extrusion of aluminium powder preforms. *Journal of Mechanical Working*, (11), 275–290.

110. Kumar, P. R. S., Kumaran, S., and Rao, T. S. (2010). Comparison study of fly ash reinforced AA6061 composites using press sinter extrusion and press extrusion approaches. *Powder Metallurgy*, 53(2), 163–168.

111. Kumar, P. R. S., Kumaran, S., Rao, T. S., and Sivaprasad, K. (2009). Transactions of The Indian Institute of Metals Microstructure and mechanical properties of fly ash particle reinforced AA6061 composites produced by press and extrusion, 62(6), 559–566.

112. LaDelpha, a. D. P., Neubing, H., and Bishop, D. P. (2009). Metallurgical assessment of an emerging Al–Zn–Mg–Cu P/M alloy. *Materials Science and Engineering: A*, 520(1-2), 105–113.

113. Lai, S., and Chung, D. (1994). Fabrication of particulate aluminium-matrix composites by liquid metal infiltration. *Journal of Materials Science*, (29), 3128–3150.

114. Lasagni, F., Acuña, J. A., and Degischer, H. P. (2008). Interpenetrating hybrid reinforcement in al2o3 short fiber preforms infiltrated by al-si alloys. *Metallurgical and Materials Transactions A*, 39(6), 1466–1474.

115. Lavernia, E. J., and Srivatsan, T. S. (2009). The rapid solidification processing of materials: science, principles, technology, advances, and applications. *Journal of Materials Science*, 45(2), 287–325.

116. Lawrence, C., Mummery, P., and Tweed, J. (1993). Observations of extrusion-induced damage of metal-matrix composites. *Journal of Materials Science Letters*, (12), 647–649.

117. Leon, C., and Drew, R. (2002). The influence of nickel coating on the wettability of aluminium on ceramics. *Composites Part A: Applied Science and Manufacturing*, (33), 1429–1432.

118. Lindroos, V. K., and Talvitie, M. J. (1995). Recent advances in metal matrix composites. *Journal of Materials Processing Technology*, (53), 273–284.

119. Liu, Z. Y., Sercombe, T. B., and Schaffer, G. B. (2007). The effect of particle shape on the sintering of aluminium. *Metallurgical and Materials Transactions A*, 38(6), 1351–1357.

120. Lloyd, D. (1994). Particle reinforced aluminium and magnesium matrix composites. *International Materials Reviews*, 39(1), 1–23.

121. Lloyd, D., and Chaturvedi, M. (1982). A calorimetric study of aluminium alloy AA-7075. *Journal of Materials Science*, (17), 1819–1824.

122. Lumley, R. N., and Schaffer, G. B. (1996). The effect of solubility and particle size on liquid phase sintering, *Scripta Materialia* 35(5), 589–595.

123. Lumley, R. N., and Schaffer, G. B. (1998). The effect of additive particle size on the mechanical properties of sintered aluminium-copper alloys, *Scripta Materialia* 39(8), 1089–1094.

124. Lumley, R. N., Sercombe, T. B., and Schaffer, G. M. (1999). Surface oxide and the role of magnesium during the sintering of aluminium. *Metallurgical and Materials Transactions A*, 30(2), 457–463.

125. Rittner, M. (2000). Metal matrix composites in the 21st century: markets and opportunities. Norwalk CT: BCC Inc.

126. MacAskill, I. A., Hexemer, R. L., Donaldson, I. W., and Bishop, D. P. (2010). Effects of magnesium, tin and nitrogen on the sintering response of aluminium powder. *Journal of Materials Processing Technology*, 210(15), 2252–2260.

127. MacAskill, I. A., LaDepha, a. D. P., Milligan, J. H., Fulton, J. J., and Bishop, D. P. (2009). Effects of cold and hot densification on the mechanical properties of a 7XXX series powder metallurgy alloy. *Powder Metallurgy*, 52(4), 304–310.

128. Malas, J., Venugopal, S., and Seshacharyulu, T. (2004). Effect of microstructural complexity on the hot deformation behavior of aluminium alloy 2024. *Materials Science and Engineering: A*, 368(1-2), 41–47.

129. Maleki, A., Shafyei, A., and Niroumand, B. (2008). Effects of squeeze casting parameters on the microstructure of LM13 alloy. *Journal of Materials Processing Technology*, doi:10.1016/j.jmatprotec.2008.08.035

130. Mandal, D., Dutta, B. K., and Panigrahi, S. C. (2004). Wear and friction behavior of stir cast aluminium-base short steel fiber reinforced composites. *Wear*, 257(7-8), 654–664.

131. Mandal, D., Dutta, B. K., and Panigrahi, S. C. (2007a). Effect of coating on the wear properties of stir cast Al–2Mg base short steel fiber reinforced composites. *Materials Science and Engineering: A*, (460-461), 485–493.

132. Mandal, D., Dutta, B. K., and Panigrahi, S. C. (2007b). Influence of coating on short steel fiber reinforcements on corrosion behavior of aluminium base short steel fiber reinforced composites. *Journal of Materials Science*, 42(8), 2796–2801.

133. Mandal, D., Dutta, B. K., and Panigrahi, S. C. (2007). Influence of mechanical working on properties of aluminium base short steel fiber reinforced composites. *Journal of Materials Science*, 42(20), 8622–8628.

134. Mandal, D., Dutta, B. K., and Panigrahi, S. C. (2008). Effect of wt% reinforcement on microstructure and mechanical properties of Al–2Mg base short steel fiber composites. *Journal of Materials Processing Technology*, 198(1-3), 195–201.

135. Mandal, D., Dutta, B., and Panigrahi, S. (2006). Microstructure and mechanical properties of Al–2Mg alloy base short steel fiber reinforced composites prepared by vortex method. *Journal of Materials Science*, (41), 4764–4770.

136. Mann, R. E. D. et al., (2011). Hot deformation of an Al–Cu–Mg powder metallurgy alloy. *Materials Science and Engineering: A*, 528(16-17), 5476–5483.

137. Mannan, S. K., Seetharaman, V., and Raghunathan, V. S. (1983). A Study of Interdiffusion between AISI Type 316 Stainless Steel and Aluminium. *Materials Science and Engineering: A*, (60), 79–86.

138. Marketing and the Technical and Standards Committees of the Pigments and Powder Division of The Aluminium Association, I. (1986). *Aluminium Powder Metallurgy* (38), 30–32.

139. Markaki, A, V. Gergely, A. Cockburn, T. W. C. (2003). Production of a highly porous material by liquid phase sintering of short ferritic stainless steel fibres and a preliminary study of its mechanical behaviour. *Composites Science and Technology*, 63(16), 2345–2351.

140. Martín, J., and Castro, F. (2003). Liquid phase sintering of P/M aluminium alloys: effect of processing conditions. *Journal of Materials Processing Technology*, (143-144*)*, 814–821.

141. http://www.matweb.com/search/datasheet_print.aspx?matguid=e30d1d1038164808a85cf7ba6aa87ef7

142. Malvern Mastersizer 2000. (n.d.). Retrieved from http://www.malvern.com/labeng/products/mastersizer/ms2000/mastersizer2000.htm

143. Mazahery, A., and Shabani, M. O. (2012). Study on microstructure and abrasive wear behavior of sintered Al matrix composites. *Ceramics International*, 38(5), 4263–4269.

144. McDermid, J. R., Kaye, M. H., & Thompson, W. T. (2007). Fe Solubility in the Zn-Rich Corner of the Zn-Al-Fe System for Use in Continuous Galvanizing and Galvannealing. *Metallurgical and Materials Transactions B*, *38*(2), 215–230.

145. Miracle, D. (2005). Metal matrix composites – From science to technological significance. *Composites Science and Technology*, (65), 2526–2540.

146. Miyajima, T., and Iwai, Y. (2003). Effects of reinforcements on sliding wear behavior of aluminium matrix composites. *Wear*, 255(1-6), 606–616.

147. MMC Assess. (n.d.). No Title. Retrieved from http://mmc-assess.tuwien.ac.at/mmc/Home.html

148. Mohammadi, M. S., Simchi, a., and Gierl, C. (2010). Phase formation and microstructural evolution during sintering of Al–Zn–Mg–Cu alloys. *Powder Metallurgy*, 53(1), 62–70.

149. Molybond 122L. (2006). Retrieved from http://www.itwpf.com.au/molybond_lubricants/pdfs/technical_data/1_tds.pdf

150. Mosher, W. G. E. et al., (2011). On hot deformation of aluminium-silicon powder metallurgy alloys. *Powder Metallurgy*, 54(3), 366–375.

151. Nakagawa, Takeo, T. U. and K. S. (1980). Production of short length steel fibre for composite material on a milling machine. *International Journal of Machine Tool Design and Research*, (20), 251–264.

152. Naoi, D., and Kajihara, M. (2007). Growth behavior of Fe2Al5 during reactive diffusion between Fe and Al at solid-state temperatures. *Materials Science and Engineering: A*, 459(1-2), 375–382.

153. Oberacker, R. (2011). Powder compaction by dry pressing. In Ralf Riedel and I-Wei Chen (Ed.), *Ceramics Science and Technology*, (3), 1–38.

154. Odani, Y. (1994). Powder forged Al alloy to challenge ferrous metals. *Metal Powder Report*, 36(April), 36–41.

155. Ortiz, J. L., and Salvador, M. D. (2000). Microstructure and mechanical behavior of 6061-Al reinforced with silicon nitride particles processed by powder metallurgy Scripta Materialia (42), 383–388.

156. Padmavathi, C., Upadhyaya, A., and Agrawal, D. (2011). Effect of microwave and conventional heating on sintering behavior and properties of Al–Mg–Si–Cu alloy. *Materials Chemistry and Physics*, 130(1-2), 449–457.

157. Padmavathi, C., and Upadhyaya, A. (2011). Sintering Behaviour and Mechanical Properties of Al–Cu–Mg–Si–Sn Aluminium Alloy. *Transactions of the Indian Institute of Metals*, 64(4-5), 345–357.

158. Pai, B., and Kulkarni, A. (1983). Interface stability in vacuum infiltrated stainless steel and nichrome reinforced aluminium composites. *Journal of Materials*, (2), 553–557.

159. Park, J. et al., (2001). An experimental study on the optimization of powder forging process parameters for an aluminium-alloy piston. *Journal of Materials Processing Technology*, (113), 486–492.

160. Park, J., Park, C., and Kim, Y. (2001). A study on the powder forging of aluminium alloy pistons. *International Journal of the Korean Society of Precision Engineering*, 2(4), 69–74.

161. Pemberton, S. R. et al., (2011). The fracture energy of metal fibre reinforced ceramic composites (MFCs). *Composites Science and Technology*, 71(3), 266–275.

162. Pérez, F., Hierro, M., and Pedraza, F. (1999). Aluminizing and chromizing bed treatment by CVD in a fluidized bed reactor on austenitic stainless steels. *Surface and Coatings Technology*, (121), 151–157.

163. Pickens, J. R. (1981). Review Aluminium powder metallurgy technology for high-strength applications. *Journal of Materials Science*, (16), 1437–1457.

164. Pieczonka, T., Schubert, T., Baunack, S., and Kieback, B. (2008). Dimensional behaviour of aluminium sintered in different atmospheres. *Materials Science and Engineering: A*, 478(1-2), 251–256.

165. Prasad, S. (1992). Aluminium metal matrix composites tailored for antifriction applications. *Surface and Coatings Technology*, (54-55), 442–446.

166. Prasad, V. V. B., Bhat, B. V. R., Mahajan, Y. R., and Ramakrishnan, P. (2001). Effect of extrusion parameters on structure and properties of 2124 aluminium alloy matrix composites. *Materials and Manufacturing Processes*, 16(6), 841–853.

167. Thompson R. et al., (1976). Glass-fibre-reinforced aluminium alloys formed by hot extrusion: part ii: heat-treatment. *Powder Metallurgy*, (4), 189–195.

168. Rack, H. J. (1991). Powder Techniques in Processing of Metal Matrix Composites. In R. Everett (Ed.), *Metal matrix composites: Processing and Interfaces* (pp. 85–99). Academic Press.

169. Rajan T. P. D. , Pillai R. M., P. B. C. (1998). Reinforcement coatings and interfaces in aluminium metal matrix composites. *Journal of Materials Science*, (33), 3491–3503.

170. Ralston, K. D., Fabijanic, D., Jones, R. T., and Birbilis, N. (2011). Achieving a chromium rich surface upon steels via FBR-CVD chromising treatments. *Corrosion Science*, 53(9), 2835–2842.

171. Reynoldson, R. (1995). Advances in surface treatments using fluidised beds. *Surface and Coatings Technology*, (71), 102–107.

172. Rosso, M. (2006). Ceramic and metal matrix composites : routes and properties, *Journal of Materials Processing Technology* (175), 364–375.

173. Jain S., Chandra K., Agarwla. V. (2009). Processing of aluminium matrix composites by squeeze casting. In *Proceedings of the 63rd Annual Technical Meeting, Indian Institute of Metals, Kolkata, India*. 142–143.

174. Shahani, R., and Clyne, T.W. (1991). Recrystallization in fibrous and particulate metal matrix composites. *Materials Science and Engineering A*, (135), 281–285.

175. Sahin, Y. (1998). Wear behaviour of planar-random fibre-reinforced metal matrix composites. *Wear*, (223), 173–183.

176. Sahin, Y., and Murphy, S. (1998). The effect of sliding speed and microstructure on the dry wear properties of metal-matrix composites. *Wear*, (214), 98–106.

177. Samuel, M. (2003). A new technique for recycling aluminium scrap. *Journal of Materials Processing Technology*, 135(1), 117–124.

178. Sánchez, L. et al., (2007). Effects of reactive gaseous mixture and time on the growth rate and composition of aluminium diffusion coatings by CVD-FBR on 12Cr-ferritic steel. *Surface and Coatings Technology*, 201(18), 7626–7634.

179. Sanctis, A. De, and Evangelista, E. (1996). Hot formability studies on 359/SiC/20p and their application in forging optimisation. *Applied Composite Materials*, 3(3), 179–198.

180. Sannino, P., and Rack, H. J. (1995). Dry sliding wear of discontinuously reinforced aluminium composites: review and discussion. *Wear*, *189*(1-2), 1–19.

181. Satyanarayana, K.G., Pillai R.M., Pai. B. C. (1999). Metal matrix composites- an overview. In R. S. Agarwala, R.C., Agarwala V., Kumar S. (Ed.), *Institute Industry*

Interaction Meet, University of Roorkee, (pp. 1–12). Department of Metallurgical and Materials Engineering, University of Roorkee, RRL CSIR Thiruvananthapuram.

182. Sawtell, R., Hunt Jr, W., and Rodjom, T. (1996). Method of producing structural metal matrix composite products from a blend of powders. *US Patent 5,561,829*

183. Schaffer, G. (2004). Powder processed aluminium alloys. *Materials Forum*, (28), 65–74.

184. Schaffer, G., and Hall, B. (2002). The influence of the atmosphere on the sintering of aluminium. *Metallurgical and Materials Transactions A*, 33(October), 3279–3284.

185. Schaffer, G., Hall, B., Bonner, S., Huo, S., and Sercombe, T. (2005). The effect of the atmosphere and the role of pore filling on the sintering of aluminium. *Acta Materialia*, (54), 131–138.

186. Schaffer, G., and Huo, S. (1999). On development of sintered 7xxx series aluminium alloys. *Powder Metallurgy*,(42) 3, 219–226.

187. Schaffer, G., Sercombe, T., and Lumley, R. (2001). Liquid phase sintering of aluminium alloys. *Materials Chemistry and Physics*, (67), 85–91.

188. Sercombe, T. (2003). On the sintering of uncompacted, pre-alloyed Al powder alloys. *Materials Science and Engineering: A*, 341(1-2), 163–168.

189. Sercombe, T., and Schaffer, G. (1999a). On the use of trace additions of Sn to enhance sintered 2xxx series Al powder alloys. *Materials Science and Engineering: A*, 268(1-2), 32–39.

190. Sercombe, T., and Schaffer, G. (1999b). The effect of trace elements on the sintering of Al–Cu alloys. *Acta Materialia*, 47(2), 689–697.

191. Seyed Reihani, S. M. (2006). Processing of squeeze cast Al6061–30vol% SiC composites and their characterization. *Materials and Design*, 27(3), 216–222.

192. Shahmohammadi, M., Simchi, A., Danninger, H., and Arvand, a. (2007). An investigation on the sintering behavior of high strength Al-Zn-Mg-Cu alloy prepared from elemental powders. *Materials Science Forum*, (*534-536)*, 489–492.

193. Shahverdi, H., (2002a). Microstructural analysis of interfacial reaction between molten aluminium and solid iron. *Journal of Materials Processing Technology*, 124(3), 345–352.

194. Shahverdi, H. R. et al., (2002b). Kinetics of interfacial reaction between. *Journal of Materials Science*, (37), 1061–1066.

195. Sheppard, T., and McShane, H. (1976). Analyses of pressure requirements for powder compact extrusions. *Powder Metallurgy*, (3), 121–125.

196. Sheppard, T., McShane, H., Zaidi, M., and Tan, G. (1983). The extrusion of atomised aluminium alloy compacts and composites. *Journal of Mechanical Working Technology*, (8), 43–70.

197. Sheppard, T., Zaidi, M. a., and Tan, G. H. (1983). Production of high strength aluminium alloys by extrusion of atomized powders. *Powder Metallurgy*, 26(1), 10–16.

198. Sherafat, Z., Paydar, M. H., and Ebrahimi, R. (2009). Fabrication of Al7075/Al, two phase material, by recycling Al7075 alloy chips using powder metallurgy route. *Journal of Alloys and Compounds*, 487(1-2), 395–399.

199. Shercliff, H. R., and Ashby, M. F. (1994). Design with metal matrix composites. *Materials Science and Technology*, 10(June), 443–451.

200. Showaiter, N., and Youseffi, M. (2008). Compaction, sintering and mechanical properties of elemental 6061 Al powder with and without sintering aids. *Materials and Design*, 29(4), 752–762.

201. Siegert, K., and Ringhand, D. (1994). Flashless and precision forging of connecting rods from P/M aluminium alloys. *Journal of Materials Processing Technology*, (46), 157–167.

202. Singh, J., and Alpas, A. T. (1995). Elevated temperature wear of Al6061. *Scripta Metallurgica et Materiala*, 32(7), 1099–1105.

203. Singh, J., and Alpas, A. T. (1996). High-Temperature Wear and Deformation Processes in Metal Matrix Composites. *Metallurgical and Materials Transactions A*, (27), 3135–3148.

204. Springer, H., Kostka, A., and Payton, E. J. (2011). On the formation and growth of intermetallic phases during interdiffusion between low-carbon steel and aluminium alloys. *Acta Materialia*, 59(4), 1586–1600.

205. Springer, H. et al., (2011). Influence of intermetallic phases and kirkendall-porosity on the mechanical properties of joints between steel and aluminium alloys. *Materials Science and Engineering: A*, 528(13-14), 4630–4642.

206. Srivatsan, T. S., Ibrahim I.A., Mohamed F.A., L. E. J. (1991). Processing techniques for particulate-reinforced metal aluminium matrix composites. *Journal of Materials Science*, (26), 5965–5978.

207. Stanford-Beale, C. A., and Clyne, T. W. (1989). Extrusion and high-temperature deformation of fibre-reinforced aluminium. *Composites Science and Technology*, 35(2), 121–157.

208. Stoloff, N. S., Liu, C. T., and Deevi, S. C. (2000). Emerging applications of intermetallics. *Intermetallics*, (8), 1313–1320.

209. Stoloff, N. (1998). Iron aluminides: present status and future prospects. *Materials Science and Engineering: A*, (258), 1–14.

210. Suh, N. P. (1977). An overview of the delamination theory of wear. *Wear*, (44), 1–16.

211. Surappa, M. (2003). Aluminium matrix composites: challenges and opportunities. *Sadhana*, 28(February/April), 319–334.

212. Suzuki, K., Huang, X. S., Watazu, A., Shigematsu, I., and Saito, N. (2007). Recycling of 6061 aluminium alloy cutting chips using hot extrusion and hot rolling. *Materials Science Forum*, (544-545), 443–446.

213. Massalski T.B., U. R. K. (1990). *Binary Alloy Phase Diagrams*. (H. Baker, Ed.) (p. 147). ASM International, Materials Park, OH.

214. Tang, F., Liao, C.-P., Ahn, B., Nutt, S. R., and Schoenung, J. M. (2007). Thermal stability in nanostructured Al-5083/SiC composites fabricated by cryomilling. *Powder Metallurgy*, 50(4), 307–312.

215. Tavangar, R., Weber, L., and Mortensen, A. (2005). Damage evolution in Saffil alumina short-fibre reinforced aluminium during tensile testing. *Materials Science and Engineering: A*, 395(1-2), 27–34.

216. Tekkaya, A. E., Schikorra, M., Becker, D., Biermann, D., Hammer, N., and Pantke, K. (2009). Hot profile extrusion of AA-6060 aluminium chips. *Journal of Materials Processing Technology*, 209(7), 3343–3350.

217. Ter Haar, J. H., and Duszczyk, J. (1992). Cold compaction of an aluminium/short fibre alumina powder composite. *Journal of Materials Science*, 27(23), 6495–6505.

218. Thompson, R., Badzioch, S., Biddulph, R. H., Creffield, G. K., Martin, J. B., and Wickens, a. J. (1976). Glass-fibre-reinforced aluminium alloys formed by hot extrusion: part i: preparation and properties. *Powder Metallurgy*, 19(4), 181–188.

219. Tiwari, S., Tiwari, A., and Gopinathan, V. (1987). High temperature interfacial studies in aluminium-stainless steel composites. *Journal of Materials Science*, (22), 1–5.

220. Topping, T. D., Ahn, B., Nutt, S. R., and Lavernia, E. J. (2013). Influence of hot isostatic pressing on microstructure and mechanical behaviour of nanostructured Al alloy. *Powder Metallurgy*, 56(4), 276–287.

221. Torralba, J., da Costa, C., and Velasco, F. (2003). P/M aluminium matrix composites: an overview. *Journal of Materials Processing Technology*, 133(1-2), 203–206.

222. Toshimasa M., E. Y. and T. S. (1985). Preparation of fine steel wire-reinforced composite by the powder rolling of aluminium. *Journal of Japan Iistitute of Light metals*, 37(3), 199–206.

223. Türk, A., Ok, O., and Bindal, C. (2005). Structural characterization of fluidized bed nitrided steels. *Vacuum*, 80(4), 332–342.

224. Ünal, A. (1990). Production of rapidly solidified aluminium alloy powders by gas atomisation and their applications. *Powder Metallurgy*, 33(1).

225. Upadhyaya, G. S. (1997). *Powder Metallurgy Technology* (First., pp. 96–117). Cambridge International Science Publishing.

226. Usta, M., Oney, I., Yildiz, M., Akalin, Y., and Ucisik, A. H. (2004). Nitriding of AISI 316L surgical stainless steel in fluidized bed reactor. *Vacuum*, 73(3-4), 505–510.

227. Vaillant, P., and Petitet, J. (1995). Interactions under hydrostatic pressure of a mild steel with liquid aluminium alloys. *Journal of Materials Science*, (30), 4659–4668.

228. Vedani, M., and Gariboldi, E. (1996). Damage and ductility of particulate and short-fibre al-al2o3 composites. *Acta Materialia*, 44(8), 3077–3088.

229. Venugopal, P., Venugopal, S., and Seetharaman, V. (1990). Influence of strain rate and temperature on the friction factor of commercialy pure titanium. *Journal of Materials Processing Technology*, (22), 91–97.

230. Viala, J., Peronnet, M., and Barbeau, F. (2002). Interface chemistry in aluminium alloy castings reinforced with iron base inserts. *Composites Part A:*, (33), 1417–1420.

231. Vijayaram, T. R. et al., (2006). Fabrication of fiber reinforced metal matrix composites by squeeze casting technology. *Journal of Materials Processing Technology*, (178), 34–38.

232. Wang, A., and Rack, H. J. (1991a). Abrasive wear of silicon carbide particulate and whisker reinforced 7091 aluminium matrix composites. *Wear*, (146), 337–348.

233. Wang, A., and Rack, H. J. (1991b). Dry sliding wear in 2124 Al-Sicw /1 7-4 PH stainless steel syatems. *Wear*, (147), 355–374.

234. Weber, L., Tavangar, R., and Mortensen, a. (2005). Ductility of Saffil short fibre reinforced metals. *Scripta Materialia*, 53(1), 17–21.

235. Whitehouse, A. F., and Clyne, T. W. (1993). Effects of reinforcement content and shape on cavitation and failure in metal-matrix composites. *Composites*, 24(3), 256–261.

236. Whitehouse, A., and Clyne, T. (1994). Effect of test conditions on cavitation and failure during tensile loading of discontinuous metal matrix composites. *Materials Science and Technology*, 10(June), 468–474.

237. Williams, J., Piotrowski, G., Saha, R., and Chawla, N. (2002). Effect of overaging and particle size on tensile deformation and fracture of particle-reinforced aluminium matrix composites. *Metallurgical and Materials Transactions A*, 33(December), 3861–3869

238. Wong, W., Gupta, M., and Lim, C. (2006). Enhancing the mechanical properties of pure aluminium using hybrid reinforcement methodology. *Materials Science and Engineering: A*, (423), 148–152.

239. Woods, T. O., Berghaus, D. G., and Peacock, H. B. (1998). Interparticle movement and the mechanical behavior of extruded powder aluminium at elevated temperature. *Experimental Mechanics*, 38(2), 110–115.

240. Yamasaki, M., and Kawamura, Y. (2004). Effect of Vacuum Degassing on Surface Characteristics of Rapidly Solidified Al-Based Alloy Powders. *Materials Transactions*, 45(4), 1335–1338.

241. Youseffi, M., Showaiter, N., and Martyn, M. T. (2006). Sintering and mechanical properties of prealloyed 6061 Al powder with and without common lubricants and sintering aids. *Powder Metallurgy*, 49(1), 86–95.

242. Yoon, B. E. and Kim, M. H. (1996) Reinforced material for an automobile connecting rod, *United States Patent 5523171*.

243. Yu, S., He, Z., and Chen, K. (1996). Dry sliding friction and wear behaviour of short fibre reinforced zinc-based alloy composites. *Wear*, 198(1-2), 108–114.

244. Yu, S., Li, W., and He, Z. (2007). Study on tensile strengths of Al2O3 short fiber reinforced Zn–Al alloy composites at elevated temperatures. *Journal of Alloys and Compounds*, 431(1-2), 8–11.

245. Yue, T. M., and Chadwick, G. A. (1996). Squeeze casting of light alloys and their composites, *Journal of materials processing technology* (58), 302–307.

246. Zhu, Y., Zong, G., Manthiram, A., and Eliezer, Z. (1994). Strength analysis of random short-fibre-reinforced metal matrix composite materials. *Journal of Materials Science*, (29), 6281–6286.

247. Zubizarreta, C. et al., (2009). Effect of the heat treatment prior to extrusion on the direct hot-extrusion of aluminium powder compacts. *Journal of Alloys and Compounds*, 467(1-2), 191–201.